Development of an Inertial Generator for Embedded Applications in Rotating Environments

by

Stephen D. Conrad

B.S. Mechanical Engineering
University of Cincinnati, 2005

Submitted to the Department of Mechanical Engineering
in Partial Fulfillment of the Requirements for the Degree of

Master of Science in Mechanical Engineering

at the

MASSACHUSETTS INSTITUTE OF TECHNOLOGY

June 2007

© 2007 Massachusetts Institute of Technology.
All rights reserved.

Signature of Author:……………………………………………
Department of Mechanical Engineering
May 21, 2007

Certified by:……………………………………………
Steven R. Hall
Professor of Aeronautics and Astronautics
Thesis Supervisor

Read by:……………………………………………
David L. Trumper
Professor of Mechanical Engineering
Department Thesis Reader

Accepted by:……………………………………………
Lallit Anand
Professor of Mechanical Engineering
Department Committee on Graduate Students

Development of an Inertial Generator for Embedded Applications in Rotating Environments

by

Stephen D. Conrad

Submitted to the Department of Mechanical Engineering
on May 21, 2007, in Partial Fulfillment of the
Requirements for the Degree of
Master of Science in Mechanical Engineering

Abstract

Inertial generators are devices that generate electrical energy from their inertial motion, and have only one mechanical connection with their surroundings. This makes them suitable power sources for embedded systems operating in environments that experience some inertial excitation. Typical inertial generators are designed to generate electricity from linear vibrations, and are often termed vibrational energy harvesters. Traditional sprung mass vibrational energy harvesters must be tuned to achieve resonance at a specific frequency, and perform poorly when the excitation does not fall within a narrow band around this natural frequency.

In this thesis, a novel inertial generator is proposed that is specifically designed to take advantage of the unique inertial loads experienced by a system embedded within a large scale rotating part with a horizontal axis of rotation, such as the propeller of a large ship. The design process begins with the identification of the inertial path and then proceeds with the development of a device that takes advantage of the unique inertial loads experienced along that path. The device is designed to achieve resonance at any steady state rotation rate, without any active forms of actuation. This is achieved by utilizing centrifugal forces to produce a natural frequency that tracks the excitation frequency.

Experimental results from full-scale spin testing verify that the device has a monotonically increasing power output with increasing frequency. This result contrasts sharply with the frequency response of a traditional sprung mass vibrational energy harvester, which typically has a single peak at the resonant frequency. Experimental results are also presented showing that the device can successfully deliver a charging current to a battery over a wide range of operating speeds.

Thesis Supervisor: Steven R. Hall
Title: Professor of Aeronautics and Astronautics
Margaret MacVicar Faculty Fellow

Acknowledgments

This research would truly not have been possible without the support, advice and inspiration that I received from numerous individuals throughout the project. I would like to extend special thanks to my adviser Prof. Steven Hall for making this project available to me and supporting this work with his advice and his many resources. I would like to thank Bob O'Handley, Jiankang Huang, and Kevin O'Handley at Ferro Solutions, Inc., for their input at all stages of the project, and for sharing their expertise in vibrational energy harvester design. I would also like to thank Prof. David Trumper for acting as a reader for this thesis and for teaching me a great many things in his courses that were useful throughout the completion of this research. I also have much gratitude to express to Prof. Alan Epstein for allowing me to conduct the spin testing in the gas turbine laboratory in a safely contained environment.

Along the course of this research, there have been a number of individuals who have supported my efforts to procure, construct, and build the equipment necessary for laboratory testing. I would like to extend thanks to James Letendre for supplying me with every sort of tool imaginable, including several that I have never before imagined, and entrusting me with their proper use. Many thanks to Todd Billings for allowing me to fabricate a great deal of hardware in the Aero-Astro machine shop despite the fact that I kept bringing in large pieces of structural steel into a shop that is accustomed to aluminum. I also appreciate his instruction on the use of the various CNC machines that allowed me to improve my designs considerably, and his help on completing a great many machining tasks that at first seemed impossible. My thanks to Dave Robertson for his help locating useful items and occasionally lifting the especially heavy ones, all while maintaining a good natured hostility toward grad students and those who study mechanical engineering in particular. Thanks also to Dick Perdichizzi for help locating hard to find items and for advice regarding safety concerns.

The students in the Aerospace Controls Lab in building 41 were wonderful neighbors and supported me in many ways. It was always relaxing to take breaks to see

their computer controlled flying contraptions perform increasingly amazing maneuvers in such a confined space. I also appreciate the many times they offered their advice and assistance on microcontroller programming and electrical circuit design. I would like to recognize my friends Mario and Brett in particular for going out of their way to get to know me and for sharing their love for ice hockey.

I would like to thank Tony, Tatsuya, and Jinshan for being both great roommates and great friends, and Tao for making my life a great deal more interesting than it would otherwise have been. I also appreciate the stress relieving role that my friends in the SUSHIS hockey team and the MIT Easyriders motorcycle club have played in my life and will hopefully continue to play in the future.

I owe much to my family who have always supported my endeavors and who has been the stable platform in my life from which I have always felt secure to reach toward my dreams. Ultimately I owe everything to my Lord and Savior who has granted me the opportunity, the ability, and the strength to accomplish every good thing in my life.

This research was supported by Ferro Solutions, Inc., through funding provided from the Navy STTR phase II project. Topic: N04-T022 energy scavenging. Contract number: N00014-05-C-0420.

Contents

Chapter 1

Introduction

1.1 Background

With the ever-advancing fields of embedded sensors, low power electronics, and wireless communications, there is a healthy demand for completely self-contained systems capable of supplying power to such devices. For some applications, it is feasible to use batteries as a source of energy; however, when the target device has a lifetime power requirement that exceeds the capabilities of a battery, and it is not possible or economical to perform battery changes, it becomes necessary to generate the needed electricity from the energy available in the devices immediate environment [10]. This is the case in many applications such as embedded sensor networks, medical implants, distributed micro computers, and even wearable electronics [17, 15, 5]. Energy sources that may be available in a remote environment and can be harnessed to generate electrical energy include thermal gradients, solar radiation, ambient flow, and mechanical vibrations [9].

Generating electricity on location to power an embedded system from vibration has popularly been approached with the idea that energy can be obtained for free. The devices used to generate electricity from environmental vibration have often been called *energy scavengers* or *energy harvesters*, giving the impression that energy is gained without expense [8]. The term *energy reclamation* gives some acknowledgment to the fact that vibration in a mechanical structure is often due to undesirable losses in an unrelated system and that converting this vibrational energy into usable electricity is a way of reclaiming energy that would otherwise be lost [2]. While it is true that unwanted vibration can yield useful electrical energy, it must be taken into consideration that the manufacturing cost of the energy harvester itself may greatly exceed the value of the electricity generated. The true value of such devices is not their ability to save small quantities of wasted energy, but rather their ability to supply electrical power to embedded systems indefinitely with no external electrical connections. A more appropriate name for such devices is the term *inertial generator*, which both acknowledges that the devices convert energy from one form to another, and that they depend upon inertial motion to generate electricity, with only one external physical connection to their environment [17].

Inertial generators use any of several methods to converting inertial motion into electrical energy, including the use of electromagnetic, piezoelectric, magnetostrictive, or electrostatic transducers [8]. Many inertial generators focus on single axis vibration as a source of energy, but other interesting configurations have emerged that focus on other excitations such as mechanical impact [13]. The configuration optimized for impacts is attractive, because it attempts to avoid one of the most significant challenges faced by conventional vibrational inertial generators, which is the uncertainty in the vibrational excitation. Most inertial generators have a sprung mass configuration that allows them to achieve resonance at a specific frequency, and, if the excitation frequency deviates from the natural frequency of the device, there is a sharp decline in power output [12].

One strategy to deal with this narrow range of useful operation is to store energy when the vibrations fall in the favorable frequency range, and to expend this stored energy when they do not [16]. An alternate strategy is to modify the device parameters to optimize the power conversion at each frequency. Modification of the power storage circuitry has been shown to alter the damping of the device, allowing the device to be somewhat more useful at frequencies away from its natural frequency. However, using electrical actuation to modify the natural frequency itself has been shown never to result in higher net power conversion [7, 11]. Modifying the physical properties of the device through actuation that only requires power at the time the change is made, is a feasible solution, but it adds a large amount of complexity to the system [9].

1.2 Motivation

The motivation for the work contained in this body of research stems from the desire to develop a device which is capable of powering a system that is completely embedded within a large rotating part that rotates about a horizontal axis, such as the propeller of a large ship. The powered subsystem may require any range of power, from the small amounts required for health monitoring and wireless transmissions, to the large quantities that would be required to drive actuators for the purpose of modifying the flow characteristics of the propeller [6]. The inaccessibility of the propeller of a large ship, the harsh environment during operation, and the long service life required from the power source make batteries an unacceptable solution. Due to the completely enclosed environment with no significant thermal gradients or sources of radiation, it is necessary to rely on an inertial generator as a source of power.

The goals for this research are to develop and test a device suitable for embedded installation within a large scale propeller. The device may need to be mounted at any radius from the hub of the propeller, and a one meter radius was chosen as a focus for the research as a representative quantity. The target operating rotation rate of the device was chosen to be 250 RPM. Large ships often cruise for extended periods of time at a constant throttle setting, so the device should be capable of achieving resonance and producing appreciable power at steady state operation for a wide range of rotation rates, both above and below the chosen target. The designed device should also have a mechanical structure that is capable of operating under the centrifugal loads experienced at the target radius and rotation rate and have a long expected service life.

1.3 Previous Work and Chosen Approach

Prior to the work presented in this thesis, research was conducted toward this goal and a device was designed to generate electrical power from the fore-aft vibration of the propeller blade [1]. This device was designed with linearized natural frequency that would allow the device to target vibration at five times the rotation rate. This approach of using the free vibrations of the propeller was found to be unsatisfactory due to the low amounts of power that were available in the vibration of the structure. In order to generate significantly more power at the low frequency of the target rotation rate, a more powerful excitation was necessary.

The previous work conducted on this problem was done from the mindset of *vibrational energy harvesting*, and naturally the fore-aft vibration mode of the propeller would be expected to contain the most unwanted vibrational energy. The work presented in this thesis takes the more general mindset of *inertial generation* and arrives at a much more satisfactory result. From the mindset of inertial generation, it is natural to first look at the inertial trajectory of the device, which includes all forced motions including vibration, and then to design a device that takes the greatest advantage of that inertial trajectory.

1.3.1 The Inertial Trajectory

For this project, the device that is to generate the electricity is to be embedded at some radius r in the interior of the propeller of a large ship, and several important observations about the inertial motion of the device can be made. First, the path of the device is circular, and that the circular path has a horizontal axis of rotation. Second, the rotational inertia of a typical large scale propeller is more than sufficient to ensure that any reaction forces caused by the device do not affect the steady rate of rotation of the propeller. The inertial path of the device is illustrated in Figure 1-1, which shows the device embedded in the propeller at radius r, defines the rotation rate of the propeller as ω, and shows the angle of the point of attachment from the vertical as ϕ.

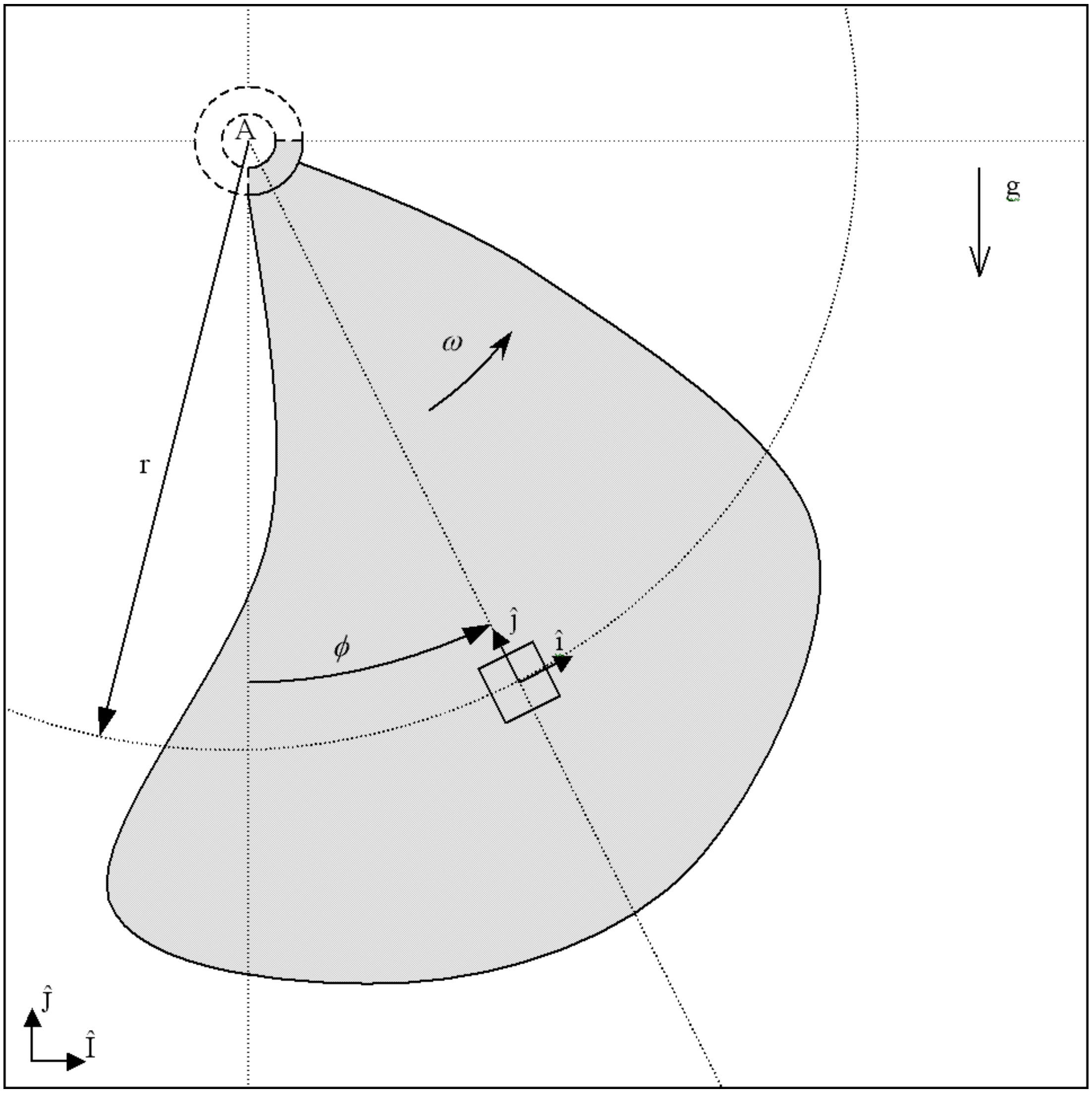

Figure 1-1: The box in the figure represents the location at which the device is embedded within the propeller blade as viewed from the inertial frame $\hat{I}, \hat{J}$. The device frame $\hat{\imath}, \hat{\jmath}$ is attached to the device and rotates with the device.

At this point the problem can be viewed from two perspectives. The first perspective is in the $\hat{I}, \hat{J}$ reference frame shown in Figure 1-1. This is a fixed point of reference that sees the propeller rotating in the counterclockwise direction about its center, and sees the device both traveling in a circular path and rotating as it processes along that path. From this fixed point of reference, gravity is a conservative potential field, and the net work done on the device can only be found by evaluating the reaction forces acting on the device over a full revolution.

A perspective that offers much more intuition on the situation is to view the problem from the $\hat{\imath}, \hat{\jmath}$ reference frame. This reference frame is attached to the device and rotates with it. From this perspective, the device is stationary, and the centrifugal forces that the device experiences can be viewed as being the result of a conservative potential field that extends radially outward from the center of rotation of the propeller. The gravitational acceleration vector now rotates in the clockwise direction with a positive rate of ω, as shown in Figure 1-2. Now it is clear that, along a given axis of the device, gravity produces a sinusoidal excitation at a fixed amplitude of 1 g and at an exact frequency of ω. Viewed from the device frame $\hat{\imath}, \hat{\jmath}$, the excitation force due to gravity is not conservative, and can do net work on the internal components of the device. It is now possible to take advantage of the fact that the excitation acceleration is both large and well known in the development of a device that will efficiently take in energy from this excitation and convert it into usable electrical energy.

In Chapter 2, various device configurations are evaluated, and a configuration is chosen that takes advantage of the circular inertial path experienced in the stated application. Chapter 3 presents the details of the design of a prototype that is used to verify the expected dynamics and performance of the chosen configuration. The experimental equipment developed for use in testing the prototype device is presented in Chapter 4. Chapter 5 discusses the key results of the experimental testing and discusses their importance. The concluding remarks, summarizing the findings of this body of research are included in Chapter 6.

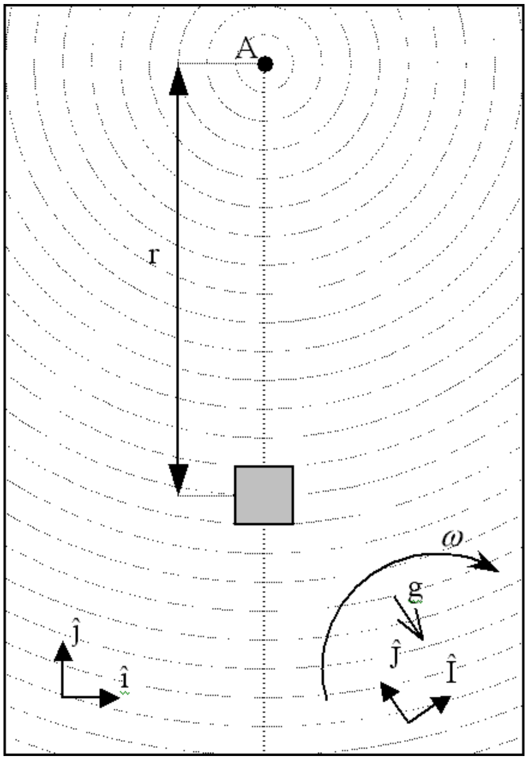

Figure 1-2: Viewed from the device frame $\hat{\imath}, \hat{\jmath}$ the fixed frame $\hat{I}, \hat{J}$ and the gravitational acceleration vector are seen to rotate clockwise at an angular rate of ω, and the centrifugal acceleration appears as a potential field.

Chapter 2

Device Configuration

2.1 Explored Device Configurations

As explained in Chapter 1, any device that has internal motion as a result of being driven through an inertial trajectory can be used as an inertial generator by damping the motion through electromagnetic or piezoelectric means. In this section, several devices of various configurations are compared to determine the characteristics that are important to the function of the inertial generator. In order to make fair comparisons between the devices that will be explored, it is necessary to develop a method of comparing the amount of energy that each configuration can generate per revolution at a given mass and length scale.

The maximum amount of work that the excitation force can do on the device twice per revolution is the product of the gravitational constant, the mass of the device, and the distance over which the center of gravity of the device can move. To draw fair comparisons between the devices that are explored below, they are normalized such that they all have the same moving mass M, and a maximum length L. With these constraints in place, the maximum displacement of the center of gravity of the moving mass can be used as a measure of the maximum amount of work that the excitation force can do on the device.

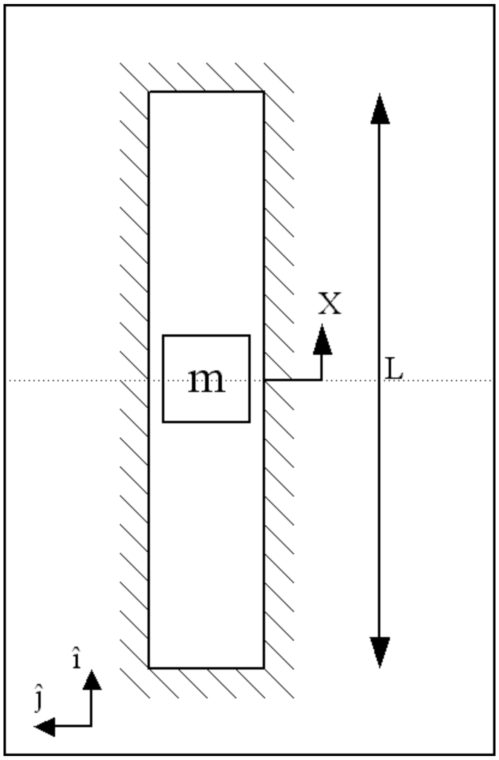

Figure 2-1: Diagram of falling mass configuration.

2.1.1 Falling Mass

One simple configuration is a magnet of mass M constrained to slide in a tube of length L as shown in Figure 2-1. At slow speeds, the acceleration of gravity causes the mass to slide back and forth hitting the ends of the tube, and energy can be removed from the system through a coil that damps the motion of the mass. The problem with this class of systems is that, at high frequencies, there is not enough time in each half cycle for the mass to travel the entire length of the tube.

The dynamics of the falling mass system are

$$m\ddot{x} = f \tag{2.1}$$

in the time domain, and taking the Laplace transform, the system transfer function can be written as

$$\frac{X}{F} = \frac{1}{ms^2} \tag{2.2}$$

The target operating speed is 250 RPM, which is an angular velocity of

$$\omega = 26 \ \frac{\text{rad}}{\text{sec}} \tag{2.3}$$

At this frequency, and for an excitation of 1 g, the magnitude of the displacement of the mass is found to be

$$|x| = \left| \frac{g}{s^2} \right| = 0.0143 \text{ m} \tag{2.4}$$

This displacement of 14 mm is only achieved when no damping is applied, and therefore no power is produced. The application of damping will further reduce the amplitude, and the amount of work done on the system by the excitation force, which is proportional to the displacement, is limited. For a system on the general length scale of a approximately 10 cm to effectively take in energy at frequencies in the range of the the target operation condition of 250 RPM, it must have a resonant response that boosts the amplitude of motion significantly. Adding a spring that connects the mass to the frame of the device as shown in Figure 2-2 results in a system with natural frequency

$$\omega_n = \sqrt{\frac{k}{m}} \tag{2.5}$$

When the mass spring system is driven at its natural frequency, large amplitudes can be achieved and greater amounts of work can be done on the device in each revolution, however when the driving frequency is not sufficiently near the natural frequency the amplitude, and power output drops back to unsatisfactory levels.

2.1.2 Simple Pendulum

The simple pendulum shown in Figure 2-3 has a natural frequency for small motion is given by

$$\omega_n = \sqrt{\frac{g}{L}} \tag{2.6}$$

when it is swinging about a fixed point in a gravitational field. This is interesting, because the natural frequency changes as the strength of the potential field changes.

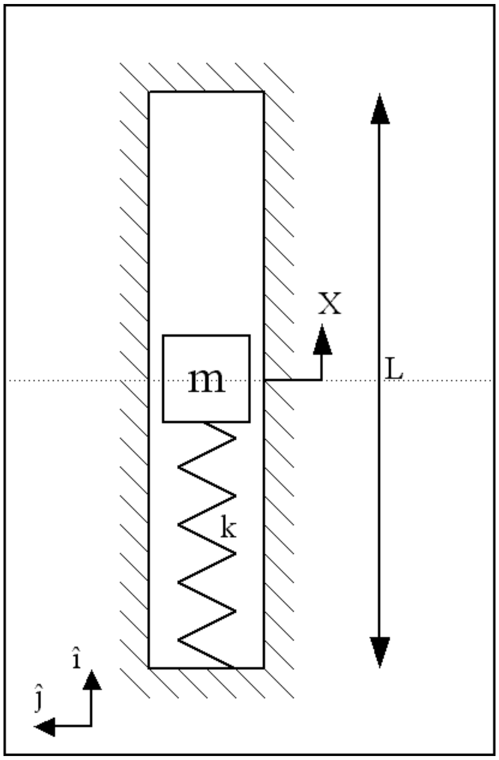

Figure 2-2: Diagram of sprung mass configuration.

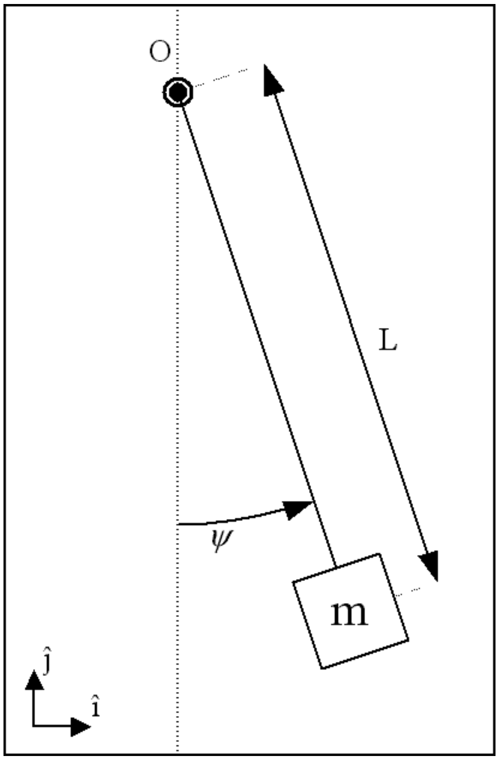

Figure 2-3: Diagram of simple pendulum configuration.

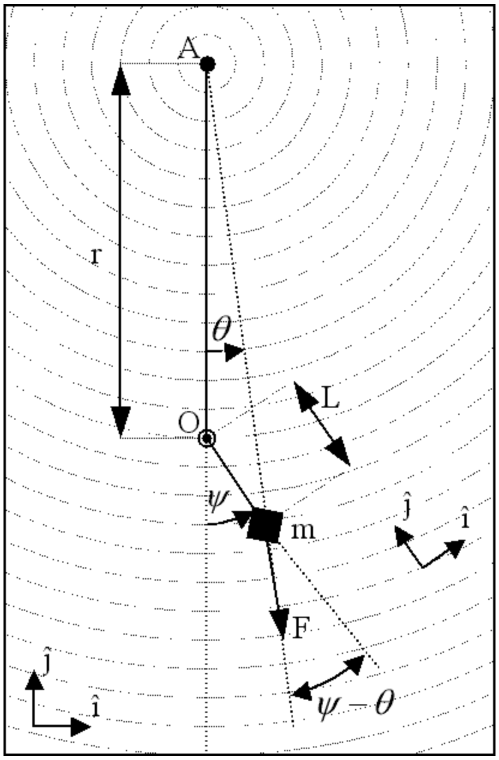

Figure 2-4: Diagram of a simple pendulum of length L swinging about point O in a potential field that expands radially from point A which is at a fixed distance of r from point O.

In considering the pendulum as a possible configuration, it is necessary to determine how the pendulum will behave when it is swinging in a centrifugal potential field as opposed to a gravitational potential field.

2.1.2.1 Restoring Torques on a Simple Pendulum in a Centrifugal Potential Field

As shown in Figure 2-4, the force acting on the mass of the simple pendulum is applied at an angle θ from vertical due to the curvature of the potential field. The restoring torque acting on the pendulum is given by

$$T = -L\sin\left(\psi - \theta\right)F \tag{2.7}$$

and the magnitude of the force due to the centrifugal potential field can be calculated as

$$F = \omega^2 m \left(r\cos\theta + L\cos\left(\psi - \theta\right)\right) \tag{2.8}$$

From the geometry of the system, it can be shown that

$$r\sin\theta = L\sin\left(\psi - \theta\right) \tag{2.9}$$

Solving for L, we have

$$L = r\frac{\sin\theta}{\sin\left(\psi - \theta\right)} \tag{2.10}$$

Combining Equation (2.7), Equation (2.8), and Equation (2.10), and using standard trigonometric identities, the expression for the restoring torque can be simplified to

$$T \;=\; -m\omega^2 rL\sin\psi \tag{2.11}$$

Comparing this result to the restoring torque of a simple pendulum in a gravitational field which is given as

$$T = -mgL\sin\psi \tag{2.12}$$

it is interesting to find that the two relations have similar form despite the differing geometries of the potential fields.

2.1.2.2 Simple Pendulum Performance

From the similarity between Equation 2.11 and Equation 2.12, it can be shown that a simple pendulum attached to a rotating part, as shown in Figure 2-4, will have a natural frequency for small motion given by

$$\omega_n = \sqrt{\frac{\omega^2 r}{L}} = \omega\sqrt{\frac{r}{L}} \tag{2.13}$$

The key result is that the system has a natural frequency that is always proportional to the driving frequency. However, in the case of interest, $r \gg L$, and the natural

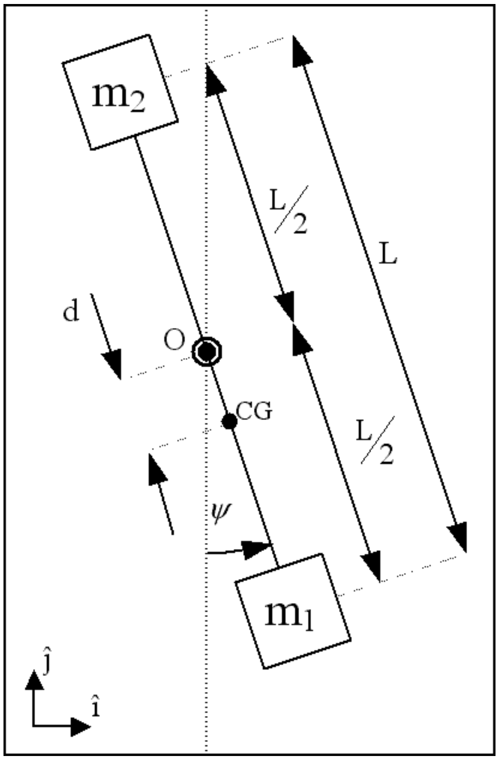

Figure 2-5: Diagram of a counterbalanced pendulum with unequal point masses and equal arm lengths.

frequency of the pendulum is always higher than the driving frequency. This mismatch of natural frequency leads to the same problems seen in the falling mass configuration and amplitude and power intake suffer.

2.1.3 Distributed Pendulum

The natural frequency of a distributed pendulum for small angles of motion when swinging in a gravitational field is given by

$$\omega_n = \sqrt{\frac{mgd}{I_O}} \tag{2.14}$$

where d is the distance between the pivot O and the center of gravity of the pendulum. The rotational inertia about the pivot is found from

$$I_O = \int_V \rho l^2 \, dV \tag{2.15}$$

where ρ is the density of the part, l is the distance from the differential unit of volume to the rotational axis passing through the point O, and the integration is taken over the volume V of the pendulum. In the case where the pendulum is swinging in a centrifugal potential field, the natural frequency can be written as

$$\omega_n = \sqrt{\frac{m\omega^2 rd}{I_O}} = \omega\sqrt{\frac{mrd}{I_O}} \tag{2.16}$$

For the case where the relation

$$mrd = I_O \tag{2.17}$$

is satisfied, the natural frequency will match the rotational rate under all operating conditions, and resonance can be achieved.

A simple configuration that nearly optimizes the distributed pendulum configuration with length constraint L and mass constraint m is shown in Figure 2-5. The mass of the pendulum is represented by two point masses m_1 and m_2 situated at a distance of

$$l = \frac{L}{2} \tag{2.18}$$

from the pivot and the rotational inertia about the pivot becomes

$$I_O = (m_1 + m_2)\left(\frac{L}{2}\right)^2 = \frac{mL^2}{4} \tag{2.19}$$

By varying the distribution of the total mass m between the two points m_1 and m_2 the distance d between the pivot and the center of gravity can be set to satisfy Equation (2.17). The resulting value of the distance from the center of gravity to the pivot is

$$d = \frac{I_O}{mr} = \frac{L^2}{4r} \tag{2.20}$$

At the target radius of 1 m and taking the length scale L of the device to be 0.1 m, evaluation of Equation (2.20) yields an offset distance of

$$b = 0.0025 \text{ m} \tag{2.21}$$

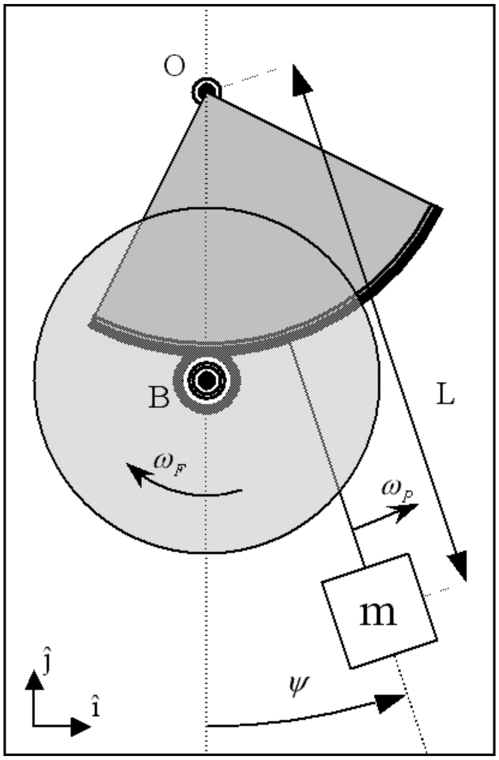

Figure 2-6: Diagram of a simple pendulum which swings about the point O that drives a flywheel which rotates about point B. The thickest lines in the figure represent the teeth of the limited angle gear attached to the pendulum and the full gear attached to the flywheel.

This result shows that for a distributed pendulum, even though resonance is attainable at any input frequency and large angular motion can be achieved, the maximum motion of the center of gravity of the device remains quite small, resulting in poor performance.

2.1.4 Simple Pendulum With Geared Flywheel

Another method that will increase the rotational inertia of a pendulous system is to employ a flywheel driven from the pendulum through a gear ratio, as shown in Figure 2-6. The kinetic energy of the system can be written in terms of the rotational inertia of the pendulum about its pivot I_O, the rotational inertial of the flywheel about its axis of rotation I_B, and the angular velocities of the pendulum and the flywheel ω_P and ω_F respectively. Using the gear ratio R to relate the rotational velocities of the pendulum and the flywheel, the flywheel's rotation rate can be written as

$$\omega_F = R\omega_P \tag{2.22}$$

With use of this relation, the kinetic energy of the system can be written in terms of only the angular velocity of the pendulum as

$$E_{\mathrm{K}} = \frac{1}{2}{I_O}^2 + \frac{1}{2}{I_B}^2 = \frac{1}{2}\left(I_O + I_B R^2\right)\omega_P^2 \tag{2.23}$$

and the equivalent rotational inertia I'_O can be defined as

$$I'_O \equiv I_O + I_B R^2 \tag{2.24}$$

The natural frequency of the system can then be expressed as

$$\omega_n = \sqrt{\frac{m\omega^2 rL}{I'_O}} = \omega\sqrt{\frac{mrL}{I'_O}} \tag{2.25}$$

and the relation that must be satisfied to achieve resonance at every driving frequency becomes

$$mrL = I'_O = I_O + I_B R^2 \tag{2.26}$$

These relations show that, by taking advantage of a gear ratio, a flywheel can be employed to set the natural frequency of the system to be always equal to the driving frequency of the excitation. Furthermore, if a conventional generator of rotational inertial I_B is used in place of the flywheel, the energy can be conveniently removed from the system at that point. This system does not suffer from any of the problems that have reduced the motion of the center of gravity of the previously considered configurations. The theoretical maximum displacement amplitude of the center of the pendulum mass is the full length parameter L.

2.1.5 Conclusions

From the analysis of the configurations presented above, it has been seen that it is possible to devise a system that when spun in the vertical plane at a radius r will exhibit a resonant response to the excitation of gravity at any steady rotation rate ω. It has been shown that this resonant response is key to achieving large amplitudes of the internal motion that is necessary for the inertial excitation to do net work on the device. Both the distributed mass pendulum and the pendulum with the geared flywheel can achieve the requirements for resonance, but, among the presented configurations, only the pendulum with the geared flywheel has the potential of generating significant amounts of energy per cycle.

The pendulum with geared flywheel does, however, have several key drawbacks when the operating conditions of the system are considered. The gear teeth will be subjected to cyclic loading, making them vulnerable to wear and fatigue. The contact between the gears is also a point of frictional energy loss. If a belt were used instead, the deterioration of the belt itself over time would limit the life of the device. The use of a conventional generator in the place of a flywheel also has the drawbacks of the frictional losses and wear associated with commutation brushes. Taking these drawbacks into consideration, a new type of device was developed with long lifespan as a primary design goal.

2.2 Slider Augmented Pendulum

The slider augmented pendulum was designed to preserve the desirable features of the pendulum with geared flywheel configuration by both achieving resonance at any rotation rate, and also allowing for large motion of the center of gravity of the pendulum. The design does not include any of the wear items mentioned above, and is expected to have a long life of service. This configuration relies solely on the centrifugal forces acting on the device to produce restoring torques, and is therefore capable of operating at a natural frequency that is matched to the excitation for all driving frequencies. In the previously explored devices, the constant of proportionality between the natural frequency and the driving frequency was set to unity by increasing the rotational inertia of the system. In this configuration, the opposite approach is taken. The rotational inertia is left essentially unchanged, and the natural frequency is altered by reducing the net restoring torques acting on the pendulum by means of an additional linkage and mass.

2.2.1 Configuration

The diagram of the the slider augmented pendulum system, shown in Figure 2-7, gives a broad view of the system from the inertial reference frame $\hat{I}, \hat{J}$. One blade of the propeller is shown with the device attached such that the pivot point O of the pendulous link is fixed at a radius r from the hub of the propeller at point A. The device reference frame $\hat{\imath}, \hat{\jmath}$ is fixed to the point O and translates and rotates in the inertial frame, but is stationary as observed from the attachment point of the device. Figure 2-8 shows the device in greater detail as viewed from the device reference frame. The device consists of a pendulous link of mass m and length L_1, and a secondary shorter link of length L_2 which attaches the pendulous link to a slider of mass m_S, which is constrained to linear motion along the midline of the device. Though called a slider, the mass m_S can be constrained by flexures, due to its small motion, and will not have the losses and wear associated with a sliding constraint. The distance between the center of gravity of the pendulous link and the point O is not depicted in the diagrams, but appears as the parameter L in the equations of the system dynamics. Also appearing in the dynamic equations are the parameters F_C and L_C, which represent the electromagnetic damping force exerted by a coil onto a magnetic portion of mass m and the moment arm at which it the force is applied, respectively. The system employed to provide electromagnetic damping to the device is described in detail in Chapter 3.

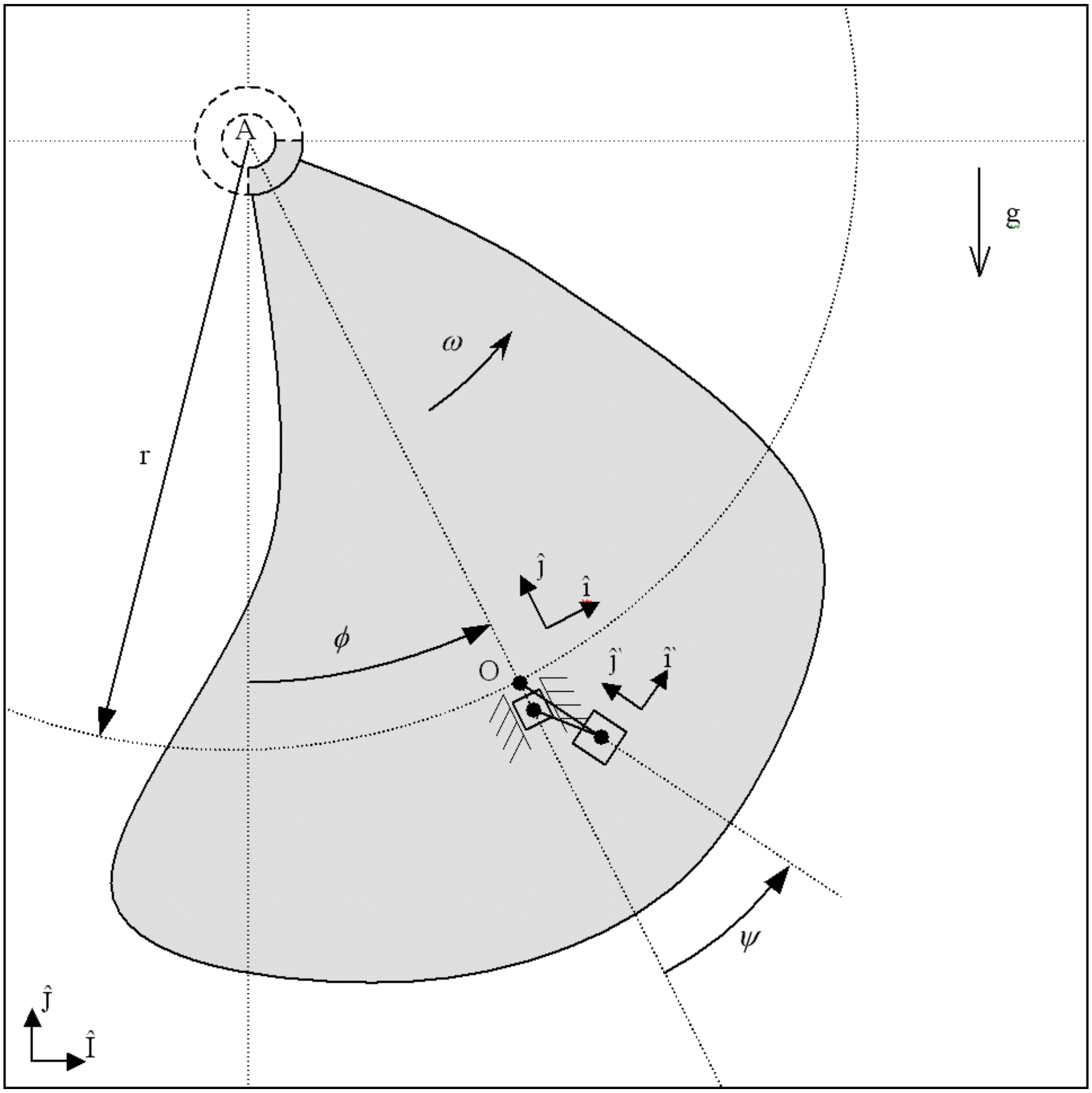

Figure 2-7: Slider augmented pendulum system overview showing the device attached to a propeller blade as viewed from the inertial frame $\hat{I}, \hat{J}$. The device frame $\hat{\imath}, \hat{\jmath}$ is attached to the device and rotates with the propeller. The frame $\hat{\imath}', \hat{\jmath}'$ is attached to the pendulous portion of the device.

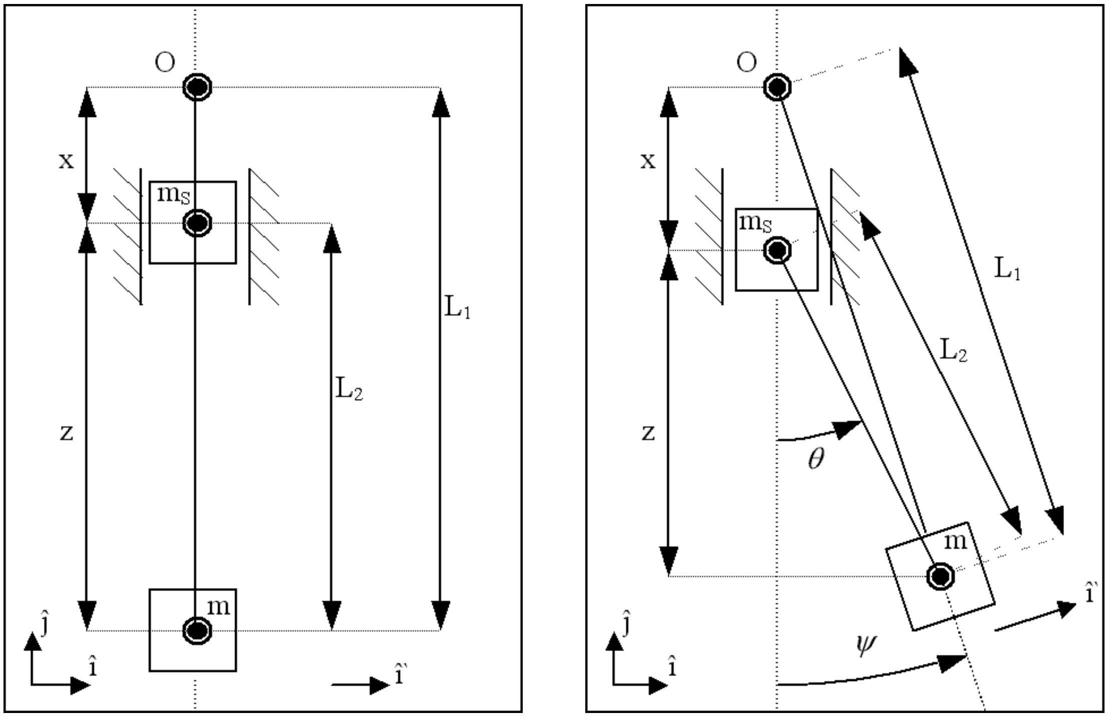

(a) (b)

Figure 2-8: Slider augmented pendulum system showing the linkage in the centered state (a) and the deflected state (b). Both views are shown in the device frame $\hat{\imath}, \hat{\jmath}$. The slider of mass m_S is constrained to linear motion along the midline of the device.

2.2.2 Slider Augmented Pendulum Dynamics

The equations of motion for the slider augmented pendulum were derived with two assumptions. First, it is assumed that the slider mass m_S is constrained to move precisely along the center line of the device, as shown in Figure 2-7, without friction. The second assumption is that the secondary link connecting the slider to the pendulous link has both negligible mass and rotational inertia. With these two assumptions, the equations of motion for the slider augmented pendulum were derived with both Newton's Method and Lagrange's Method. The derivation by each method is presented in detail in Appendix A. Three parameters

$$Z \equiv \sqrt{L_2^2 - (L_1 \sin\psi)^2} \tag{2.27}$$

$$Y \equiv L_1 \sin\psi \left(\frac{L_1 \cos\psi}{Z} - 1 \right) \tag{2.28}$$

and

$$A \equiv \left[L_1 \cos\psi \left(\frac{L_1 \cos\psi}{Z} - 1 \right) + \frac{L_1^2 \sin^2\psi}{Z} \left(\frac{L_1^2 \cos^2\psi}{Z^2} - 1 \right) \right] \tag{2.29}$$

are defined during the derivation to allow the final equation of motion to be written in the compact form

$$\begin{aligned} \ddot{\psi} \;=\; & \frac{-mL\left(r\omega^2 \sin\psi + g\sin\left(\phi+\psi\right)\right) + m_S Y \omega^2 \left(r + L_1\cos\psi - Z\right)}{I_O + m_S Y^2} \\ & + \frac{m_S Y \left(-\dot{\psi}^2 A + g\cos\phi\right) + L_C F_C}{I_O + m_S Y^2} \end{aligned} \tag{2.30}$$

2.2.3 Natural Frequency Tracking

2.2.3.1 Frequency Tracking in Linearized Model

In order to consider the changes in the natural frequency of the system with changes in the rotation rate for small angles of deflection, the excitation force and external electromagnetic forces in Equation (2.30) are set to zero, and the free undamped equation of motion is linearized about the point $\psi = 0$, $\dot{\psi} = 0$. The linearization procedure is documented in detail in Section A.3, and the linearized dynamics are found to be

$$\ddot{\psi} = \frac{\omega^2 \left[-mLr + m_S L_1 \left(r + L_1 - L_2\right)\left(\frac{L_1}{L_2} - 1\right)\right]}{I_O}\psi \tag{2.31}$$

By similarity to the classic undamped mass spring system, the linearized system has a natural frequency of

$$\begin{aligned}\omega_n &= \sqrt{\frac{\omega^2 \left[mLr - m_S L_1 \left(r + L_1 - L_2\right)\left(\frac{L_1}{L_2} - 1\right)\right]}{I_O}} \\ &= \omega\sqrt{\frac{mLr - m_S L_1 \left(r + L_1 - L_2\right)\left(\frac{L_1}{L_2} - 1\right)}{I_O}} \qquad (2.32)\end{aligned}$$

This result shows that, within the linear regime, the natural frequency ω_n is directly proportional to the rotation rate ω. Now, all that is required to make the linearized natural frequency equal to the forcing frequency for any rotation rate is to set the constant of proportionality to unity, which leads to the requirement that

$$m_S L_1 \left(r + L_1 - L_2\right)\left(\frac{L_1}{L_2} - 1\right) = mLr - I_O \tag{2.33}$$

Frequency tracking can therefore be achieved by selecting appropriate parameters m_S, L_1, and L_2 for any pendulous link with parameters m, L, and I_O mounted at a radius of r. For the general case where $r \gg L$, it is naturally expected that $mLr - I_O > 0$, and therefore $L_1 > L_2$, as depicted in Figure 2-7.

2.2.3.2 Frequency Tracking in Full Nonlinear Model

In order to verify the frequency tracking ability of the nonlinear device, the system was simulated numerically from the full nonlinear equations of motion shown in Equation (2.30). The simulation was performed in MATLAB using the ode45 solver, with no gravitational forces or Lorentz forces acting on the system. Simulations were run from the initial conditions of $\psi_0 = 10°$ and $\dot{\psi}_0 = 0$ to the point at which the linkage reached the midline of the device at $\psi = 0$. The time at the termination of the simulation, representing one fourth of the total period of oscillation, was used to find the undamped natural frequency of the system. Representative values were used for the

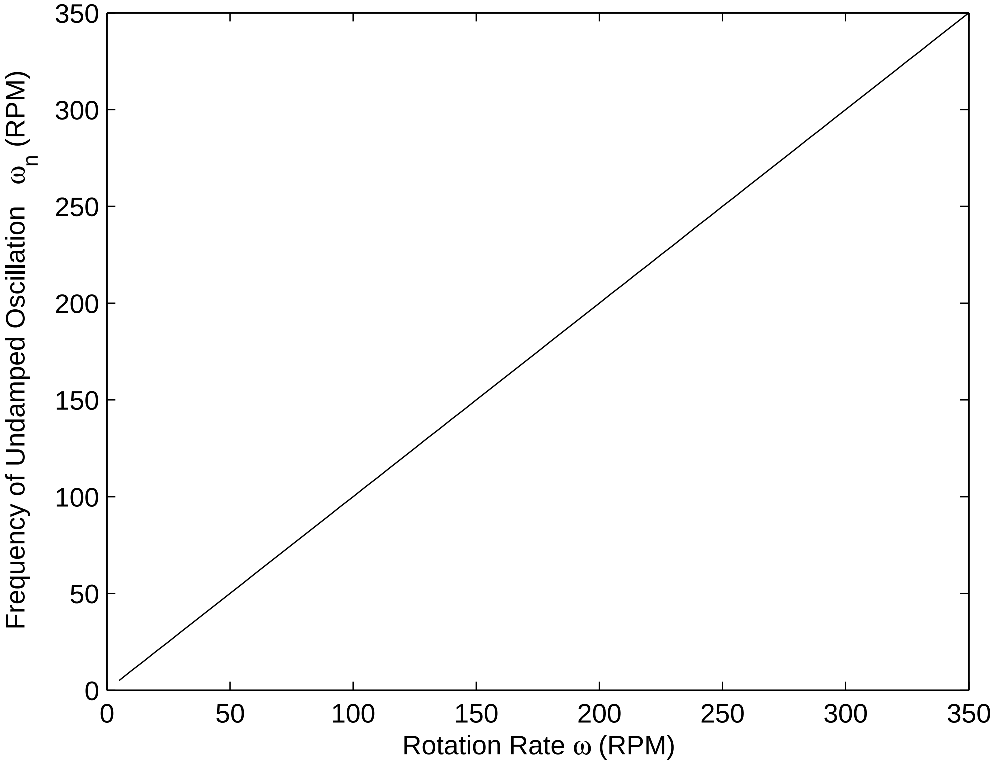

Figure 2-9: Nonlinear simulation results showing the natural frequency of the undamped system when released from rest at an initial deflection of $\psi_0 = 10°$ and no forcing excitation $g = 0$. Representative system parameters used and m_S hand tuned at a single frequency.

physical parameters of the system. The slider mass m_S was hand tuned at a single rotation rate of 250 RPM, such that the natural frequency of the system matched the driving frequency precisely at that rate of rotation. The system was then simulated over a range of driving frequencies and the period and natural frequency of the system was recorded at each rotational rate.

The simulation results are presented in Figure 2-9, and verify the precise frequency tracking of the nonlinear system operating at a fixed amplitude of motion. The frequency tracking ability shown by the system was expected, because all of the potential energy terms in Equation 2.30, viewed from the device frame $\hat{\imath}, \hat{\jmath}$, are proportional to ω^2.

2.2.3.3 Amplitude Dependency of Natural Frequency

For the system parameters used in the nonlinear simulations, it was noted that the slider mass m_S required to tune the device did not satisfy Equation (2.33), which was found to be the requirement for natural frequency tracking in the linearized model. This apparent discrepancy is due to the fact that the natural frequency depends on the amplitude of the motion, and the natural frequency for small displacements found in the linearized model is not the same as the natural frequency when released from $\psi_0 = 10°$.

It is interesting that the system shows its nonlinearities in the relation between the natural frequency ω_n and the angle at release ψ_0 at each rotation rate ω, but at any given ψ_0 there is a linear relationship between ω and ω_n. Plotting the ratio ω_n/ω as a function of the angle at release for any rotation rate produces the single curve shown in Figure 2-10. It should be noted that the shape of this curve is dependent on the parameters of the system, but can be expected to start at a higher frequency for small motion and drop to lower frequencies as the motion increases, due to the increased effectiveness of the force produced by the slider mass as the angles θ and $(\psi - \theta)$ increase with increasing ψ.

2.2.4 Statically Stable Range of Motion

At every position within its allowed range of motion, it is important that link 1 will have a restoring torque that will accelerate it back toward the $\psi = 0$ to ensure that the linkage cannot become trapped in some local energy minima. As the rotation rate is increased, the centrifugal forces increasingly outweigh the excitation force provided by gravity and the force provided by the coil, so these forces are not taken into consideration in the analysis of the stable range of motion. It is, however, necessary to note that at relatively low rotation rates, where the excitation of gravity exceeds all other forces, the linkage will have large deflections, and will move until the mechanical stops are reached. It is, therefore, guaranteed that the linkage will, at some time, reach every point within its mechanically limited travel and, due to the unknown

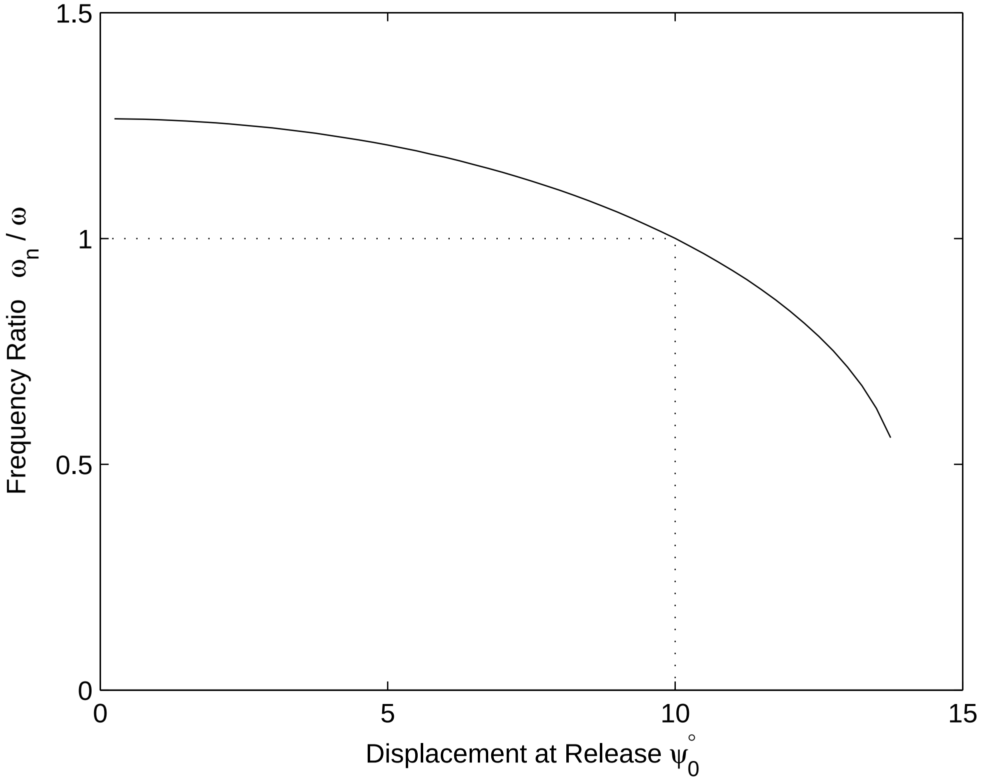

Figure 2-10: Nonlinear simulation results showing the amplitude dependence of the frequency ratio ω_n/ω for the system with the same parameters as used in Section 2.2.3.2. The system was released from rest at various initial deflections ψ_0 and at various rotation rates ω, with each rotation rate producing an identical curve.

transient accelerations $\dot{\omega}$, the linkage may conceivably achieve any deflection at any rotational rate. It is therefore necessary to ensure that the linkage is stable for any deflection within its mechanically limited range of motion for the conditions $g = 0$, $F_C = 0$.

Stability can be tested by finding the range of deflection for which there is a restoring torque that tends to bring the linkage back to center. From the equation of motion given in Equation (2.30) and setting $g = 0$, $F_C = 0$, and $\dot{\psi} = 0$, and assuming a positive deflection in ψ, the stability condition can be written as

$$\frac{-mLr\omega^2 \sin\psi_{\max} + m_S Y \omega^2 \left(r + L_1 \cos\psi_{\max} - Z\right)}{I_O + m_S Y^2} < 0 \tag{2.34}$$

Recognizing that $I_O > 0$ and $m_S > 0$ and rearranging terms simplifies the condition to

$$mLr \sin\psi_{\max} - m_S Y \left(r + L_1 \cos\psi_{\max} - Z\right) > 0 \tag{2.35}$$

Substituting in the value of Y from Equation (2.28) gives the stability condition as

$$mLr \sin\psi_{\max} - m_S L_1 \sin\psi_{\max} \left(\frac{L_1 \cos\psi_{\max}}{Z} - 1\right) \left(r + L_1 \cos\psi_{\max} - Z\right) > 0 \tag{2.36}$$

In the expected case that $L_1 > L_2$, $\sin\psi_{\max} > 0$ due to the geometric constraints of the linkage itself, and further simplification leads to the relation

$$\frac{mLr}{m_S L_1} > \left(\frac{L_1 \cos\psi_{\max}}{Z} - 1\right) \left(r + L_1 \cos\psi_{\max} - \sqrt{L_2^2 - Z}\right) \tag{2.37}$$

Substituting the value of Z from Equation (2.27) the stability condition becomes

$$\frac{mLr}{m_S L_1} > \left(\frac{L_1 \cos\psi_{\max}}{\sqrt{L_2^2 - \left(L_1 \sin\psi_{\max}\right)^2}} - 1\right) \left(r + L_1 \cos\psi_{\max} - \sqrt{L_2^2 - \left(L_1 \sin\psi_{\max}\right)^2}\right) \tag{2.38}$$

This result gives some insight on the system by showing that as m_S is increased, the range of stable motion is decreased. It can be shown that the linkage will become unstable at some $\psi_{\max} < \sin^{-1}\left(L_2/L_1\right) < (\pi/2)$ by substituting $\psi = \sin^{-1}\left(L_2/L_1\right)$

into the right side of Equation (2.38) and recalling that for $\psi < (\pi/2)$, $\cos\psi > 0$. With this substitution, the right hand side of Equation (2.38) becomes

$$\left(\frac{L_1 \cos\psi}{0} - 1\right)(r + L_1 \cos\psi) = \infty \tag{2.39}$$

which clearly cannot satisfy the stability condition.

Since the right side of Equation (2.38) has been shown to increase without bound while $\psi < \sin^{-1}(L_2/L_1)$, the linkage will always have some deflection at which stability is lost before inversion can occur. Mechanical stops must be placed to ensure that the linkage does not travel beyond the stable range of motion, or the device could become trapped at the end of its range of motion until the rotation rate is lowered to the point that the excitation force becomes large in comparison to the centrifugal force.

2.2.5 Sensitivity to Misalignment

The slider mass and link 2 can be thought of as a subsystem that acts as a positive feedback loop, reducing the natural stability of the pendulous link 1. Using this perspective from the controls discipline, it is reasonable to expect that this positive feedback will cause the system to become more sensitive to disturbances. This characteristic is seen in the increased sensitivity of the system to misalignment, which can cause the linkage to become trapped against its mechanical stops during high speed operation.

Figure 2-11 shows the device mounted to the base part with a misalignment angle of γ between the midline of the device and the true radial ray that passes from the center of rotation of the base part outward through the main pivot of the device at point O. Starting with Equation (2.30) and evaluating the expression at $\ddot{\psi} = 0$, $\dot{\psi} = 0$, and $F_C = 0$, the static torque balance about point O is obtained as

$$mLr \sin\psi = m_S Y (r + L_1 \cos\psi - Z) \tag{2.40}$$

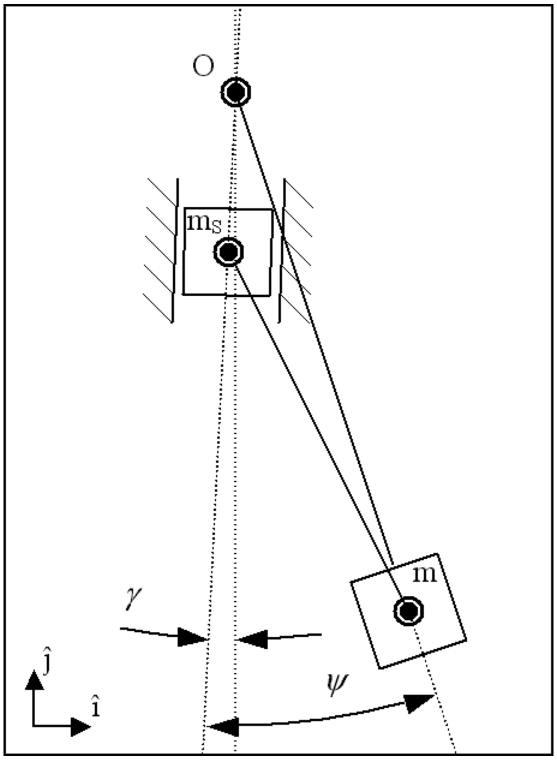

Figure 2-11: Diagram of device mounted at a misalignment angle γ between the device center line and true radial line passing through the center of rotation of the propeller at A and the main pivot of the device at O.

To find the relation between the misalignment angle γ and the resulting deflection ψ at which static equilibrium is achieved, the torque balance can be written as

$$mLr\sin(\psi-\gamma) = m_S\cos\gamma Y\left(r + L_1\cos\psi - Z\right) \tag{2.41}$$

to accommodate the misalignment angle. Substituting the trigonometric relation

$$\sin(\psi-\gamma) = \sin\psi\cos\gamma - \cos\psi\sin\gamma \tag{2.42}$$

and rearranging terms yields

$$\tan\gamma = \frac{\sin\psi}{\cos\psi} - \frac{m_S}{mrL\cos\psi}Y\left(r + L_1\cos\psi - Z\right) \tag{2.43}$$

Substituting for Y from Equation (2.28) and further simplifying gives the condition for equilibrium as

$$\gamma = \tan^{-1}\left(\tan\psi\left[1 - \frac{m_S L_1}{mrL}\left(\frac{L_1\cos\psi}{Z} - 1\right)\left(r + L_1\cos\psi - Z\right)\right]\right) \tag{2.44}$$

Linearizing about the point $\psi = 0$ with the approximation that

$$\gamma \approx \gamma|_{\psi=0} + \left.\frac{\partial\gamma}{\partial\psi}\right|_{\psi=0}\psi \tag{2.45}$$

was performed. The first term in the approximation

$$\gamma|_{\psi=0} = \tan^{-1}\left(0\left[1 - \frac{m_S L_1}{mrL}\left(\frac{L_1}{L_2} - 1\right)\left(r + L_1 - L_2\right)\right]\right) = \tan^{-1}(0) = 0 \tag{2.46}$$

and the second term can be found by defining a variable for substitution

$$B \equiv \left[1 - \frac{m_S L_1}{mrL}\left(\frac{L_1\cos\psi}{Z} - 1\right)\left(r + L_1\cos\psi - Z\right)\right] \tag{2.47}$$

and using the relation

$$\frac{d\tan^{-1}u}{dx} = \frac{1}{1+u^2}\frac{du}{dx} \tag{2.48}$$

Substitution allows the partial derivative to be written as

$$\frac{\partial \gamma}{\partial \psi} = \frac{1}{1 + (\tan \psi B)} \left(\frac{B}{\cos^2 \psi} + \tan \psi \frac{\partial B}{\partial \psi} \right) \tag{2.49}$$

which can then be evaluated as

$$\begin{aligned} \left. \frac{\partial \gamma}{\partial \psi} \right|_{\psi=0} &= \frac{1}{1 + (0)} \left(B|_{\psi=0} + 0 \frac{\partial B}{\partial \psi} \right) \\ &= 1 - \frac{m_S L_1}{mrL} \left(\frac{L_1}{L_2} - 1 \right) (r + L_1 - L_2) \end{aligned} \tag{2.50}$$

Assembling Equation (2.45), Equation (2.46), and Equation (2.50) the linearized sensitivity transfer function relating the misalignment angle γ to the equilibrium angle ψ is obtained as

$$\frac{\psi}{\gamma} = \frac{1}{1 - \frac{m_S L_1}{mrL} \left(\frac{L_1}{L_2} - 1 \right) (r + L_1 - L_2)} \tag{2.51}$$

When the system is tuned for frequency tracking by satisfying Equation (2.33), we have that

$$\frac{\psi}{\gamma} = \frac{1}{1 - \frac{mrl - I_O}{mrL}} = \frac{mrL}{I_O} \tag{2.52}$$

Noting that the natural frequency of an uncompensated pendulum (without the slider and linkage) is

$$\omega_{n\,\mathrm{U}} = \sqrt{\frac{m\omega^2 rL}{I_O}} = \omega \sqrt{\frac{mrL}{I_O}} \tag{2.53}$$

The sensitivity transfer function can be expressed as

$$\frac{\psi}{\gamma} = \frac{mrL}{I_O} = \frac{\omega_{n\,\mathrm{U}}^2}{\omega_{n\,\mathrm{C}}^2} \tag{2.54}$$

where $\omega_{n\,\mathrm{C}}$ is the compensated natural frequency. When the pendulum is approximated to have no rotational inertia about its own center of gravity, so that

$$I_O = ml^2 \tag{2.55}$$

we finally obtain

$$\frac{\psi}{\gamma} = \frac{r}{L} \tag{2.56}$$

This result, that the sensitivity to misalignment is directly proportional to the square of the ratio of the uncompensated and compensated natural frequencies, becomes an important factor in designing and mounting a device of this configuration. In the point mass approximation of the pendulum this sensitivity is proportional to the ratio of the radius at which the device is mounted to the length of the pendulous link. This clearly shows that alignment will be a primary concern for the system if attempts are made to reduce the length scale of the device to very small fractions of the radius at which it is mounted. It also implies that the device, at a given length scale, becomes more robust as the mounting point is brought toward the axis of rotation of the part on which it is mounted.

2.3 Extracting Energy Through Damping

The slider augmented pendulum system has been shown to be able to achieve a resonant response to a steady input of any frequency for a fixed target amplitude of motion. This resonance allows energy to build within the system to produce and maintain large motion, and also indicates that the phase relationship between the excitation and the motion is such that the excitation is always transmitting energy into the system. It has also been shown that mechanical stops must be utilized to limit the travel of the linkage to its stable range of motion. In order to obtain usable electrical energy from the system, a coil and magnet pair are used to damp the motion of the linkage. From Lenz Law, the relative motion between the magnet and the coil will cause a current to flow through the coil, creating an electromagnetic field that oppose the relative motion. This section focuses on investigating the parameters that are important to the optimization of the power transfer to the load.

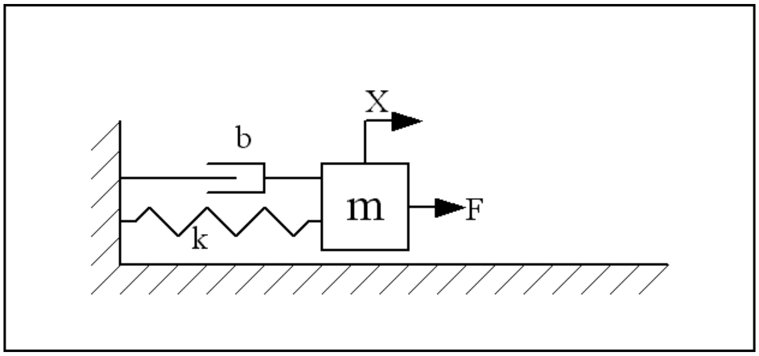

Figure 2-12: Damped harmonic oscillator system which captures the important dynamics of the slider augmented pendulum system when a frequency dependent spring rate is applied.

2.3.1 Damped Harmonic Oscillator

Due to the complexity and nonlinearities of the slider augmented pendulum system, it is somewhat difficult to gain an intuitive grasp of the optimization of the power transfer to the load. For this reason, it is beneficial to first consider instead a linear mass spring system that captures the important aspects of the slider augmented pendulum configuration. Such an analogous system is shown in Figure 2-12. The block of mass m is acted upon by a sinusoidal excitation force

$$f(t) = f \sin(\omega t) \tag{2.57}$$

a reaction force from a spring with a frequency-dependent spring constant

$$k(\omega) = \omega^2 m \tag{2.58}$$

and a force due to the damping b. The choice of the frequency-dependent spring constant gives the simple linear system the same frequency tracking and matching properties as the slider augmented pendulum, with

$$\omega_n = \sqrt{\frac{k}{m}} = \omega \tag{2.59}$$

The transfer function of the system

$$\frac{X(s)}{F(s)} = \frac{1}{ms^2 + bs + k} \tag{2.60}$$

evaluated at $s = j\omega$, gives

$$\frac{X(j\omega)}{F(j\omega)} = \frac{1}{j\omega b} \tag{2.61}$$

and shows that the amplitude of motion is inversely proportional to both the damping constant and the driving frequency. The transfer function

$$\frac{V(j\omega)}{F(j\omega)} = \frac{X(j\omega)\,j\omega}{F(j\omega)} = \frac{1}{b} \tag{2.62}$$

between the velocity of the system and the excitation shows the relation between velocity and excitation is the damping value itself. The relation can be brought into the time domain as

$$\frac{\dot{x}(t)}{f(t)} = \frac{1}{b} \tag{2.63}$$

In the time domain, the instantaneous power being damped from the system is given by

$$P(t) = f(t)\,\dot{x}(t) = \frac{f(t)^2}{b} = \frac{f^2 \sin^2(\omega t)}{b} \tag{2.64}$$

and the average power can be found by integrating over one complete cycle and dividing by the period, to arrive at

$$P = \frac{f^2}{b} \int_0^{\frac{2\pi}{\omega}} \sin^2(\omega t)\ dt\, \frac{\omega}{2\pi} = \frac{f^2}{2b} \tag{2.65}$$

From the expression for the average power, it can be seen that the power increases without bound as the damping is reduced toward zero, but at the same time the amplitude given in Equation (2.61) also grows without bound.

In any physical system, there will be a limit to the allowable mechanical motion, and some minimum damping level will be required to prevent the device from hitting its mechanical stops. This optimal damping level is found from the system transfer

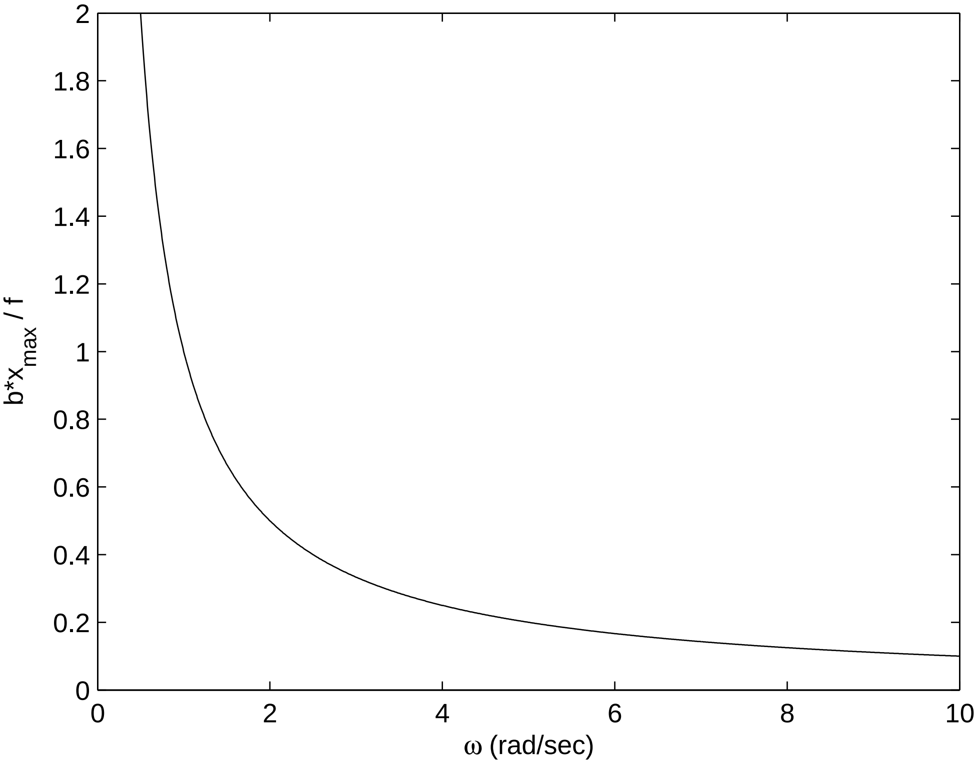

Figure 2-13: Normalized optimal damping as a function of frequency.

function as a function of frequency to be

$$b_{\mathrm{O}} = \frac{f}{x_{\mathrm{max}}} \frac{1}{\omega} \tag{2.66}$$

and is plotted in Figure 2-13. Combining this result with Equation (2.65), the optimal power output of the device is found to be

$$P_{\mathrm{O}} = \frac{f^2}{2b} = \frac{f x_{\mathrm{max}} \omega}{2} \tag{2.67}$$

and increases linearly with frequency.

2.3.2 Applying Electromagnetic Damping

In the calculations above, the optimal damping and optimal power output were found as a function of frequency for a system of limited range of motion. Next, we consider

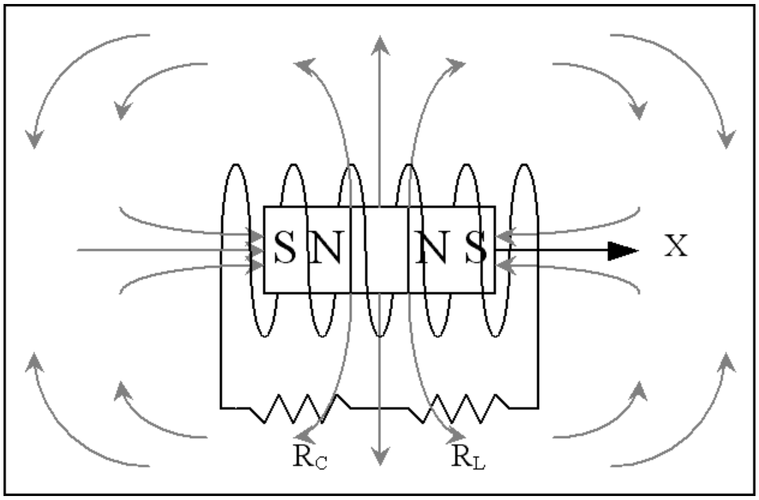

Figure 2-14: Magnet coil configuration that results in electromagnetic damping of the motion of the magnet assembly relative to the fixed coil. R_C represents the internal resistance of the coil and R_L the impedance of the attached electrical load.

how damping is applied to the system electromagnetically. The system shown in Figure 2-14 has a configuration often used in maglev linear actuators, and consists of a two magnet assembly which moves within a fixed coil of wire [3, 14]. By Faraday's Law, the motion of the magnet will produce an electromotive force in the coil

$$V_{\mathrm{C}} = VBL_TN \tag{2.68}$$

which is proportional to the velocity V, the density of the magnetic field B, and the linear length of wire in the field given by the product of the length per turn L_T and the number of turns N. The Lorentz force

$$F_{EM} = IBL_TN \tag{2.69}$$

relates the electromagnetic force F_{EM} exerted on the magnet to the current in the coil using the same parameters. Rearranging terms, the electromagnetic constant of the magnet-coil pair can be defined as

$$K_{EM} \equiv \frac{V_C}{V} = \frac{F_{EM}}{I} = BL_TN \tag{2.70}$$

With the assumption that the reactance of the coil can be considered purely resistive at the excitation frequency, the resistances in the coil and in the load can be used to relate the voltage and current across the coil, and the damping constant can be written as

$$b = \frac{K_{EM}^2}{R_C + R_L} \tag{2.71}$$

This result is important because it introduces two key deviations from the ideal case investigated in Figure 2-12. First, the resistance of the coil introduces losses in the system, so that even if ideal damping is applied, only a portion of the damped power will make it to the load. The second deviation is that the damping has a finite upper limit, set by the internal resistance of the coil

$$b_{\max} = \frac{K_{EM}^2}{R_C} \tag{2.72}$$

and at low frequencies the system will not be able to achieve the high levels of damping required to prevent collision with the mechanical stops.

At high frequencies, when the damping is set to the optimal value in Equation (2.66) to maximize the total power removed through damping, the portion of the power that is delivered to the load is given by

$$P_L(t) = P(t) - P_C(t) = f x_{\max} \omega \sin^2(\omega t) - I_{C(t)}^2 R_C = \left(f x_{\max} \omega - \frac{f^2 R_C}{K_{EM}} \right) \sin^2(\omega t) \tag{2.73}$$

and the average power delivered is found to be

$$P_L = \frac{f x_{\max} \omega}{2} - \frac{f^2 R_C}{2 K_{EM}^2} \tag{2.74}$$

The first term in this expression is the maximum rate at which energy can be removed through damping, and the second term represents the losses in the coil due to its internal resistance. The second term shows that the coil losses are constant when optimal damping is applied to the system.

At low frequencies, the maximum damping that the coil can provide is insufficient to prevent collision with the mechanical stops, and if maximum damping is applied by directly shorting the leads of the coil, no power is transmitted to the load. This condition occurs when P_L in Equation (2.74) reaches zero, showing that the coil loss term is equal to the rate at which the excitation does work on the system.

$$\omega_A = \frac{f R_C}{x_{\max} K_{EM}^2} \tag{2.75}$$

At these low frequencies, the mechanical stops will be reached by the mass, and the electromagnetic forces will have little impact on the motion of the device. Under these conditions, the motion of the device, and therefore the voltage across the coil, can be considered to be of constant amplitude, and maximum power is delivered to the load when the load is impedance matched to the coil by setting

$$R_L = R_C \tag{2.76}$$

Mid-range frequencies exist at which it is possible to provide enough damping that the system will not impact the mechanical stops. However, the load resistance must be lowered below the coil resistance. Because impedance matching is desirable at low frequencies, it is reasonable to use the resistance of the coil as the minimum load resistance for all frequencies, and therefore allow the mechanical stops to be reached at these mid-range frequencies as well. The frequency ω_B at which the damping applied by impedance matching the load to the coil is the optimal damping, is found from Equation (2.71) and Equation (2.66) to be

$$\omega_B = 2\omega_A = \frac{2 f R_C}{x_{\max} K_{EM}^2} \tag{2.77}$$

To reduce coil losses at frequencies above ω_B and to shift both ω_A and ω_B to lower frequencies, it is desirable to maximize the ratio K_{EM}^2/R_C.

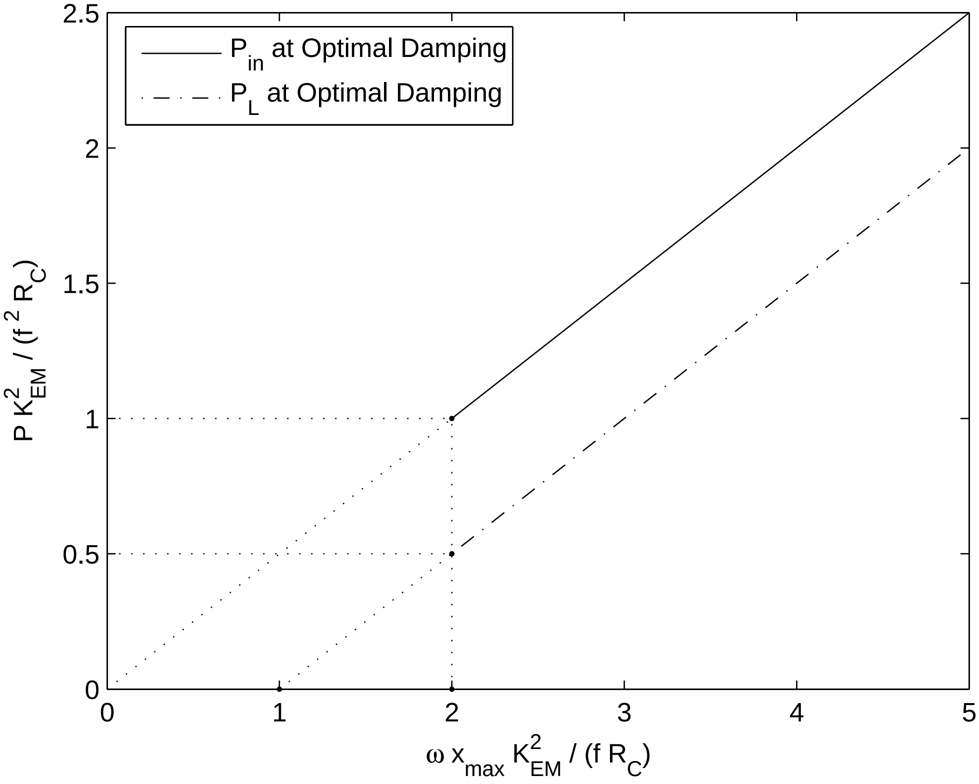

Figure 2-15: Normalized curves showing power taken into the system and power delivered to the load as a function of frequency. On the normalized plot $\omega_A = 1$ and $\omega_B = 2$.

Chapter 3

Prototype Design

3.1 Choosing Nondimensional System Parameters

With the dynamics and performance of the device and the dependency on each parameter laid out in detail in the previous chapter, the task becomes to choose a desirable set of parameters for use in the design of a prototype device. It is convenient to begin with the parameters that can be represented in non-dimensional form and therefore have the least dependence on the details of the final mechanical structure. It has been shown that the necessary frequency tracking can be achieved for a system of any given set of parameters through the choice of the slider mass m_S and the link lengths L_1 and L_2. Taking a representative set of system parameters that includes the target radius of 1 m and appropriate values for m, L, and I_O, numerical simulation using various lengths L_1, and L_2 can determine the required value of m_S and the natural frequency of the system ω_n as a function of displacement ψ.

By defining the linkage ratio as L_2/L_1 and the frequency ratio as ω_n/ω, the amplitude dependence and stable range of motion can be evaluated in terms of these nondimensional parameters. Figure 3-1 shows the amplitude dependence on the frequency ratio for various linkage ratios. Each curve begins at zero displacement and is extended to the point at which static stability is lost. The key result from this family of curves is that, for a set desired amplitude, the linkage ratio defines the deviation from unity of the frequency ratio at low amplitudes. This result is important to the

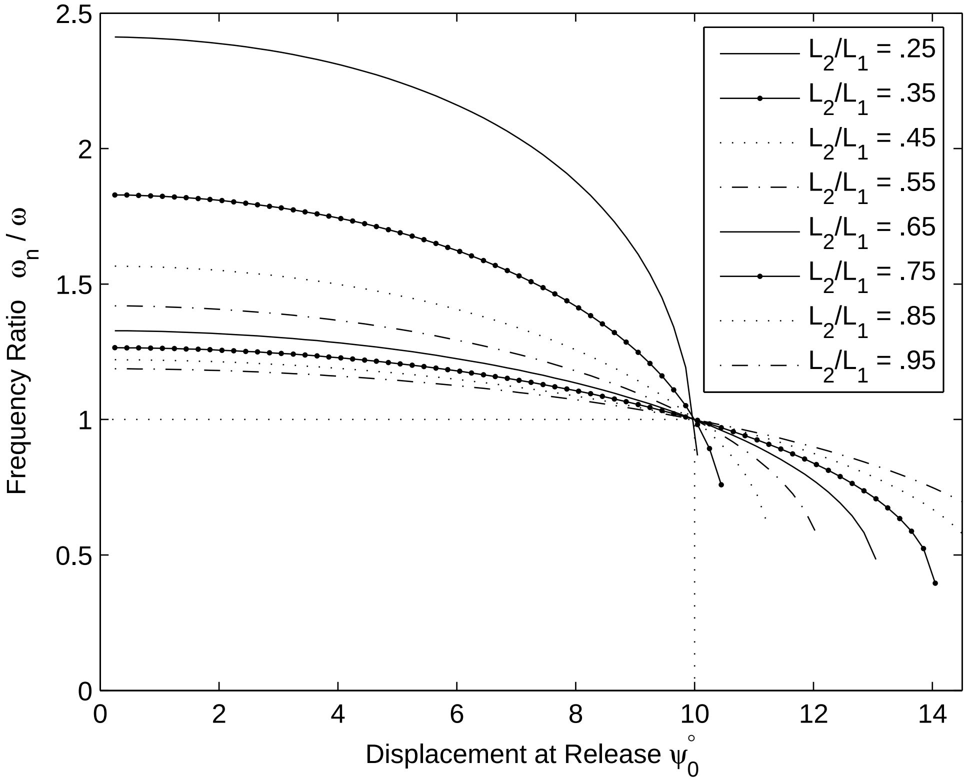

Figure 3-1: Plot of the ratio between the natural frequency and the driving frequency ω_n/ω as a function of release amplitude ψ_0 for several values of the linkage ratio L_2/L_1. For each curve a slider mass m_S has been chosen to achieve a frequency ratio of unity at an amplitude of $\psi = 10°$ for a representative set of system parameters. Each curve extends to the limit of static stability.

dynamics of the device because if the mismatch is too large, the device will not be capable of building up amplitude from rest at the centered position while spinning at high frequencies. It is therefore desirable to have a large linkage ratio to minimize the deviation of the frequency ratio from unity. Considering the endpoints of the curves, at which point stability is lost, it is seen that a large linkage ratio offers the largest stable range of motion.

When the proportions of link 1 are held constant, the rotational inertia I_O scales linearly with the mass m and it becomes meaningful to define the mass ratio as m_S/m. The linkage ratio, for an otherwise constant set of parameters, will dictate the mass ratio required to set ω_n equal to ω. This relationship is presented in Figure 3-2, and shows that the mass ratio increases without bound as the length ratio of unity

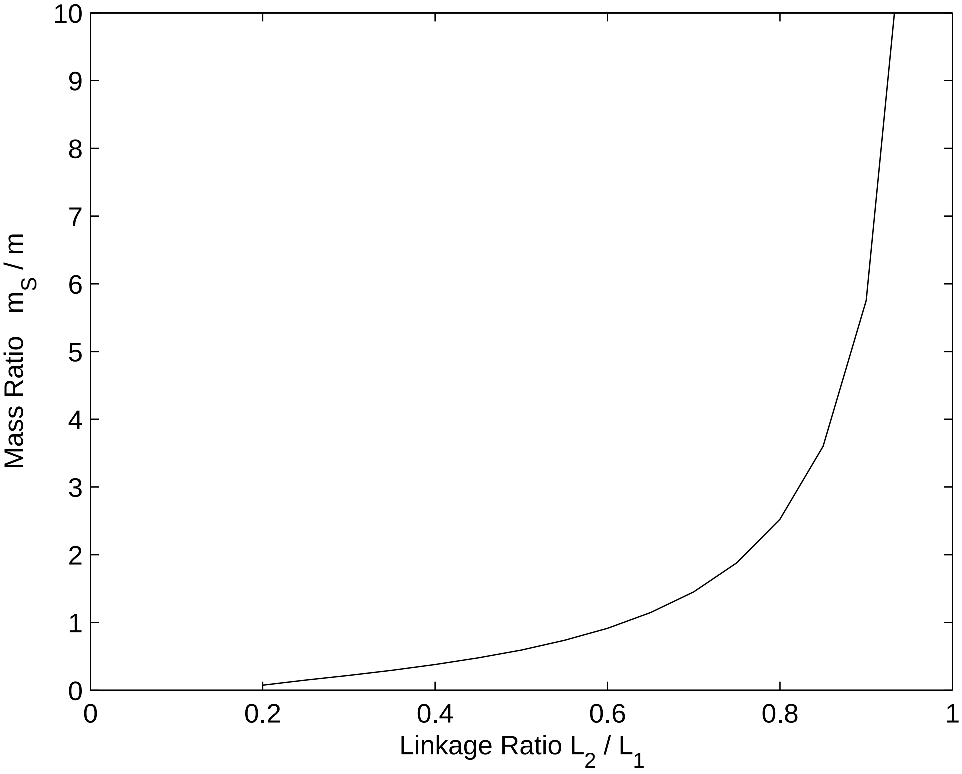

Figure 3-2: Plot of the required mass ratio m_S/m as a function of linkage ratio L_2/L_1 for a frequency ratio of unity $\omega_n = \omega$ at an amplitude of $\psi = 10^\circ$ for a representative set of system parameters.

is approached. The required travel of the slider mass as a function of linkage ratio is shown in Figure 3-3, and shows the opposite trend. Small slider displacements are desirable to enable the use of flexures as a means of constraining the slider with minimal losses. From these results, the choice of the linkage ratio becomes a trade off between reduced nonlinearities in natural frequency, enhanced stability, and reduced slider motion at large ratios and reduced slider mass at low ratios. Weighing all of the benefits for a target amplitude of $\psi = 10^\circ$, a length ratio of $L_2/L_1 = 0.75$ was chosen for use in the prototype design, resulting in a mass ratio of $m_S/m = 1.88$, and a normalized slider displacement of 0.005.

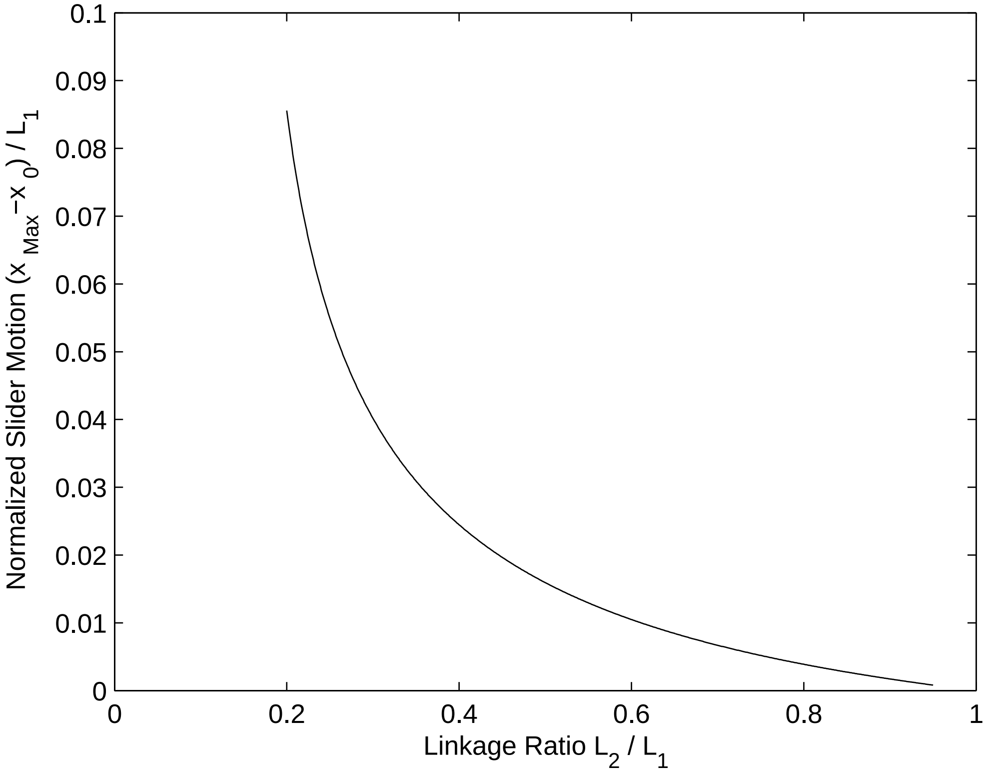

Figure 3-3: Relationship between normalized slider maximum displacement $(x_{\max} - x_0)/L_1$ and linkage ratio L_2/L_1.

3.2 Magnet Assembly and Coil Design

The magnet assembly consists of two magnets placed on either side of a spacer, as shown in Figure 2-14, with a flux return path provided around the outer loop to contain the field and to reduce losses associated with eddy currents that may otherwise be induced in nearby components. Because the magnet assembly has significantly more weight than the coil, the coil is held stationary and the magnet assembly is integrated into the the pendulous link. In order to achieve a range of motion of $\psi = \pm 10^\circ$ while still holding the tight clearances that are desired to maximize efficiency, the magnet assembly was designed with the curvature shown in Figure 3-4. The design consists of many flat plates to reduce the manufacturing complexity of the steel parts. Simplifying the geometry of the magnet assembly did, however, pose challenges on the shaping of the magnets themselves. The magnets were cut using a wire EDM processes after the magnet stack was assembled.

The magnet assembly is designed to provide a very concentrated magnetic field at a right angle to the motion of the coil to obtain a large effective field density B. This high field density helps to increase the electromagnetic constant K_{EM} defined in Equation (2.70), and therefore increases the efficiency of the device as described in Section 2.3.2 by increasing the ratio

$$\frac{K_{EM}^2}{R_C} = \frac{(BL_TN)^2}{R_C} \tag{3.1}$$

The coil itself was also designed to maximize this ratio to achieve better efficiency. Because the length of a single turn of wire in the coil L_T was fixed by the geometry of the magnet assembly, coil design focused on maximizing the ratio N^2/R_C. The cross sectional area of the coil is limited by the tolerances between the coil and magnet assembly and the maximum number of turns that will fit into the available space is given by

$$N = r_P \frac{A_S}{A_W} \tag{3.2}$$

where A_s is the area of the cross section of the coil, A_W is the cross section of the wire,

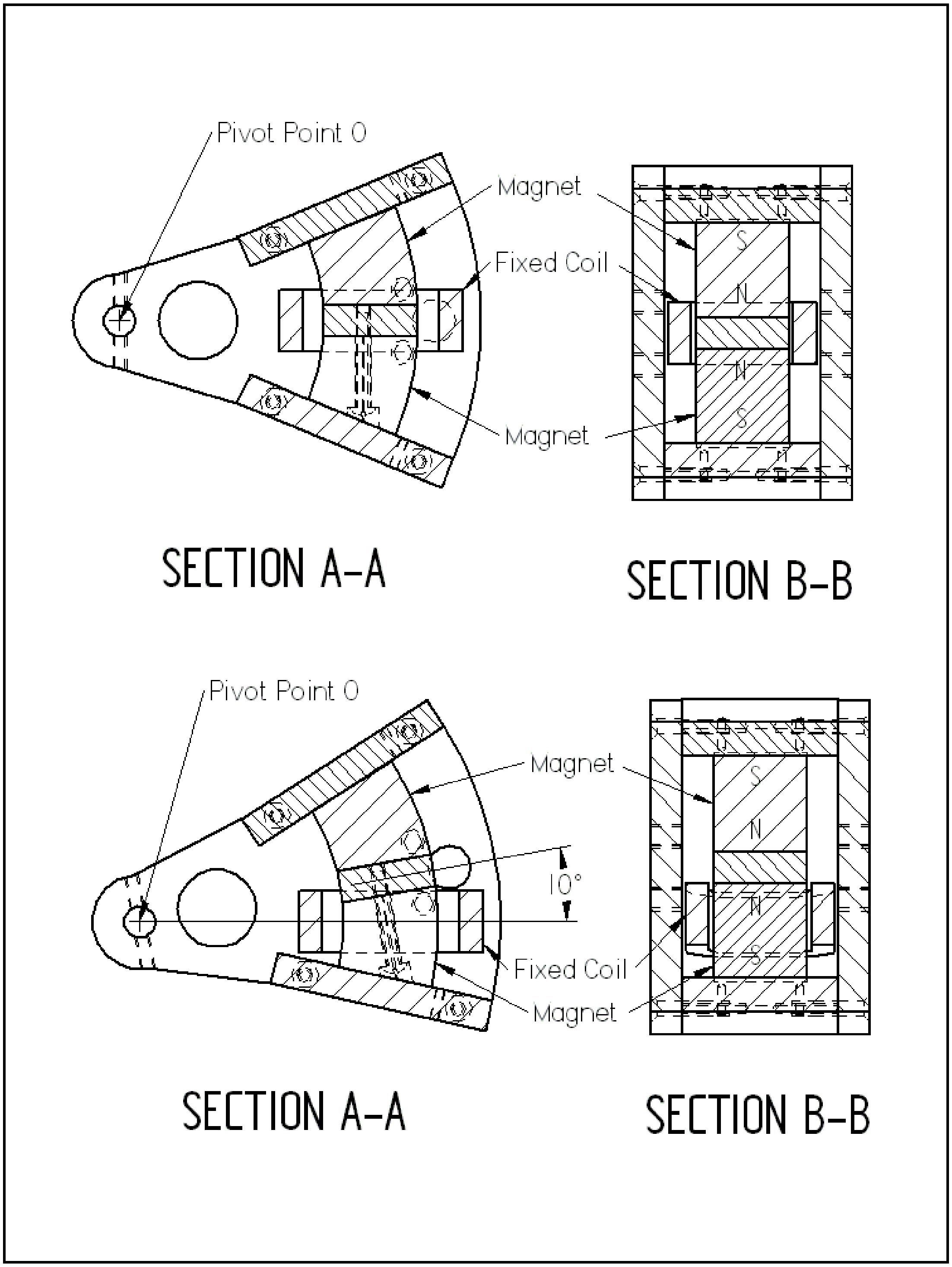

Figure 3-4: Integrated pendulum and magnet assembly structure showing magnet orientations and coil position in centered (top) and deflected (bottom) state. The coil is held fixed by an external structure not included in the diagram.

and r_P is the packing ratio. The internal resistance of the coil R_C can be calculated as a function of the resistivity of the copper in the wire ρ, the cross sectional area of the wire A_W, and the total length of wire NL_T as

$$R_C = \frac{\rho N L_T}{A_W} \tag{3.3}$$

Combining these equations shows that

$$\frac{N^2}{R_C} = \frac{N A_W}{\rho L_T} = \frac{r_P A_S}{\rho L_T} \tag{3.4}$$

and the packing ratio is the only term that can be altered to decrease the internal losses in a copper coil of given geometry.

The coil design reflects the desire to maximize the packing ratio by allowing the wire to round the corner of the coil with a large enough radius that the windings can be maintained in a flat and parallel orientation. A section view of the coil situated in the magnet assembly is presented in Figure 3-5 and shows the tight tolerances that are held between the coil and the surrounding structures. To further increase the packing ratio, magnet wire with a thin non-bonding insulation was used, and the coil was wound and epoxied by hand on a custom CNC cut winding fixture. It should be noted that while only the packing ratio affects the efficiency of the coil, the choice of wire will affect the number of turns, and will therefore affect the balance of voltage and current delivered to the load. The choice of wire can therefore be made to minimize the losses in the load. For the prototype device, it was desirable to match the coil voltage output to the input range of the data acquisition system, and 32 AWG magnet wire was selected. A photograph of the wound coil is shown in Figure 3-6.

3.3 Mechanical Linkage Design

The physical design of the mechanical linkage is a critical challenge of its own. At the testing condition of $r = 1$ m and rotation rates up to the desired 350 RPM, the

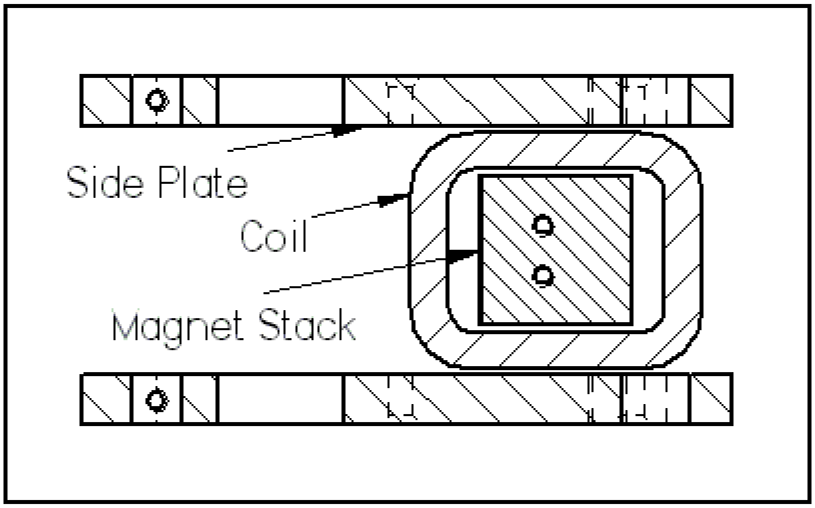

Figure 3-5: Section view of coil and magnet assembly along the midline of the device showing the fit of the coil between the magnet stack and the side plates of the assembly.

Figure 3-6: Photograph of the hand wound coil showing the organized orientation of the windings to maximize the packing ratio.

device will experience centripetal accelerations of

$$\omega^2 r = \left(350\frac{2\pi}{60}\right)^2 = 1343\ \frac{\mathrm{m}}{\mathrm{s}^2} = 137\ \mathrm{g} \tag{3.5}$$

Because of these high loads, it is necessary to carefully design the linkage to avoid mechanical failure and to prevent the high loads from causing friction or deflections that would prevent the device from preforming as desired. The design was completed with a factor of safety of $n \geq 2$ against failure in both shear and bending at all critical points in the design.

3.3.1 Link Forces

The force in each link varies with time and has components due to both the centrifugal forces and reaction forces produced by the dynamic motion of the linkage itself. The forces in each link and the reaction forces of the slider against its constraint were found from the dynamics of the system using the Newtonian approach. The resulting tensile forces in each link are

$$\begin{aligned} F_{L_1} &= mA_{CG}\hat{\jmath}' + F_S\cos(\theta - \psi) \\ &= m\left(A_{CG}\hat{\imath}\sin\psi + A_{CG}\hat{\jmath}\cos\psi\right) - F_{L_2}\left(\frac{Z}{L_2}\cos\psi + \frac{L_1}{L_2}\sin^2\psi\right) \\ &= m\left(L\left(\omega + \dot{\psi}\right)^2 + r\omega^2\cos\psi\right) - F_{L_2}\left(\frac{Z}{L_2}\cos\psi + \frac{L_1}{L_2}\sin^2\psi\right) \end{aligned} \tag{3.6}$$

and

$$\begin{aligned} F_{L_2} &= -F_S = \frac{-m_S}{\cos\theta}\left(g\cos\phi - \ddot{\psi}Y - \dot{\psi}^2 A + \omega^2\left(r + L_1\cos\psi - Z\right)\right) \\ &= \frac{m_S L_2}{Z}\left(\ddot{\psi}Y + \dot{\psi}^2 A - \omega^2\left(r + L_1\cos\psi - Z\right) - g\cos\phi\right) \end{aligned} \tag{3.7}$$

The force exerted by the slider mass on its constraint in the tangential direction is

$$F_{m_S} = F_{L_2}\sin\theta = F_{L_2}\left(\frac{L_1\sin\psi}{L_2}\right) \tag{3.8}$$

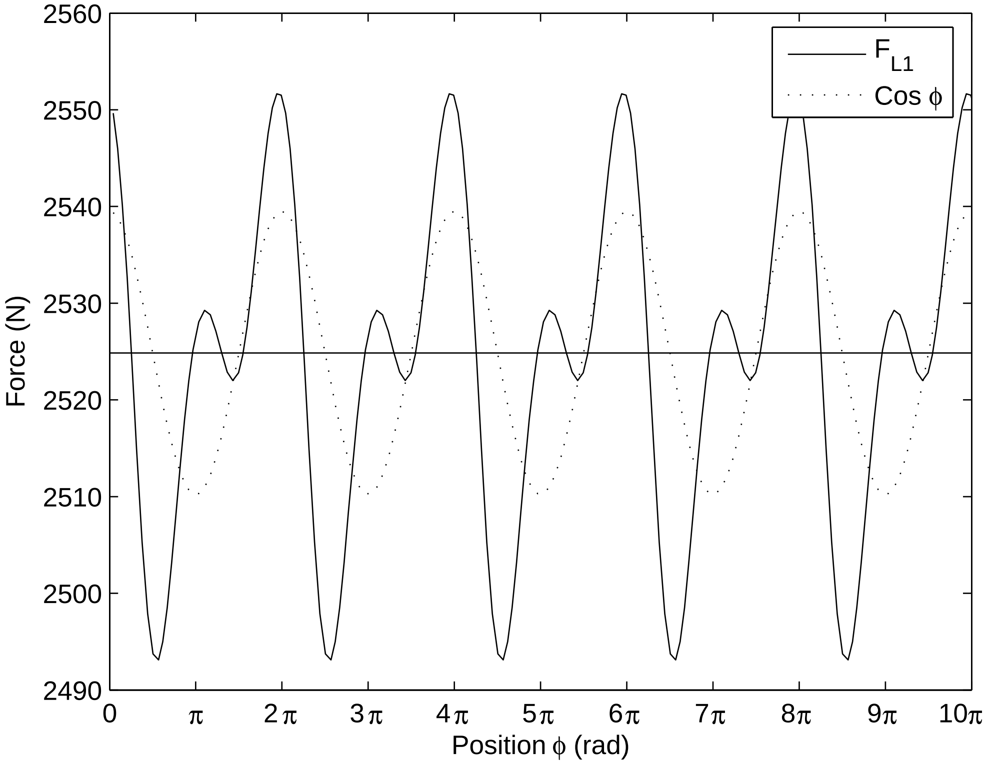

Figure 3-7: Tensile forces in link 1 as a function of propeller position calculated through numerical simulation at the maximum desired test speed of 350 RPM.

Numerical simulation was employed to generate the time varying values of the link and constraint forces plotted as a function of propeller position ϕ in Figure 3-7, Figure 3-8, and Figure 3-9.

3.3.2 Symmetrical Configuration

Due to the high forces in the links, it was necessary to use a symmetrical configuration that prevents bending moments from being transferred through the connections between links. The symmetrical configuration of the design is shown in Figure 3-10. The device is anchored by a plate and bearing block that sit between the two side plates of the integrated link 1 magnet assembly, with minimal clearance to reduce the bending moments exerted on the main pivot shaft. For logistical purposes, the paired secondary links are placed on the outside of the slider mass side plates and

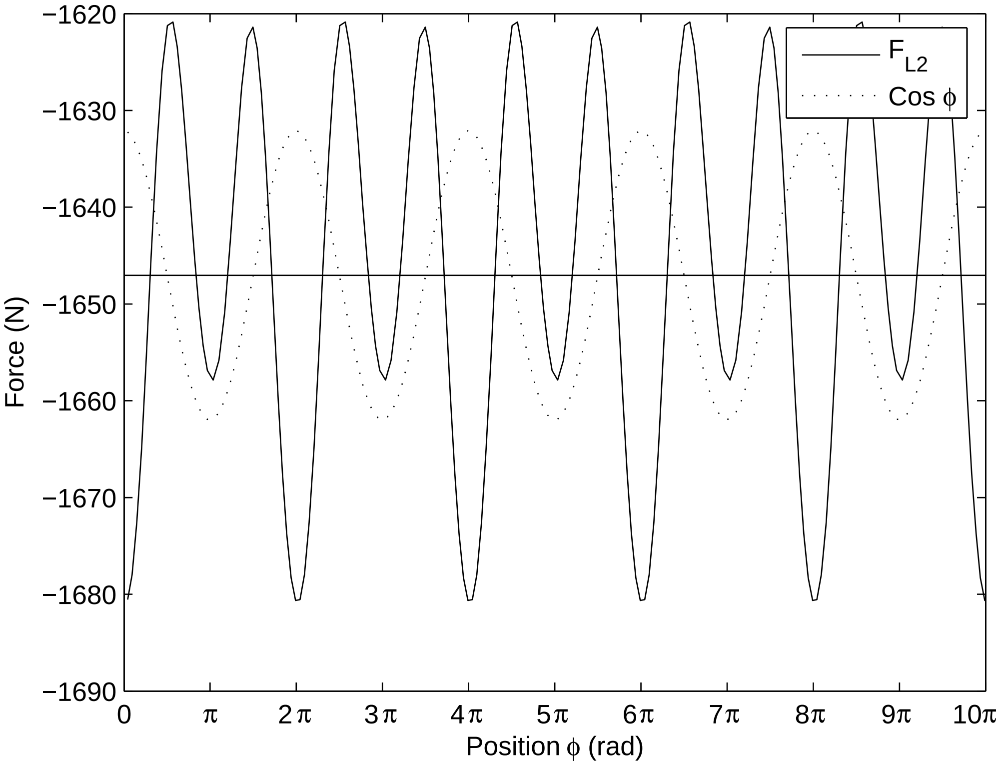

Figure 3-8: Tensile forces in link 2 as a function of propeller position calculated through numerical simulation at the maximum desired test speed of 350 RPM.

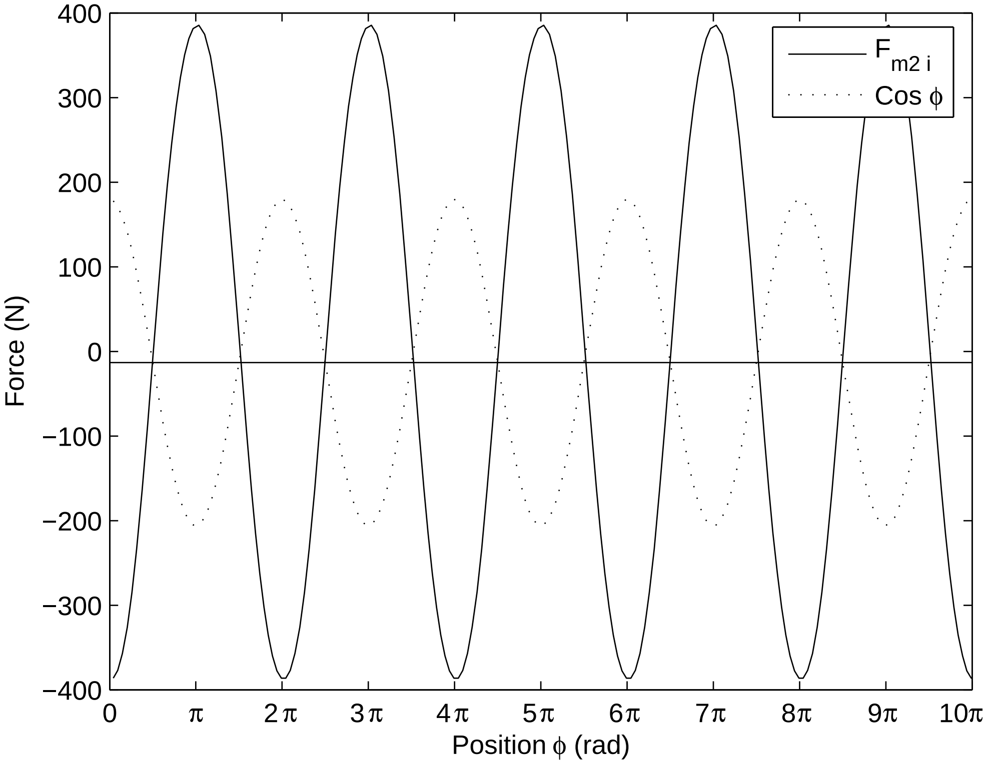

Figure 3-9: Reaction forces between slider of mass m_S and its constraint in the tangential direction calculated through numerical simulation at the maximum desired test speed of 350 RPM.

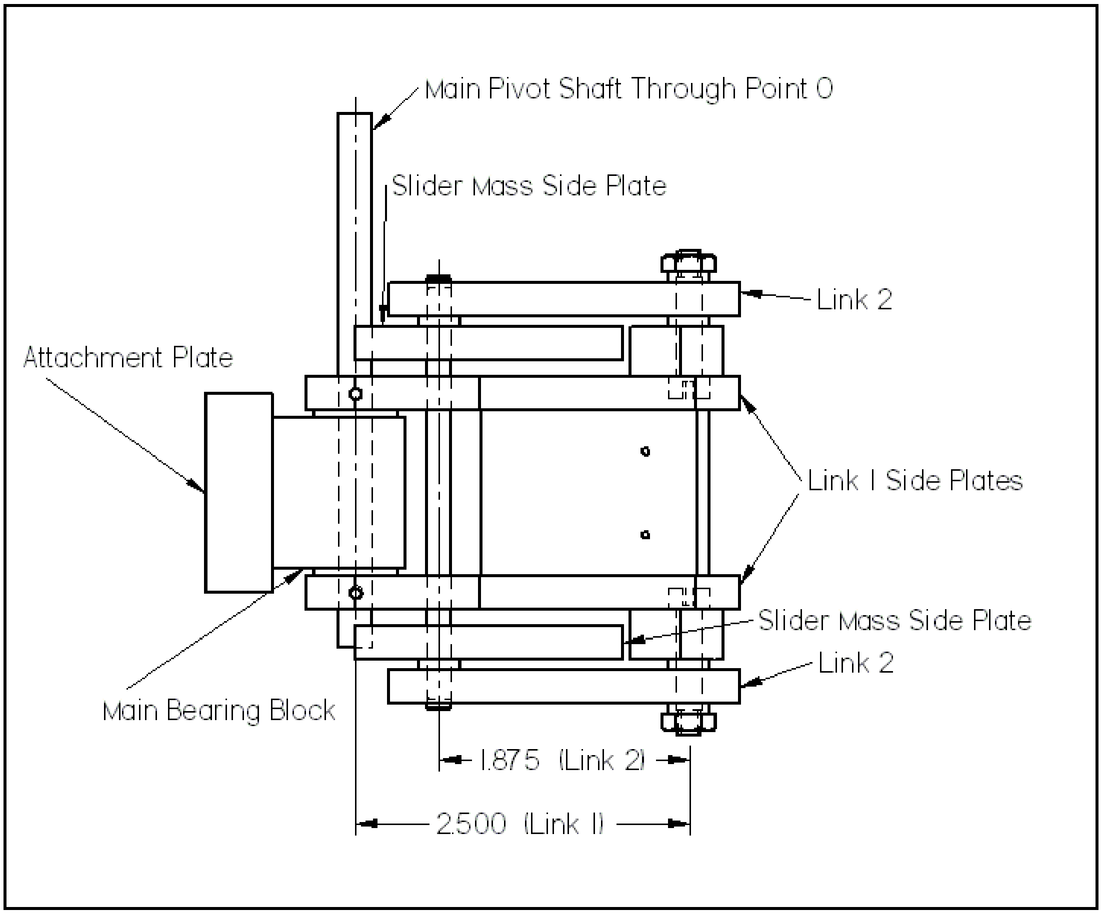

Figure 3-10: Top view of device showing the linkage configuration. Not shown in the diagram are the upper and lower plates that connect the two slider mass side plates to form a rigid box structure. All linear dimensions shown in inches.

are connected to studs that are press fit into blocks attached to the magnet assembly. This press fit configuration was chosen because the use of a through shaft was not possible, and the press fit offers much higher strength than a threaded connection. The slider mass itself is a box structure formed by the two side plates shown, and upper an lower plates that bridge across them to form a single rigid structure that prevents the linkage from warping. Various masses can be attached to these upper and lower plates to adjust the overall mass of the slider during testing.

3.4 Slider Constraints

The motion of the slider is small due to the choice of the linkage ratio in Section 3.1, and is plotted as a function of propeller position from numerical simulation as shown in Figure 3-11. The motion of the slider was deliberately designed to be small enough that flexures could be used as a low loss approximation of the sliding constraint. Flexures would be the method of choice for a production device, but a mechanical linkage based constraint was chosen for the prototype device to reduce design time and prototyping cost. The linkage design approximates linear motion over the small deflections of the slider mass by constraining it with three long links as shown in Figure 3-12. The upper ends of the links, as seen in the figure, are attached to the frame of the device and the lower ends are attached to the sides of the slider mass. Three links were chosen, two on the back side and one on the front, to prevent over-constraining the slider assembly.

3.5 Device Frame and Attachment

An outer framework for the device was designed to provide several important functions. The primary function of the framework is to rigidly support the internal components of the device, and to provide a secure attachment to the test stand. The centripetal forces acting on the linkage itself are transmitted directly through the back wall of the frame from the test stand. The remaining portions of the frame only need to rigidly support: the coil assembly with the integrated mechanical stops, the slider mass support links, and an encoder that measures deflection of the main pivot shaft. Having only light loads acting through the majority of the frame allows for a relatively lightweight aluminum construction that keeps overall device weight down, reducing the centrifugal loading on the test stand.

The frame must fully enclose all of the moving portions of the device, to prevent airflow from disturbing their motion, but still allow for quick modifications and safety checks to be performed during testing. The open box construction shown in the

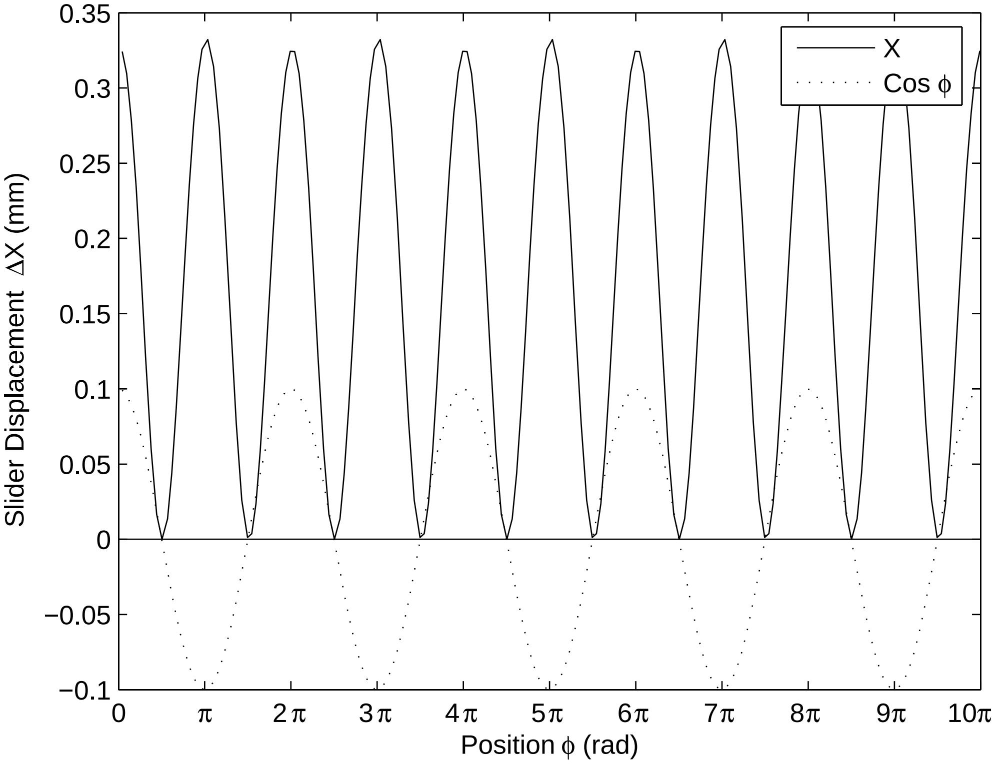

Figure 3-11: Slider deflection as a function of propeller position calculated through numerical simulation.

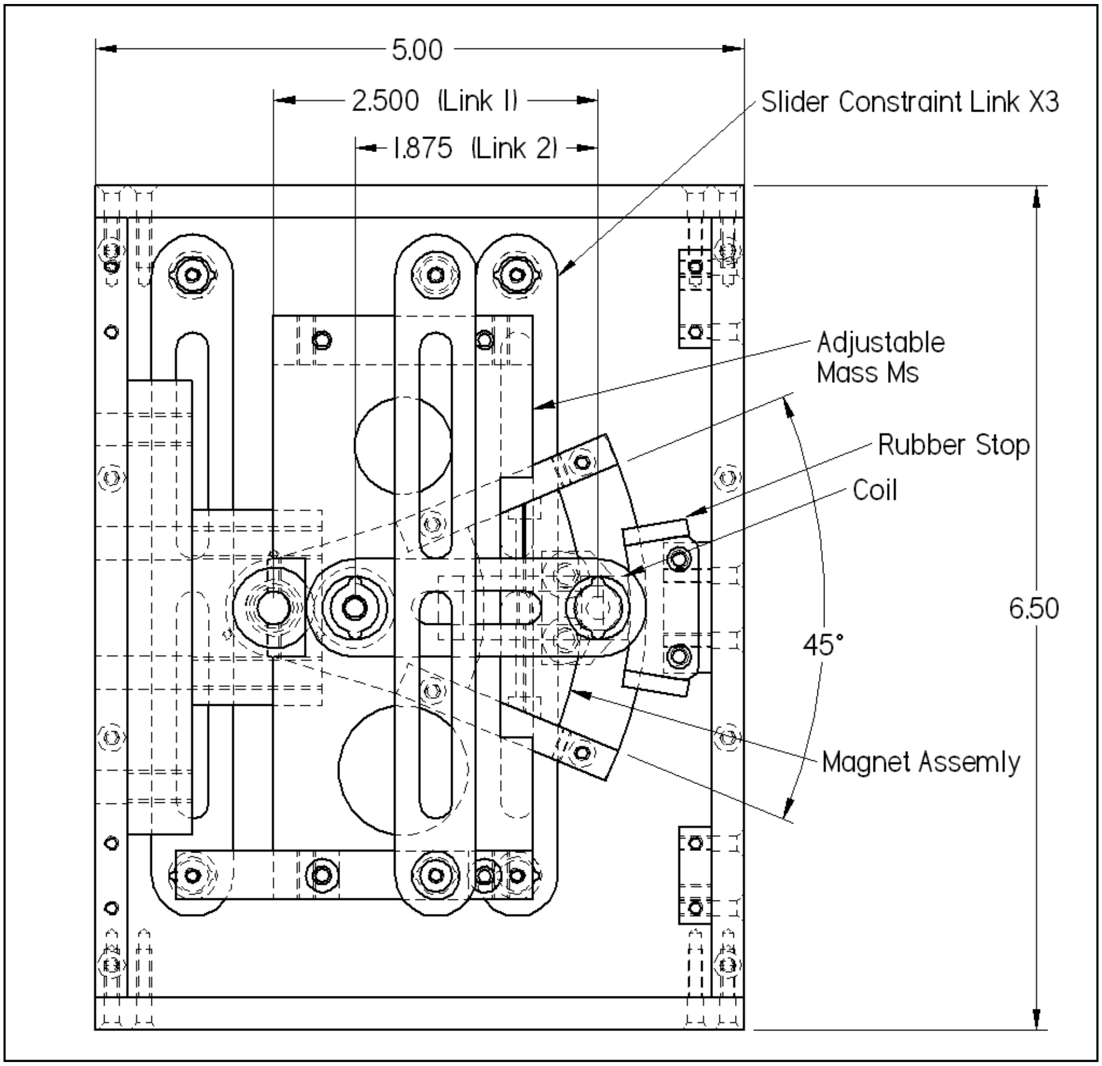

Figure 3-12: Side view of device showing coil assembly, linkage configuration, and slider constraints. All linear dimensions shown in inches.

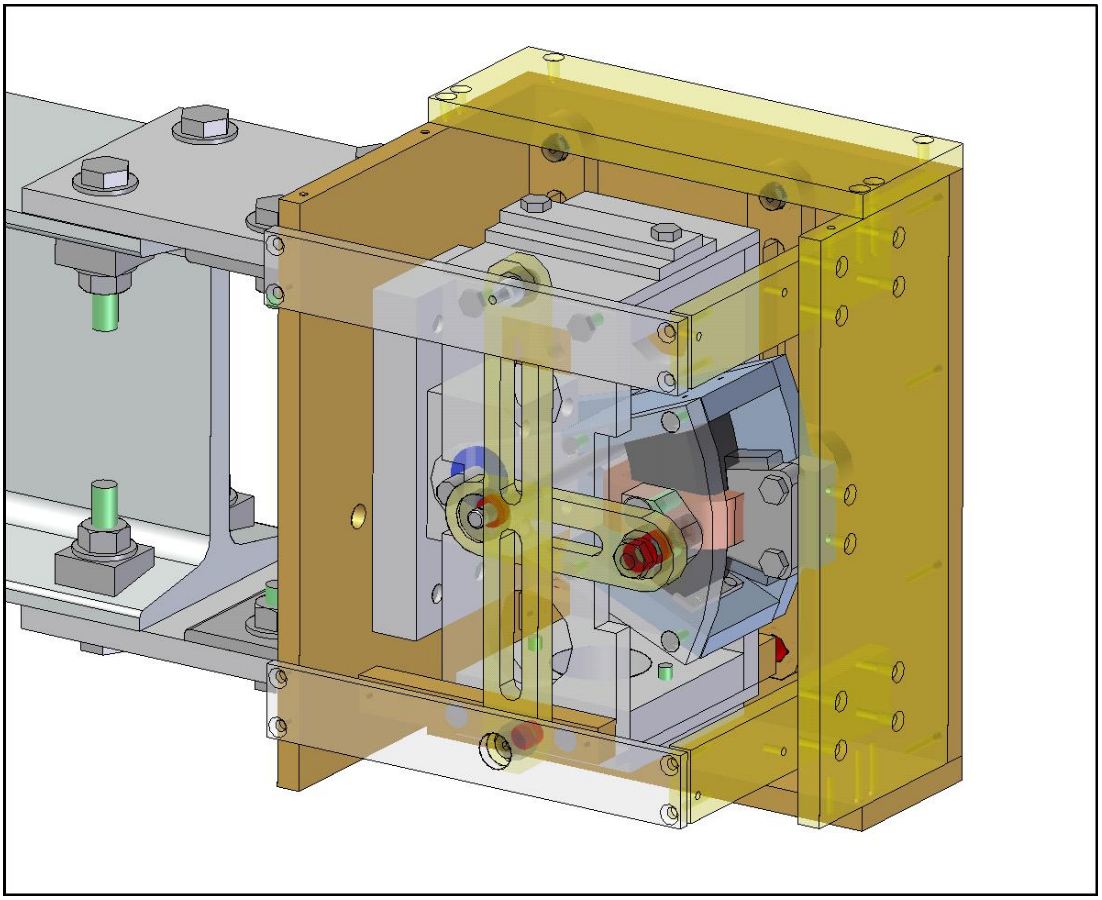

Figure 3-13: View of assembled prototype device showing the internal linkage installed in the frame, and the entire assembly mounted to the test stand arm.

Figure 3-13 incorporates four clear polycarbonate panels that allow for easy visual inspection, and can be easily removed to modify the mass of the slider. The two steel bars on the front of the device are the only components of the frame that must be removed for full linkage removal and disassembly, ensuring that the frame geometry does not change during disassembly and reassembly. These two steel bars also give the frame added strength to prevent any debris from escaping the enclosure should any component of the linkage fail.

3.6 Prototype Parameters

A summary of the parameters that were chosen for use in the design of the device that appear in Equation (2.30) are the link lengths $L_1 = 2.5$ in and $L_2 = 0.75$ in.

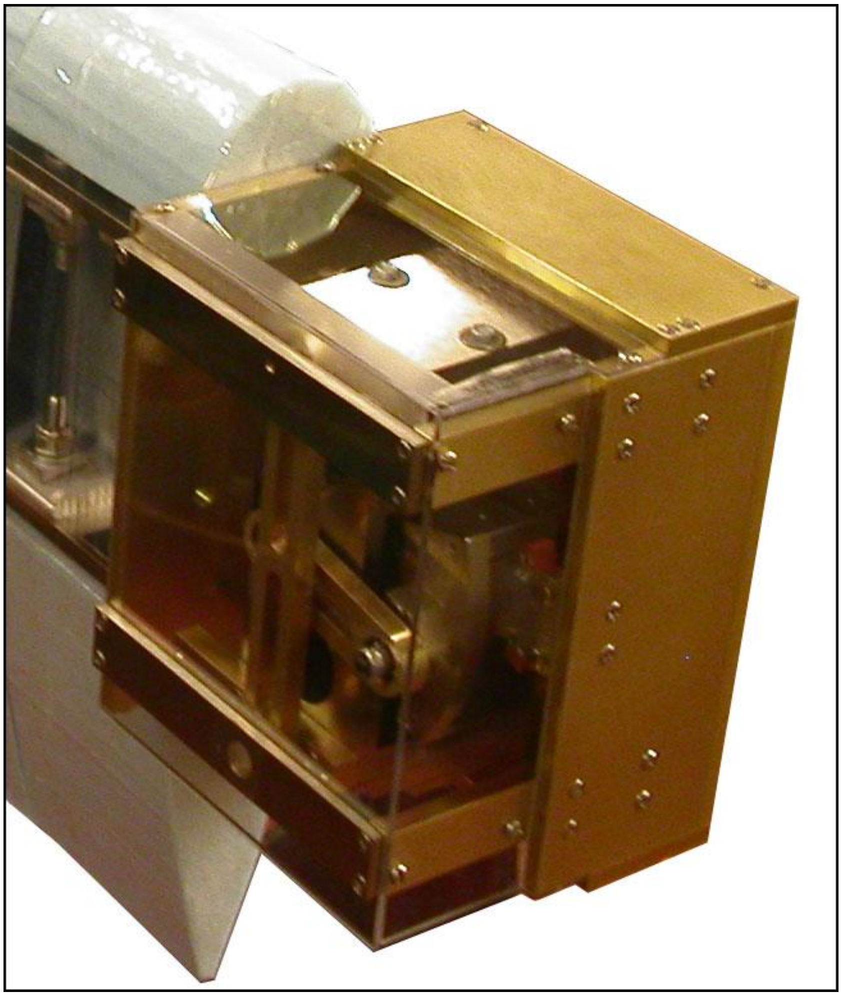

Figure 3-14: Photo of the assembled prototype device mounted to the test stand arm.

The radius at which the coil interacts with the magnet assembly is $L_C = 2$ in. The mass of the pendulous link m, the distance L between the pivot point O and the center of gravity of the link, and its rotational inertia I_O were found from the 3D solid model shown in Figure 3-13. From the solid model of the link 1 assembly, the mass, location of the center of mass, and the rotational inertia about the pivot were measured as $m = 1.39$ lbm, $L = 1.755$ in, and $I_O = 5.584$ lbm in^2 respectively. Through simulation, the required slider mass to achieve a frequency ratio of unity was found to be $m_s = 2.621$ lbm. Detailed drafts of the individual parts of the prototype system are shown in Appendix B.

Chapter 4

Experimental Setup

The goals for laboratory testing of the prototyped system were primarily to verify the dynamics of the device, and to characterize and quantify the performance of the system. It was also desirable to demonstrate the ability of the device to perform the task of charging batteries. In order to support these goals, it was necessary to provide the device with proper excitation conditions and an adjustable load. Testing required instrumentation capable of measuring the deflection of the device, its phase relative to the excitation, and the power output of the device given by the voltage and current delivered to the load. Conducting the desired testing required the design and development of custom equipment including a computer controlled spin stand to provide the designed trajectory, and two different microcontroller based adjustable loads. This chapter gives an overview of the capability of these systems, and their integration with the data acquisition and control hardware.

4.1 Spin Stand

The primary requirement of the spin stand is the ability to hold the device securely at a 1 m radius and smoothly spin it at speeds up through 350 RPM, with enough torque to overcome wind drag and provide the necessary accelerations. Full computer controlled closed loop control was desired to ensure that the device was spinning at the precise target speed, and to monitor the cyclic errors in the rotation rate. A means of transmitting the necessary data between the rotating device and the stationary instrumentation was required. Sensors are required to both close the control loop around the rotation rate of the stand ω, and provide the data acquisition system the actual angular position ϕ of the arm and the device deflection ψ in real time for phase measurements.

The spin stand configuration is shown in Figure 4-1 with key dimensions and features labeled. The mechanical structure was designed using a factor of safety of $n = 2$ against immediate failure in the event of a 10 lbm out of balance condition at 350 RPM. For the desired range of payload, an infinite expected fatigue life of the drive line was achieved by minimizing the bending moments in each of the shafts. The drive line of the spin stand consists of a Leeson model N182D17FK1B 2 hp permanent magnet DC servo rated for continuous operation at 1750 RPM, 9.5 A of current, and a supply of up to 180 V DC. The motor is coupled to a short shaft that drives the timing belt noted in the diagram. The 1 in wide H series timing belt is driven by a 16 tooth pulley, and a 60 tooth pulley is attached to the main shaft, giving a drive ratio of 3.75. The arm of the device consists of a 6 ft × 4 in standard section 6061 aluminum I beam connected to the main shaft with a custom designed hub. The hub allows the arm to freewheel on the shaft in the event of a drive line seizure without allowing it to break free. The hub design also aids in the routing of the wiring from the twelve channel Lebow 6105-12 slip ring, through a collar between the shaft and the bearing, and out onto the rotating arm.

The power amplifier used to supply current to the motor is the Advanced Motion Controls model 30A20AC Brush Type PWM Servo Amplifier. This amplifier was selected for its ability to draw power directly from the standard single phase 120V supply. The amplifier accepts an analog input command, and applies a proportional current through the motor windings, which is in turn proportional to the torque applied on the arm of the spin stand. Using the current sensing capabilities of the amplifier, the arm torque and steady state rotation rate were measured at various command levels, and the coefficient of drag of the bare beam was found to be $C_D = 1.981$. This high aerodynamic drag limited the rotation rate to less than 300 RPM

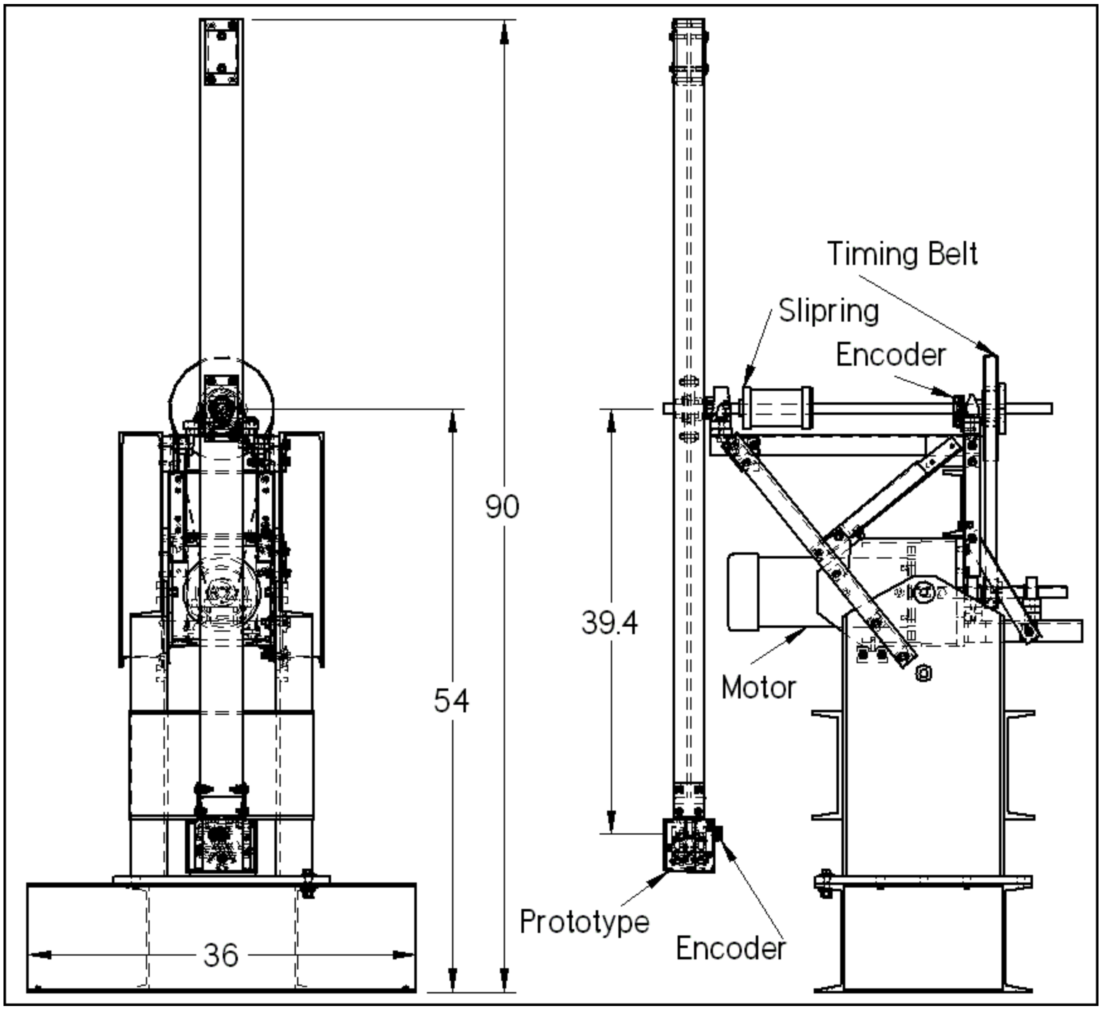

Figure 4-1: Simplified assembly diagram of the spin stand showing the overall dimensions, drive line configuration, and basic instrumentation.

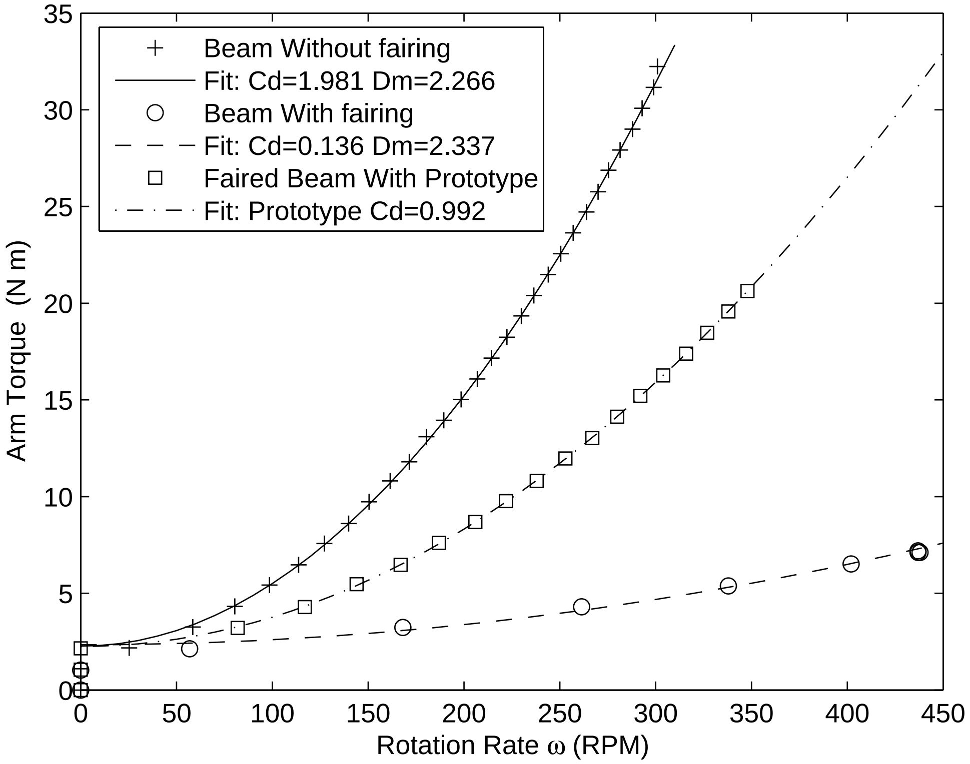

Figure 4-2: Curves characterizing the aerodynamic drag on the arm of the spin stand without fairing, with fairing, and with prototype attached. The coefficient of drag C_D and constant mechanical drag D_M values are given for each fit curve.

at the maximum continuous arm torque of 30.5 N m, as shown in Figure 4-2. An aerodynamic fairing was fabricated using a CNC wire foam cutter to produce a NACA 0012 profile large enough to encase the beam. The fairing reduced the coefficient of drag by an order of magnitude to $C_D = 0.136$, and then the rotation rate was limited by the rail voltage of the servo amplifier at 440 RPM. With the unfaired prototype attached to the faired beam, the spin stand is capable of operating at speeds up to the desired 350 RPM with ample available torque for acceleration and control.

Two incremental digital optical encoders are used in the experimental setup to measure the angles ϕ and ψ. The angle ψ is measured by a US Digital model E5S-900-250-I encoder, that, with 900 full quadrature counts per revolution, can measure the displacement of the pendulous link to a tenth of a degree. The encoder on the main shaft of the spin stand is a US Digital model E6S-1800-1000-IH and has twice

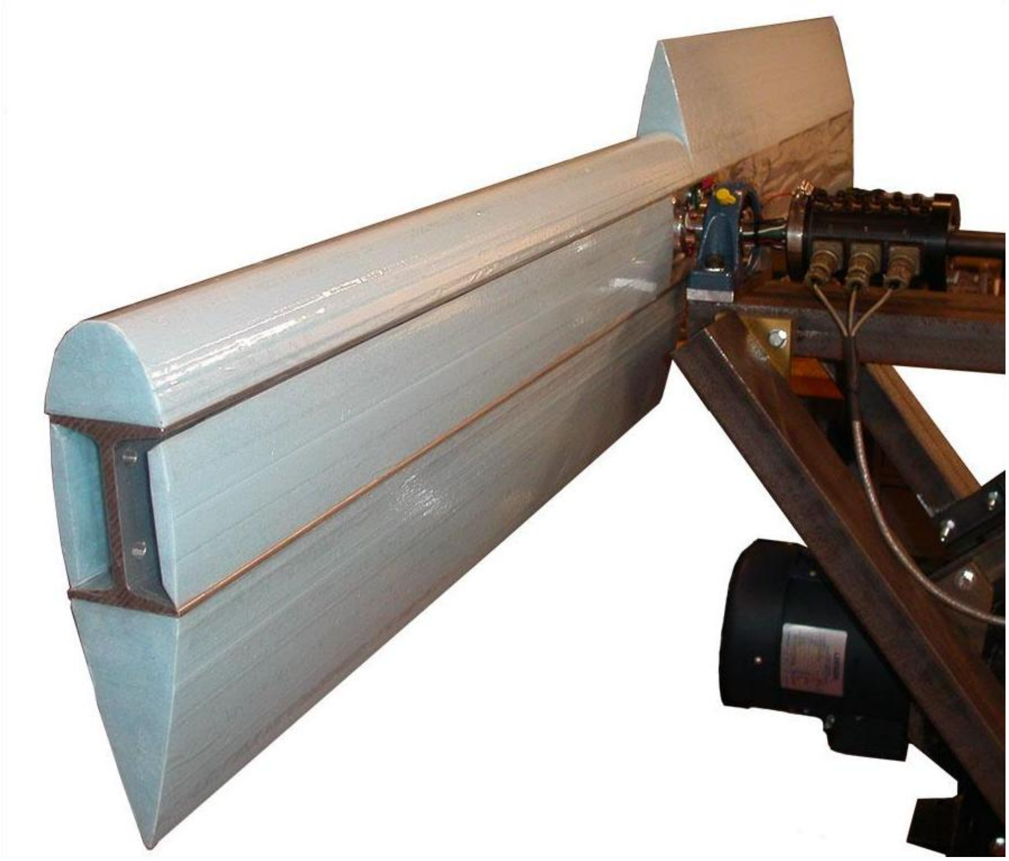

Figure 4-3: Photo of spin stand arm with CNC cut NACA 0012 fairing for reduced aerodynamic drag.

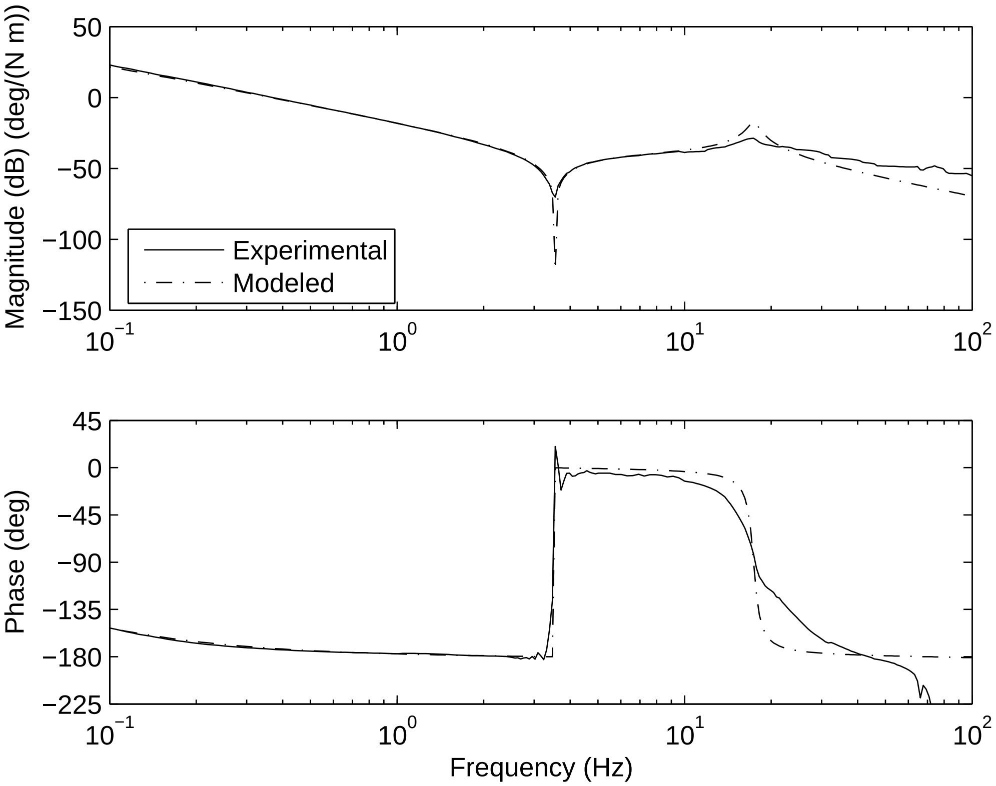

Figure 4-4: Frequency response plot measured from torque command to main shaft encoder measured displacement.

the resolution. Both encoders are interfaced directly to a dSPACE DS1103 real-time controller development board that is used for both data acquisition and closed loop control of the spin stand. Using code developed in the Precision Motion Control Laboratory at MIT, the frequency response of the system was taken with the dSPACE card and fit to the model, as shown in Figure 4-4 [4]. Taking a loop shaping approach, a controller was designed from the measured data that stabilizes the system with a 1 Hz crossover. The controller consists of a gain, a lead term centered at 1 Hz, and a complex pair of poles at 3 Hz, with a damping ratio of $\zeta = 0.5$. This gives the controlled system a phase margin of over 40°, a gain margin of over 2 dB, and phase stabilizes the resonant peak. The resonant peak is attenuated to -30 dB as measured. The actual controller as implemented in the Simulink model that is compiled to the dSPACE board can be seen in Figure C-4. The frequency response of the controlled system is shown in Figure 4-5.

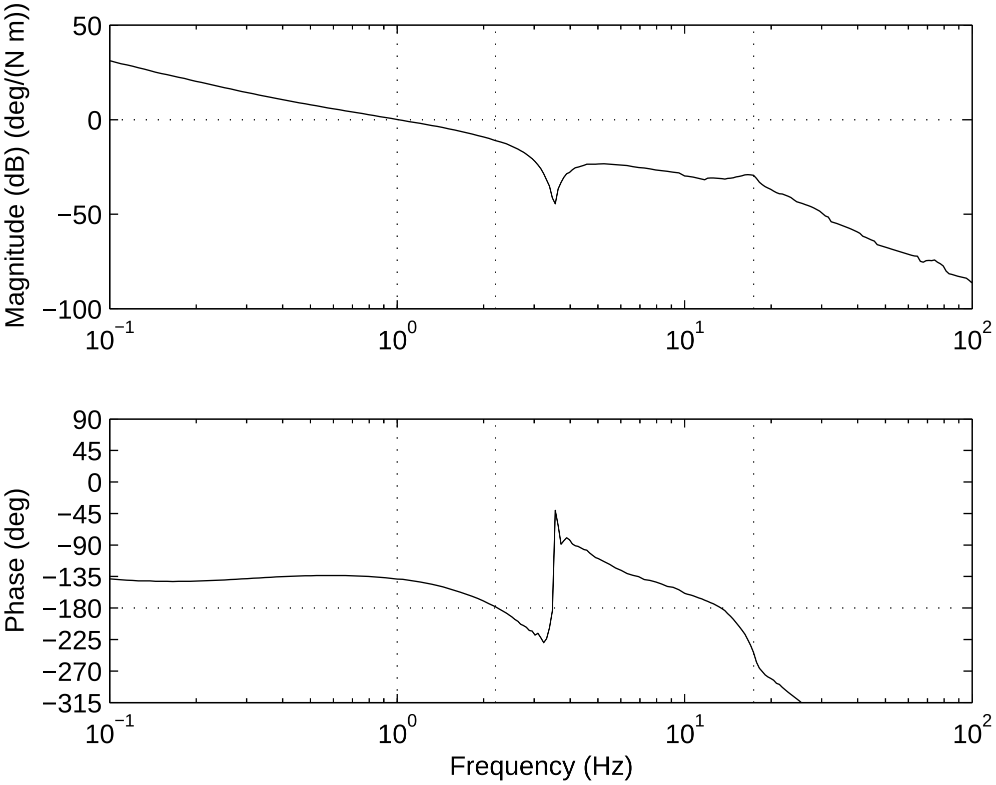

Figure 4-5: Frequency response plot of the open loop transfer function with the controller applied, showing system stability.

Implementing velocity control with digital incremental encoder feedback can be difficult, due to the discontinuous position signal from the encoder. Using the change in position between samples as a measure of the velocity becomes increasingly problematic as the velocity becomes low compared to the sampling rate. At high sample rates the velocity appears to be zero while the encoder is between counts and spikes to large values when each count is received. To eliminate this problem, position control was implemented, and the system was made to follow a position trajectory in time that results in the desired velocity. This introduces the problem of variable overflow as the position becomes large during continuous rotation. For this reason, the position error signal that goes into the controller is not generated from the difference between the absolute desired position and the actual position. The position error is stored in an integrator that is updated each time sample with a delta position desired and delta position achieved. Saturation is applied to this error storage integrator to prevent excessive windup.

In order to protect the device from sudden changes in acceleration and to prevent saturation of the amplifier during transitions, a trajectory generator is implemented. The smooth trajectories in velocity that are generated allow the system to gracefully transition from one operating speed to another. The trajectory generator was implemented in a Stateflow chart within the Simulink model and is compiled to the dSPACE board with the controller and other model components. The Stateflow chart also automates the open loop indexing process that initializes the encoders. This is accomplished by initially rotating the arm using only the open loop feed forward controller that is based on the aerodynamic measurements. Once the encoders have both been indexed, the closed loop controller is initialized to the current rotation rate, and a smooth trajectory is followed to the desired operating speed. Sample output for the the Stateflow chart can be seen in Figure 4-6, and the chart itself is shown in Figure C-3. The complete Simulink model that is compiled to the dSPACE board includes other features such as subsystems that keep track of the true arm angle and provide safeguards against exceeding the safe operating speeds. The full Simulink model is presented in Appendix C.

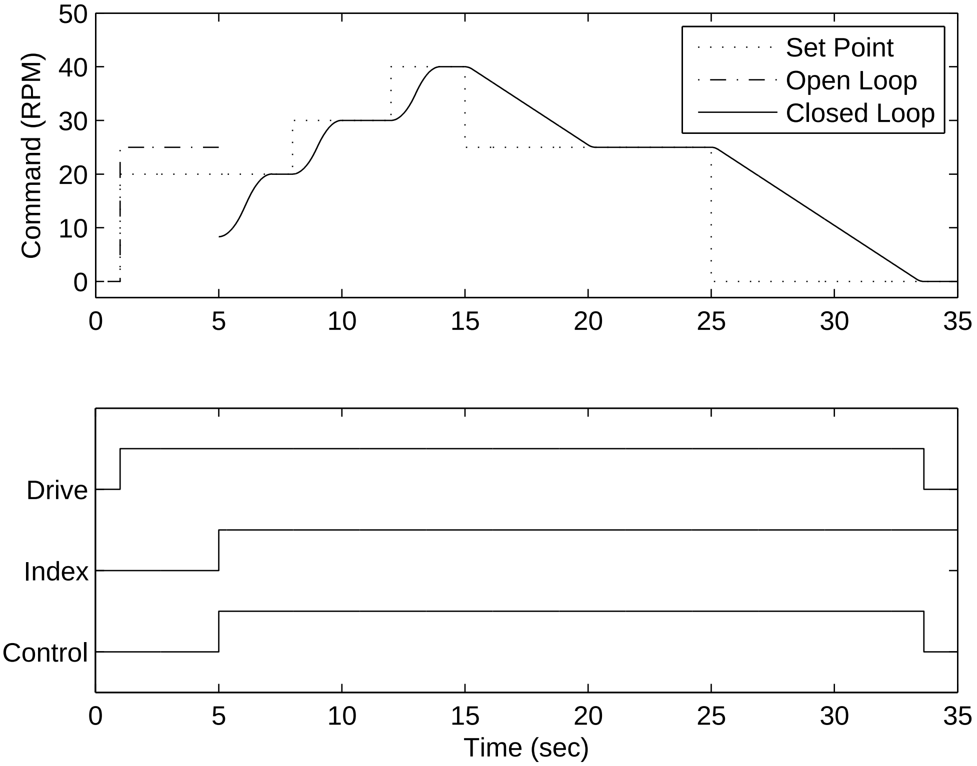

Figure 4-6: Sample output of Stateflow trajectory generator. *Set Point* is the desired operating speed set by the user, *Index* is the state of the encoders. *Open* and *Closed loop* command are outputs from the Stateflow chart to the control system, *Drive* enables the servo amplifier, and *Control* enables the closed loop controller.

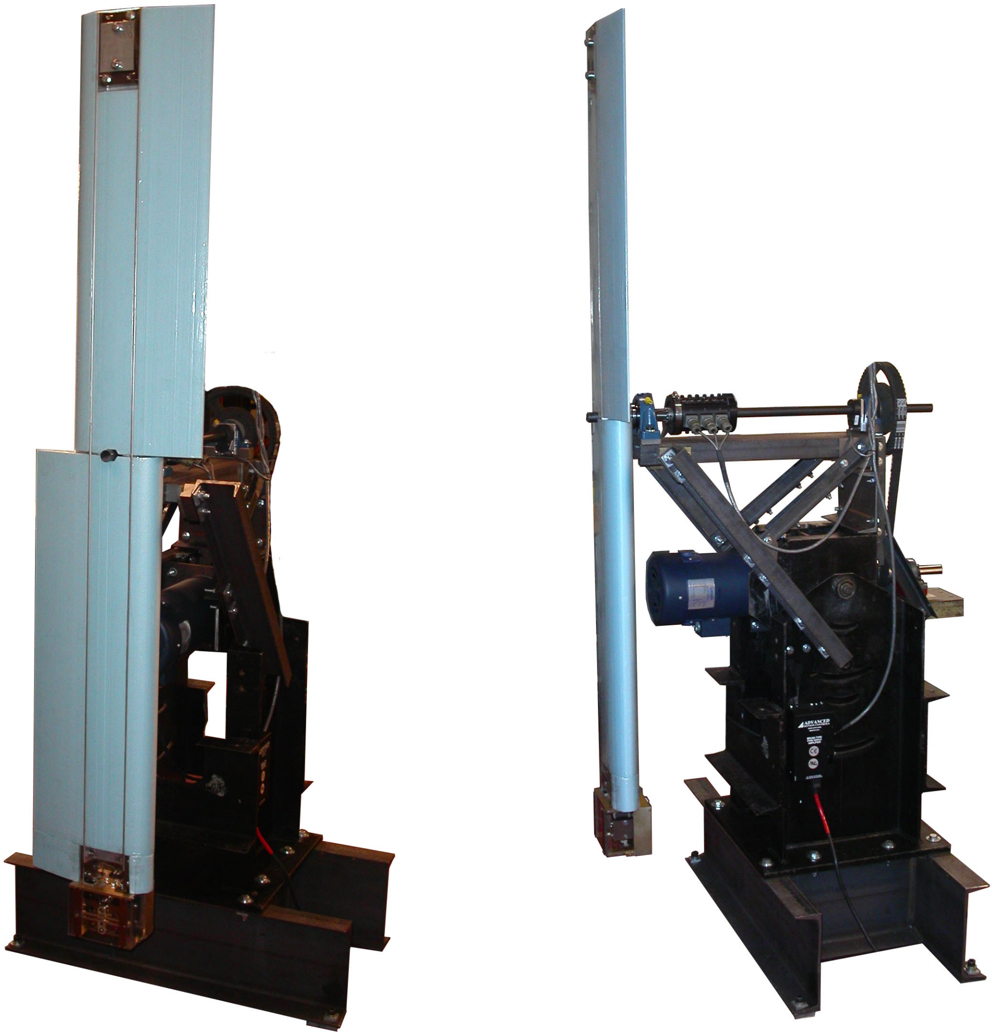

(a) (b)

Figure 4-7: Photographs of the spin stand with the prototype device mounted for testing.

4.2 On-board Variable Loads

Two different variable loads were constructed and used in the testing of the prototype device. One load was designed to provide a purely resistive load for the purpose of characterizing the device and measuring the maximum power output at various rotation rates and damping levels. The second load was designed to demonstrate the capability of the device to charge a battery through a high speed switching circuit. Both loads were designed to be mounted on the beam within the fairing to avoid the multiple connections and long stretches of wire that would be required to bring the coil leads out through the slip ring to the stationary frame. An Atmel ATmega168 microcontroller was mounted on the beam and used to control each of the loads. The microcontroller established two way RS232 communications through the slip ring with the PC that operates the spin stand to display its status, and to receive commands from the operator.

4.2.1 Resistive Load

The resistive load circuit shown in Figure 4-8 has a simple structure of resistors and relays. The six resistors placed in series range from 4 Ω to 128 Ω increasing by factors of two. The six independently controlled Hamlin HE721A0510 reed relays used to short out the resistors are switched by a parallel communications port on the microcontroller. This configuration allows the microcontroller to digitally select a load resistance ranging from short circuit to 252 Ω with a 4 Ω resolution. An additional relay is used to open or close the entire circuit, allowing the voltage of the coil to be measured under open circuit conditions. To prevent centrifugal loading from affecting the operation of the relays, the circuit is mounted near the hub of the arm with the relays oriented such that their reeds point radially outward. The circuit was found to operate without error under the maximum centrifugal loads encountered during testing.

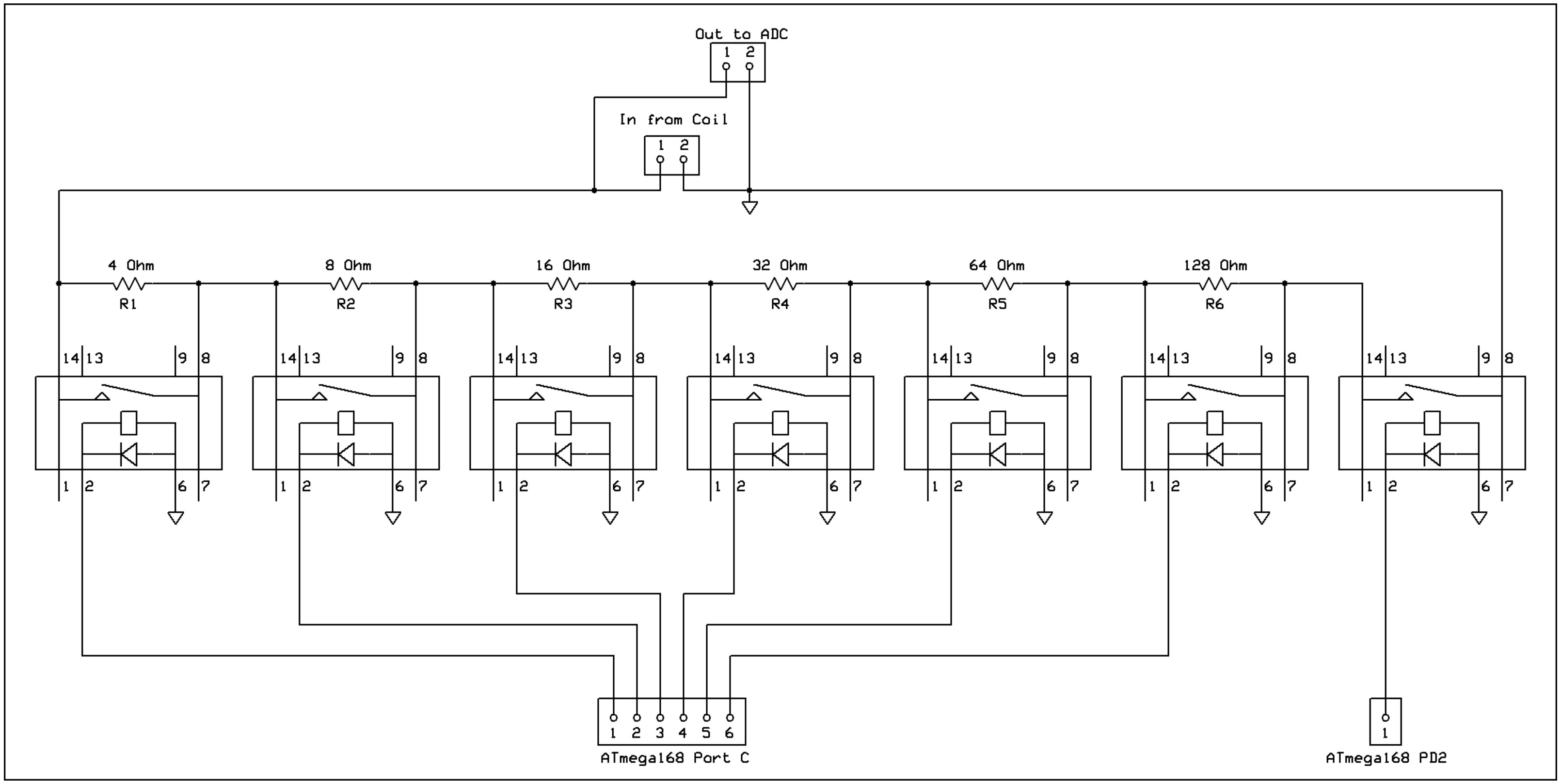

Figure 4-8: Resistive load circuit diagram showing arrangement of resistors and reed relays.

4.2.2 Switching Load and Mock Battery

The switching load and mock battery circuit, shown in Figure 4-9, was designed to demonstrate the capability of the device to charge batteries, and to investigate any changes in the dynamics of the device caused by the nonlinear load. The circuit has the ability to accurately measure the power output of the device that is delivered to the load, but the circuit itself is externally powered, and circuit efficiency was not a consideration in the design. The basic structure of the circuit is to rectify the AC voltage from the coil and to use it to charge a large storage capacitor. This large capacitor acts as a low pass filter, maintaining a nearly constant voltage despite the pulsating input current from the magnet assembly. The stored energy in the capacitor is then supplied to a high speed switching DC-DC converter, that efficiently brings the voltage down to the levels appropriate for charging a battery. In the true application, the battery would be used for long term storage and would supply power, at a stable voltage, to the attached systems.

The power conditioning portion of the circuit uses Schottky diodes in a full bridge configuration to charge the large storage capacitor. The DC-DC converter was designed with an IRFBG20 power MOSFET as the switching element, and a smaller 2N7000 MOSFET to drive the gate of the power MOSFET. The smaller MOSFET is driven by an adjustable duty cycle 25kHz PWM signal generated by the ATmega168. An inverting buffer is used to offer added protection to the microcontroller. This simple switching circuit was convenient for the desired test and functioned well for the known voltage range of the coil. In general, for high or unknown coil voltages, it would not be sufficient to drive the power MOSFET gate from a high voltage supply, and commercially available bootstrapping MOSFET driver chips would offer a better solution. After the switching stage, the standard DC-DC converter structure, using an inductor, capacitor, and diode to ground, is used to step down the voltage and step up the average current.

The use of an actual battery in the circuit is not convenient for laboratory testing, because the state of charge of the battery would become an additional variable in the system. A real battery would have varying resistance and voltage characteristics at varying levels of charge and temperature, and would not be suitable for continuous testing due to the dangers of overcharging. For these reasons, a mock battery circuit was designed to approximate the electrical characteristics of a battery without the extra variability. The circuit consists of a small sense resistor that approximates the internal resistance of the battery and a 2.4 V zener diode that is biased with a current from an external source. This configuration gives the circuit the characteristics of a standard battery model of a voltage in series with a resistance, and also provides direct measurement of the power delivered by the prototype device.

Two identical buffer amplifier circuits with a gain of 2 were used to measure the voltage before and after the mock battery resistance, to provide amplification, and to drive the long lines running through the slip ring assembly and back to the control PC without influencing the circuit. The first buffer amplifier provides the voltage across the mock battery circuit, and the difference between the two measurements is used to calculate the current passing through the circuit from the DC-DC converter. This configuration allows the true power delivered to the mock battery to be calculated.

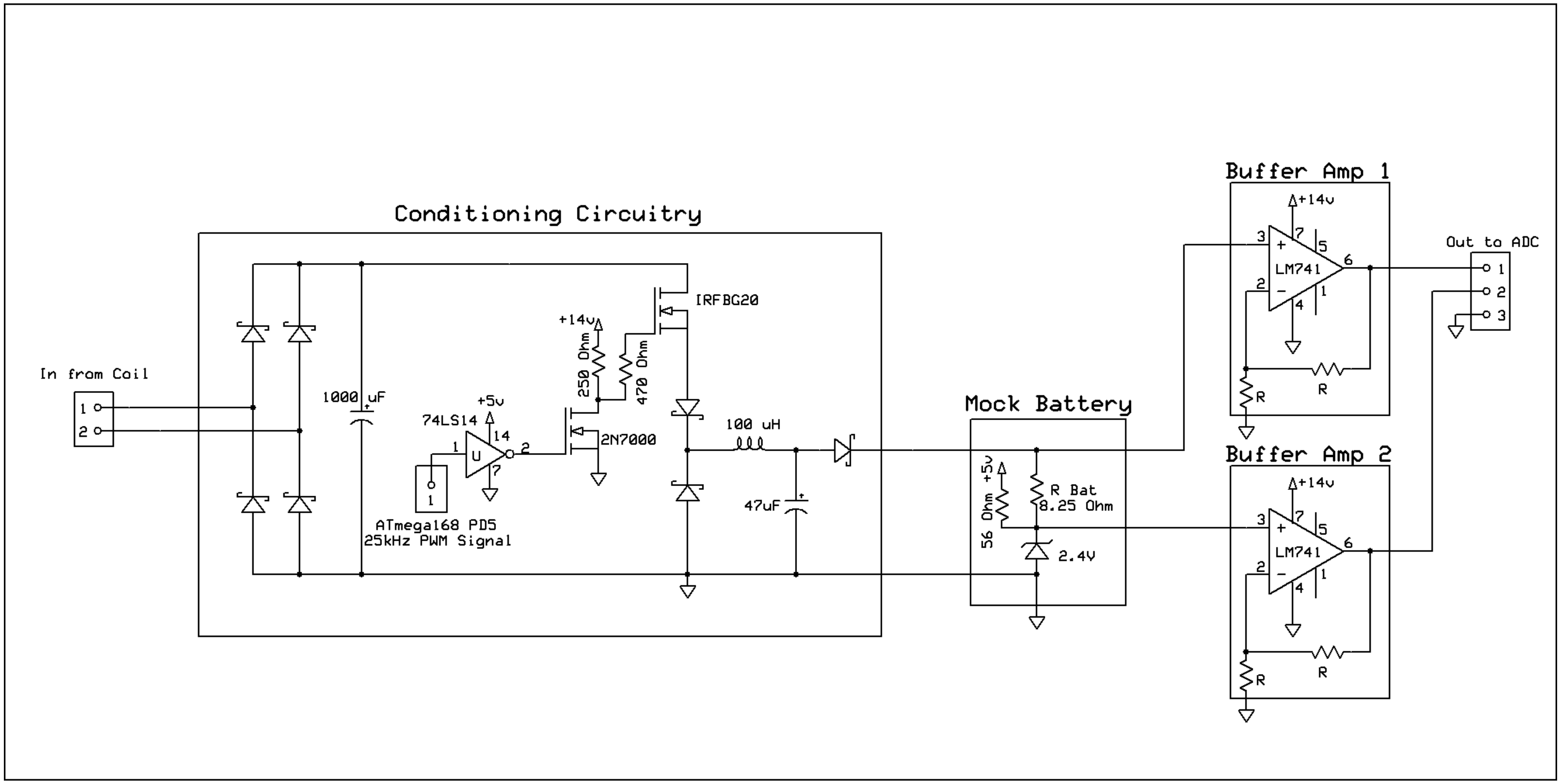

Figure 4-9: Switching load circuit diagram consisting of power conditioning circuitry, mock battery, and buffer amplifiers.

Chapter 5

Experimental Results and Discussion

Laboratory testing was conducted to measure the parameters of the prototype inertial generator experimentally and to characterize the performance of the device during operation. Static tests, conducted with the device fixed to a stationary level surface, included the measurement of the coil impedance as a function of frequency and measurement of the electromagnetic coupling coefficient as a function of displacement. These measurements were used to complete the model of the device that was developed in Chapter 2. Spin testing employed the use of the spin stand to swing the device through the circular trajectory. Spin testing was conducted with the resistive load and the high speed switching load circuits that were presented in Chapter 4. These spin testing experiments were conducted to verify the function of the device, quantify its performance, and demonstrate its ability to perform the representative task of battery charging.

5.1 Static Testing

5.1.1 Coil Impedance

In Chapter 2 the damping of the system was given in Equation (2.71) with the assumption that the impedance of the coil could be considered purely resistive over the frequency range of operation. To verify this assumption, the impedance of the coil was measured as a function of frequency to establish the resistance of the coil R_C and to measure the influence of the coil's inductance and parasitic capacitance throughout the frequency range of operation. The same code that was used to measure the frequency response of the spin stand was used with the dSPACE system to measure the impedance of the coil [4]. The sinusoidal excitation output by the DAC was amplified with a simple op-amp buffer amplifier circuit and was used to drive the coil and a sense resistor in series. The voltage across the coil was measured, and the voltage across the sense resistor was used to calculate the current passing through the coil, allowing the impedance of the coil to be found.

The impedance of the coil was measured with the coil installed within the fully assembled magnet assembly, so that the impedance would be measured with the proper core permeability. Measuring the impedance of the coil in this configuration adds the complication that the current passing through the coil tends to excite the magnet assembly, which introduces additional dynamics from the system. To isolate the dynamics of the coil from the dynamics of the mechanical system, the measurements were taken under two conditions. First, the magnet assembly was physically constrained to minimize the relative motion between the coil and magnet assembly. This procedure pushes the mechanical resonances of the system to relatively high frequencies. A second set of measurements was taken with the magnet assembly unconstrained, allowing the mechanical resonances to drop to lower frequencies. From the overlay of the two sets of data, shown in Figure 5-1, the discrepancies between the two curves can be attributed to the mechanical resonances of the system, and the common features are the true coil characteristic. The results show that the coil has a DC resistance of $R_C = 47.9\ \Omega$, and the impedance can be considered purely resistive for frequencies up to nearly 100 Hz. The desired speeds for physical testing fall at much lower frequencies, so that the purely resistive model used to represent the coil impedance is adequate.

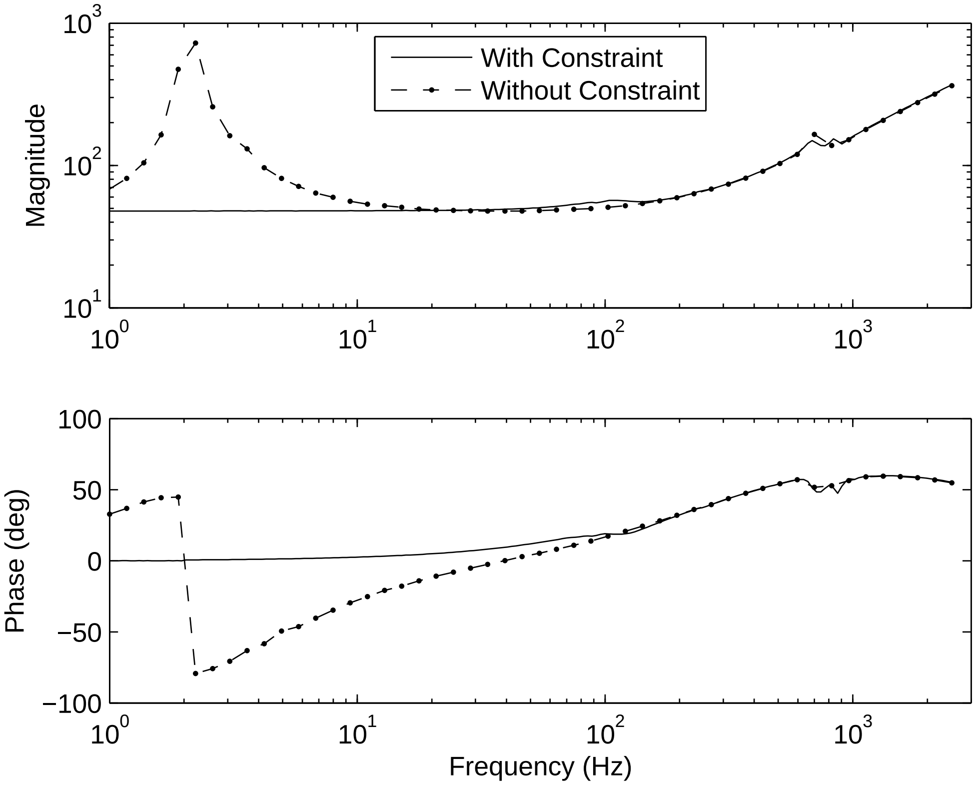

Figure 5-1: Coil impedance as a function of frequency when installed within the magnet assembly. Measurements were taken with and without physical restraints applied to magnet assembly to distinguish between actual coil impedance and mechanical resonances.

5.1.2 Electromagnetic Coupling Coefficient

The electromagnetic coupling coefficient K_{EM} was measured as a function of the displacement ψ by using the relationship between the velocity $\dot{\psi}$ and coil voltage V expressed in Equation (2.68). The prototype device was placed on a flat surface and the magnet assembly was manually displaced and released. As the magnet assembly swung back and forth through the stationary coil, the open circuit coil voltage and the encoder position ψ were recorded by the dSPACE system. The data was processed in MATLAB to determine the coupling coefficient and position at each time sample, and the data corresponding to each position was averaged over many cycles. The results from this analysis are presented in Figure 5-2 and show the expected trend, with the coupling reaching the highest values when the device is centered and the coil is in the strongest portion of the magnetic field. In this central region, the average value of the coupling coefficient was found to be

$$K_{EM} = 0.276\ \frac{\text{V}}{\text{deg/sec}} = 15.8\ \frac{\text{V}}{\text{rad/sec}} \tag{5.1}$$

This distribution of the coupling coefficient is quite acceptable, considering that the velocity $\dot{\psi}$ is highest in this central region, making it the most critical for the extraction of energy through damping. The maximum damping that the coil can provide is found from Equation (2.72) to be

$$b_{\max} = \frac{K_{EM}^2}{R_C} = \frac{\left(15.8\ \frac{\text{V}}{\text{rad/sec}}\right)^2}{47.9\,\Omega} = 5.22\ \frac{\text{Nm}}{\text{rad/sec}} \tag{5.2}$$

As discussed in previous chapters, improvements in this maximum available damping lead to increased power transmitted to the load across the entire range of frequencies. It has also been shown that for frequencies above ω_B, given by Equation (2.77), the power output is maximized when the optimal damping is applied, and for lower frequencies it is best to match the impedance of the load to the impedance of the coil.

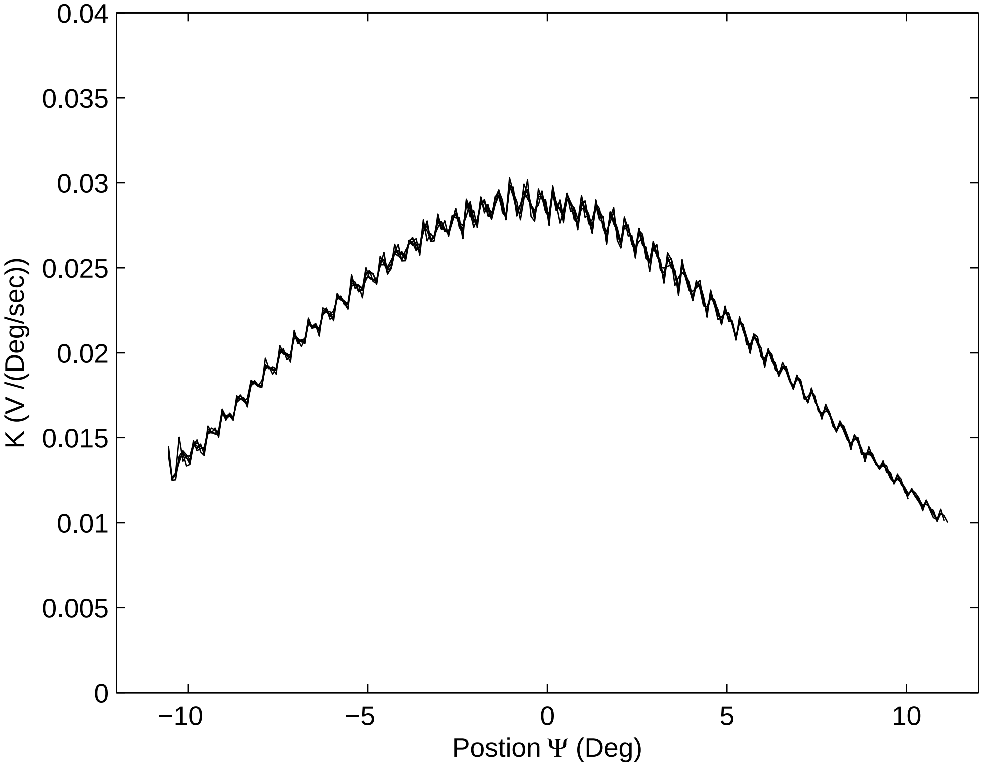

Figure 5-2: Measured electromagnetic coupling coefficient K_{EM} as a function of swing angle ψ.

5.2 Spin Testing

5.2.1 Spin Testing with Resistive Load

Spin testing with the variable resistive load was conducted over a range of rotation rates and load resistances. The power output results of this testing are presented in Figure 5-3, plotted versus rotation rate. The results show the expected trend of increasing power output with increasing frequency. It should be noted that all of the data points shown in the figure were taken in a single spinning test, and that the only changes in the system were the rotation rate and the load resistance. The output of the device contrasts sharply with that of the traditional sprung mass vibrational energy harvesters, which must be physically modified for excitation at each frequency to produce a smiler result. This monotonically increasing trend in the data and the power levels observed show that the natural frequency tracking concept can be used to achieve resonance over a broad range of frequencies.

Figure 5-4 presents the same power output data plotted versus load resistance, where it can be more clearly seen that the power transmitted to the load increases with increasing load resistance up to the point at which the load resistance is approximately impedance matched with the coil resistance at 48 Ω. A further increase in the load resistance does not tend to increase the transmitted power. This indicates that the system output is being limited by the electromagnetic coupling coefficient K_{EM}, and the mass of the pendulous link is not a limiting factor. At the highest frequency, the sharp drop in power output, as the load resistance is lowered from 28 Ω to 24 Ω, indicates that the damping of the system has increased beyond the optimal damping given by Equation (2.66). This observation is supported by the swing magnitude measurements shown in Figure 5-5. The amplitude loss that appears at load resistances below 24 Ω at 300 RPM indicates that this rotational rate falls between ω_A and ω_B on the normalized power curve presented in Figure 2-15. The fact that the other rotation rates do not show this loss of amplitude as the load resistance is lowered toward zero indicate that they fall below ω_A.

Assuming sinusoidal motion of the linkage at a fixed amplitude, it would be ex-

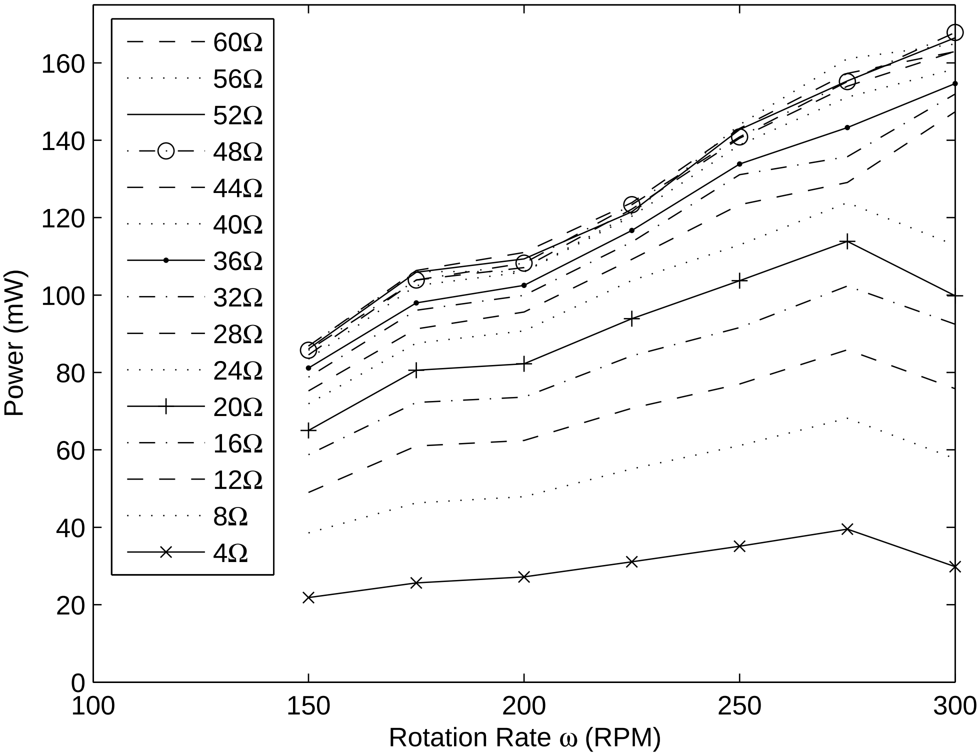

Figure 5-3: Steady state average power dissipated in the variable resistive load plotted versus rotation rate for various load resistances.

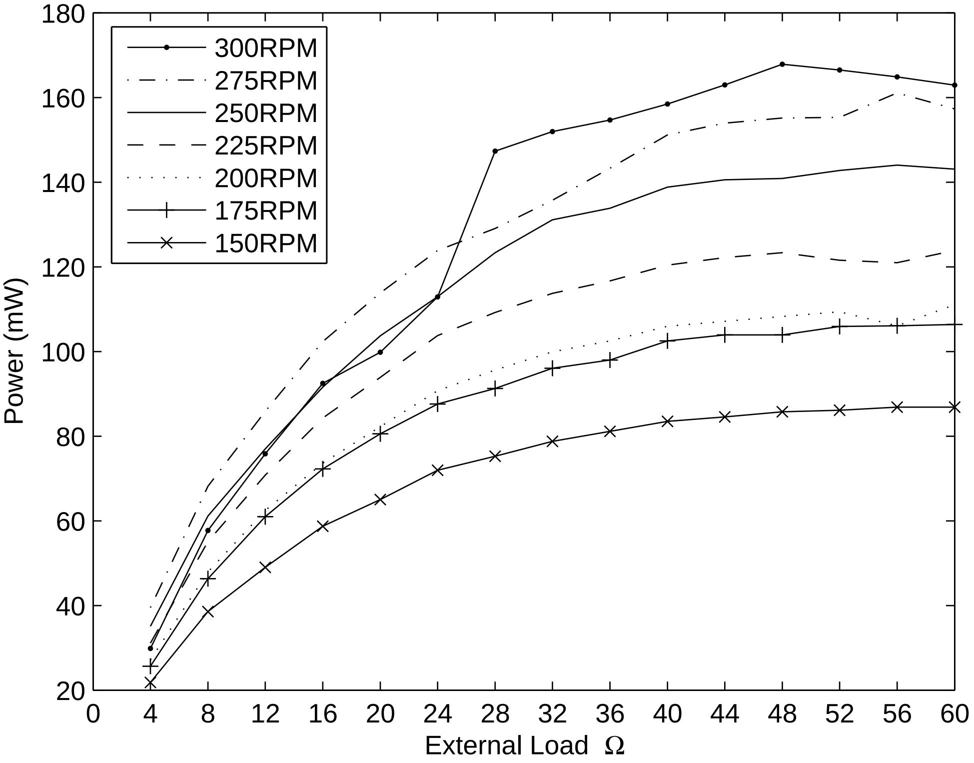

Figure 5-4: Steady state average power dissipated in the variable resistive load plotted versus load resistance for various rotation rates.

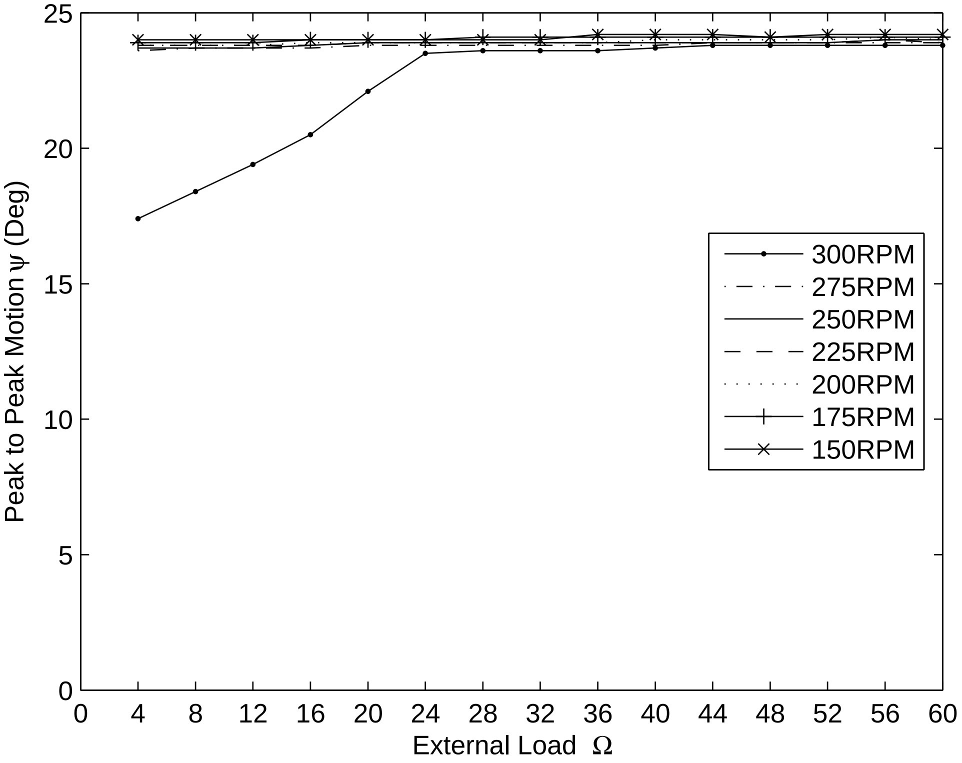

Figure 5-5: Steady state peak to peak swing magnitude plotted versus load resistance for various rotation rates.

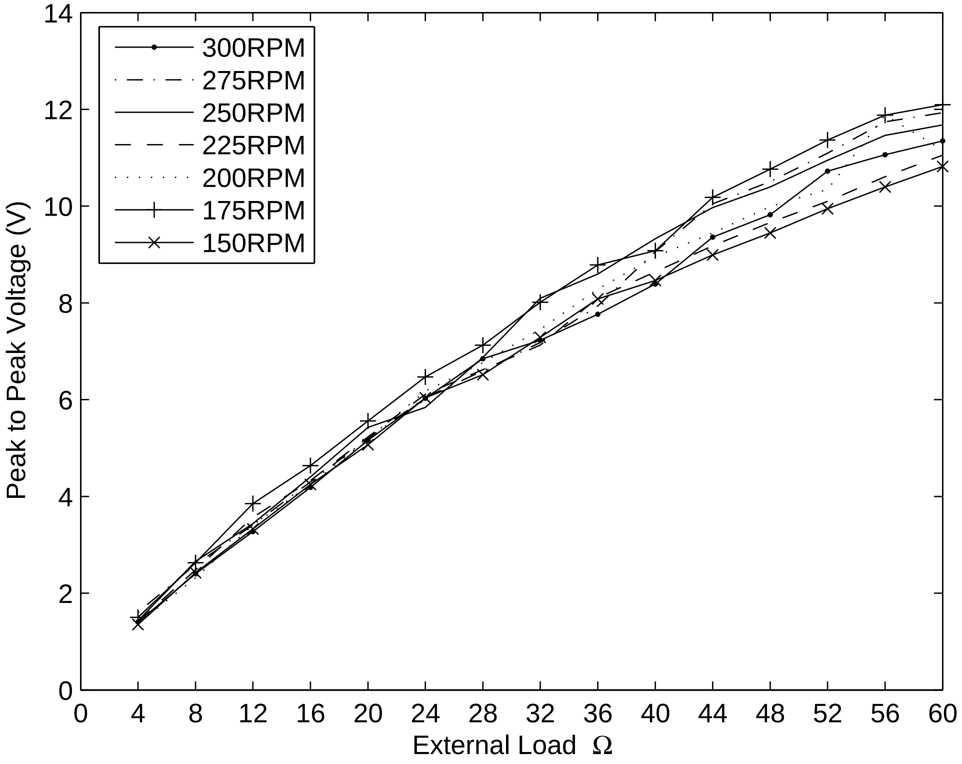

Figure 5-6: Steady state peak to peak load voltage plotted versus load resistance for various rotation rates.

pected that the voltage output from the coil with a fixed load would increase linearly with frequency. The experimental data shown in Figure 5-6 directly contradict this expectation. The data show a dependence on the load resistance, but almost no dependence on the rotation rate. In order for this behavior to occur, it must be the case that the pendulous magnet assembly is reaching nearly the same maximum velocity regardless of the rotation rate. This phenomenon is caused by the nonlinearities in the linkage and the collisions with the mechanical stops at the end of the allowed travel, and is best illustrated by sample plots of the time domain data.

Figure 5-7 shows the displacement of the pendulum ψ plotted versus time for two different operating speeds with the same 48 Ω resistive load. The upper plot shows the device in operation at 150 RPM and the lower at 300 RPM. In the time domain, it can be seen that the motion at high frequency is approximately sinusoidal, but that the motion at low frequencies is clearly nonsinusoidal. At low frequency, the system begins to behave much more like a falling mass, with collisions at the limits of travel and delays between periods of motion. The interesting thing to notice is that the deviation from sinusoidal motion at low frequencies actually improves the power output of the device. At a constant damping, the total work done over a fixed distance is proportional to the velocity at which the distance is traversed. The average power can be expressed as the product of the work done over the distance and the number of time the distance is traversed per second. From this perspective, it becomes clear that the high velocity motions between delays that appear in the low frequency data, actually cause more energy to be transduced by the electromagnetic damping than would purely sinusoidal motion.

The cosine of the arm angle ϕ is overlaid on the time domain swing angle plots in Figure 5-7 for use as a phase reference between the motion of the device and the excitation force provided by gravity. At high frequency, the figure shows that the proper resonant phase relation exists, and the excitation of gravity is therefore doing nearly the optimal amount of work of the device in each revolution. The low frequency plot shows a surprisingly similar phase relationship despite the large deviation from sinusoidal motion. This similar resonant phase relationship across a wide range of frequencies further demonstrates the effectiveness of the frequency tracking properties of the device dynamics.

The peak to peak voltage shown in Figure 5-6 showed little variation with changes in frequency, and the time domain swing angle data gave some explanation of how this occurred. Figure 5-8 shows the time domain voltage measured across the load, which is proportional to the angular velocity $\dot{\psi}$, for sample data sets at 150 RPM and 300 RPM. In addition to the similar peak to peak voltages, it can be seen that the width of the peaks are also comparable. The time domain sample data of the power transmitted to the load is presented in Figure 5-9, and shows that changes in operating frequency tend to change the spacing between the individual spikes in power more than the magnitude or width of the spikes themselves. This leads to the rather linear trend in output power as a function of frequency that was observed in Figure 5-3.

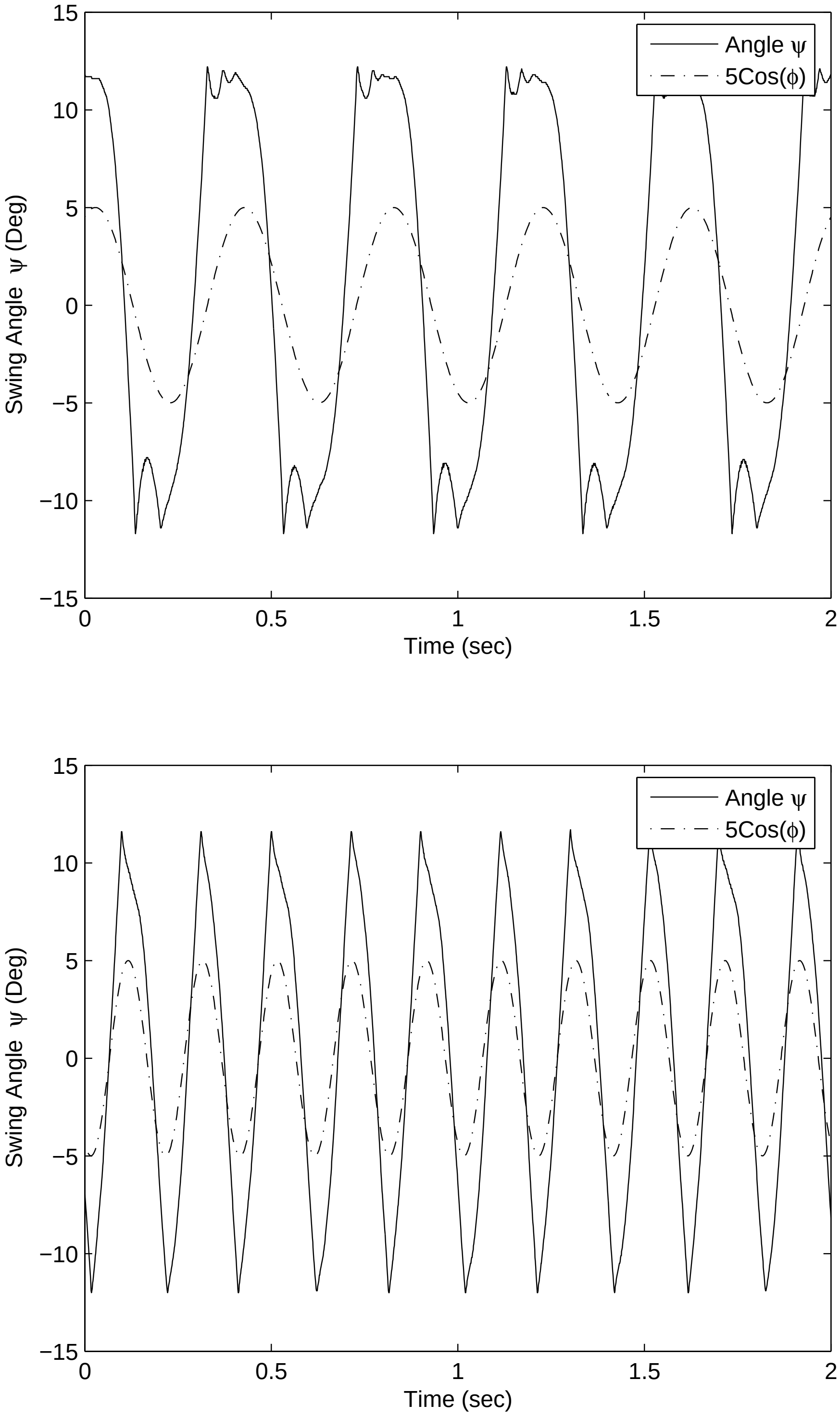

Figure 5-7: Sample plots of the time domain swing angle measurements taken at 150 RPM (top) and 300 RPM (bottom) during operation with a 48 Ω resistive load. The cosine of the arm angle ϕ is overlaid as a phase reference.

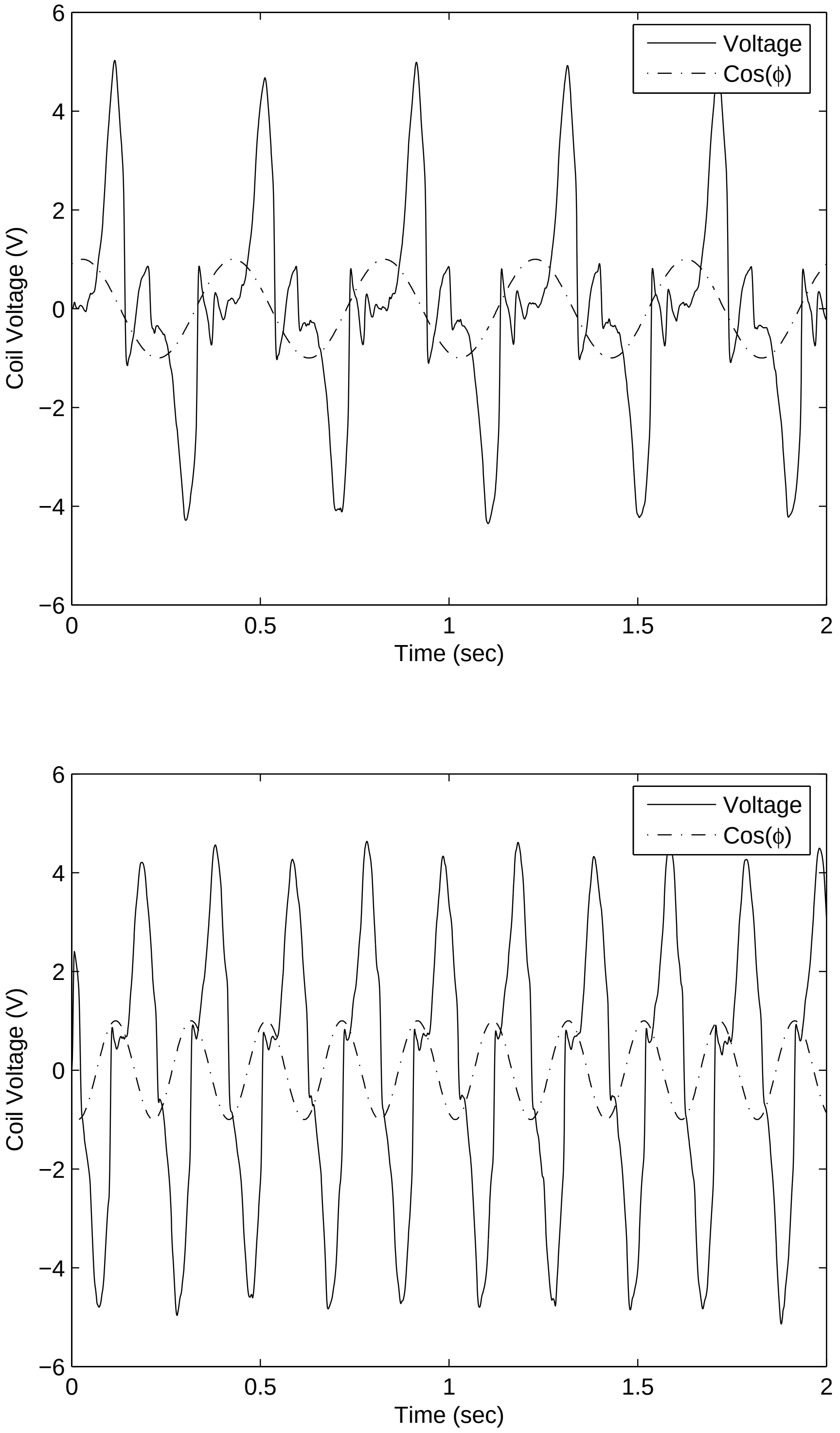

Figure 5-8: Sample plots of the time domain coil voltage measurements taken at 150 RPM (top) and 300 RPM (bottom) during operation with a 48 Ω resistive load. The cosine of the arm angle ϕ is overlaid as a phase reference.

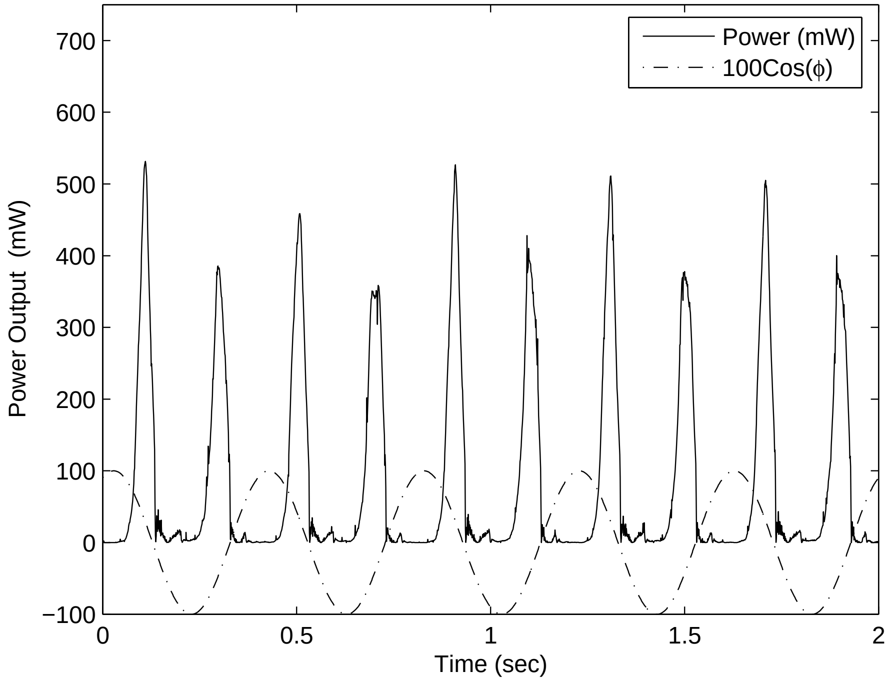

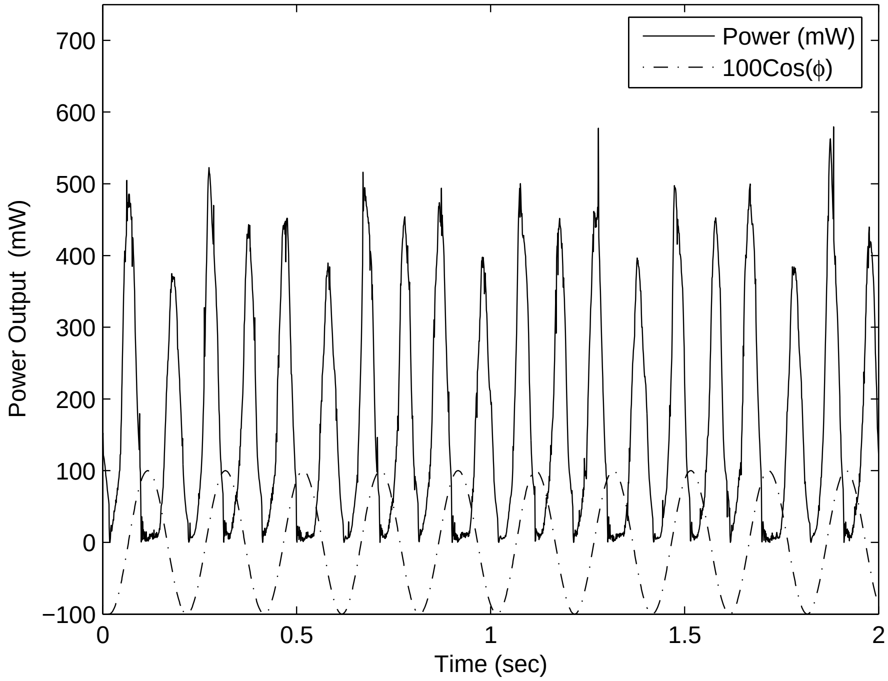

Figure 5-9: Sample plots of the time domain power output measurements taken at 150 RPM (top) and 300 RPM (bottom) during operation with a 48 Ω resistive load. The cosine of the arm angle ϕ is overlaid as a phase reference.

5.2.2 Battery Charging Demonstration with Switching Load

Testing with the high speed switching load, that approximates the loading experienced during battery charging, successfully demonstrated the ability of the device to charge batteries. The power transmitted to the mock battery as a function of rotation rate for each duty cycle is shown in Figure 5-10. One key success is that the device was able to charge the 2.4 V mock battery at some rate at all frequencies tested despite a relatively low maximum coil voltage. The ability to continue to charge the mock battery at low rotation rates is a result of the relatively constant voltage pulsed power characteristics that were observed at low frequencies with the resistive load. The power transmitted to the mock battery is also nearly linearly increasing with increasing frequency. The peak power transmitted to the mock battery is somewhat lower than the power dissipated in the resistive load, due to the multiple diode drops associated with the rectifier and the switching circuitry. Choosing a smaller diameter wire to increase the number of turns in the coil would boost the coil voltage and reduce the losses that occur in the diodes.

In the experimental results, it was seen that the highest performance was achieved at a duty cycle of 100%, and the switching portion of the circuitry was therefore unnecessary. For the tested battery voltage of 2.4 V and the tested coil a simple direct connection between the rectifier and battery would be sufficient; however, if a high voltage coil were used to reduce the diode losses, a switching circuit would be expected to be beneficial.

Figure 5-11 and Figure 5-12 show the voltage across the mock battery and the charging current, respectively. The trend of these two plots verifies that the mock battery has similar characteristics to a real battery. The voltage across the mock battery changes relatively little with changes in current, and approaches a nominal 2.4 V as the charging current is reduced to zero. The charging current shown is within the acceptable range to charge a AA two cell NiCad battery pack in a reasonable amount of time.

The device did not show any significant changes in its dynamics due to the addi-

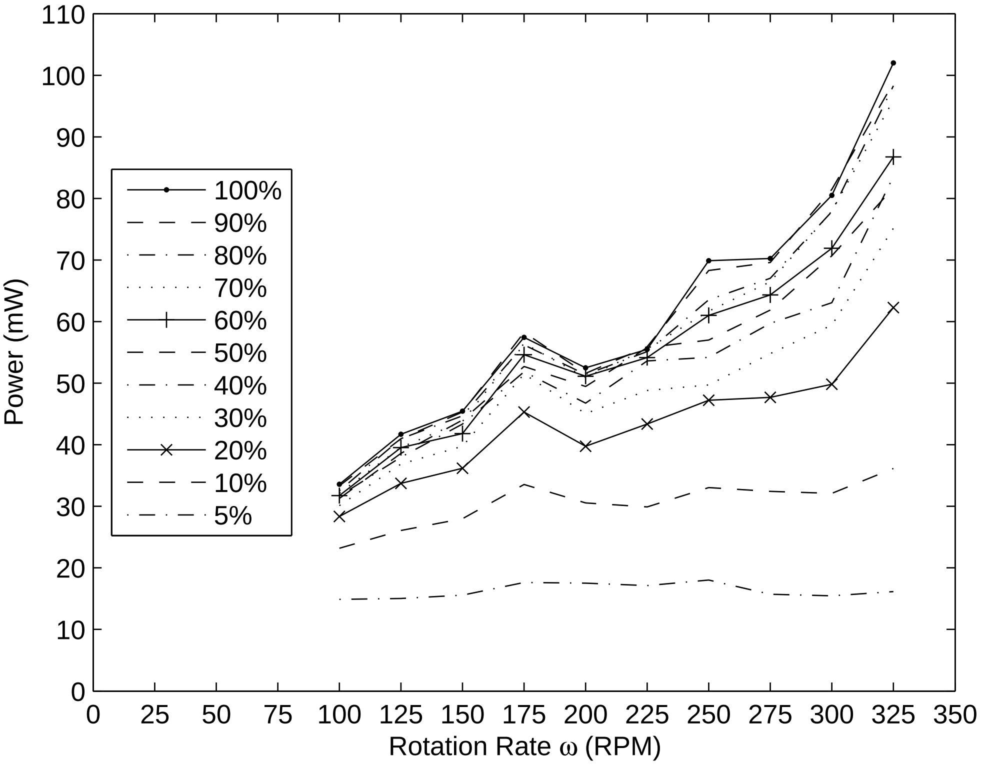

Figure 5-10: Power transmitted to the mock battery portion of the switching load circuit plotted versus frequency for various duty cycles.

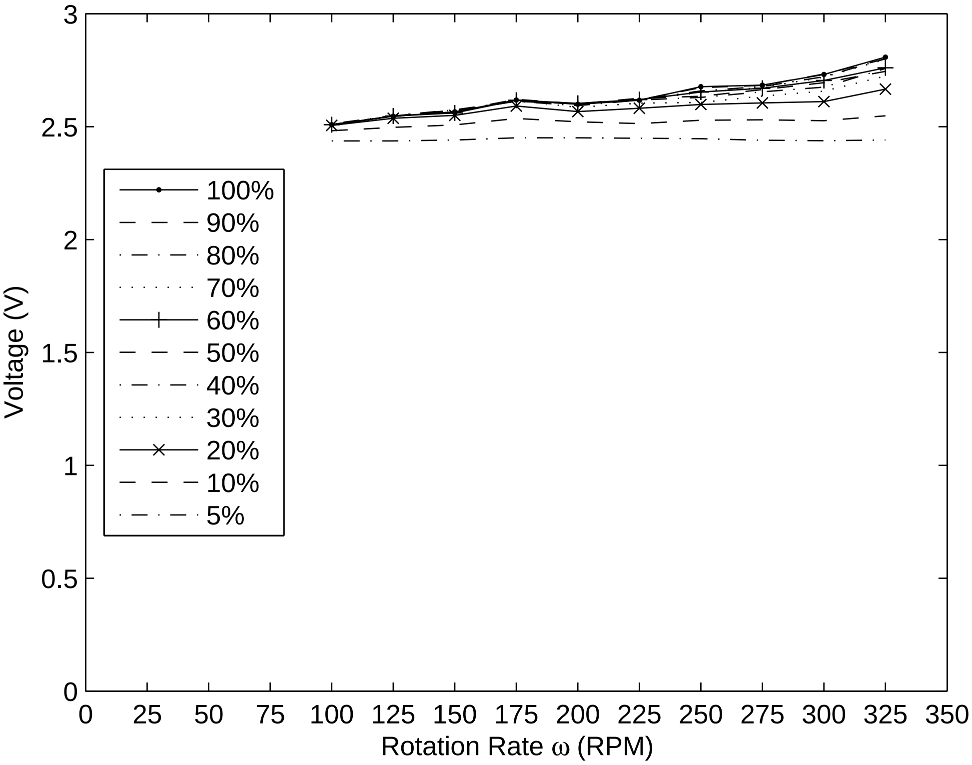

Figure 5-11: Voltage across the mock battery portion of the switching load circuit plotted versus frequency for various duty cycles.

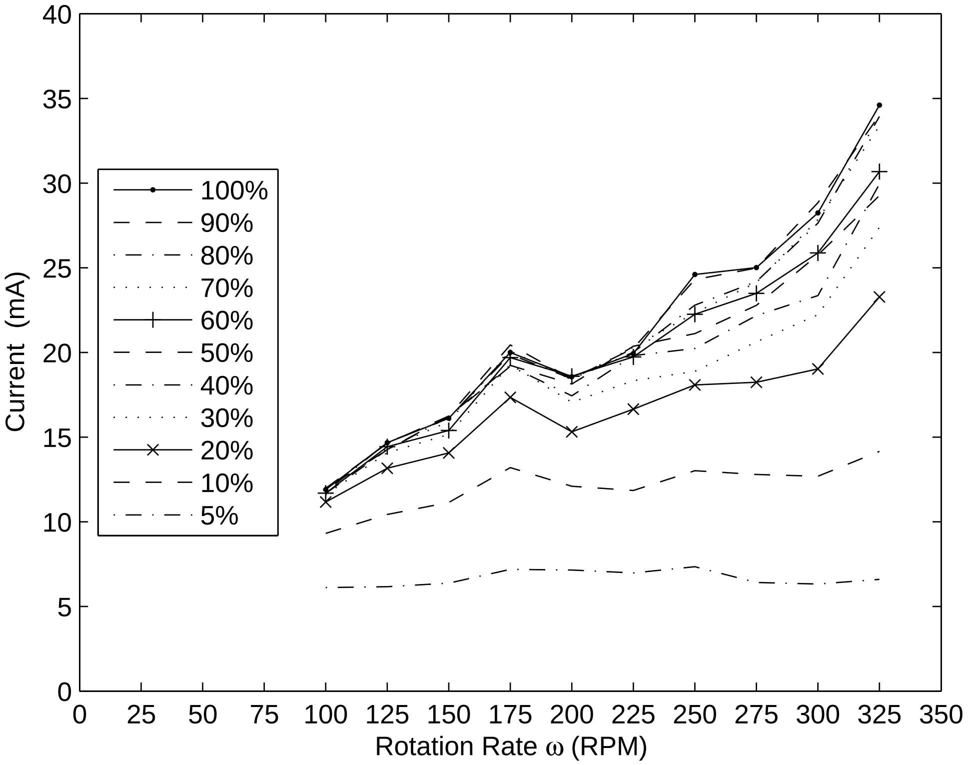

Figure 5-12: Charging current passed throughout the mock battery portion of the switching load circuit plotted versus frequency for various duty cycles.

tional nonlinearities introduced by the use of the rectifier and storage capacitor. The time domain swing angle measurements taken while the switching load was employed, shown in Figure 5-13, show no significant difference from those shown in Figure 5-7, which were taken during testing with the purely resistive load.

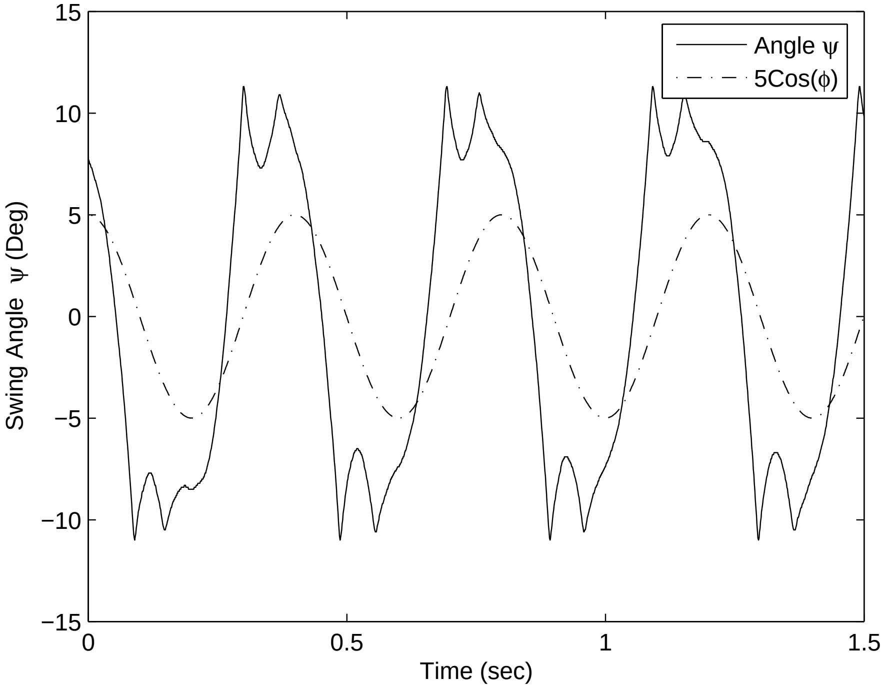

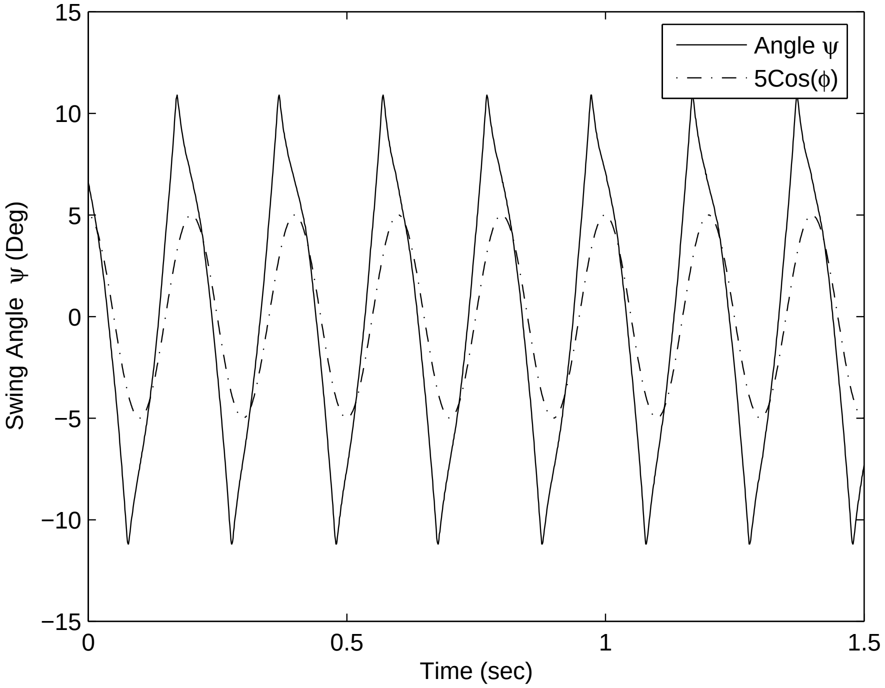

Figure 5-13: Sample plots of the time domain swing angle measurements taken at 150 RPM (top) and 300 RPM (bottom) while the system was loaded by the mock battery charging circuit at 100% duty cycle. The cosine of the arm angle ϕ is overlaid as a phase reference.

Chapter 6

Conclusion

An inertial generator for embedded operation within the propeller of a large ship has been designed and successfully tested under the expected operating conditions. The inertial generator was designed specifically for the inertial excitation experienced during rotation in the vertical plane at a radius that is large relative to the size of the device. The design relies solely on the known inertial trajectory and the presence of gravity to generate electrical energy. Within the reference frame attached to the device, gravitational forces can be viewed as the nonconservative excitation. However, in the inertial frame it is seen that the source of the energy produced by the device is the work done on the propeller by the drive shaft of the ship, which provides the reaction forces necessary to drive the device through its circular motion. The designed system has the ability to reliably provide electrical energy to an embedded system with only a single physical external connection.

The results of the laboratory testing have verified the expected dynamics of the device by demonstrating that it can achieve large resonant deflections at a wide range of operating speeds. The experimental power output of the device shows the expected monotonically increasing power output with increasing rotation rate, which has clear advantages over the narrow useful operating range associated with traditional sprung mass vibrational inertial generators. The nonlinear characteristics of the device have been investigated, revealing that the device produces peak voltages at low rotation rates that are comparable to the voltages produced at much higher rates. The relatively constant peak voltage output eliminates the dropout that other designs exhibit at low frequencies, when the voltage output falls below the level necessary to charge the storage element. Laboratory testing has also demonstrated the ability of the device to charge a battery, with acceptable charging currents delivered across the entire range of tested frequencies.

The tested prototype has proven its ability to perform at the target radius of one meter and across the desired range of frequencies. The power output of the device is limited by the coil assembly, and will increase linearly as the device is scaled in thickness. As the ratio of the length scale of the device to its radius is raised, the device becomes more stable, and less mass is required in the slider to tune the device. As the ratio is lowered by reducing the length scale of the device or mounting it at a larger radius, the device becomes more sensitive to alignment errors and requires larger slider masses to tune the system.

6.1 Opportunities for Future Research

Many opportunities exist for further improvement of the currently prototyped device. In Section 2.3.2, it was shown that increases in the ratio of the square of the electromagnetic coupling coefficient to the resistance of the coil results in improved efficiency. Improvement opportunities in this area may include modifications to the geometry of the magnet assembly, or the development of new construction techniques that do not require wire EDM machining of the magnets, which may have reduced their strength. The development of magnetic stops, that limit the travel of the device without the mechanical impacts that occur when rubber stops are employed, would reduce both the noise produced by the device and the impulsive loads on the internal mechanical components. Another interesting area for future research would be the design of a self aligning device, allowing the device to operate at larger radii and smaller length scales.

Opportunities for further development exist in optimizing the design for use with a specific load. The research presented in this thesis has focused on characterizing the devices dynamics and presenting its capabilities. Once a specific load is chosen the material presented here may be used as a guide for producing a design that is well matched to the selected load.

The slider augmented pendulum configuration was chosen in this work based on its many attractive characteristics, especially its simplicity, and the lack of elements that would be subject to wear or add mechanical drag to the system. In light of the experimental results that show that the current prototype is limited by its electromagnetic coupling, the configuration consisting of a simple pendulum with a geared flywheel may be a viable alternative. The system includes a wear item in the drive line and is expected to have increased mechanical drag, but this may be offset by the increase in electromagnetic coupling gained by integrating the flywheel with a brushless AC generator. The device would also have the advantage of a larger stable range of motion, and would not experience the problems associated with misalignment angles, while still maintaining perfect frequency tracking. Only careful prototyping and laboratory testing can verify the long term benefits of each design.

Appendix A

Slider Augmented Pendulum Dynamics Derivations

As stated in Section 2.2.2, the equations of motion for the slider augmented pendulum were derived with two assumptions. First, it is assumed that the slider mass m_S is constrained to move along the center line of the device as shown in Figure 2-8 without friction. The second assumption is that the link connecting the slider to the pendulous link has negligible mass and rotational inertia. With these two assumptions, the nonlinear equations of motion for the slider augmented pendulum are derived below using both Newton's Method and Lagrange's Method. The linearization of the equations of motion for the free undamped response of the system is also included below, and the results were utilized in the small angle analysis of the systems natural frequency and stability explored in Equation Chapter 2. Diagrams of the system and a description of variables are presented in Section 2.2.1.

A.1 Newton's Method

The motion of the center of gravity of the main pendulous link 1 has a velocity given by

$$V_{CG} = V_{O/A} + \left(\overrightarrow{\left(\omega + \dot{\psi}\right)} \times \overrightarrow{r}_{CG/O}\right)$$

$$
\begin{aligned}
&= r\omega\hat{\imath} + \left(\omega + \dot{\psi}\right) L\cos\psi\hat{\imath} + \left(\omega + \dot{\psi}\right) L\sin\psi\hat{\jmath} \\
&= \left(r\omega + L\left(\omega + \dot{\psi}\right)\cos\psi\right)\hat{\imath} + \left(L\left(\omega + \dot{\psi}\right)\sin\psi\right)\hat{\jmath} \qquad \text{(A.1)}
\end{aligned}
$$

where $\overrightarrow{r}_{CG/O}$ is the location of the center of gravity of the link with respect to the point O in the device reference frame $\hat{\imath}, \hat{\jmath}$, and $V_{O/A}$ is the velocity of the point O with respect to the point A in the inertial frame $\hat{I}, \hat{J}$. The acceleration is given by

$$
\begin{aligned}
A_{CG} &= a_{O/A} + \left(\alpha \times r_{CG/O}\right) + \overrightarrow{\left(\omega + \dot{\psi}\right)} \times \left(\overrightarrow{\left(\omega + \dot{\psi}\right)} \times \overrightarrow{r}_{CG/O}\right) \\
&= r\omega^2\hat{\jmath} + \ddot{\psi}L\left(\cos\psi\hat{\imath} + \sin\psi\hat{\jmath}\right) + \left(\omega + \dot{\psi}\right)^2 L\left(\cos\psi\hat{\jmath} + \sin\psi\hat{\imath}\right) \\
&= \left[\ddot{\psi}L\cos\psi - \left(\omega + \dot{\psi}\right)^2 L\sin\psi\right]\hat{\imath} \\
&\quad + \left[r\omega^2 + \ddot{\psi}L\sin\psi + \left(\omega + \dot{\psi}\right) L\cos\psi\right]\hat{\jmath} \qquad \text{(A.2)}
\end{aligned}
$$

The component of the acceleration of the center of gravity in the $\hat{\imath}'$ direction is

$$
\begin{aligned}
A_{CG}\hat{\imath}' &= \ddot{\psi}L\cos^2\psi - L\left(\omega + \psi\right)^2\sin\psi\cos\psi + r\omega^2\sin\psi \\
&\quad + \ddot{\psi}L\sin^2\psi + L\left(\omega + \dot{\psi}\right)^2\cos\psi\sin\psi \\
&= \ddot{\psi}L + r\omega^2\sin\psi \qquad \text{(A.3)}
\end{aligned}
$$

Taking a torque balance about point O, and utilizing the result derived in Section 2.1.2.1, we have

$$
\begin{aligned}
\ddot{\psi}I &= \sum T_O \\
&= -mL\left(\ddot{\psi}L + r\omega^2\sin\psi\right) - Lmg\sin\left(\phi + \psi\right) \\
&\quad + F_S L_1\sin\left(\phi - \psi\right) + F_C L_C \qquad \text{(A.4)}
\end{aligned}
$$

The radius of the slider mass is given by

$$
r_S = -\left(r + x\right)\hat{\jmath}
$$

and its velocity and acceleration are

$$v_S = \omega\left(r + x\right)\hat{\imath} + \dot{x}\hat{\jmath}$$

and

$$a_S = \left(2\omega\dot{x}\right)\hat{\imath} + \Big(-\ddot{x} + \omega^2\left(r + x\right)\Big)\hat{\jmath} \tag{A.5}$$

The force balance on the slider in the $\hat{\jmath}$ direction can be written as

$$\sum F\hat{\jmath} = m_s a_s \hat{\jmath} \tag{A.6}$$

or

$$F_S\cos\theta - m_S g\cos\theta = m_S\Big(-\ddot{x} + \omega^2\left(r + x\right)\Big) \tag{A.7}$$

The slider position x is dictated by the swing angle ψ, allowing the slider position to be written as

$$x = L_1\cos\psi - \sqrt{L_2^2 - \left(L_1\sin\psi\right)^2} \tag{A.8}$$

and the velocity as

$$\dot{x} = -L_1\dot{\psi}\sin\psi + \frac{L_1\sin\psi L_1\cos\psi\dot{\psi}}{\sqrt{L_2^2 - \left(L_1\sin\psi\right)^2}} = L_1\dot{\psi}\sin\psi\left(\frac{L_1\cos\psi}{\sqrt{L_2^2 - \left(L_1\sin\psi\right)^2}} - 1\right) \tag{A.9}$$

Defining the quantities

$$Z \equiv \sqrt{L_2^2 - \left(L_1\sin\psi\right)^2} \tag{A.10}$$

and

$$Y \equiv L_1\sin\psi\left(\frac{L_1\cos\psi}{Z} - 1\right) \tag{A.11}$$

allows Equation (A.8) and Equation (A.9) to be written in the more compact form

$$x = L_1\cos\psi - Z \tag{A.12}$$

and

$$\dot{x} = \dot{\psi}Y \tag{A.13}$$

Differentiation of the expression for the velocity in Equation (A.13) yields the acceleration of the slider as

$$\ddot{x} = \ddot{\psi}Y + \dot{\psi}^2 \left[L_1 \cos\psi \left(\frac{L_1 \cos\psi}{Z} - 1\right) + \frac{L_1^2 \sin^2\psi}{Z}\left(\frac{L_1^2 \cos^2\psi}{Z^2} - 1\right)\right] \tag{A.14}$$

Again, defining a quantity

$$A \equiv \left[L_1 \cos\psi \left(\frac{L_1 \cos\psi}{Z} - 1\right) + \frac{L_1^2 \sin^2\psi}{Z}\left(\frac{L_1^2 \cos^2\psi}{Z^2} - 1\right)\right] \tag{A.15}$$

allows the more compact representation of Equation (A.14) as

$$\ddot{x} = \ddot{\psi}Y + \dot{\psi}^2 A \tag{A.16}$$

Now substituting Equation (A.12), Equation (A.13), and Equation (A.16) into Equation (A.7) gives the relation

$$F_S \cos\theta = m_S g \cos\phi - m_S\left(\ddot{\psi}Y + \dot{\psi}^2 A\right) + m_S \omega^2 \left(r + L_1 \cos\psi - Z\right) \tag{A.17}$$

From the geometry of the linkage, it can be shown that

$$\cos\theta = \frac{\sqrt{L_2^2 - \left(L_1 \sin\psi\right)^2}}{L_2} = \frac{Z}{L_2} \tag{A.18}$$

and

$$\sin\theta = \frac{L_1 \sin\psi}{L_2} \tag{A.19}$$

Using these relations, equation Equation (A.17) and the last term in Equation (A.4) can be written in terms of ψ alone as

$$F_S \frac{Z}{L_2} = m_S\left(g\cos\phi - \ddot{\psi}Y - \dot{\psi}^2 A + \omega^2\left(r + L_1 \cos\psi - Z\right)\right) \tag{A.20}$$

and

$$\begin{aligned} F_S L_1 \sin(\theta - \psi) &= F_S L_1 (\sin\theta\cos\psi - \cos\theta\sin\psi) \\ &= F_S L_1 \left(\frac{L_1}{L_2}\sin\psi\cos\psi - \frac{Z}{L_2}\sin\psi \right) \\ &= F_S L_1 \frac{Z}{L_2} \left(\frac{L_1}{Z}\sin\psi\cos\psi - \sin\psi \right) \\ &= F_S \frac{Z}{L_2} \left(L_1 \sin\psi \left(\frac{L_1\cos\psi}{Z} - 1 \right) \right) \\ &= F_S \frac{Z}{L_2} Y \end{aligned} \tag{A.21}$$

It is now convenient to combine Equation (A.4), Equation (A.21), and Equation (A.20) to generate the full equation of motion for the system as

$$\begin{aligned} \ddot{\psi} I &= -mL\left(\ddot{\psi}L + r\omega^2 \sin\psi\right) - Lmg\sin(\phi + \psi) + F_C L_C \\ &\quad + Y m_S \left(g\cos\phi - \ddot{\psi}Y - \dot{\psi}^2 A + \omega^2 (r + L_1\cos\psi - Z)\right) \end{aligned}$$

which simplifies to

$$\begin{aligned} \ddot{\psi} &= \frac{-mL\left(r\omega^2\sin\psi + g\sin(\phi+\psi)\right) + m_S Y \omega^2 (r + L_1\cos\psi - Z)}{I_O + m_S Y^2} \\ &\quad + \frac{m_S Y\left(-\dot{\psi}^2 A + g\cos\phi\right) + L_C F_C}{I_O + m_S Y^2} \end{aligned} \tag{A.22}$$

where I_O is the rotational inertia of link L_1 about point O.

A.2 Lagrange's Method

The position and velocity of the center of mass of the pendulous link L_1 is given by

$$R_{CG} = [r\sin\phi + L\sin(\phi+\psi)]\,\hat{I} + [-r\cos\phi - L\cos(\phi+\psi)]\,\hat{J} \tag{A.23}$$

and

$$V_{CG} = \left[r\omega\cos\phi + L\left(\omega+\dot{\psi}\right)\cos\left(\phi+\psi\right)\right]\hat{I} + \left[r\omega\sin\phi + L\left(\omega+\dot{\psi}\right)\sin\left(\phi+\psi\right)\right]\hat{J} \tag{A.24}$$

The square of the velocity of the center of gravity of the link can be written as

$$\begin{aligned} V_{CG}^2 &= r^2\omega^2\cos^2\phi + 2rL\omega\left(\omega+\dot{\psi}\right)\cos\phi\cos\left(\phi+\psi\right) + L^2\left(\omega+\dot{\psi}\right)^2\cos^2\left(\phi+\psi\right) \\ &\quad + r^2\omega^2\sin^2\phi + 2rL\omega\left(\omega+\dot{\psi}\right)\sin\phi\sin\left(\phi+\psi\right) + L^2\left(\omega+\dot{\psi}\right)^2\sin^2\left(\phi+\psi\right) \\ &= r^2\omega^2 + L^2\left(\omega+\dot{\psi}\right)^2 + 2rL\omega\left(\omega+\dot{\psi}\right)\left(\cos\phi\cos\left(\phi+\psi\right)+\sin\phi\sin\left(\phi+\psi\right)\right) \\ &= r^2\omega^2 + L^2\left(\omega+\dot{\psi}\right)^2 + 2rL\omega\left(\omega+\dot{\psi}\right)\cos\psi \end{aligned} \tag{A.25}$$

It is convenient to define the quantities Z, Y, and A as was done in the Newtonian approach, where

$$Z \equiv \sqrt{L_2^2 - \left(L_1\sin\psi\right)^2} \tag{A.26}$$

$$Y \equiv L_1\sin\psi\left(\frac{L_1\cos\psi}{Z} - 1\right) \tag{A.27}$$

and

$$A \equiv \left[L_1\cos\psi\left(\frac{L_1\cos\psi}{Z} - 1\right) + \frac{L_1^2\sin^2\psi}{Z}\left(\frac{L_1^2\cos^2\psi}{Z^2} - 1\right)\right] \tag{A.28}$$

The motion of the slider can be defined in terms of these quantities as was done in Equation (A.12), Equation (A.13), and Equation (A.16) where

$$x = L_1\cos\psi - Z \tag{A.29}$$

$$\dot{x} = \dot{\psi}Y \tag{A.30}$$

and

$$\ddot{x} = \ddot{\psi}Y + \dot{\psi}^2 A \tag{A.31}$$

Several partial derivatives of the slider motion will be necessary in the formulation of Lagrange's equation, and are found as follows:

$$\frac{\partial x}{\partial \psi} = -L_1 \sin\psi + \frac{L_1^2 \sin\psi \cos\psi}{\sqrt{L_2^2 - \left(L_1 \sin\psi\right)^2}} = L_1 \sin\psi \left(\frac{L_1 \cos\psi}{Z} - 1\right) = Y \tag{A.32}$$

$$\frac{\partial \dot{x}}{\partial \dot{\psi}} = Y \tag{A.33}$$

and

$$\frac{dY}{dt} = \frac{d}{dt}\left(\frac{\partial \dot{x}}{\partial \dot{\psi}}\right) = \frac{\partial}{\partial \dot{\psi}}\left(\frac{d\dot{x}}{dt}\right) = \frac{\partial \ddot{x}}{\partial \dot{\psi}} = \frac{\partial}{\partial \dot{\psi}}\left(\ddot{\psi} Y + \dot{\psi}^2 A\right) = \dot{\psi} A \tag{A.34}$$

The dynamics of the system can be found from Lagrange's equation, which is given by

$$\frac{d}{dt}\left(\frac{\partial T}{\partial \dot{\psi}}\right) - \frac{\partial T}{\partial \psi} + \frac{\partial V}{\partial \psi} = L_C F_C \tag{A.35}$$

where F_C is the non-conservative force exerted by the coil on the magnet assembly and L_C is the distance at which the force is applied. The kinetic energy in the system is

$$\begin{aligned} T &= \frac{1}{2} I \left(\omega + \dot{\psi}\right)^2 + \frac{1}{2} m V_{CG}^2 + \frac{1}{2} m_S V_{m_S}^2 \\ &= \frac{1}{2} I \left(\omega + \dot{\psi}\right)^2 + \frac{1}{2} m \left(r^2 \omega^2 + L^2 \left(\omega + \dot{\psi}\right)^2 + 2 r L \omega \left(\omega + \dot{\psi}\right) \cos\psi\right) \\ &\quad + \frac{1}{2} m_S \left(\omega^2 \left(r + x\right)^2 + \dot{x}^2\right) \end{aligned} \tag{A.36}$$

The potential energy is given by

$$V = mg\left(-r\cos\phi - L\cos\left(\phi + \psi\right)\right) - m_S g \cos\phi \left(r + x\right) \tag{A.37}$$

Taking the appropriate partial derivatives of the kinetic and potential energies:

$$\frac{\partial V}{\partial \psi} = mgL \sin\left(\phi + \psi\right) - m_S g \cos\phi \frac{\partial x}{\partial \psi} = mgL \sin\left(\phi + \psi\right) - m_S g \cos\phi Y \tag{A.38}$$

$$
\begin{aligned}
\frac{d}{dt}\left(\frac{\partial T}{\partial \dot{\psi}}\right) &= \frac{d}{dt}\left(I\left(\omega+\dot{\psi}\right)+mL^2\left(\omega+\dot{\psi}\right)+mrL\omega\cos\psi+m_S\dot{x}\frac{\partial \dot{x}}{\partial \dot{\psi}}\right) \\
&= I\ddot{\psi}+mL^2\ddot{\psi}-mrL\omega\sin\psi\dot{\psi}+m_S\ddot{x}Y+m_S\dot{x}\frac{dY}{dt} \\
&= \left(I+mL^2\right)\ddot{\psi}-mrL\omega\dot{\psi}\sin\psi+m_SY\left(\ddot{\psi}Y+\dot{\psi}^2A\right)+m_S\dot{\psi}Y\dot{\psi}A \\
&= \ddot{\psi}\left(I_O+m_SY^2\right)-mrL\omega\dot{\psi}\sin\psi+2m_S\dot{\psi}^2AY
\end{aligned}
\tag{A.39}
$$

and

$$
\begin{aligned}
\frac{\partial T}{\partial \psi} &= -mrL\omega\left(\omega+\dot{\psi}\right)\sin\psi+m_S\dot{x}\frac{\partial \dot{x}}{\partial \psi}+m_S\omega^2\left(r+x\right)\frac{\partial x}{\partial \psi} \\
&= -mrL\omega^2\sin\psi-mrL\omega\dot{\psi}\sin\psi+m_S\dot{\psi}^2AY \\
&\quad +m_S\omega^2Y\left(r+L_1\cos\psi-Z\right)
\end{aligned}
\tag{A.40}
$$

Now assembling the partial derivatives into Equation (A.35), yields

$$
\begin{aligned}
L_CF_C &= \left(\ddot{\psi}\left(I_O+m_SY^2\right)-mrL\omega\dot{\psi}\sin\psi+2m_S\dot{\psi}^2AY\right) \\
&\quad +\left(mgL\sin\left(\phi+\psi\right)-m_Sg\cos\phi Y\right) \\
&\quad +mrL\omega^2\sin\psi+mrL\omega\dot{\psi}\sin\psi-m_S\dot{\psi}^2AY \\
&\quad -m_S\omega^2Y\left(r+L_1\cos\psi-Z\right)
\end{aligned}
\tag{A.41}
$$

Rearranging terms and simplifying yields

$$
\begin{aligned}
\ddot{\psi}\left(I_O+m_SY^2\right) &= -m_S\dot{\psi}^2AY-mgL\sin\left(\phi+\psi\right)+m_Sg\cos\phi Y \\
&\quad +\left(-mrL\omega^2\sin\psi+m_S\omega^2Y\left(r+L_1\cos\psi-Z\right)\right) \\
&\quad +L_CF_C
\end{aligned}
\tag{A.42}
$$

and finally

$$
\begin{aligned}
\ddot{\psi} &= \frac{-mL\left(r\omega^2\sin\psi+g\sin\left(\phi+\psi\right)\right)+m_SY\omega^2\left(r+L_1\cos\psi-Z\right)}{I_O+m_SY^2} \\
&\quad +\frac{m_SY\left(-\dot{\psi}^2A+g\cos\phi\right)+L_CF_C}{I_O+m_SY^2}
\end{aligned}
\tag{A.43}
$$

A.3 Linearization about $\psi = 0$, $\dot{\psi} = 0$

The linearized equations of motion of the systems free undamped response were used in Chapter 2 to investigate the natural frequency and stability of the system for small angles of deflection. The formal linearization of the equations of motion for that purpose are shown in detail in this section. The free undamped response of the system is obtained by setting $g = 0$ and $F_C = 0$ in Equation (A.22), and the nonlinear free undamped equation of motion is obtained as

$$\ddot{\psi} = \frac{-mLr\omega^2 \sin\psi + m_S Y \omega^2 \left(r + L_1 \cos\psi - Z\right) - m_S Y \dot{\psi}^2 A}{I_O + m_S Y^2} \tag{A.44}$$

Linearizing the equation about the centered position C where $\psi = 0$ and $\dot{\psi} = 0$ is performed with the approximation

$$\ddot{\psi} \approx \ddot{\psi}\Big|_C + \frac{\partial \ddot{\psi}}{\partial \dot{\psi}}\bigg|_C \dot{\psi} + \frac{\partial \ddot{\psi}}{\partial \psi}\bigg|_C \psi \tag{A.45}$$

Noting that

$$Y|_C = 0 \tag{A.46}$$

it follows that the first term is

$$\ddot{\psi}\Big|_C = 0 \tag{A.47}$$

The partial derivative in the second term can be written as

$$\frac{\partial \ddot{\psi}}{\partial \dot{\psi}} = \frac{-2m_S Y \dot{\psi} A}{I_O + m_S Y^2} \tag{A.48}$$

and evaluation at the centered position yields

$$\frac{\partial \ddot{\psi}}{\partial \dot{\psi}}\bigg|_C = 0 \tag{A.49}$$

The remaining partial derivative is given by

$$
\begin{aligned}
\frac{\partial \ddot{\psi}}{\partial \psi} &= \left(-mLr\omega^2 \sin\psi + m_S Y \omega^2 \left(r + L_1 \cos\psi - Z\right) - m_S Y \dot{\psi}^2 A\right) \frac{\partial \left(\frac{1}{I_O + m_S Y^2}\right)}{\partial \psi} \\
&\quad + \frac{1}{I_O + m_S Y^2} \left[\frac{\partial \left(-mLr\omega^2 \sin\psi\right)}{\partial \psi} + \frac{\partial Y}{\partial \psi} \left(m_S \omega^2 \left(r + L_1 \cos\psi - Z\right)\right)\right] \\
&\quad + \frac{1}{I_O + m_S Y^2} \left[\left(m_S Y \omega^2\right) \frac{\partial \left(r + L_1 \cos\psi - Z\right)}{\partial \psi} - \dot{\psi}^2 \frac{\partial Y A}{\partial \psi} \right]
\end{aligned}
\tag{A.50}
$$

and evaluation at C results in

$$
\begin{aligned}
\left.\frac{\partial \ddot{\psi}}{\partial \psi}\right|_C &= (0) \frac{\partial \left(\frac{1}{I_O + m_S Y^2}\right)}{\partial \psi} + \frac{1}{I_O + 0} \left[\left.\frac{\partial \left(-mLr\omega^2 \sin\psi\right)}{\partial \psi}\right|_C \right] \\
&\quad + \frac{1}{I_O + 0} \left.\frac{\partial Y}{\partial \psi}\right|_C \left(m_S \omega^2 \left(r + L_1 - \left.Z\right|_C\right)\right) \\
&\quad + \frac{1}{I_O + 0} (0) \frac{\partial \left(r + L_1 \cos\psi - Z\right)}{\partial \psi} \\
&= \frac{1}{I_O} \left[\left.\frac{\partial \left(-mLr\omega^2 \sin\psi\right)}{\partial \psi}\right|_C + \left.\frac{\partial Y}{\partial \psi}\right|_C \left(m_S \omega^2 \left(r + L_1 - \left.Z\right|_C\right)\right)\right]
\end{aligned}
\tag{A.51}
$$

The first partial derivative in Equation (A.51) can be taken and evaluated as

$$
\left.\frac{\partial \left(-mLr\omega^2 \sin\psi\right)}{\partial \psi}\right|_C = \left.\left(-mLr\omega^2 \cos\psi\right)\right|_C = -mLr\omega^2
\tag{A.52}
$$

The remaining partial derivative in Equation (A.51) is

$$
\begin{aligned}
\left.\frac{\partial Y}{\partial \psi}\right|_C &= \left.\left[L_1 \cos\psi \left(\frac{L_1 \cos\psi}{Z} - 1\right) + L_1 \sin\psi \frac{\partial}{\partial \psi} \left(\frac{L_1 \cos\psi}{Z} - 1\right)\right]\right|_C \\
&= L_1 \left(\frac{L_1}{\left.Z\right|_C} - 1\right) + 0 \frac{\partial}{\partial \psi} \left(\frac{L_1}{Z} - 1\right) \\
&= L_1 \left(\frac{L_1}{L_2} - 1\right)
\end{aligned}
\tag{A.53}
$$

Substituting Equation (A.52) and Equation (A.53) into Equation (A.51) gives the expression

$$
\left.\frac{\partial \ddot{\psi}}{\partial \psi}\right|_C = \frac{1}{I_O} \left[-mLr\omega^2 + \left(L_1 \left(\frac{L_1}{L_2} - 1\right)\right) \left(m_S \omega^2 \left(r + L_1 - L_2\right)\right)\right]
$$

$$= \quad \frac{\omega^2 \left[-mLr + m_S L_1 \left(r + L_1 - L_2\right) \left(\frac{L_1}{L_2} - 1\right)\right]}{I_O} \tag{A.54}$$

Substituting Equation (A.47), Equation (A.49), and Equation (A.54) into Equation (A.45) gives the linearized equation of the free undamped motion about the point C, where $\psi = 0$, $\dot{\psi} = 0$, as

$$\ddot{\psi} \approx \frac{\omega^2 \left[-mLr + m_S L_1 \left(r + L_1 - L_2\right) \left(\frac{L_1}{L_2} - 1\right)\right]}{I_O} \psi \tag{A.55}$$

Appendix B

Prototype Drafts

Contained within this appendix are the assembly and part drafts showing the details of the components of the prototype device. All dimensions are in inches. Purchased parts are are listed in Table B.1 and are not presented in individual drafts.

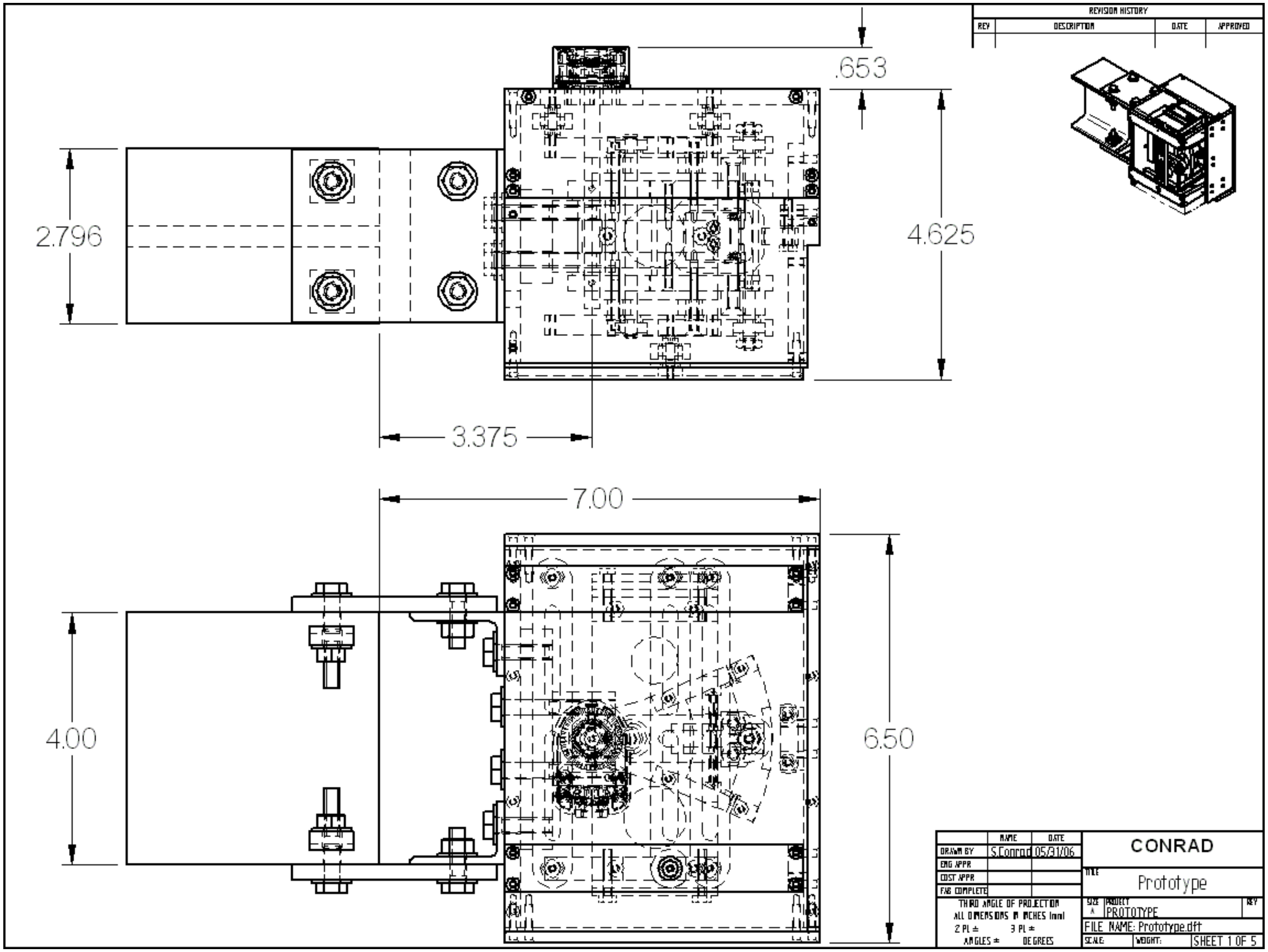

Figure B-1: Prototype Assembly, Sheet 1 of 5

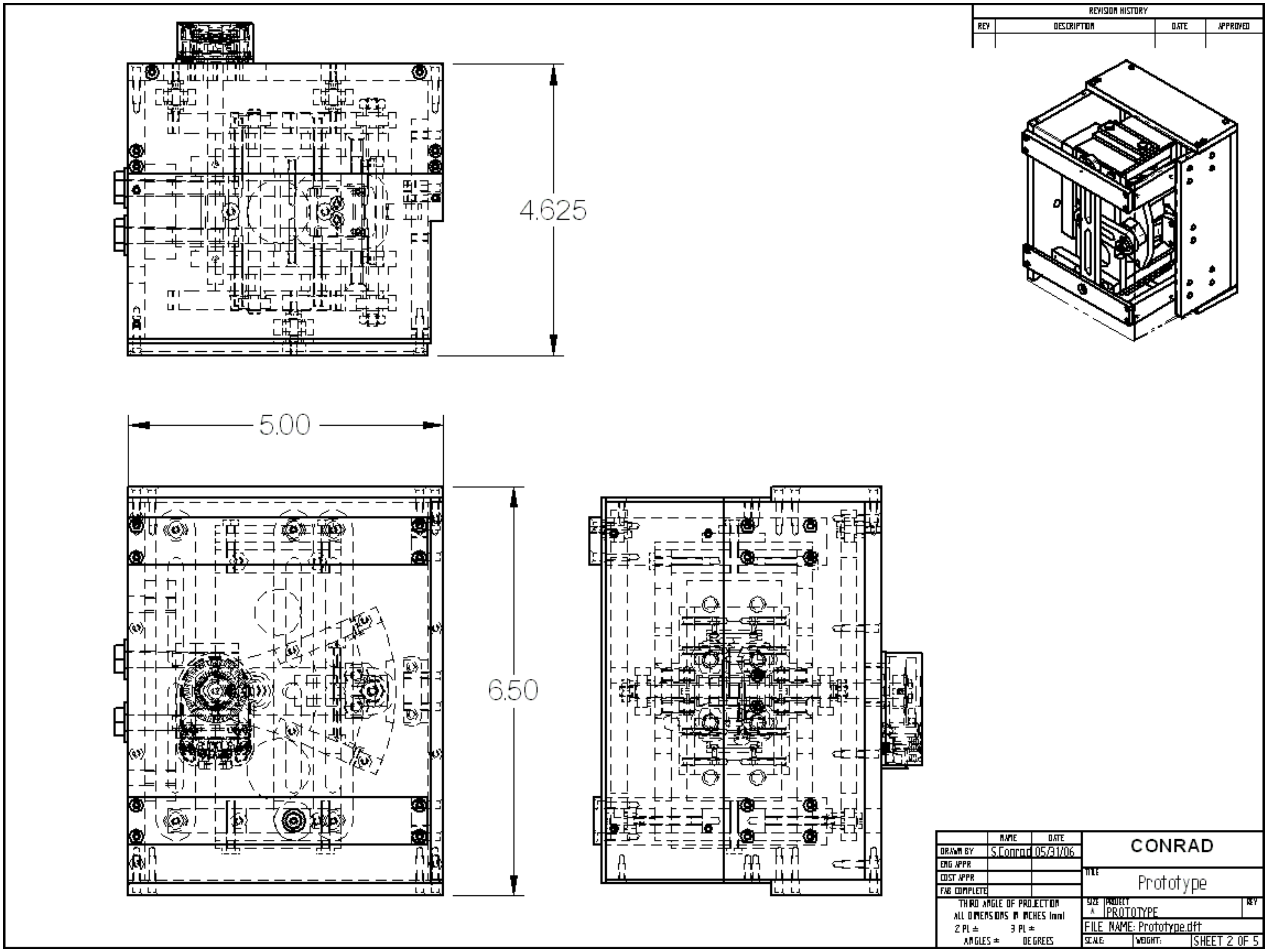

Figure B-2: Prototype Assembly, Sheet 2 of 5

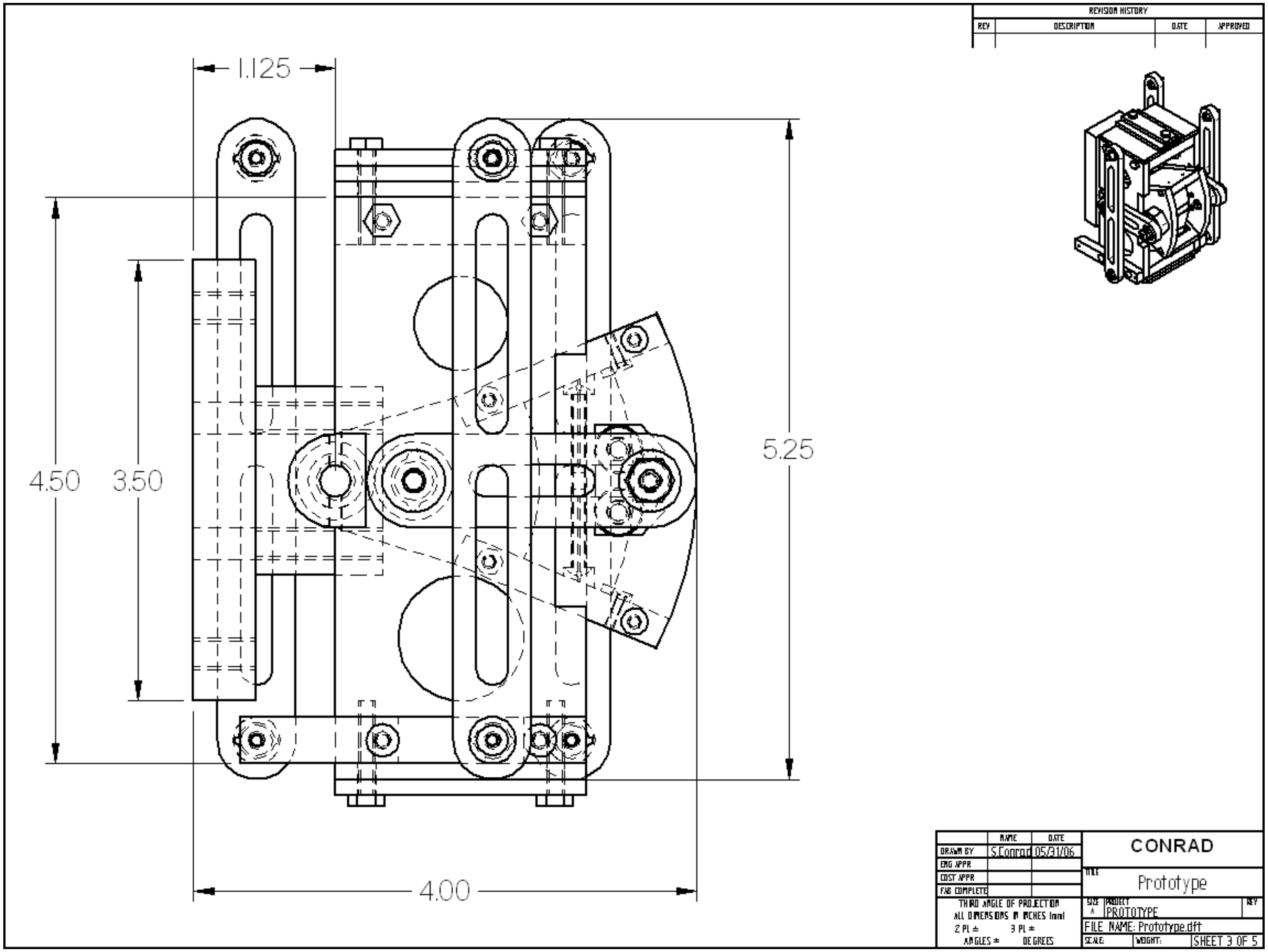

Figure B-3: Prototype Assembly, Sheet 3 of 5

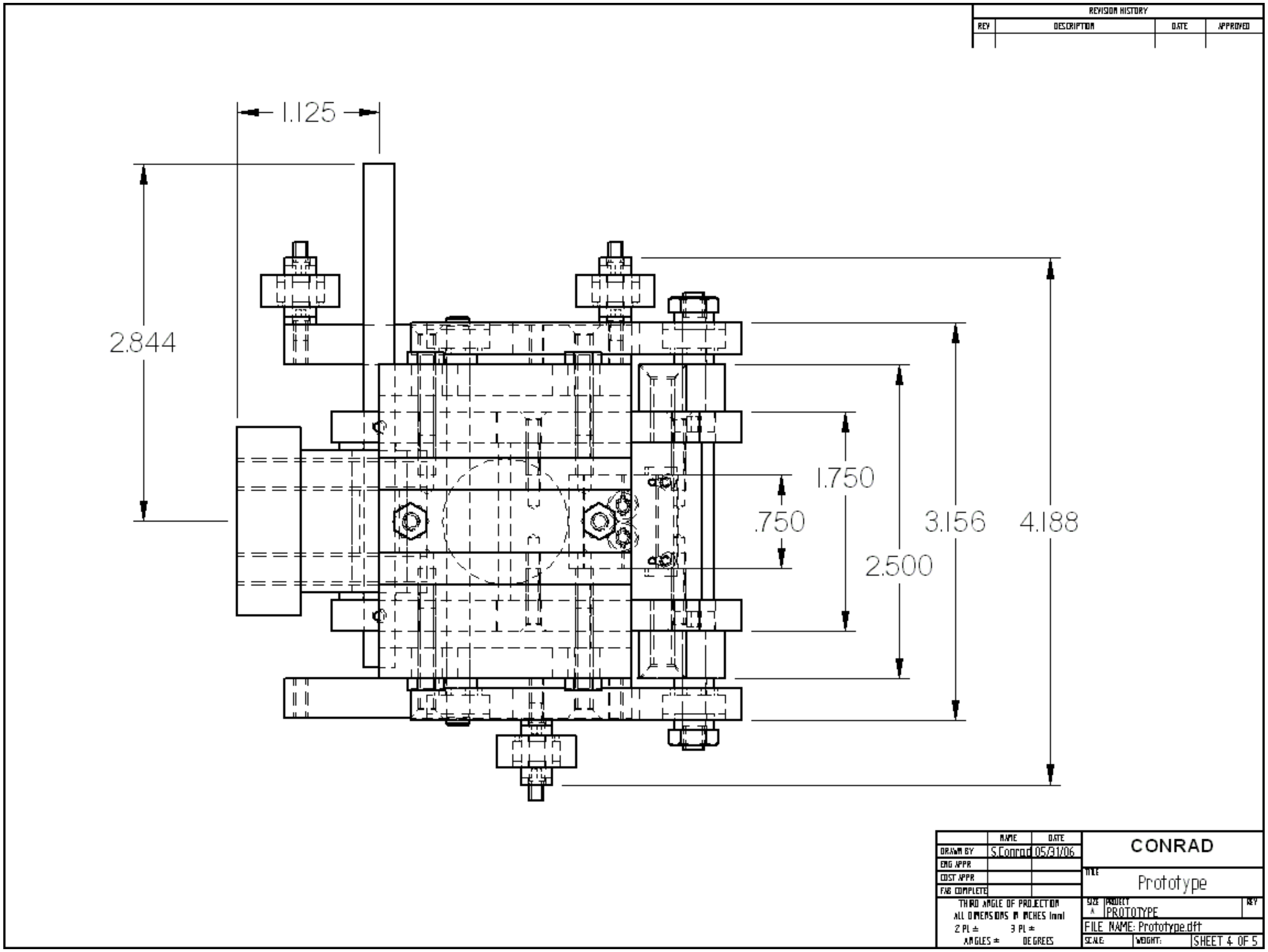

Figure B-4: Prototype Assembly, Sheet 4 of 5

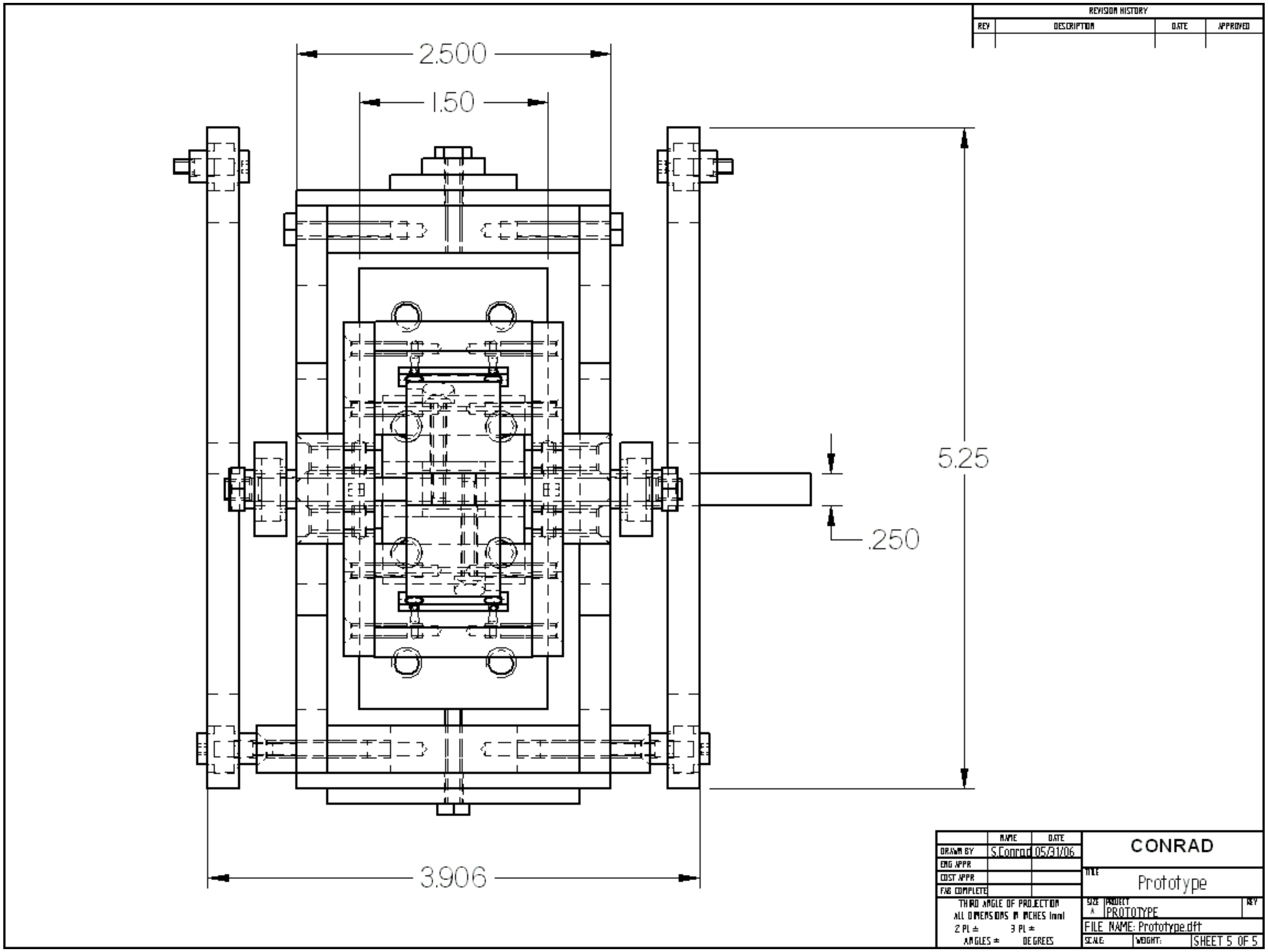

Figure B-5: Prototype Assembly, Sheet 5 of 5

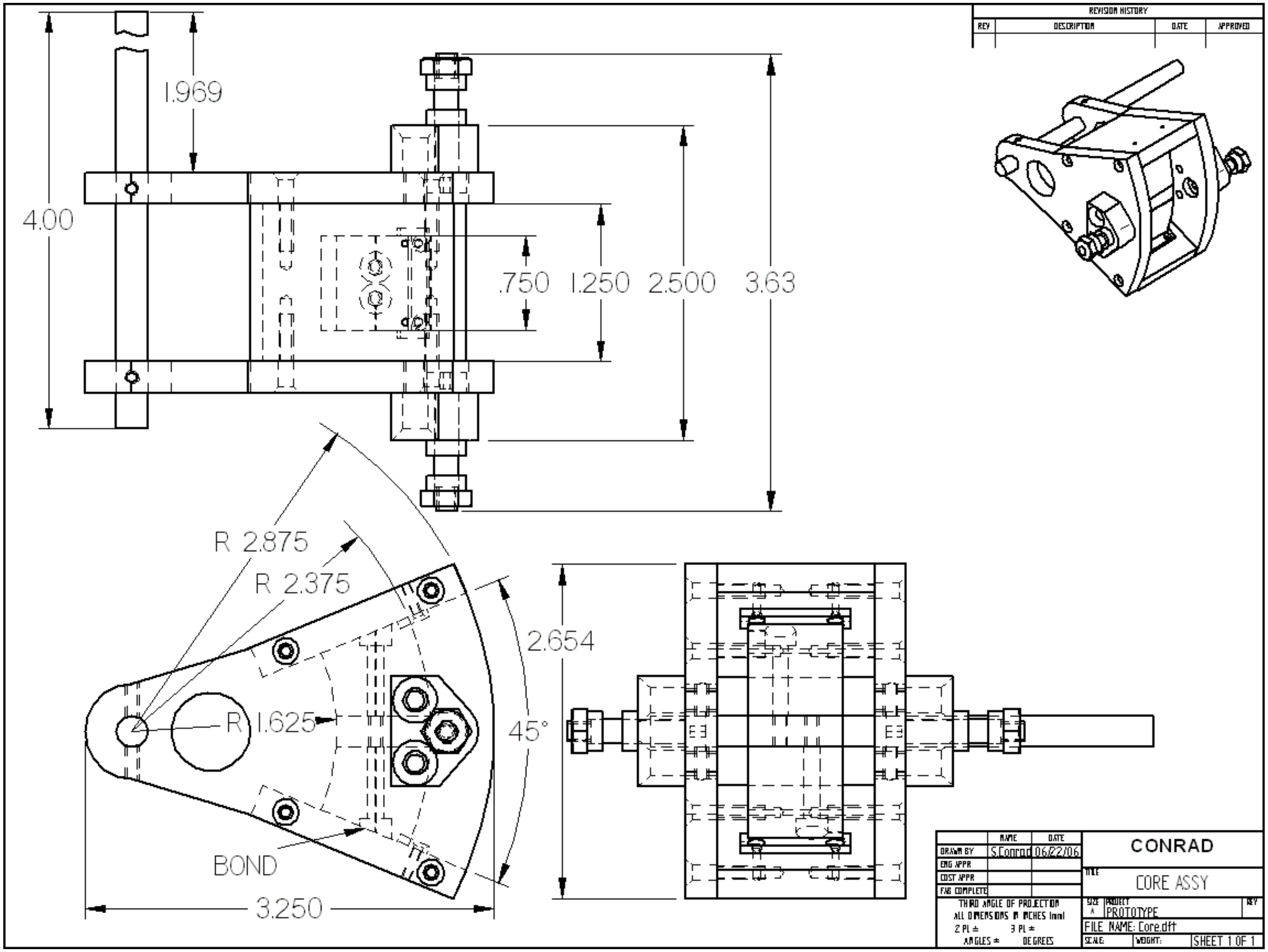

Figure B-6: Core Assembly

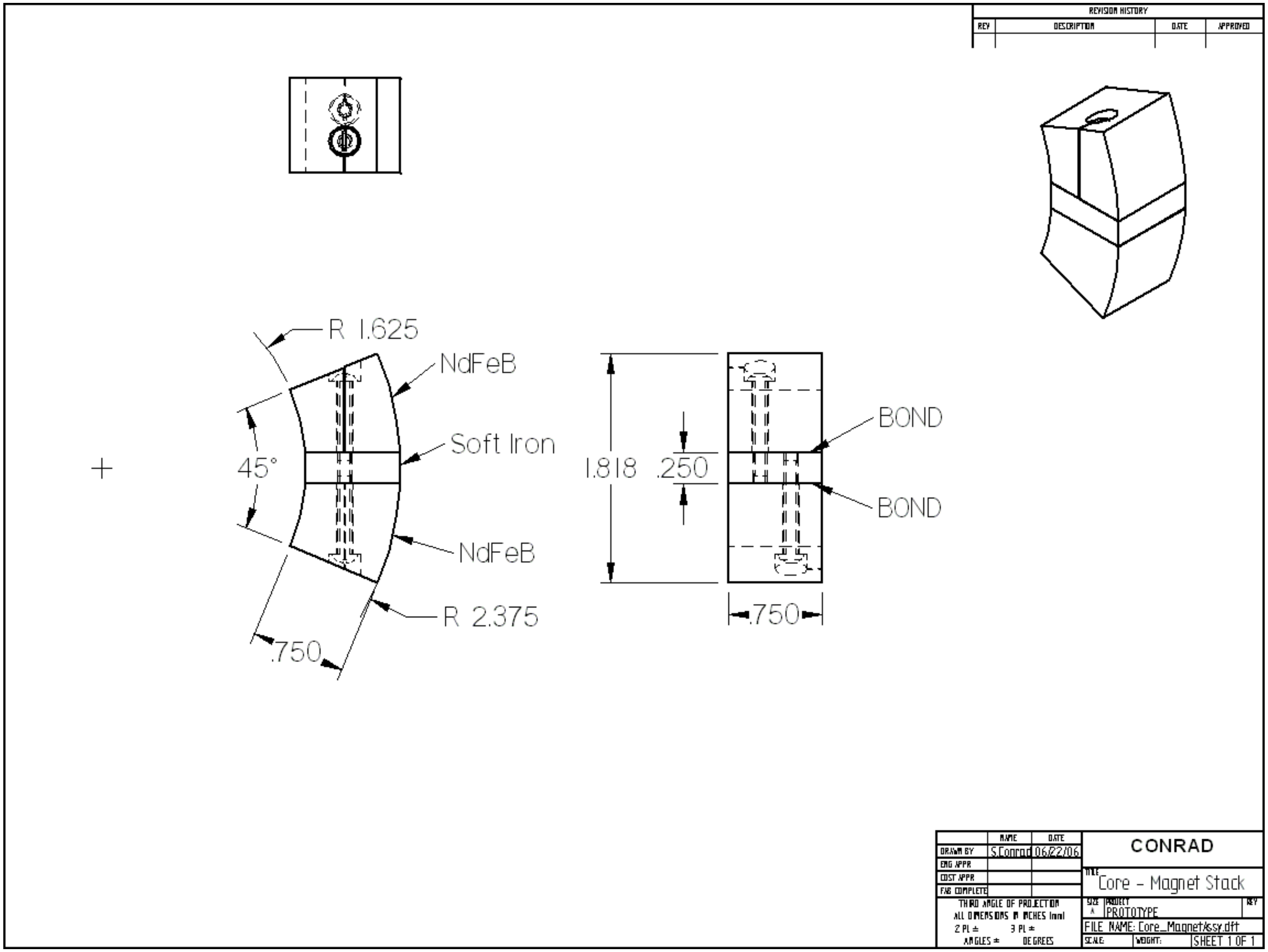

Figure B-7: Magnet Stack Assembly

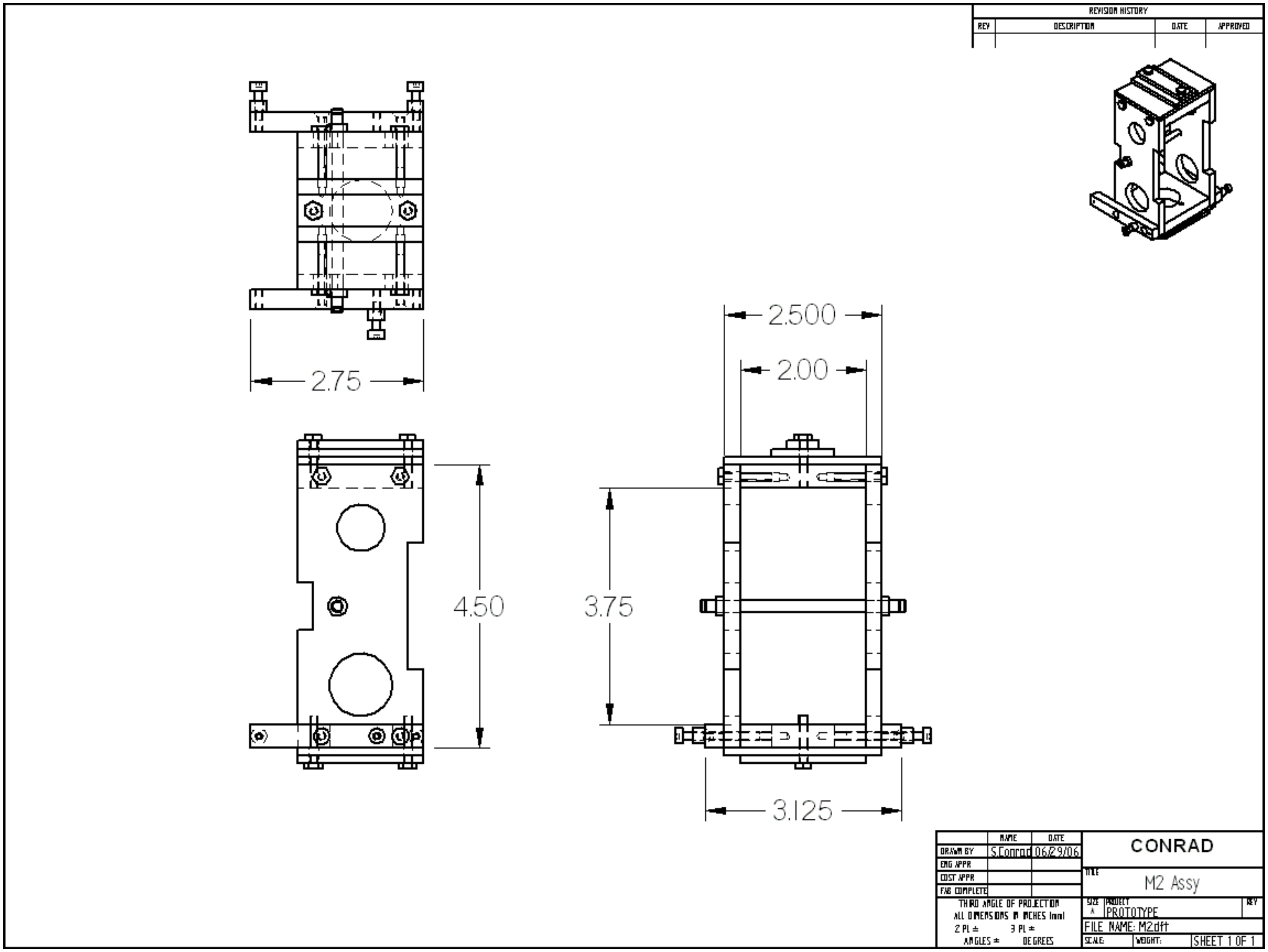

Figure B-8: Slider Mass Assembly

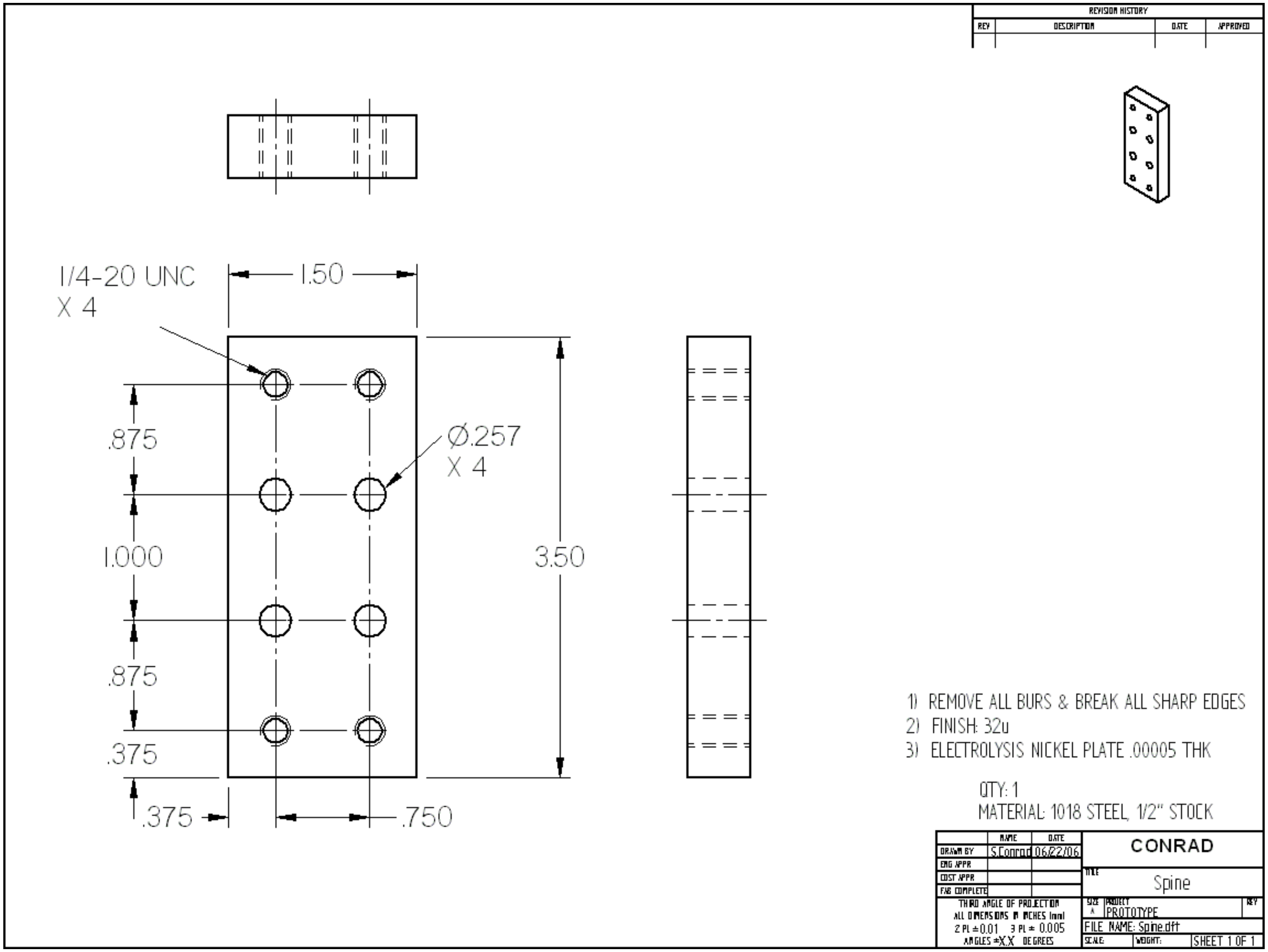

Figure B-9: Spine

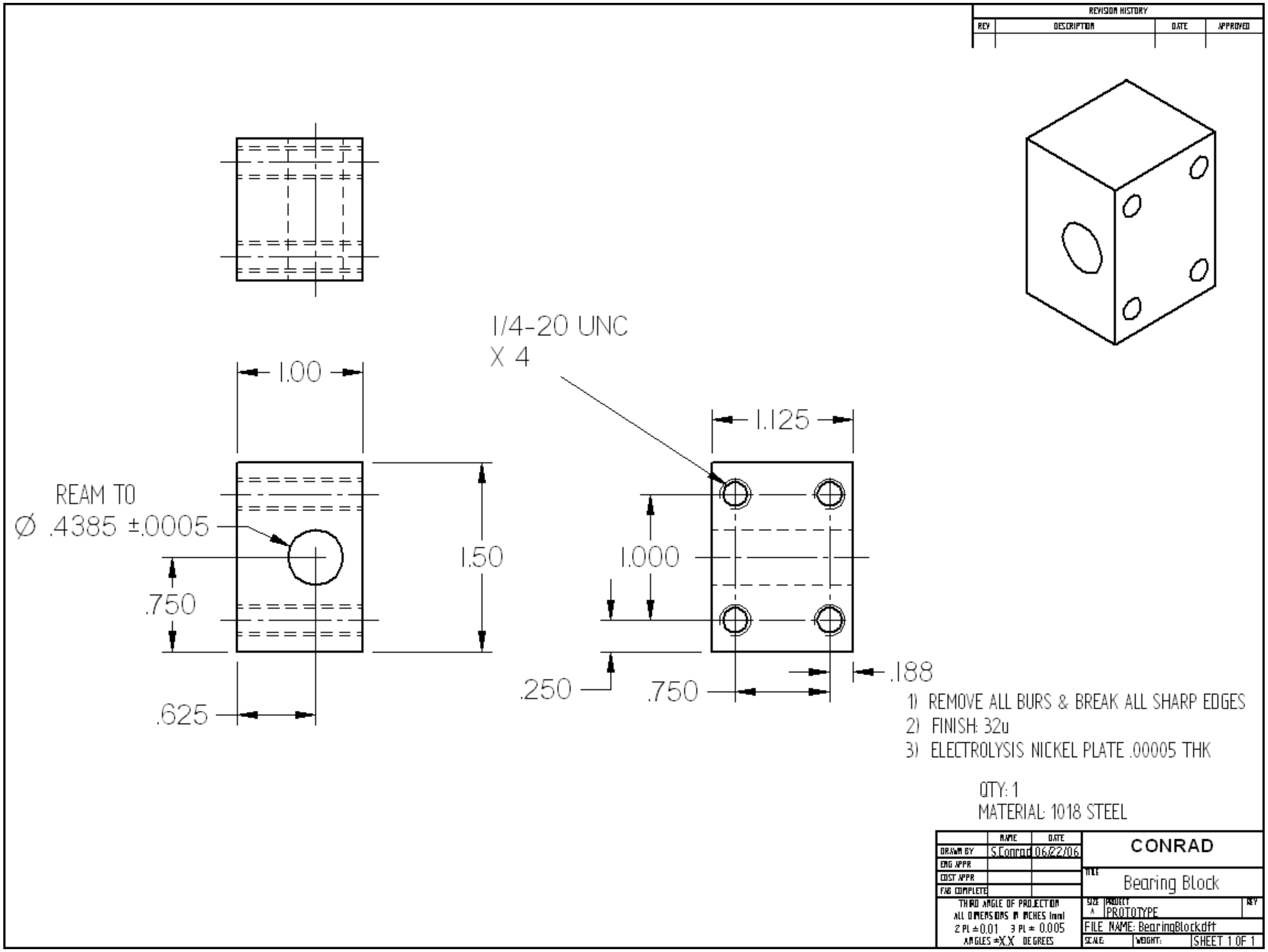

Figure B-10: Bearing Block

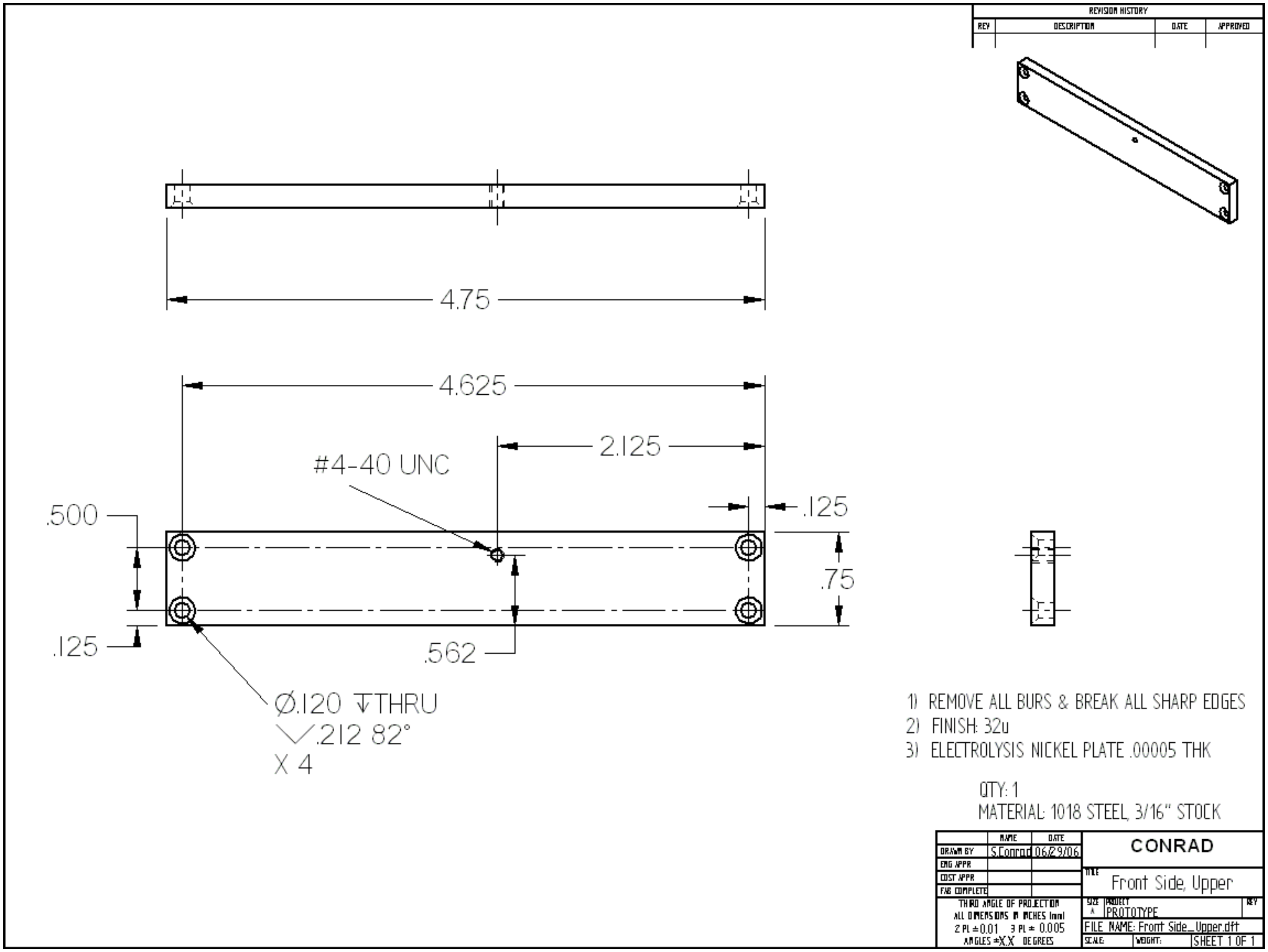

Figure B-11: Front Upper Rail

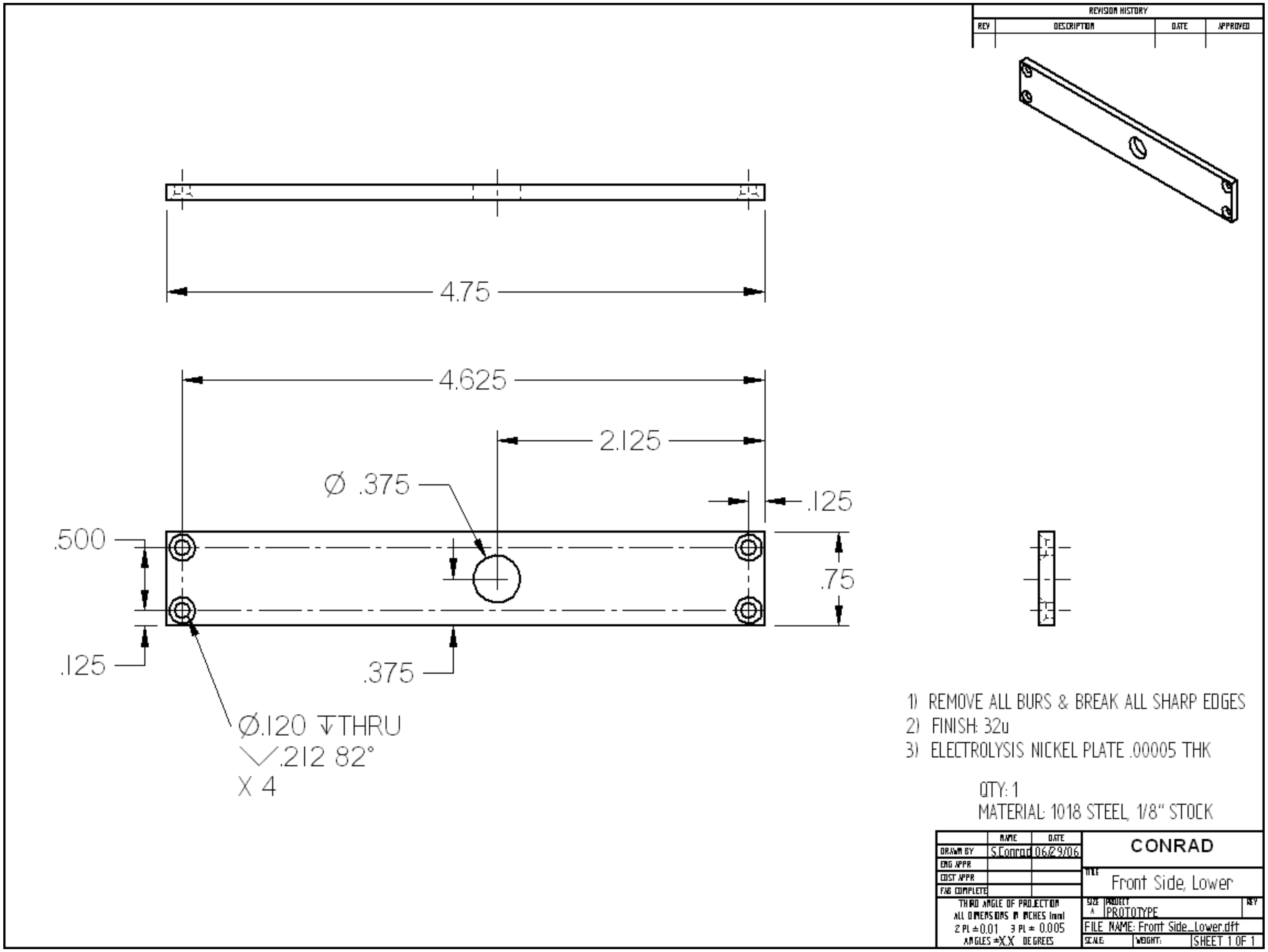

Figure B-12: Front Lower Rail

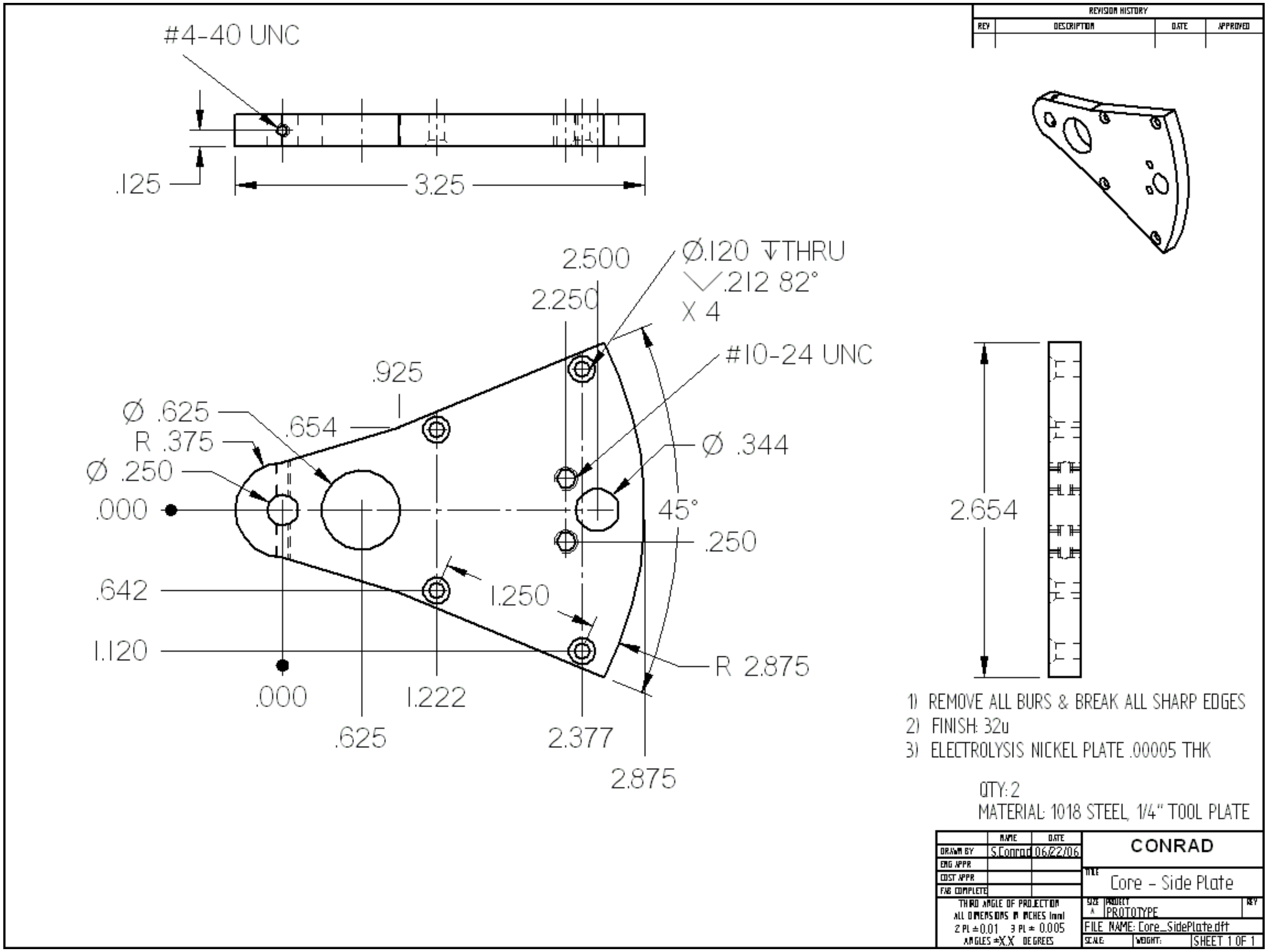

Figure B-13: Core - Side Plate

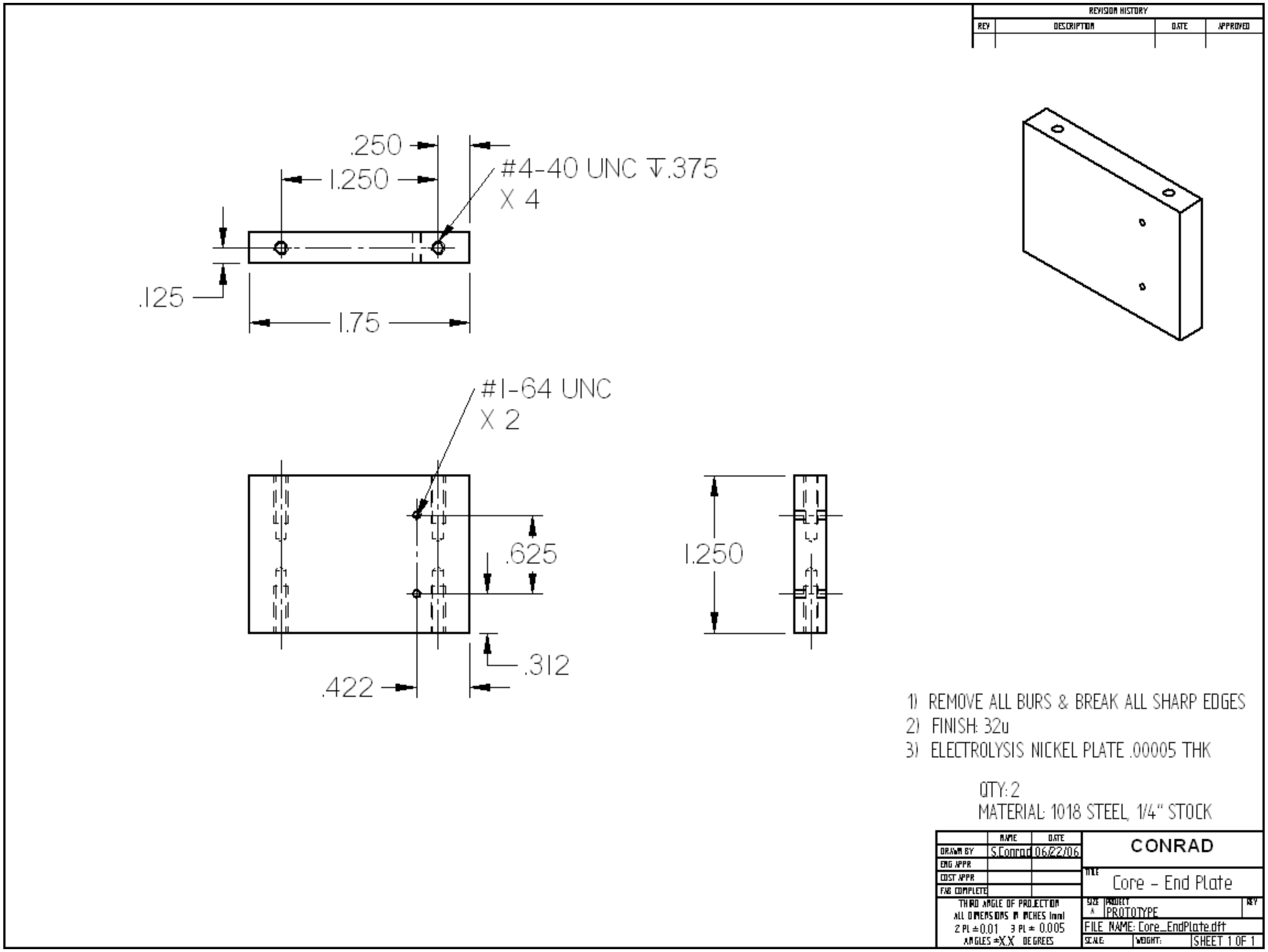

Figure B-14: Core - End Plate

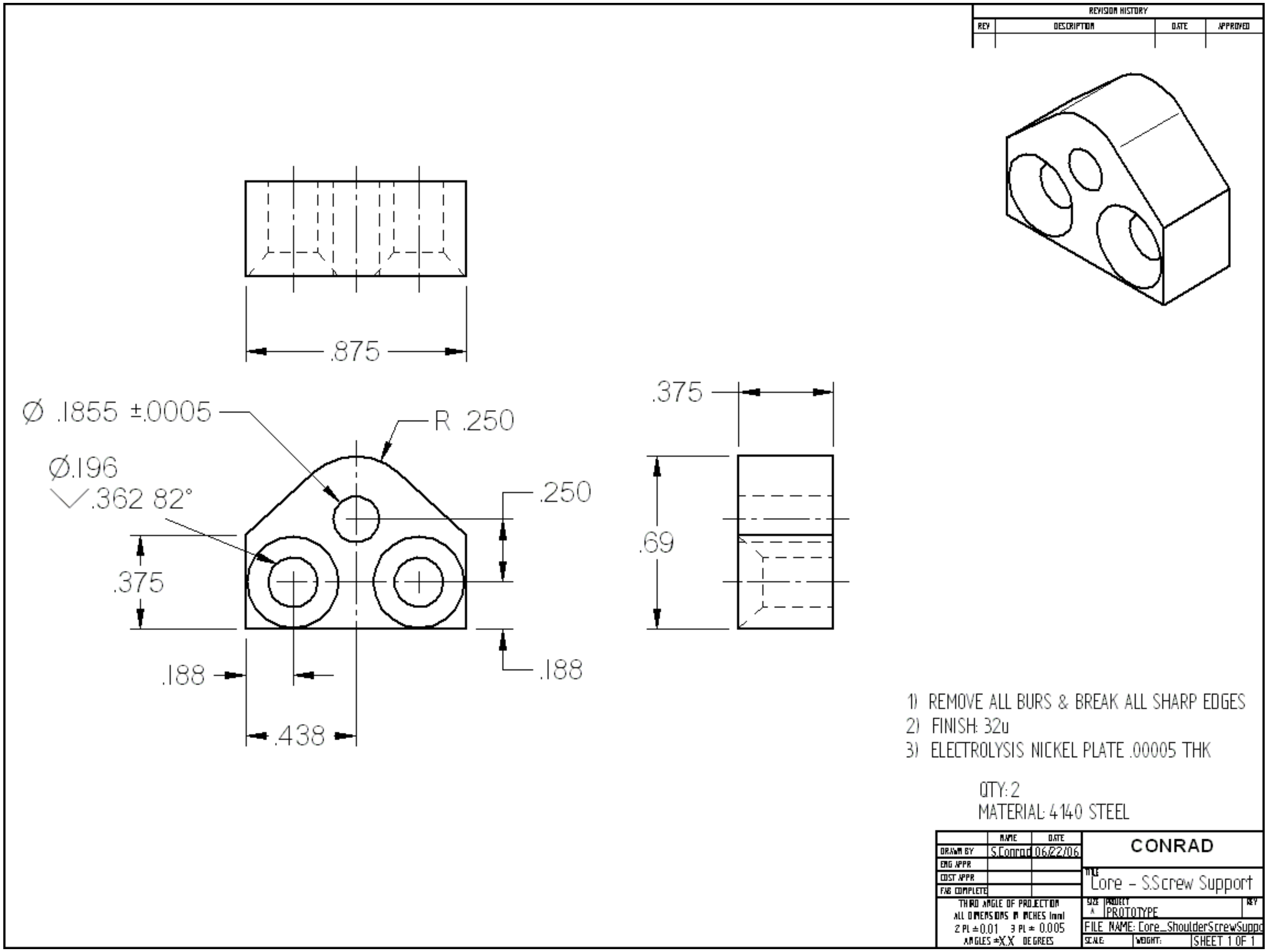

Figure B-15: Core - Shoulder Screw Support

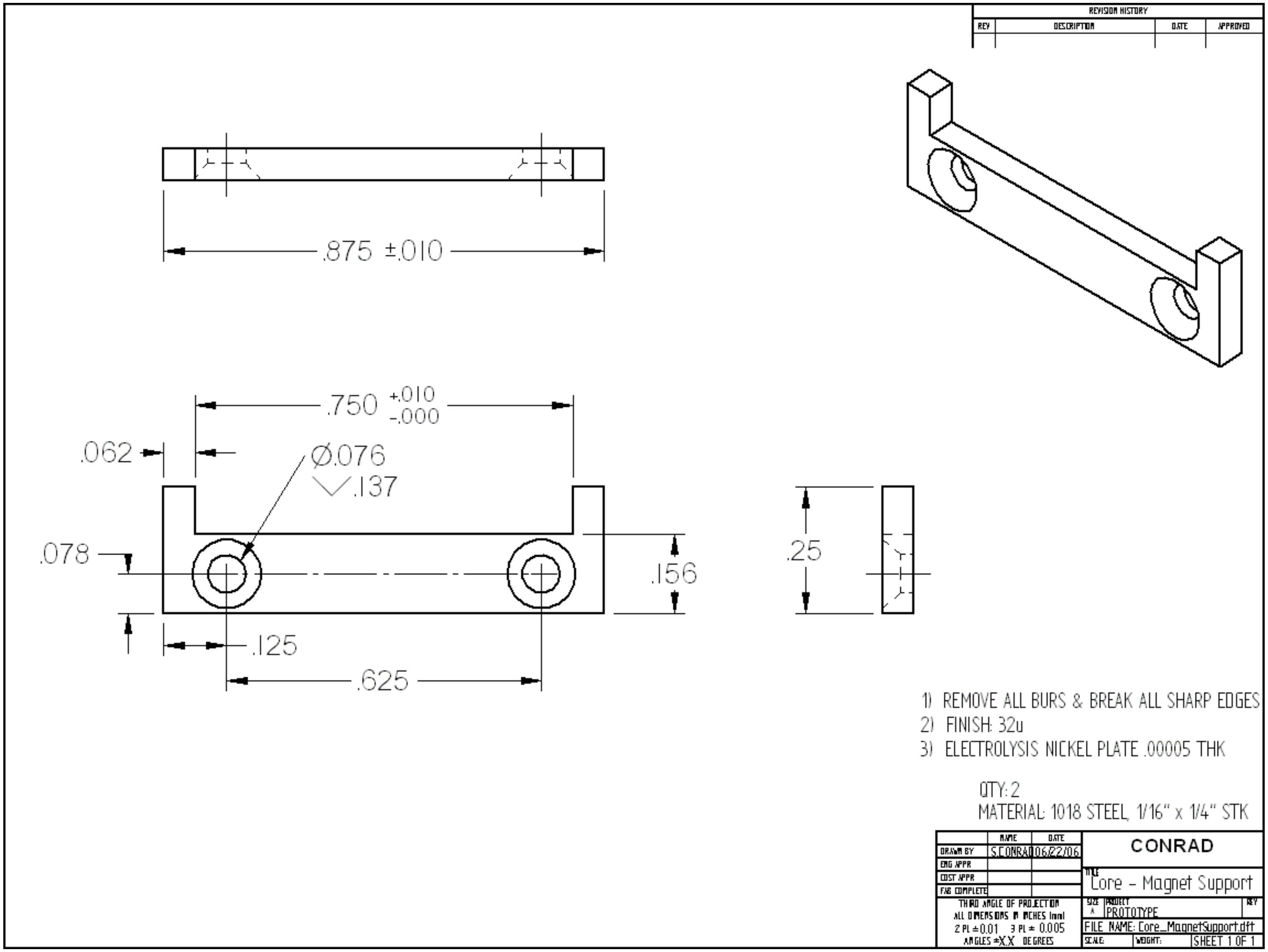

1) REMOVE ALL BURS & BREAK ALL SHARP EDGES
2) FINISH: 32u
3) ELECTROLYSIS NICKEL PLATE .00005 THK

QTY: 2
MATERIAL: 1018 STEEL, 1/16" x 1/4" STK

	NAME	DATE
DRAWN BY	S.CONRAD	06/22/06
ENG APPR		
COST APPR		
FAB COMPLETE		

THIRD ANGLE OF PROJECTION
ALL DIMENSIONS IN INCHES (mm)
2 PL ±0.01 3 PL ± 0.005
ANGLES ±X.X DEGREES

CONRAD

TITLE
Core - Magnet Support

SIZE A
PROJECT PROTOTYPE
REV

FILE NAME: Core_MagnetSupport.dft

SCALE:
WEIGHT:
SHEET 1 OF 1

Figure B-16: Core - Magnet Support

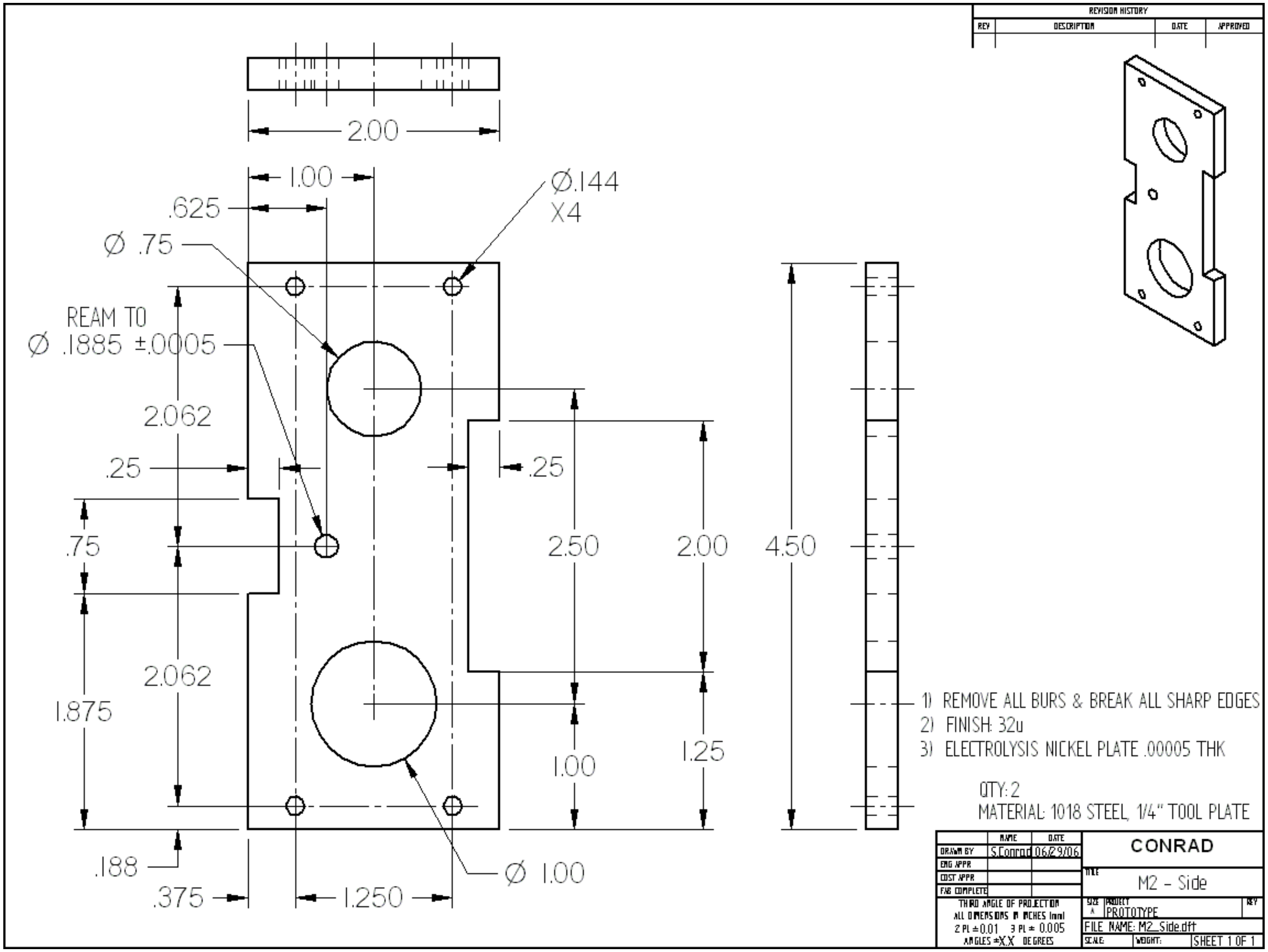

Figure B-17: Slider Mass - Side

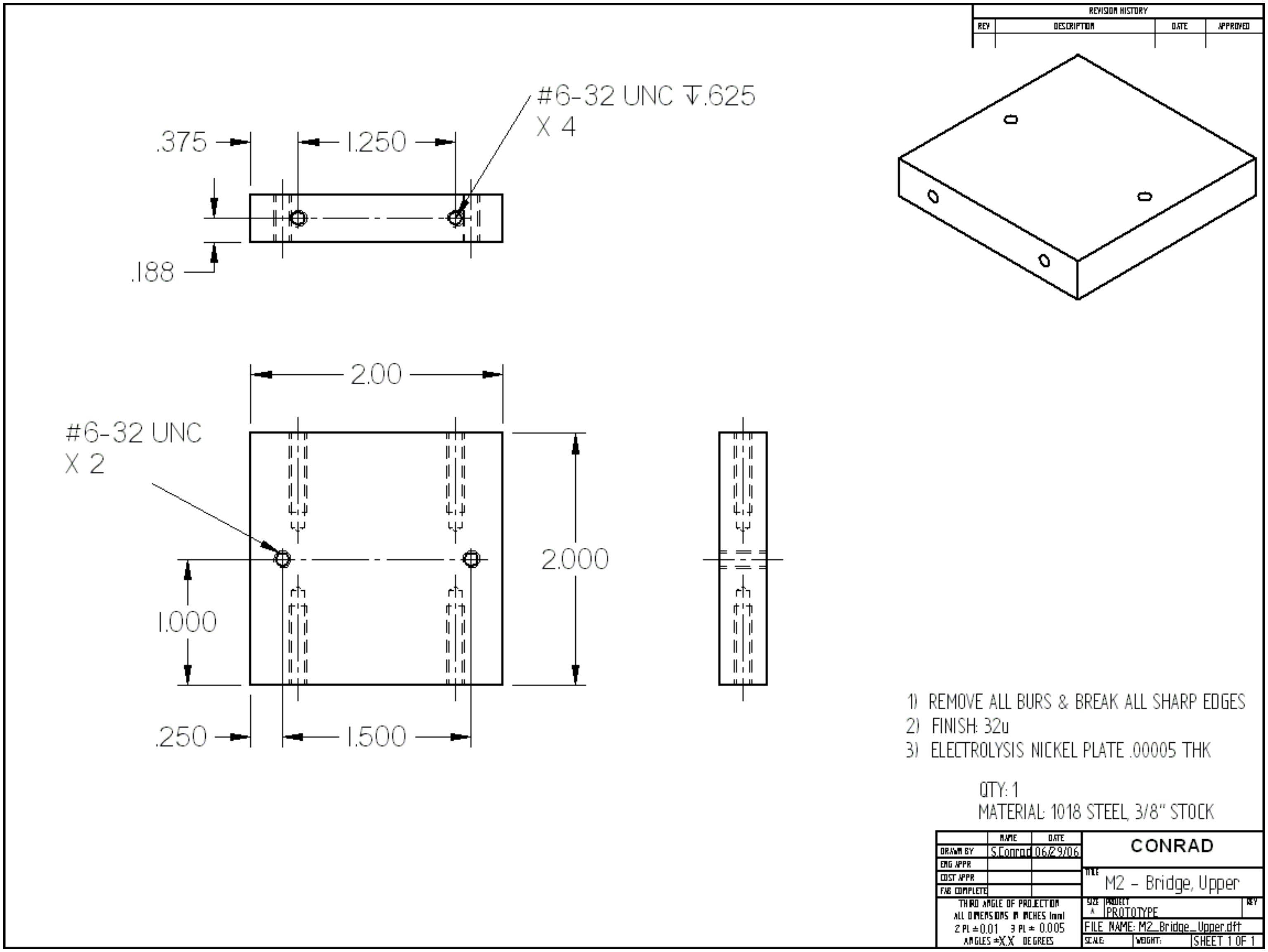

Figure B-18: Slider Mass - Upper Bridge

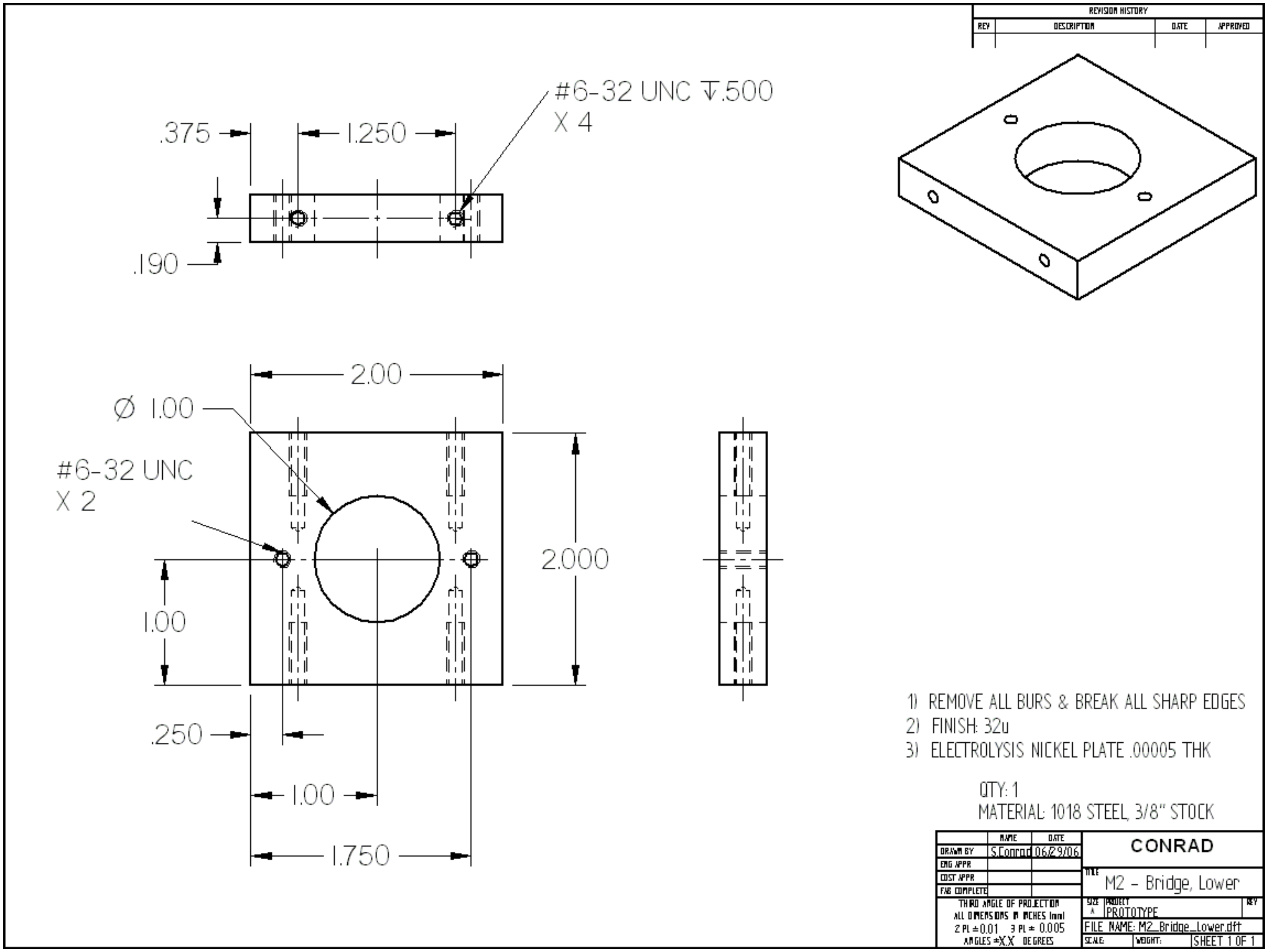

Figure B-19: Slider Mass - Lower Bridge

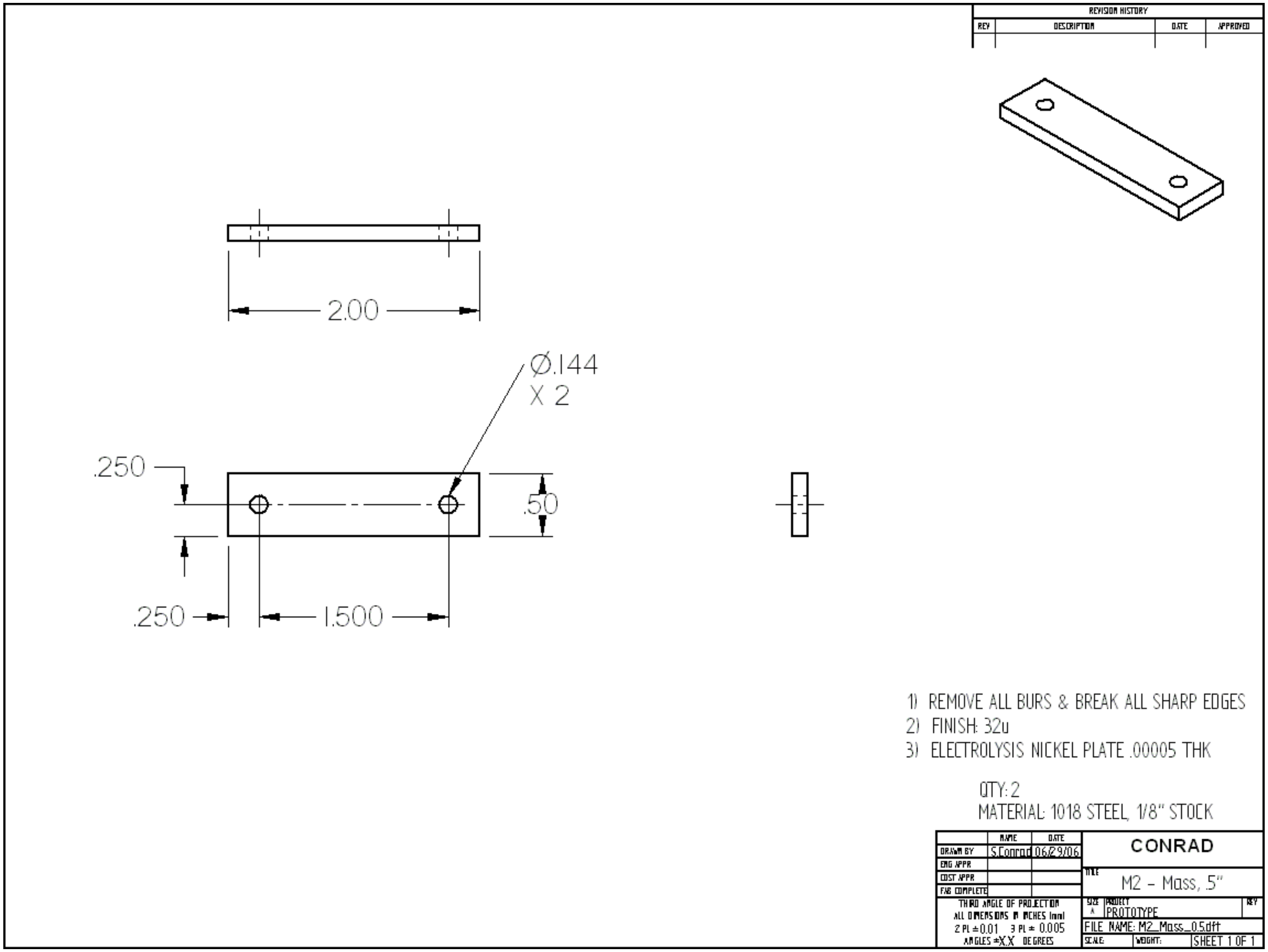

Figure B-20: Slider Mass - Adjustment Plate - 0.5 in

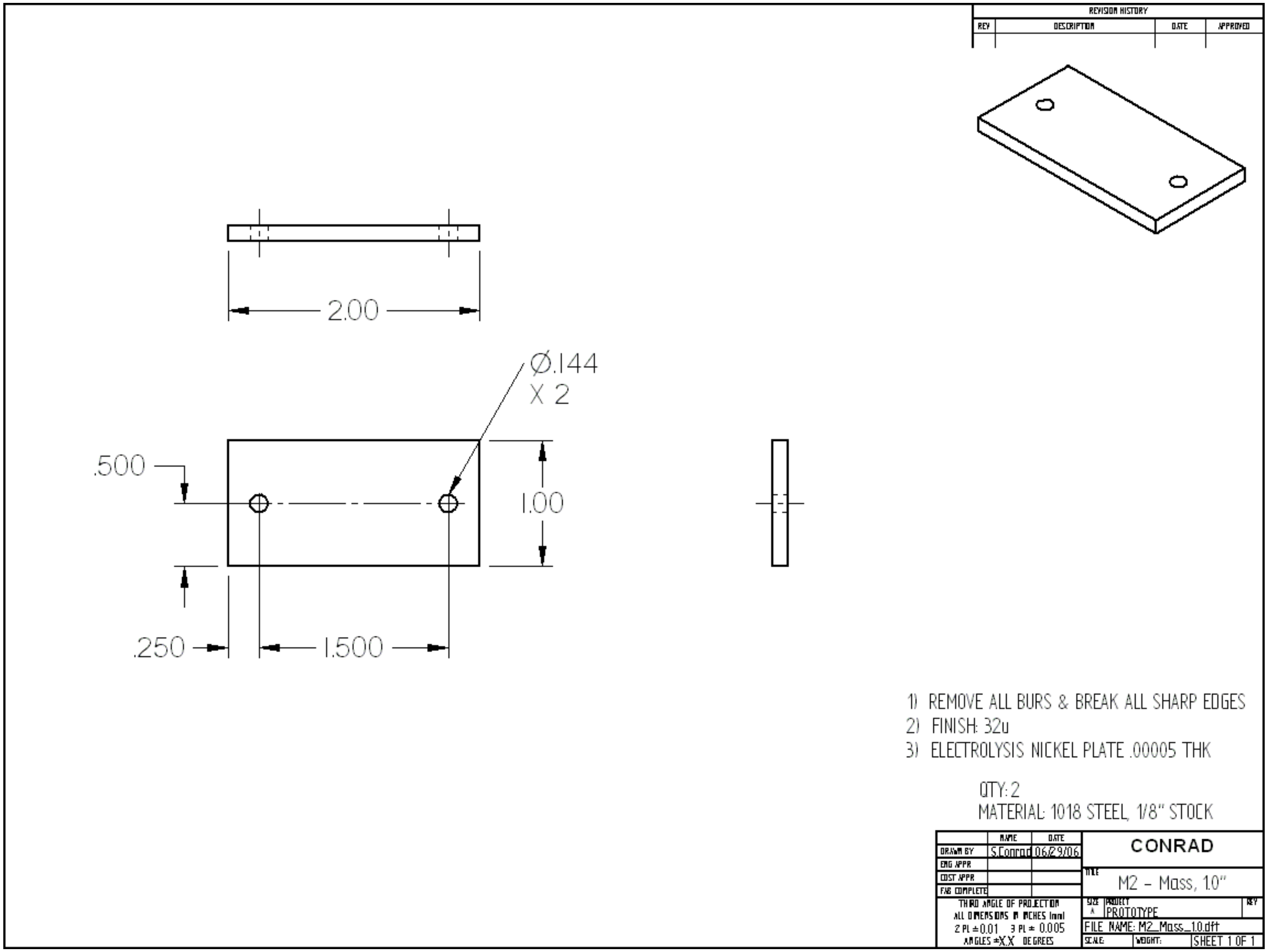

Figure B-21: Slider Mass - Adjustment Plate - 1.0 in

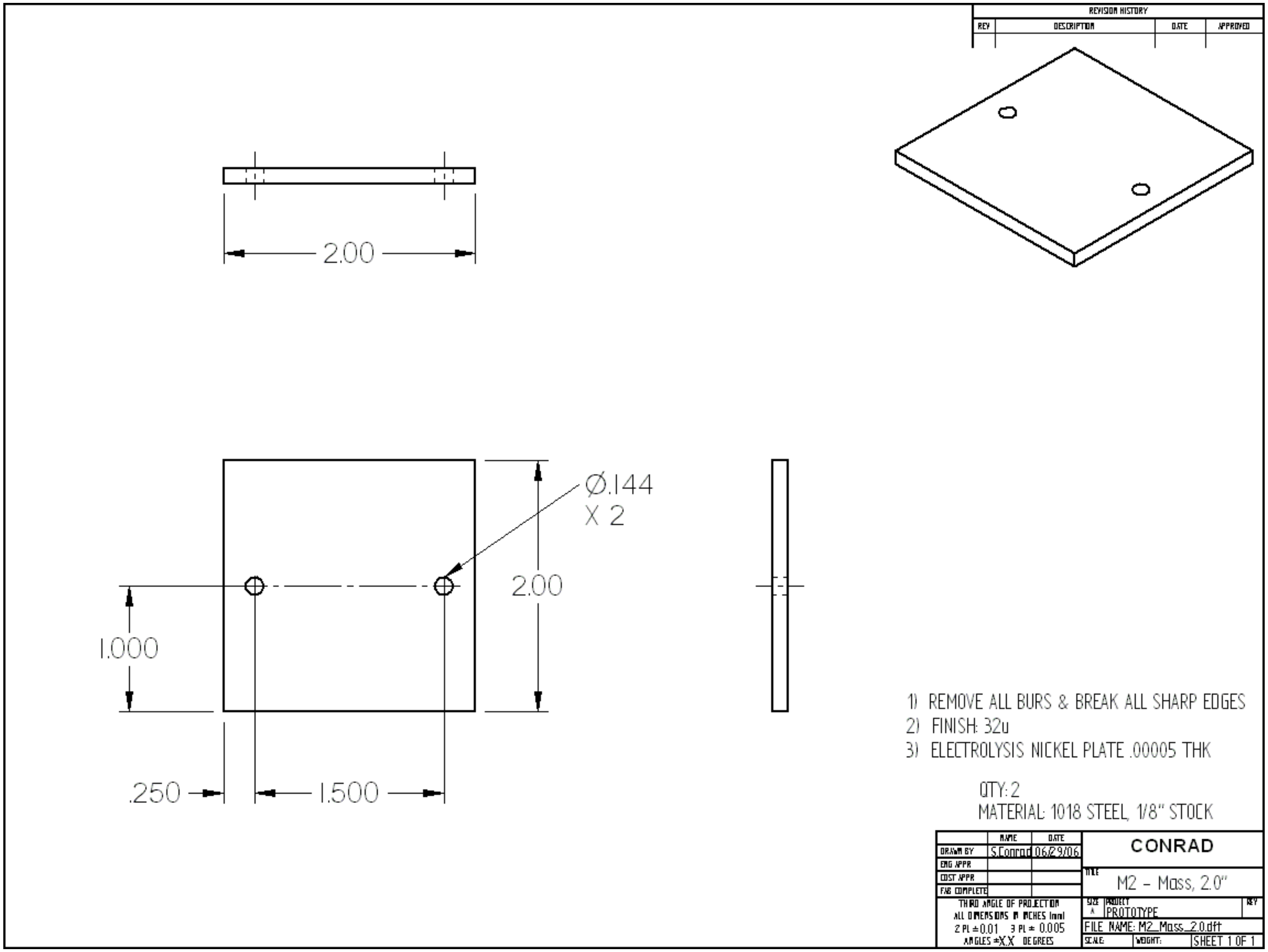

Figure B-22: Slider Mass - Adjustment Plate - 2.0 in

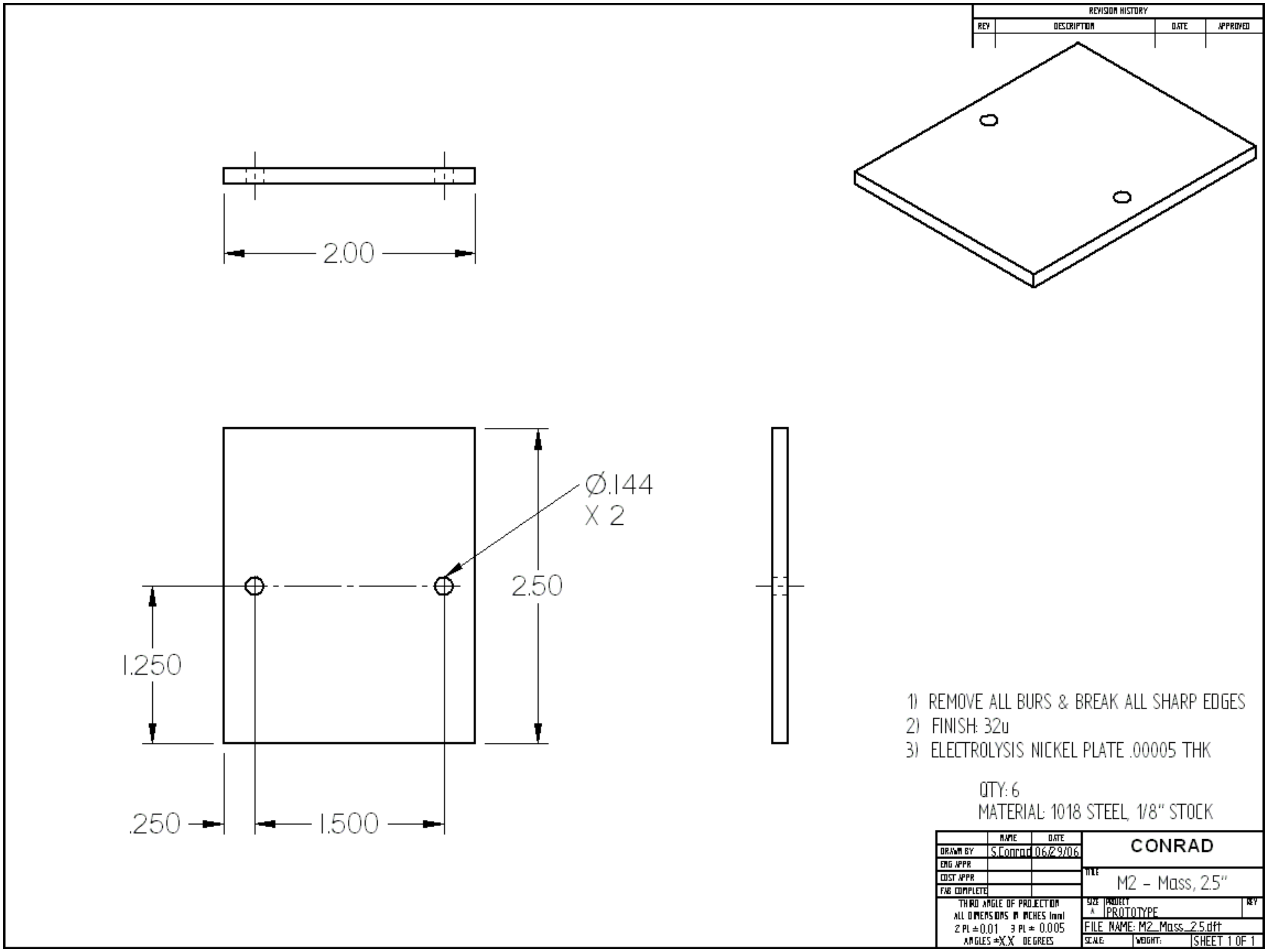

Figure B-23: Slider Mass - Adjustment Plate - 2.5 in

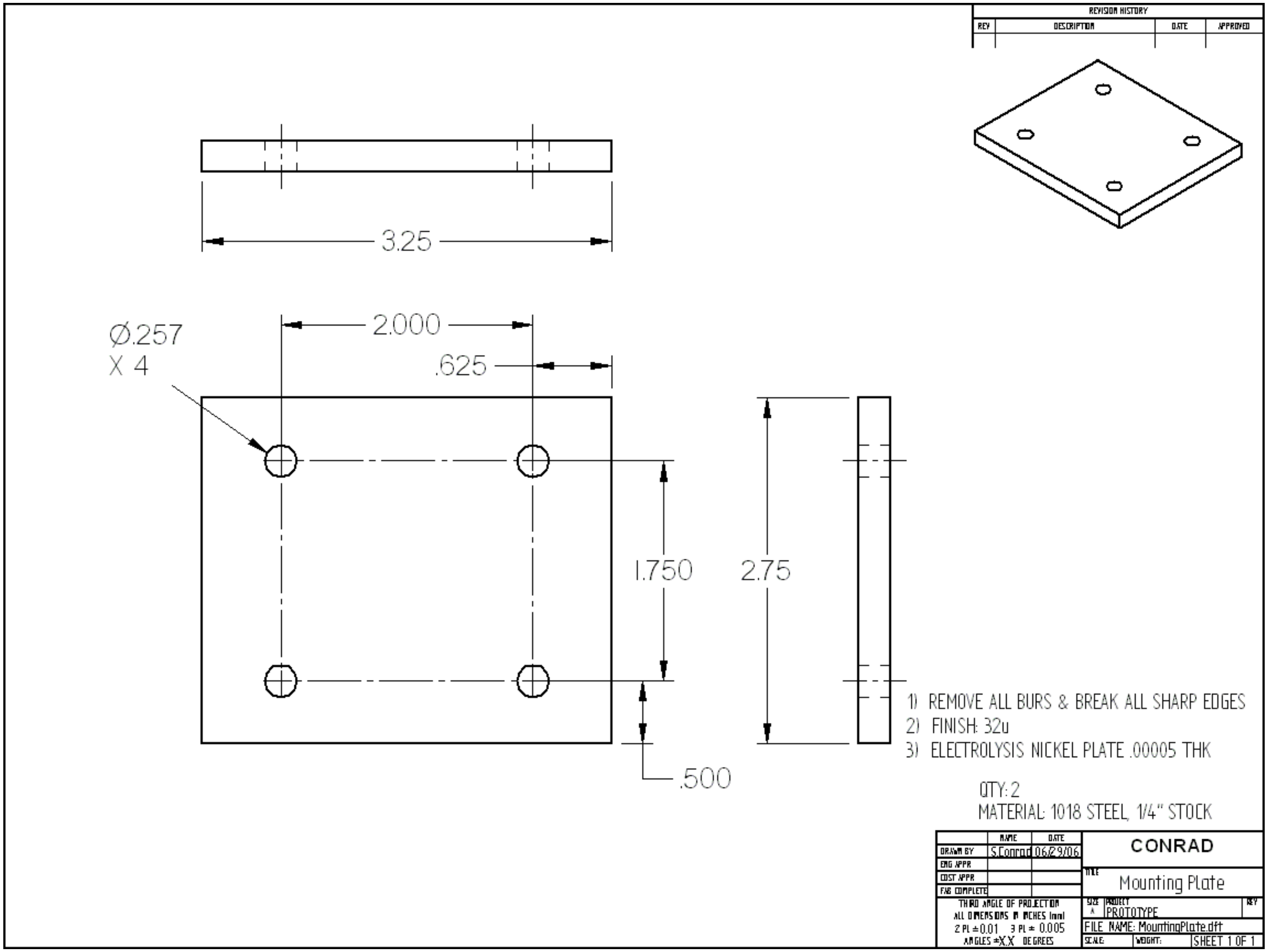

Figure B-24: Mounting Plate

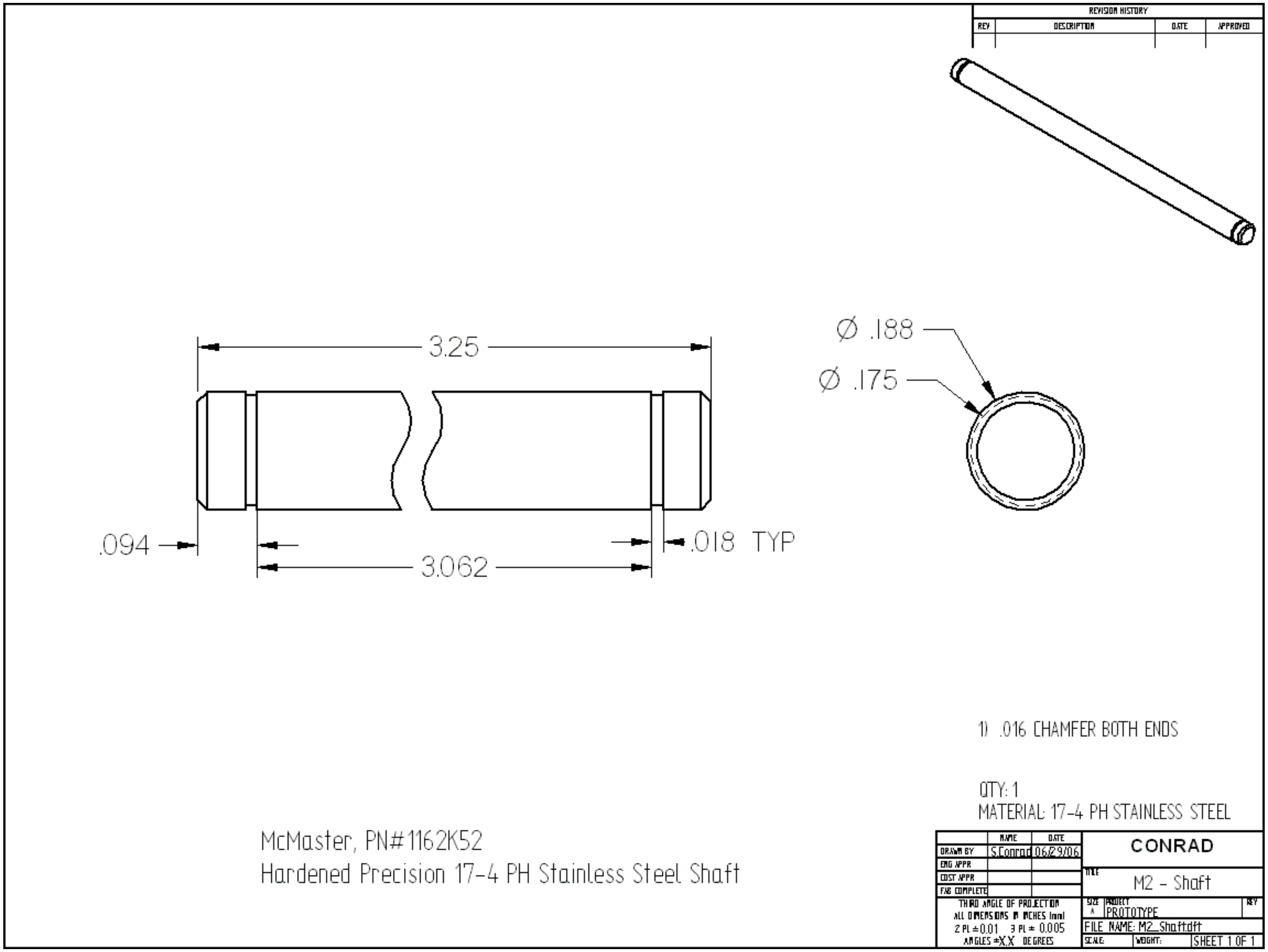

Figure B-25: Slider Mass - Shaft

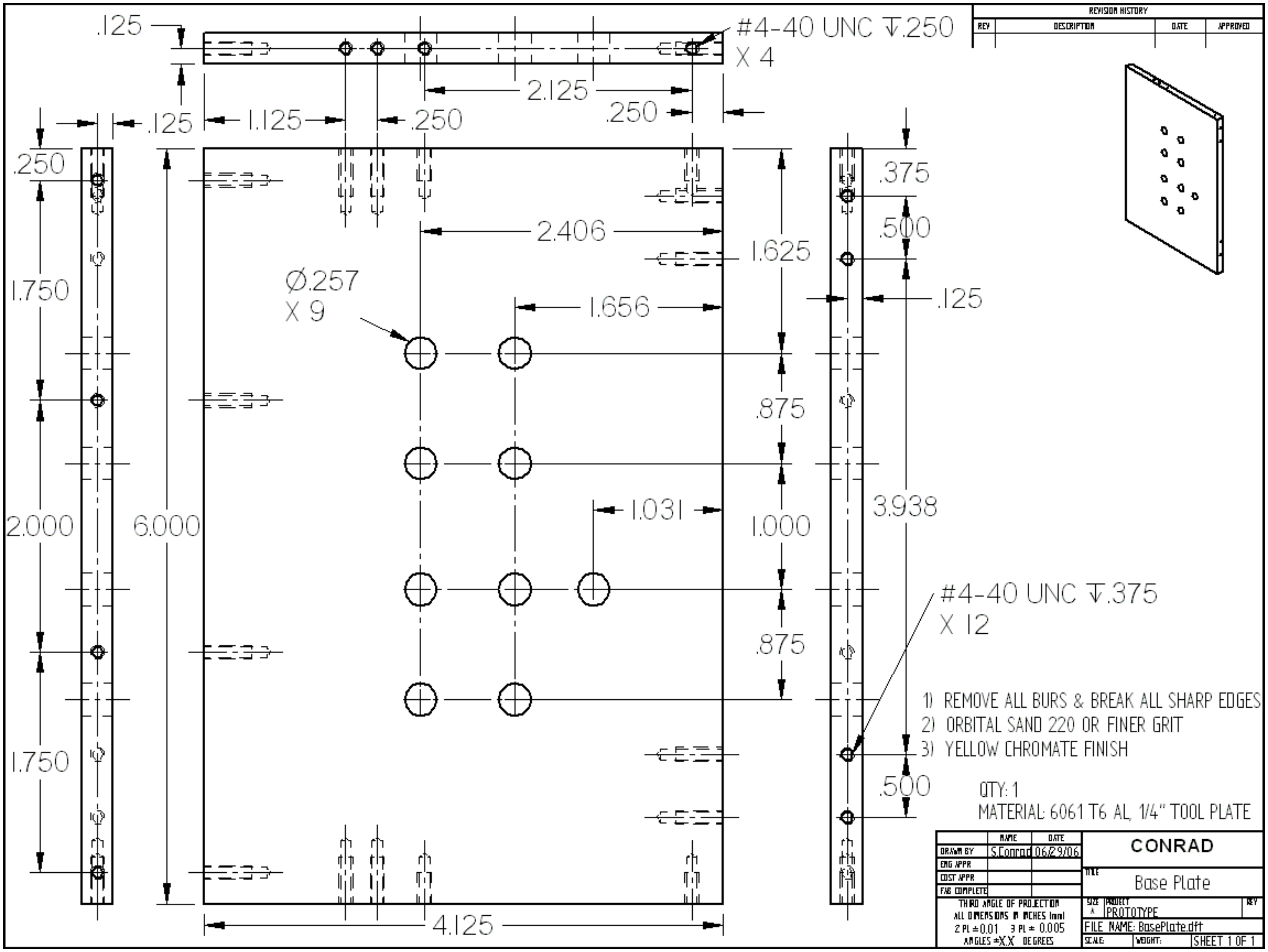

1) REMOVE ALL BURS & BREAK ALL SHARP EDGES
2) ORBITAL SAND 220 OR FINER GRIT
3) YELLOW CHROMATE FINISH

QTY: 1
MATERIAL: 6061 T6 AL, 1/4" TOOL PLATE

REVISION HISTORY			
REV	DESCRIPTION	DATE	APPROVED

	NAME	DATE
DRAWN BY	S.Conrad	06/29/06
ENG APPR		
COST APPR		
FAB COMPLETE		

THIRD ANGLE OF PROJECTION
ALL DIMENSIONS IN INCHES [mm]
2 PL ±0.01 3 PL ± 0.005
ANGLES ±X.X DEGREES

CONRAD

TITLE Base Plate

SIZE A
PROJECT PROTOTYPE
REV

FILE NAME: BasePlate.dft

SCALE:
WEIGHT:
SHEET 1 OF 1

Figure B-26: Base Plate

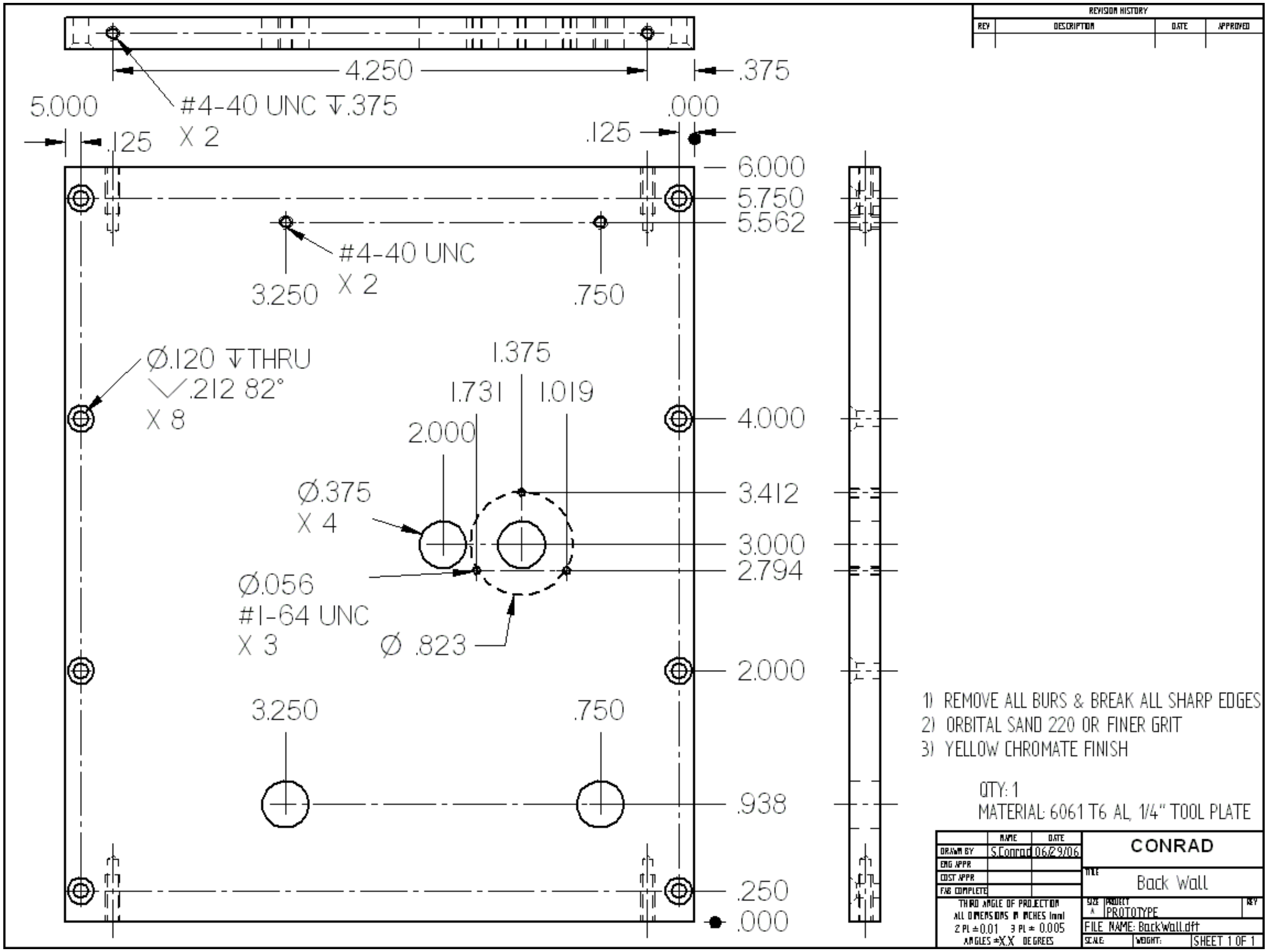

Figure B-27: Back Wall

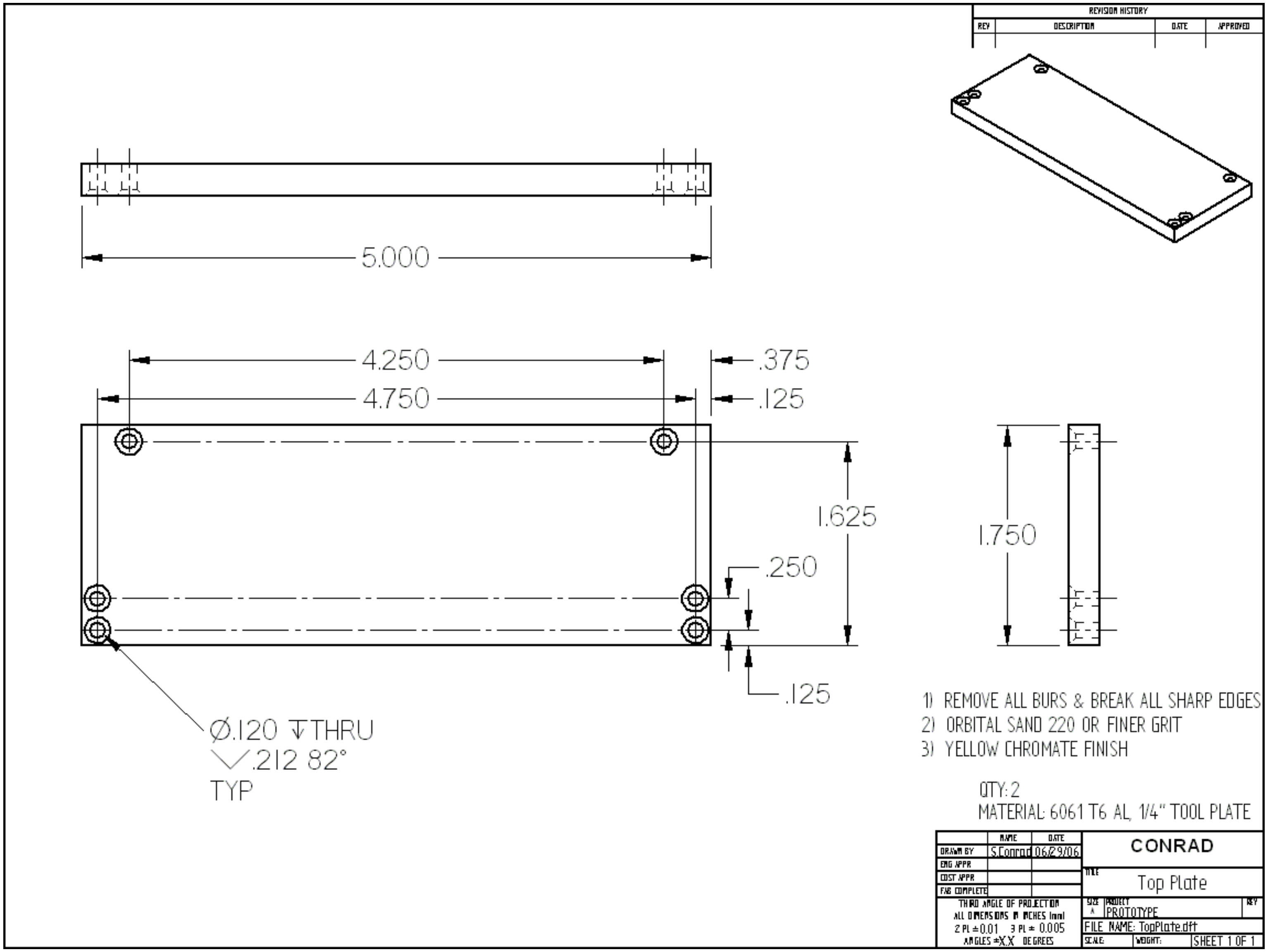

Figure B-28: Top Plate

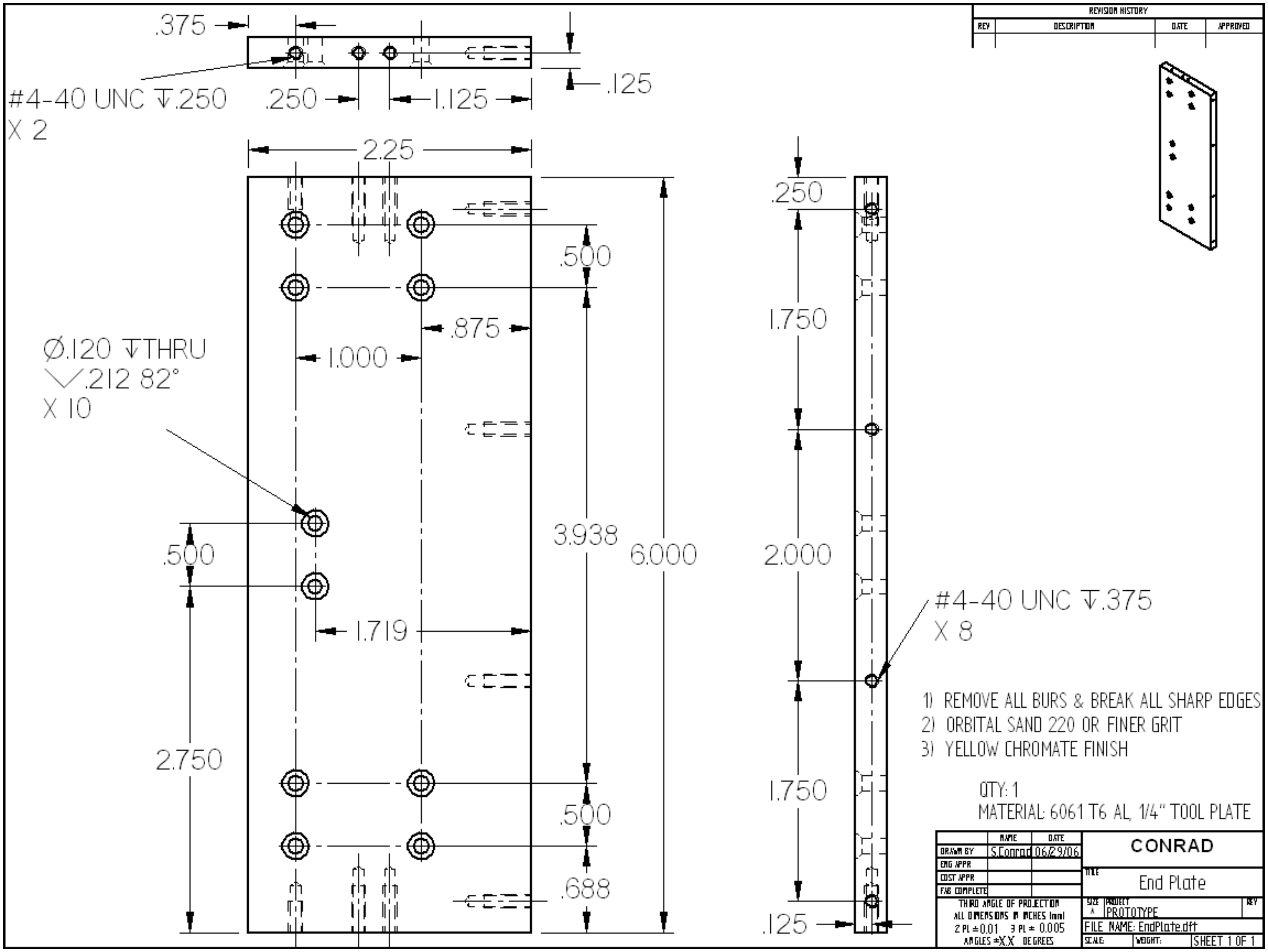

Figure B-29: End Plate

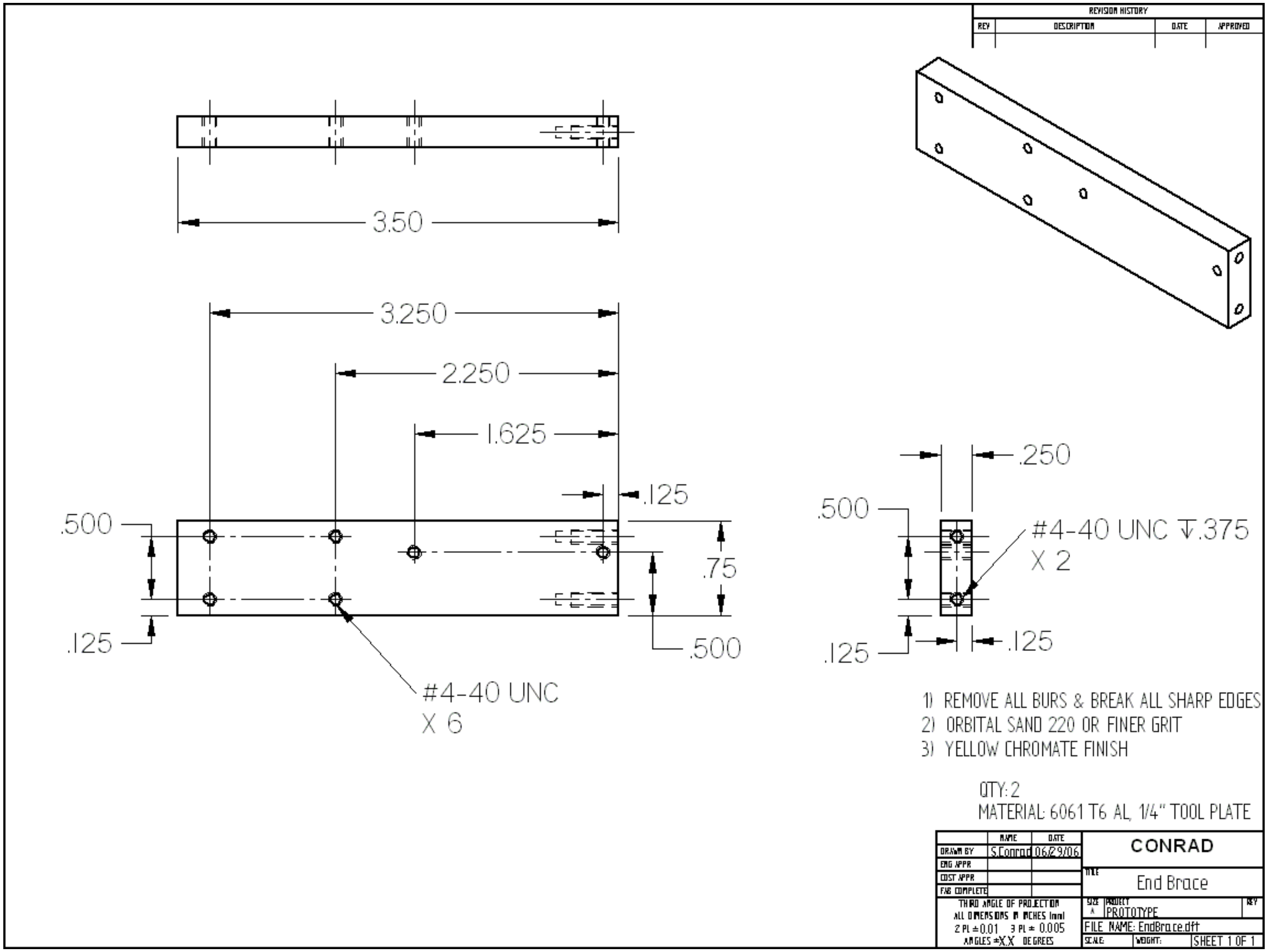

Figure B-30: End Brace

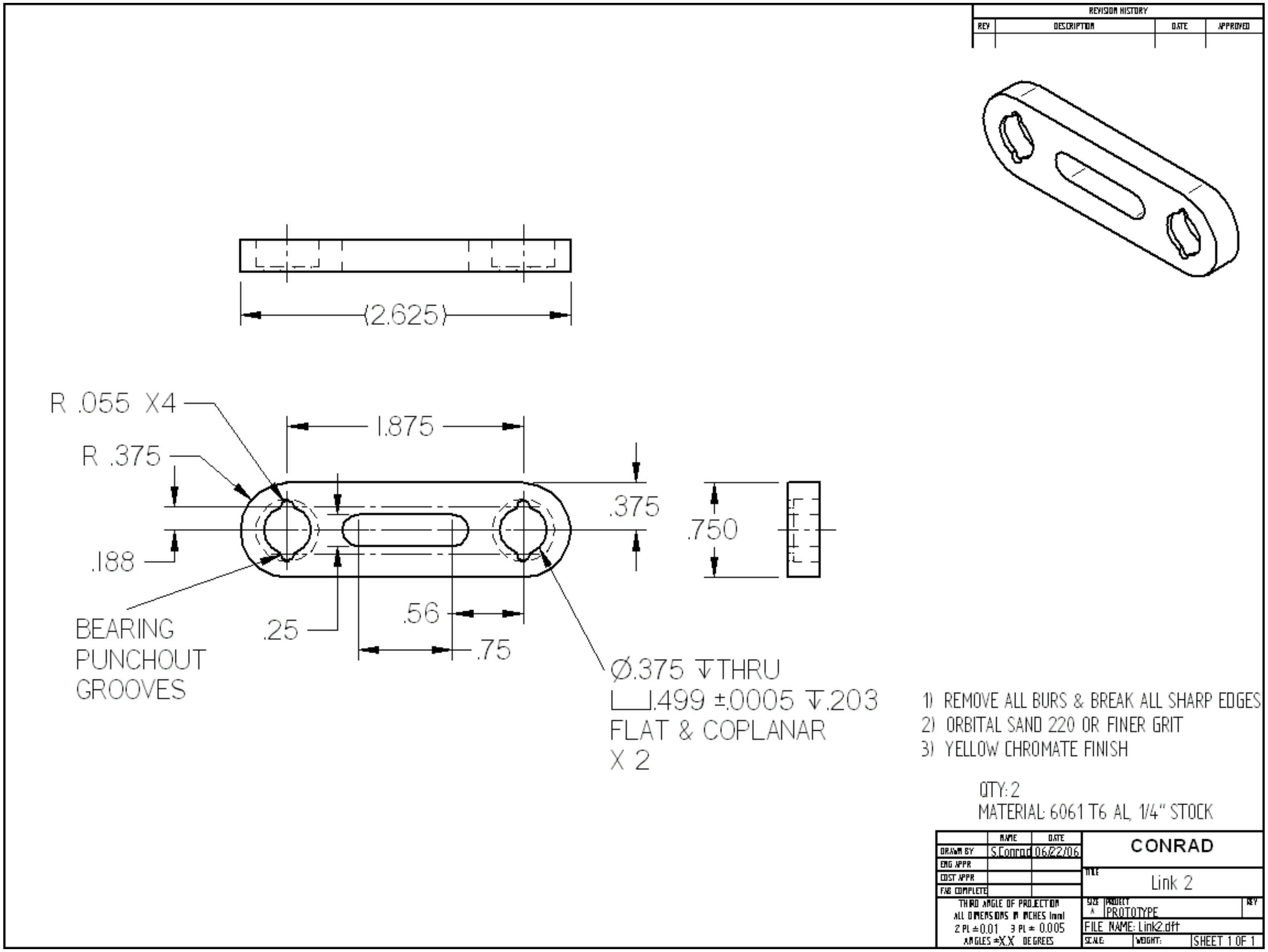

Figure B-31: Link 2

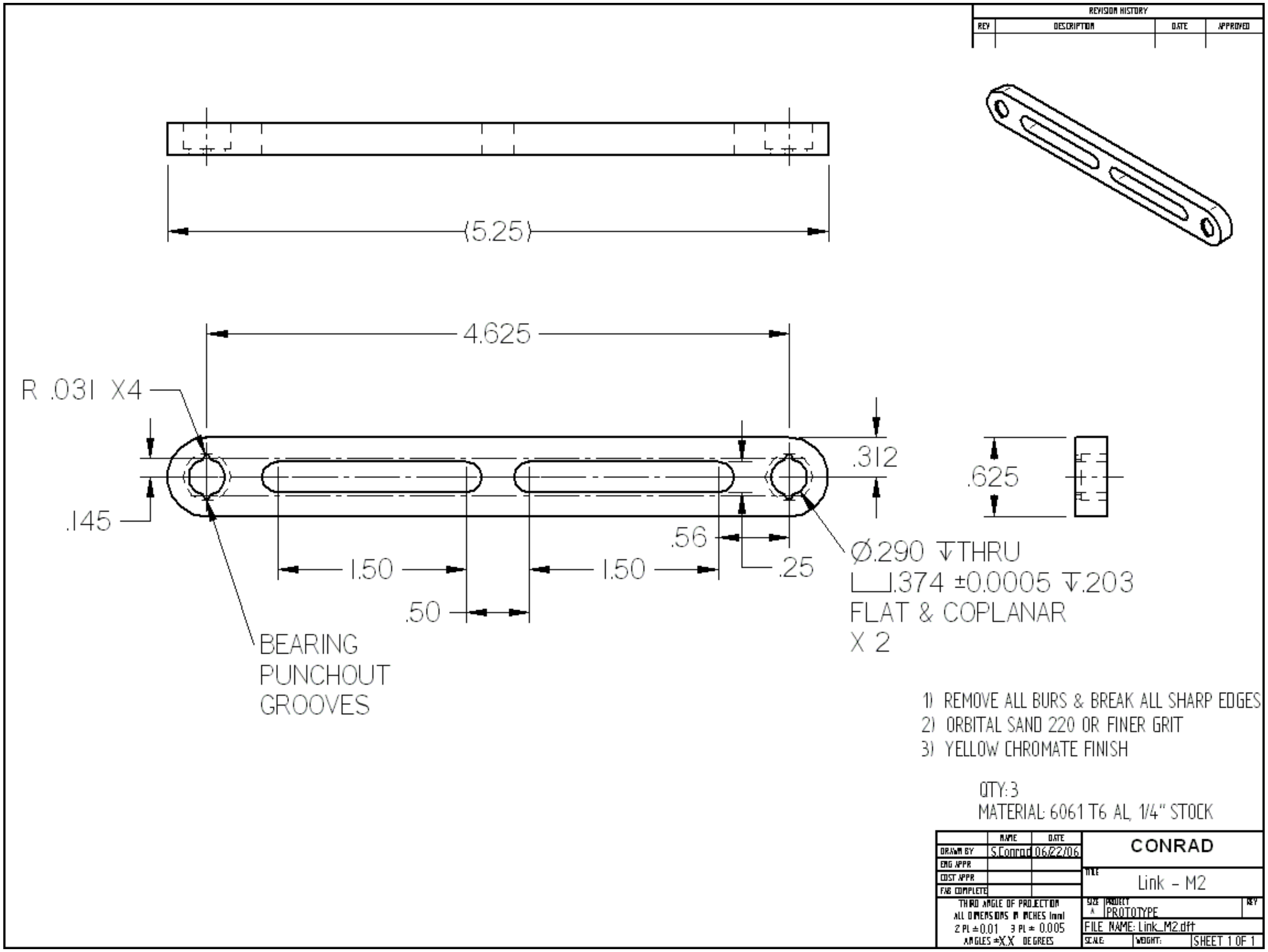

Figure B-32: Slider Mass - Constraint Link

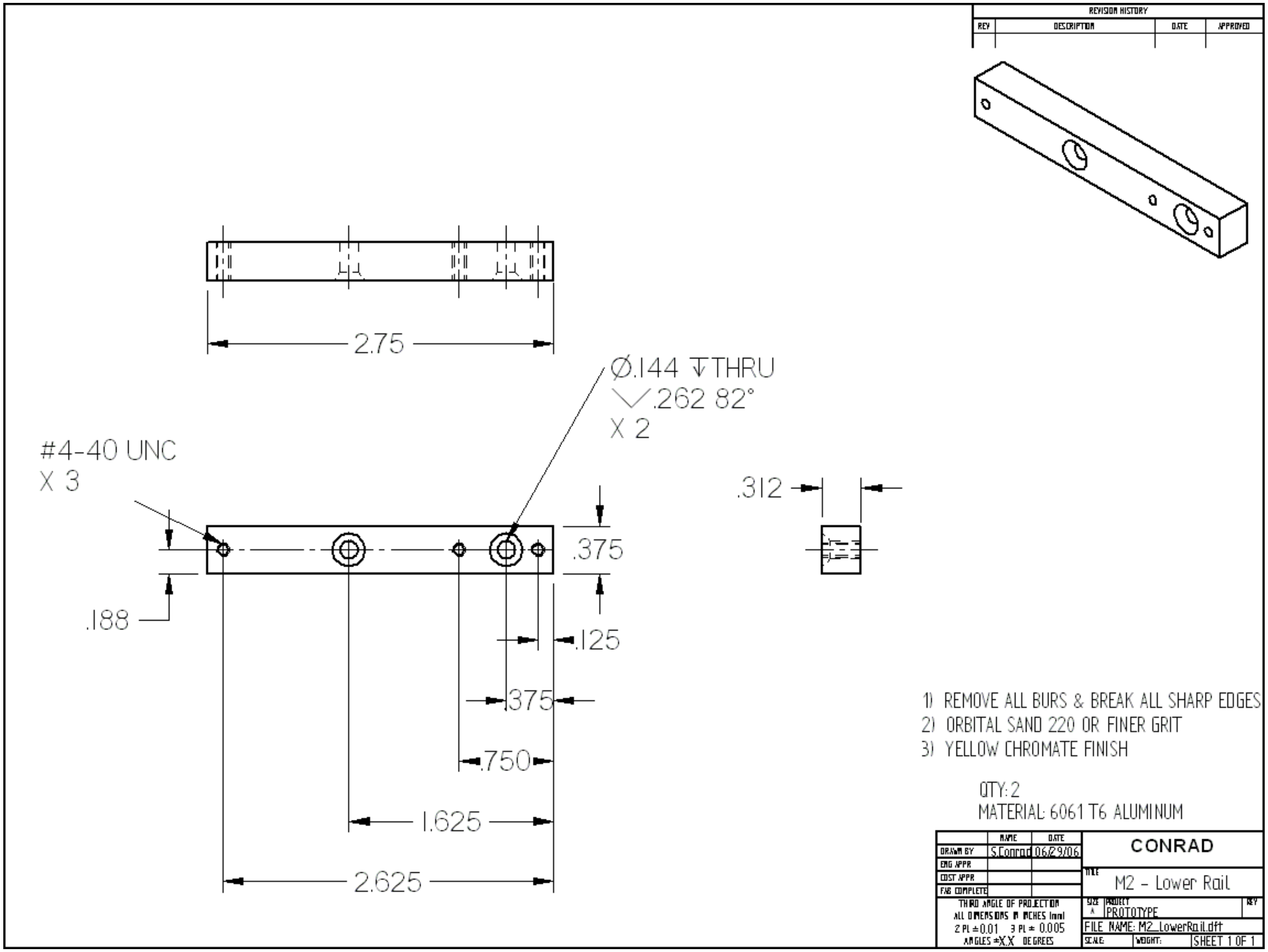

Figure B-33: Slider Mass - Lower Rail

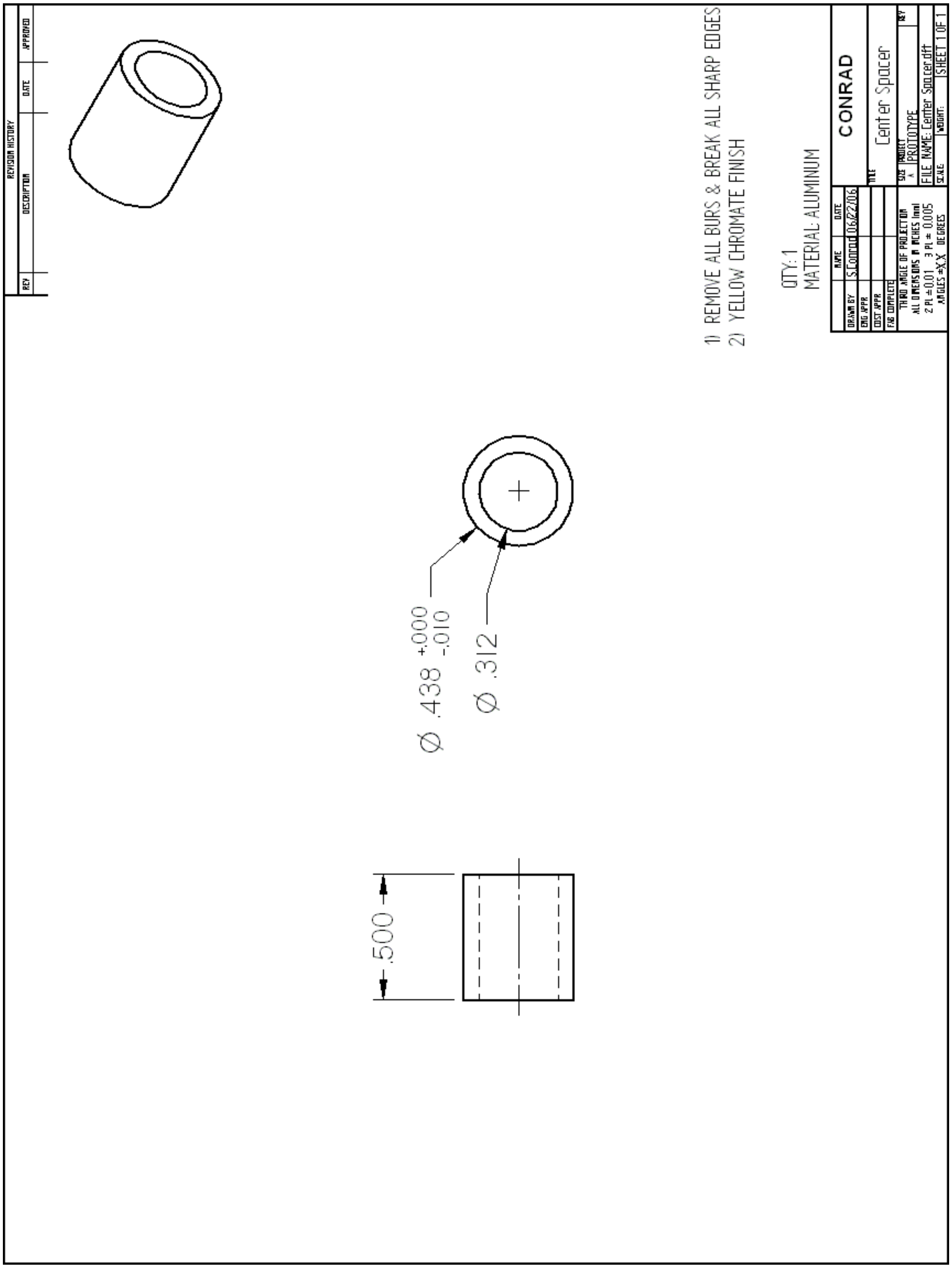

Figure B-34: Center Spacer

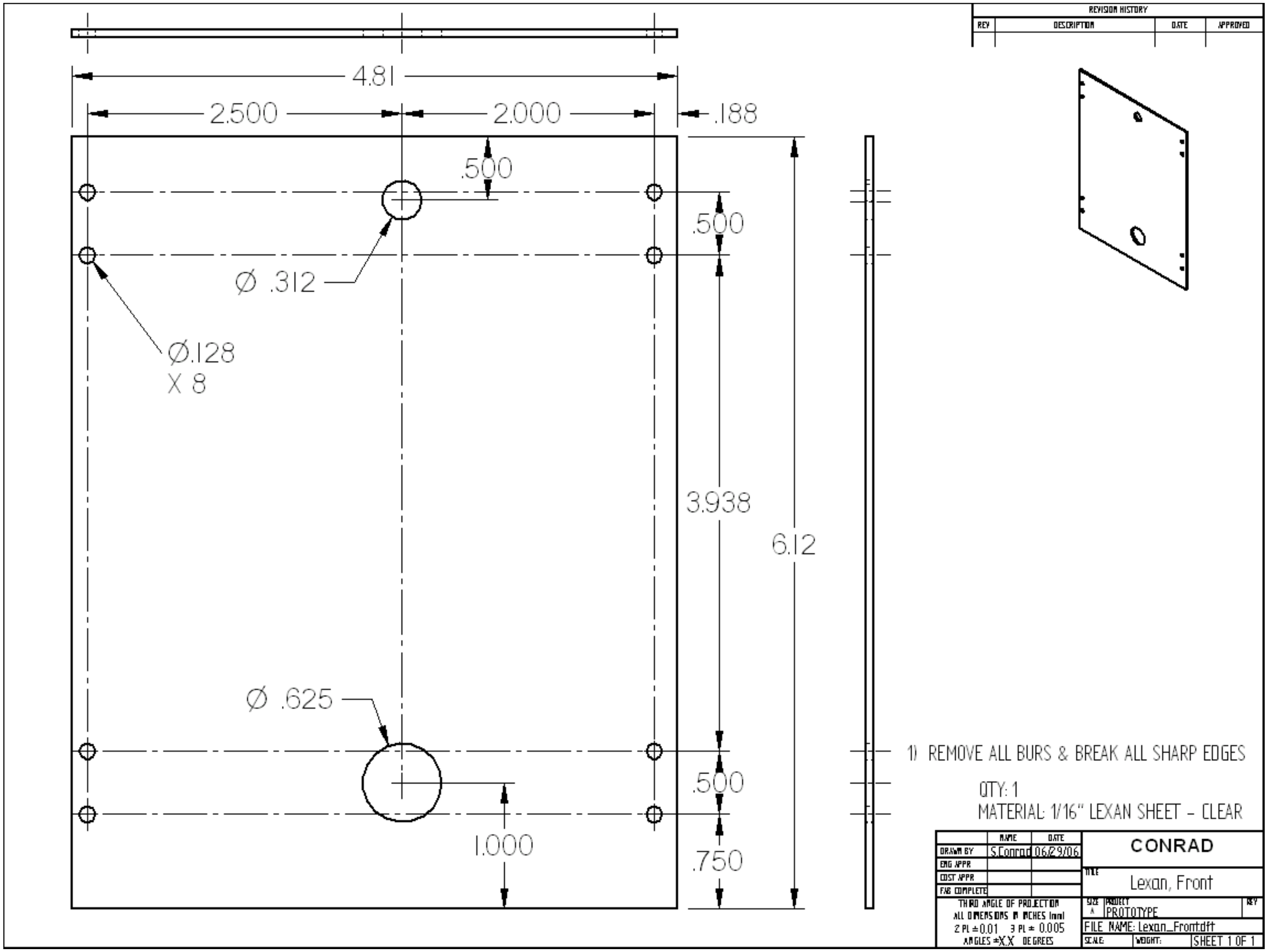

Figure B-35: Lexan Front

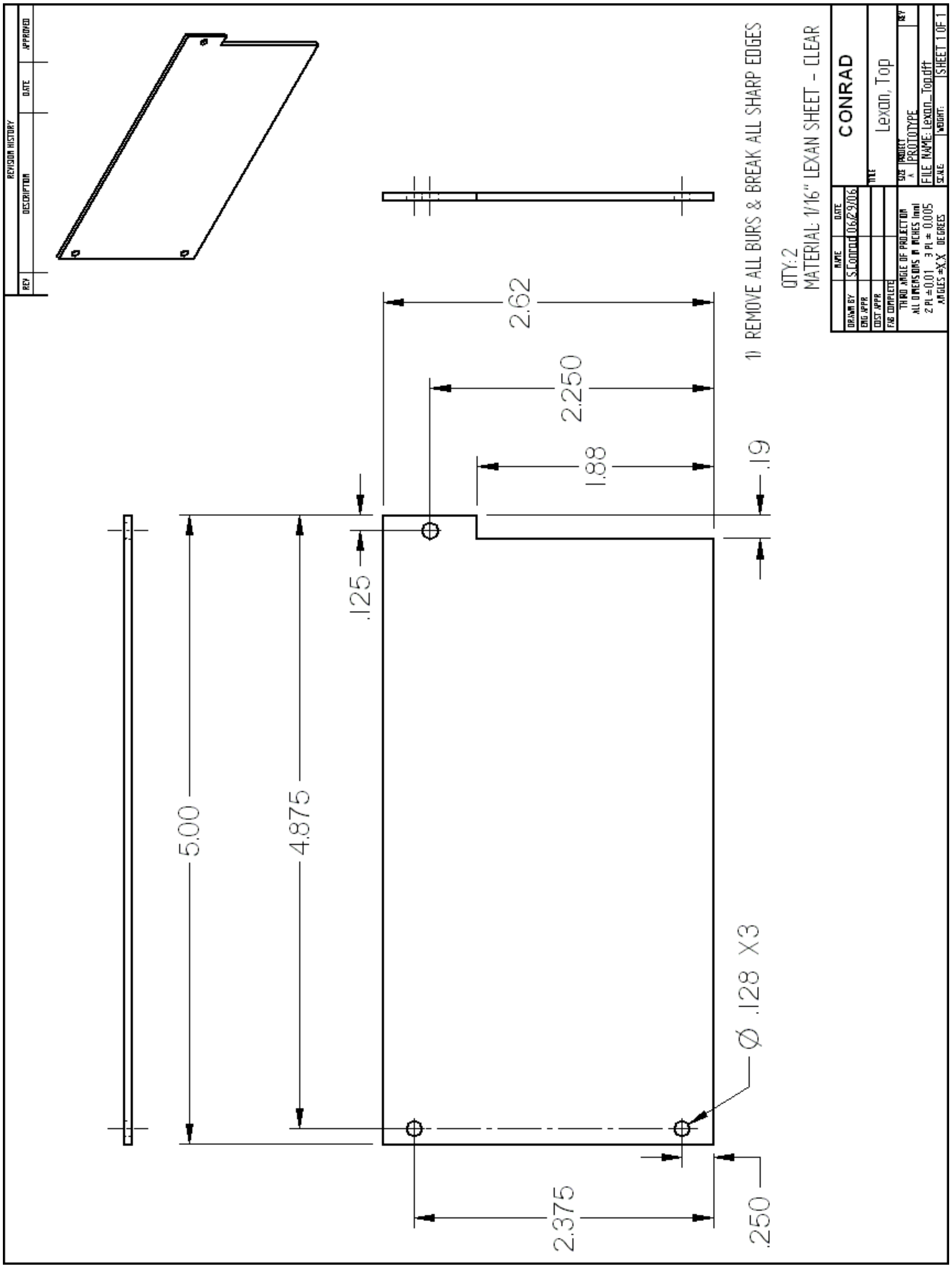

Figure B-36: Lexan Top

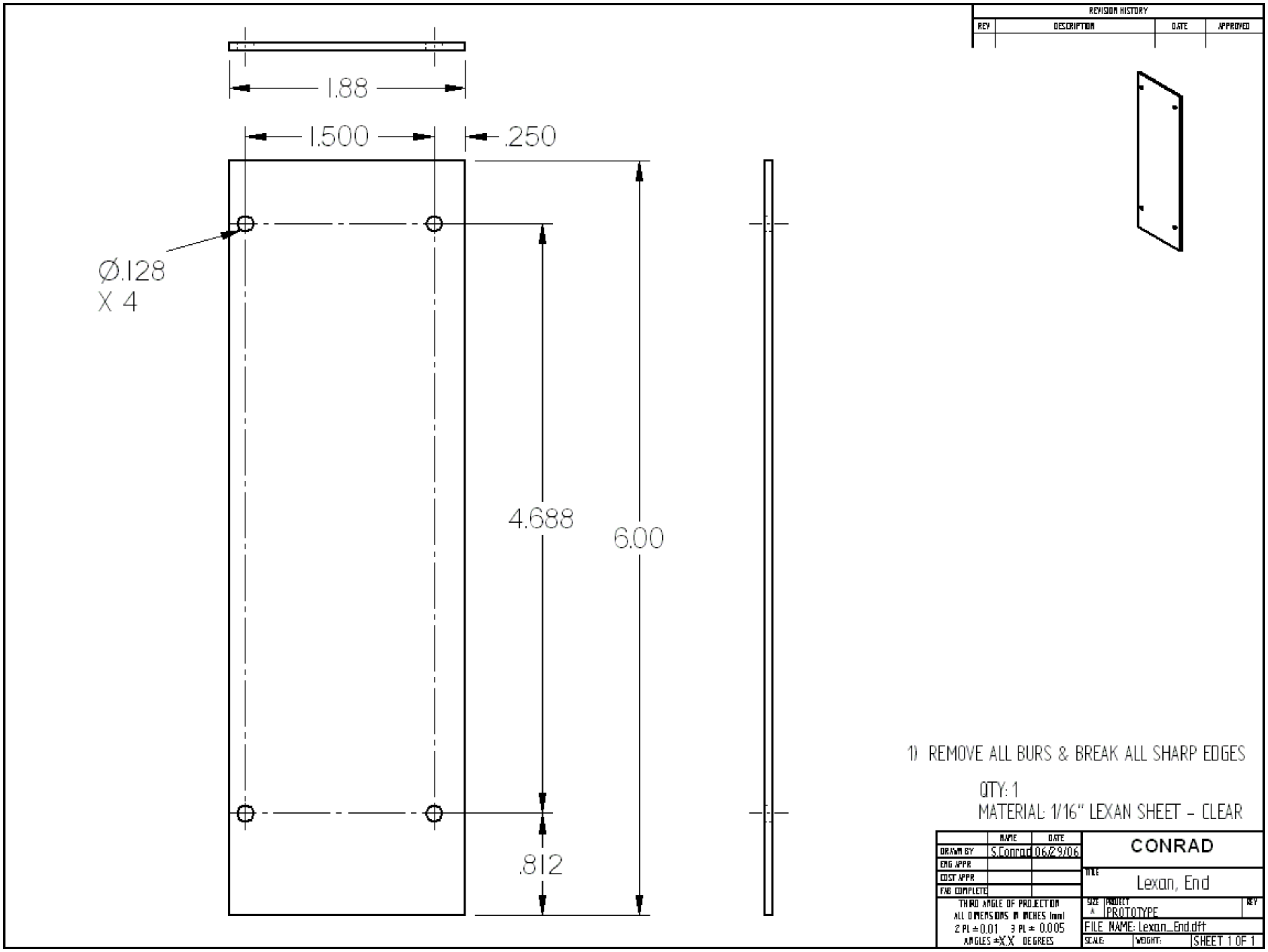

Figure B-37: Lexan End

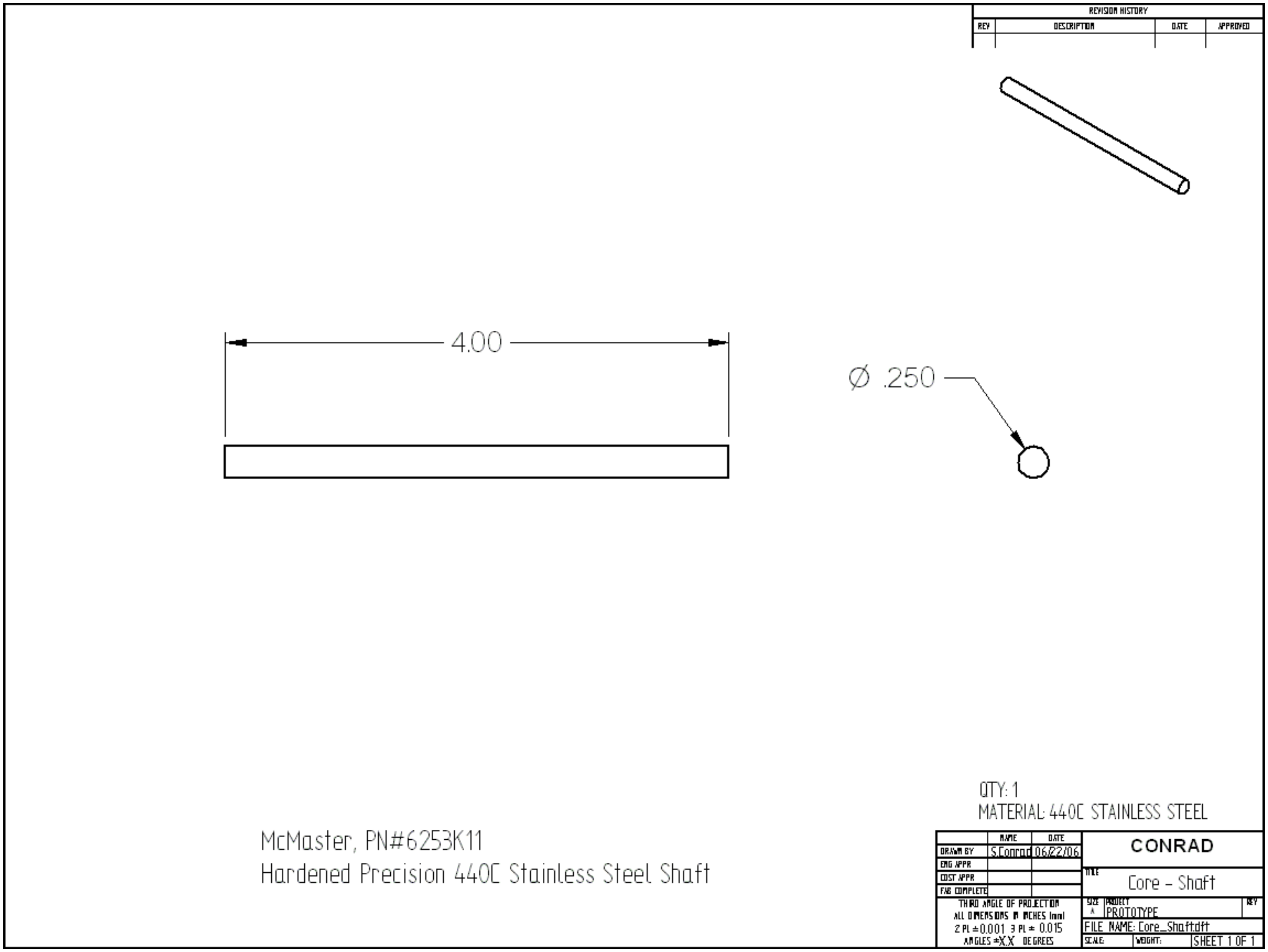

Figure B-38: Core - Shaft

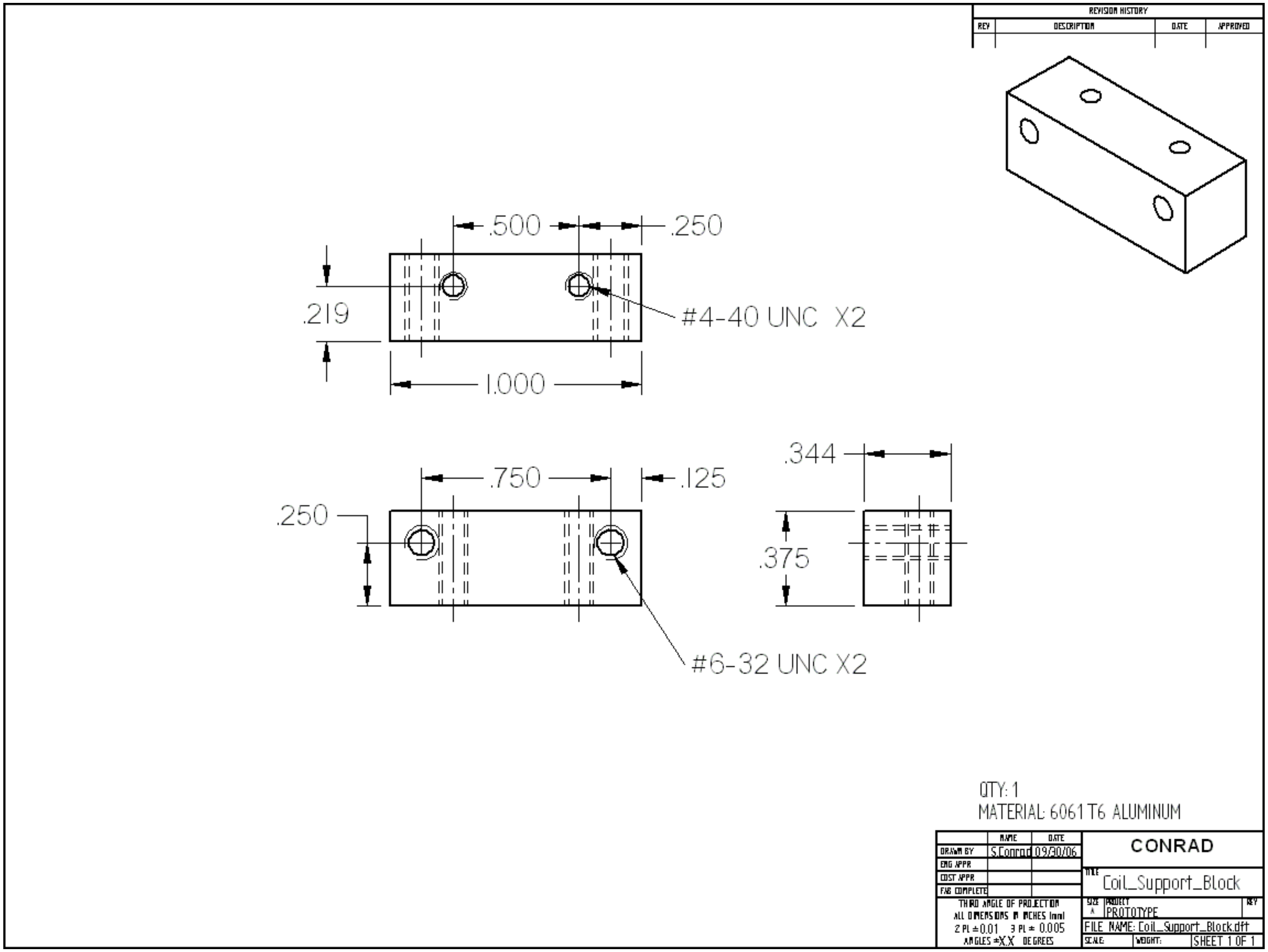

Figure B-39: Coil Support Block

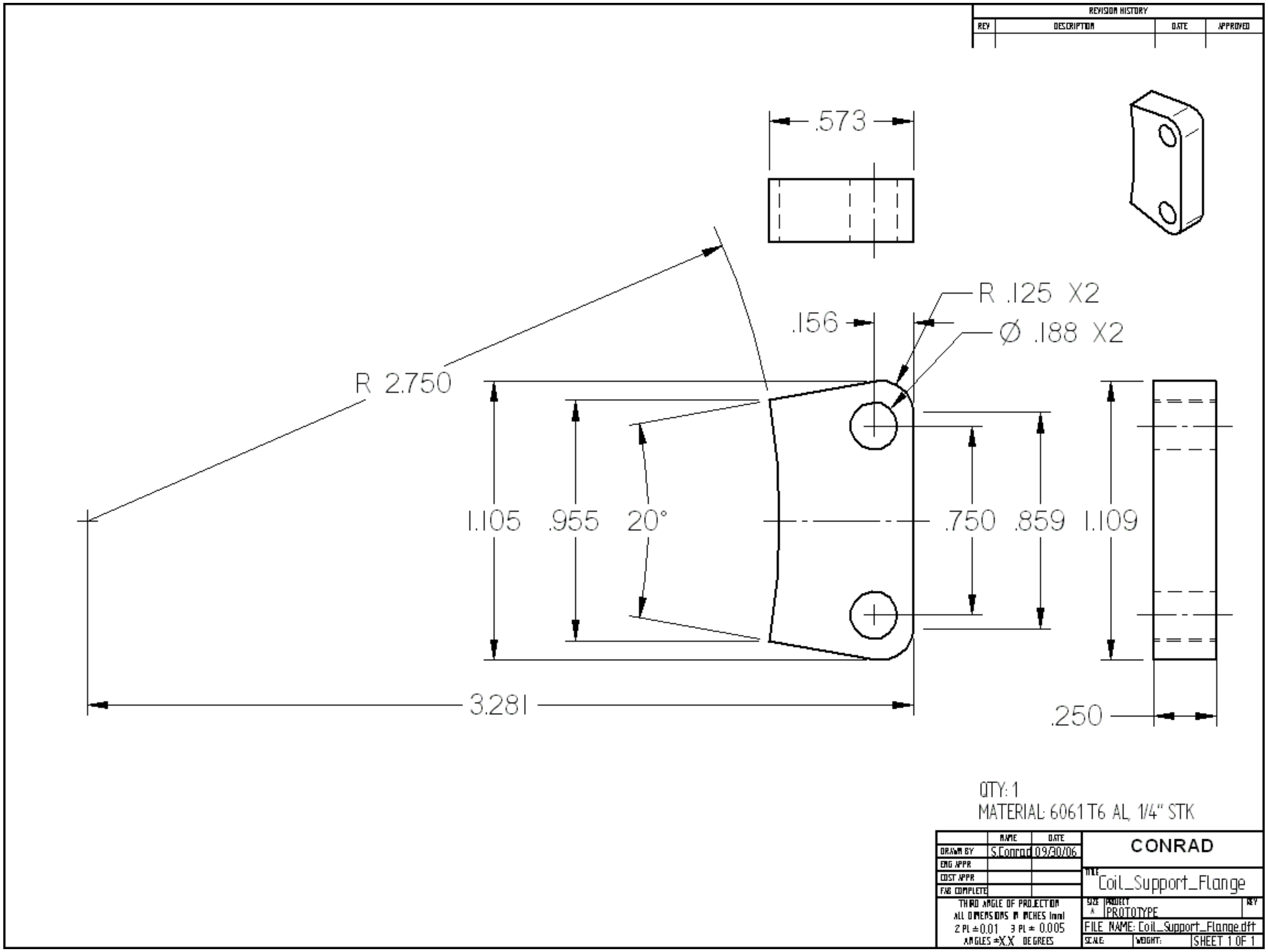

Figure B-40: Coil Support Flange

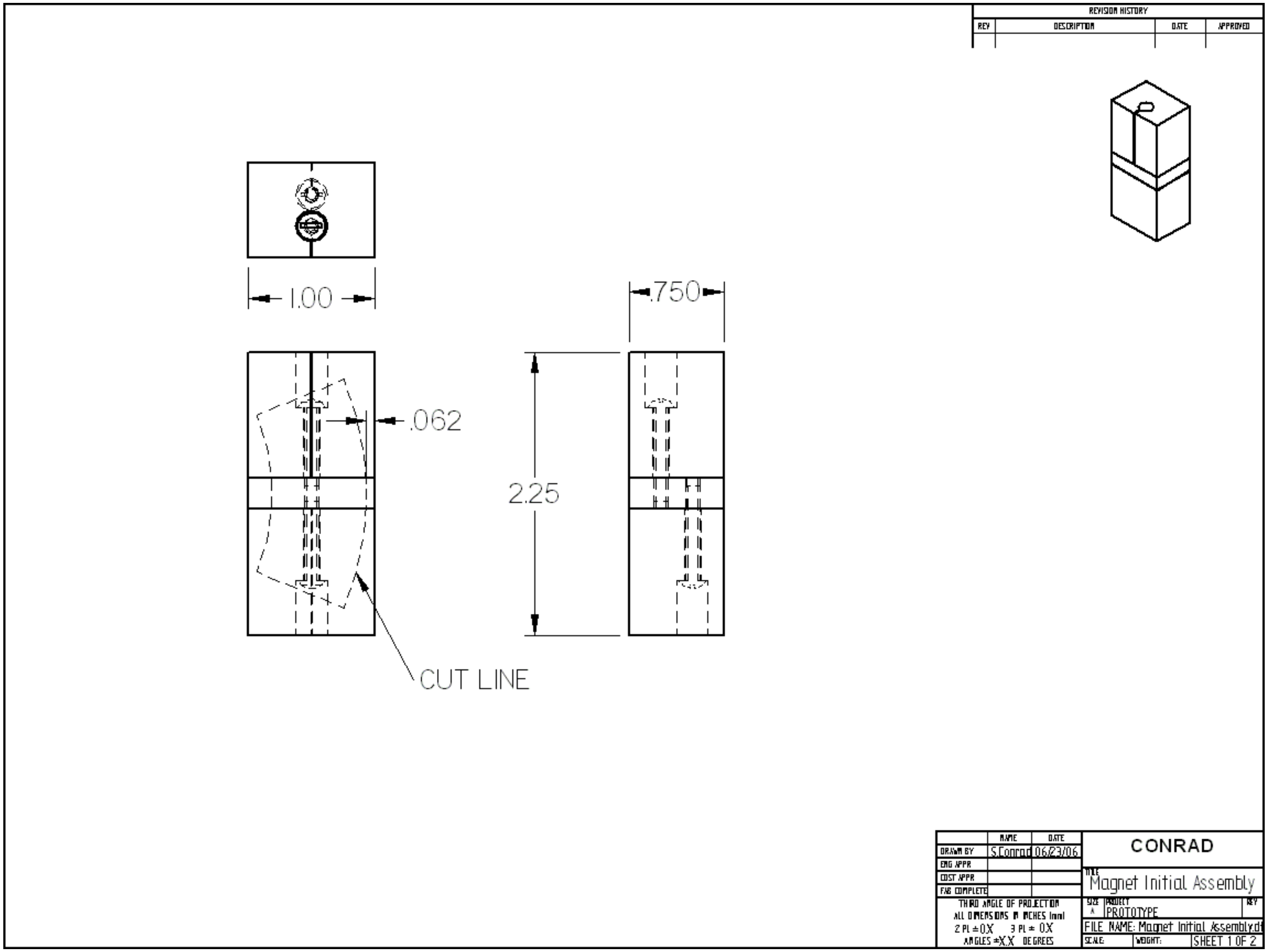

Figure B-41: Magnet Assembly Prior to Cutting

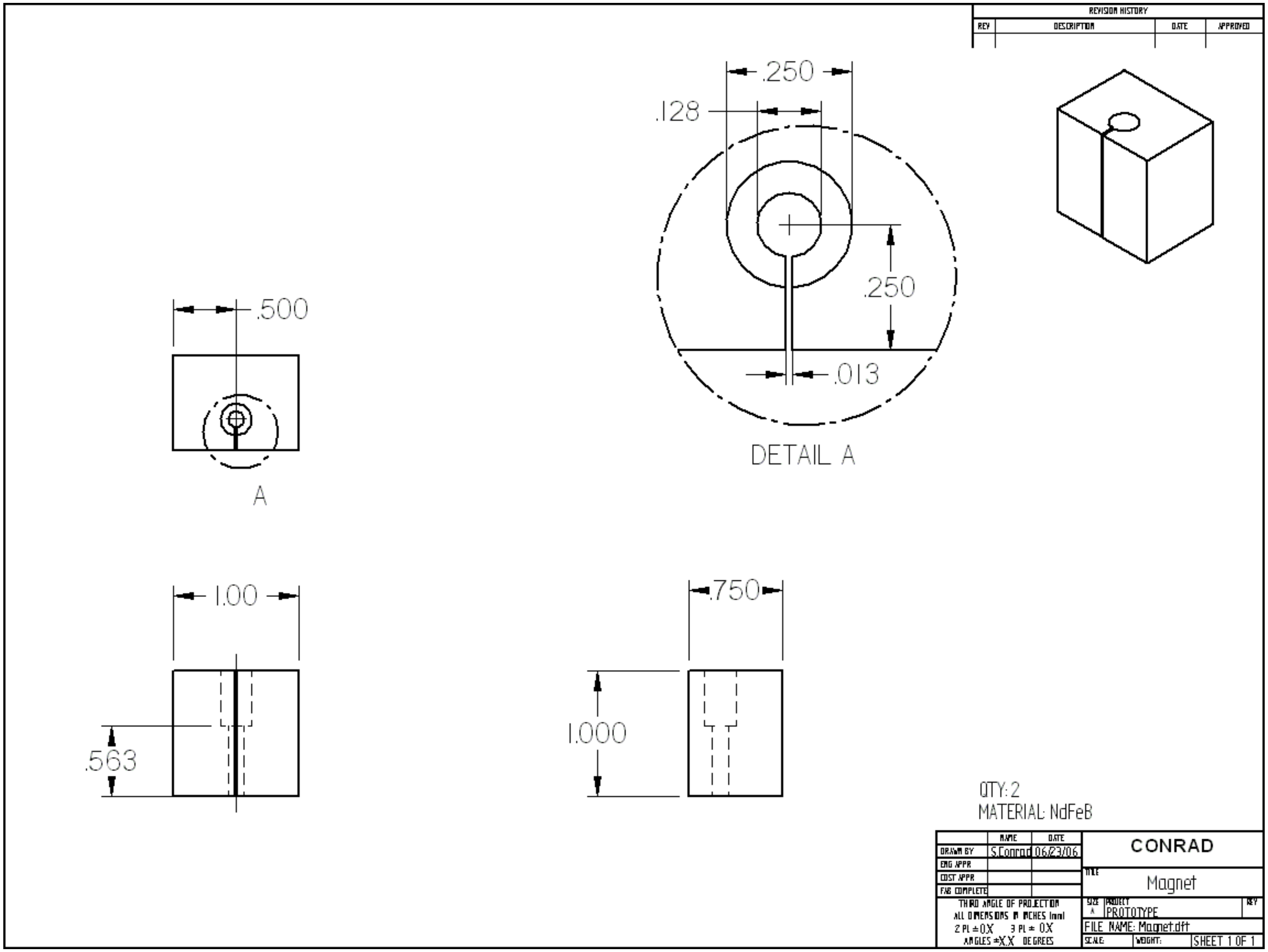

Figure B-42: Magnet Assembly - Magnet

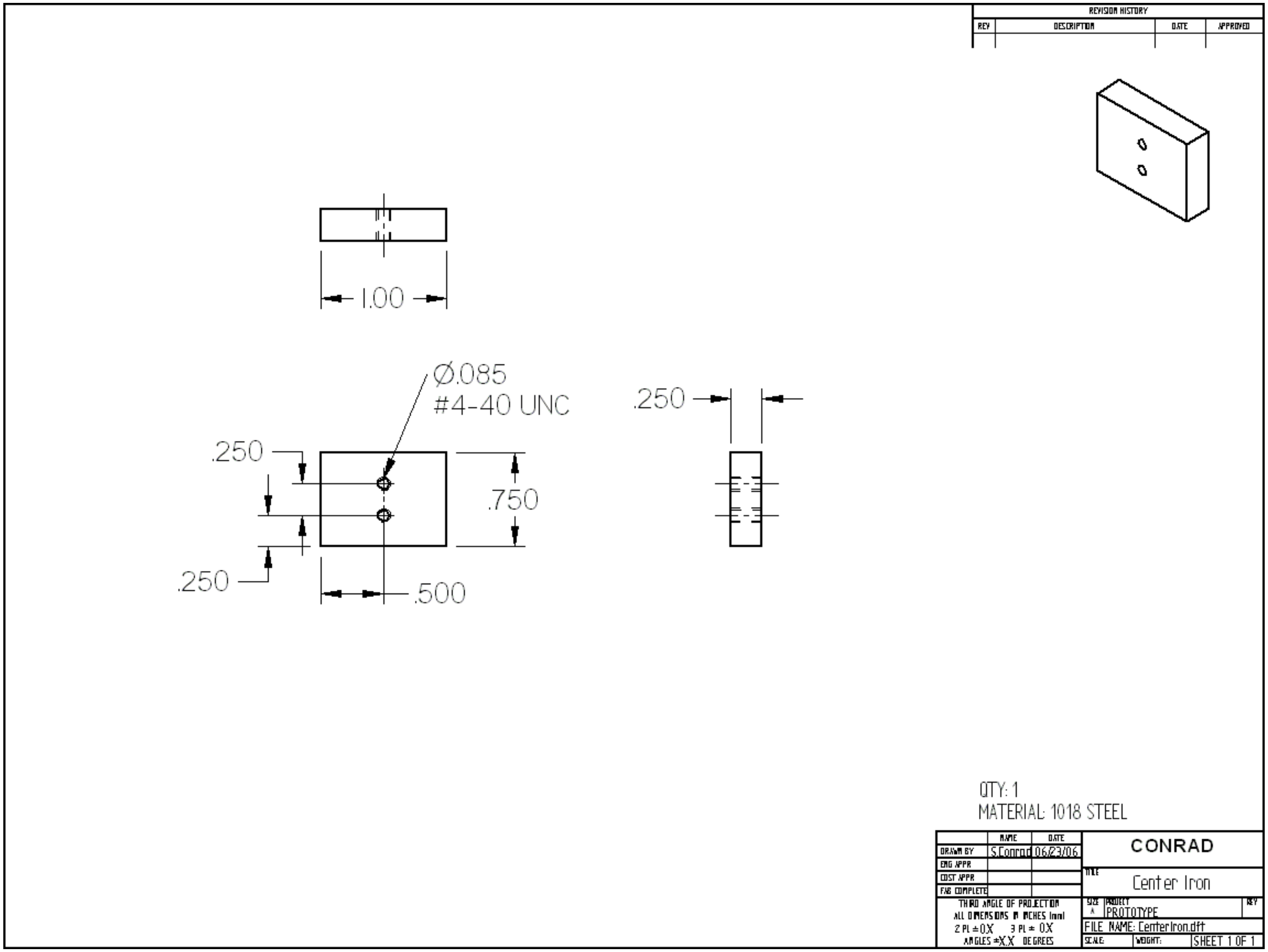

Figure B-43: Magnet Assembly Center Iron

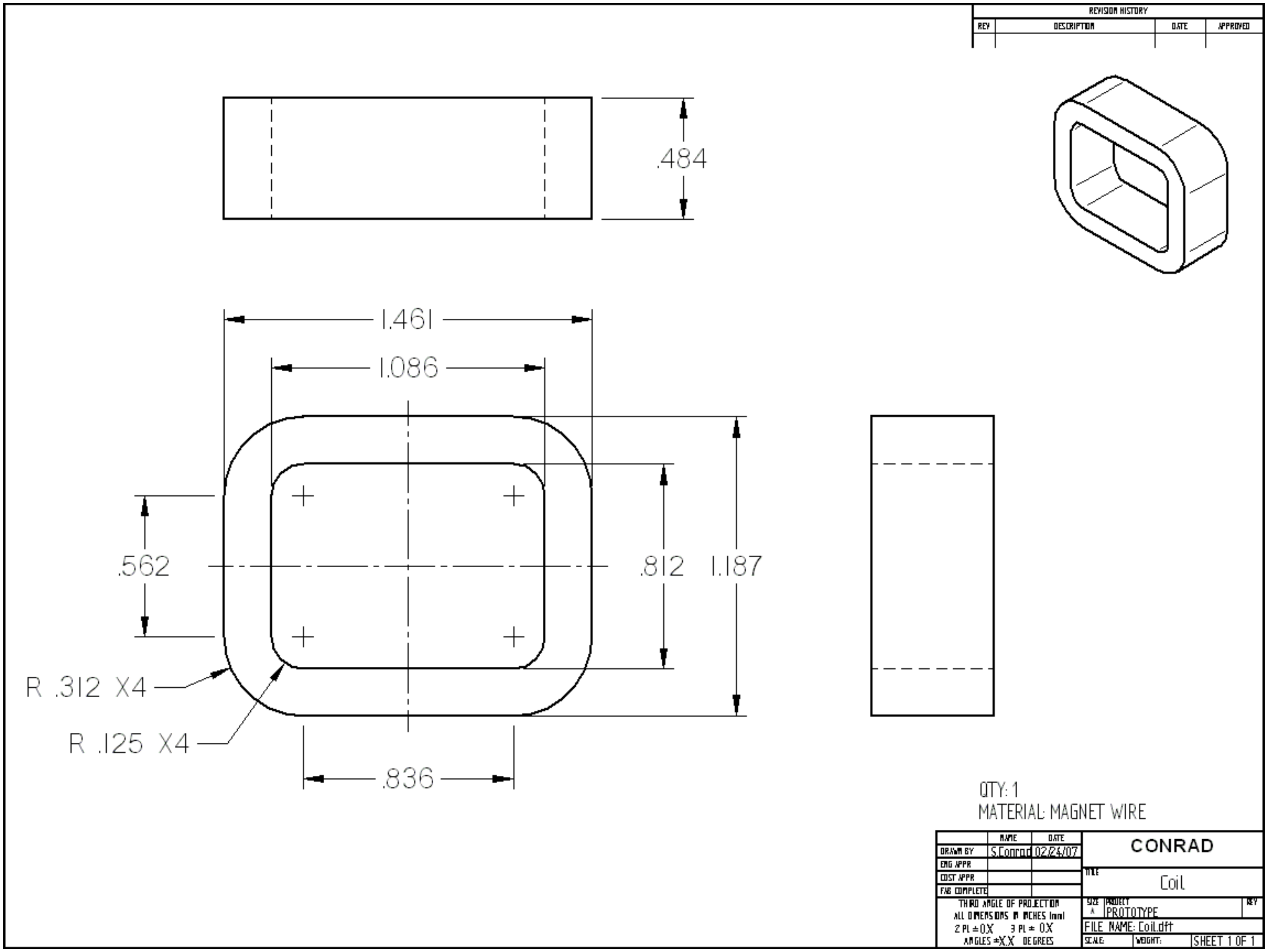

Figure B-44: Coil Dimensions

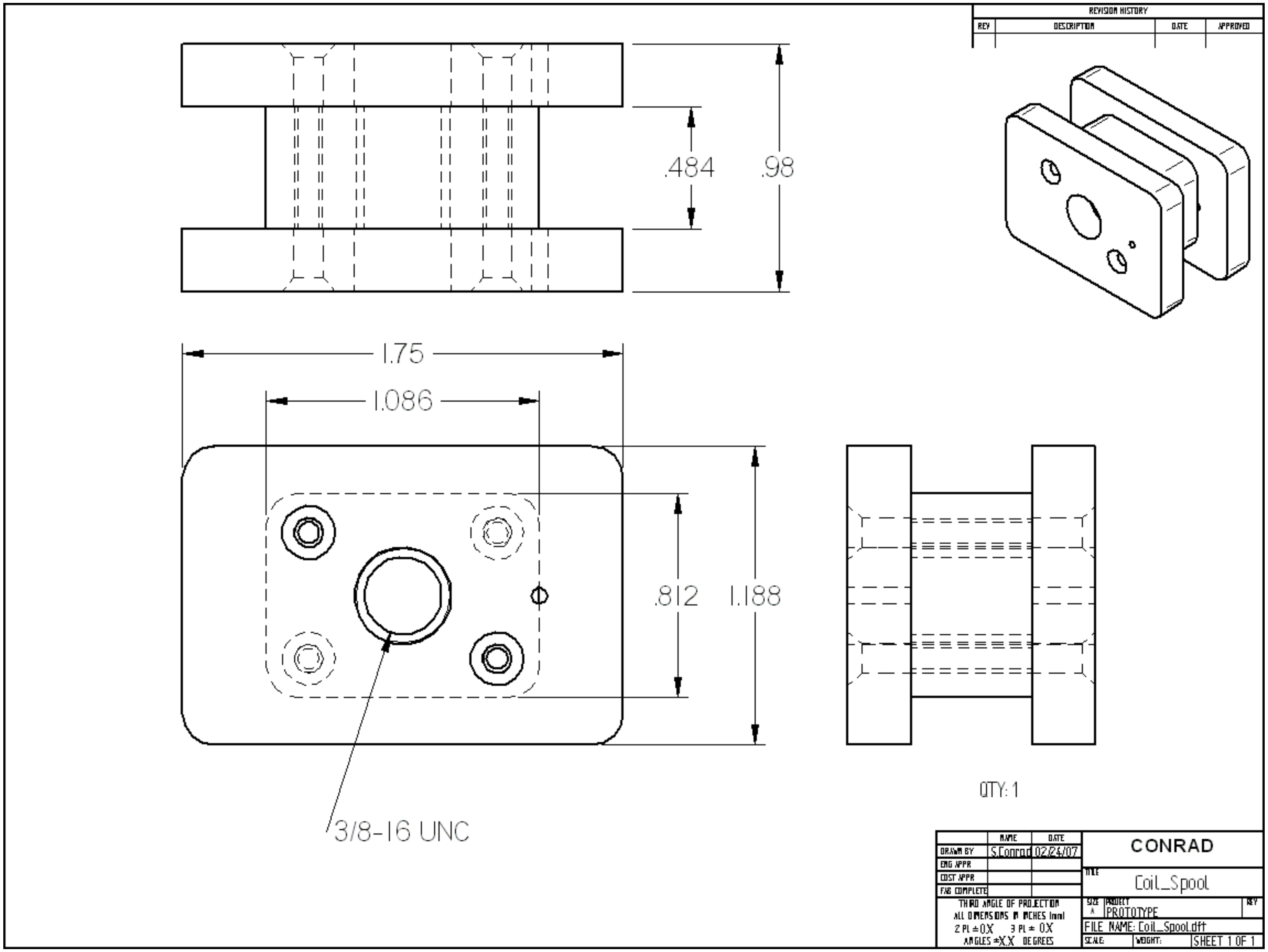

Figure B-45: Coil Winding Fixture Assembly

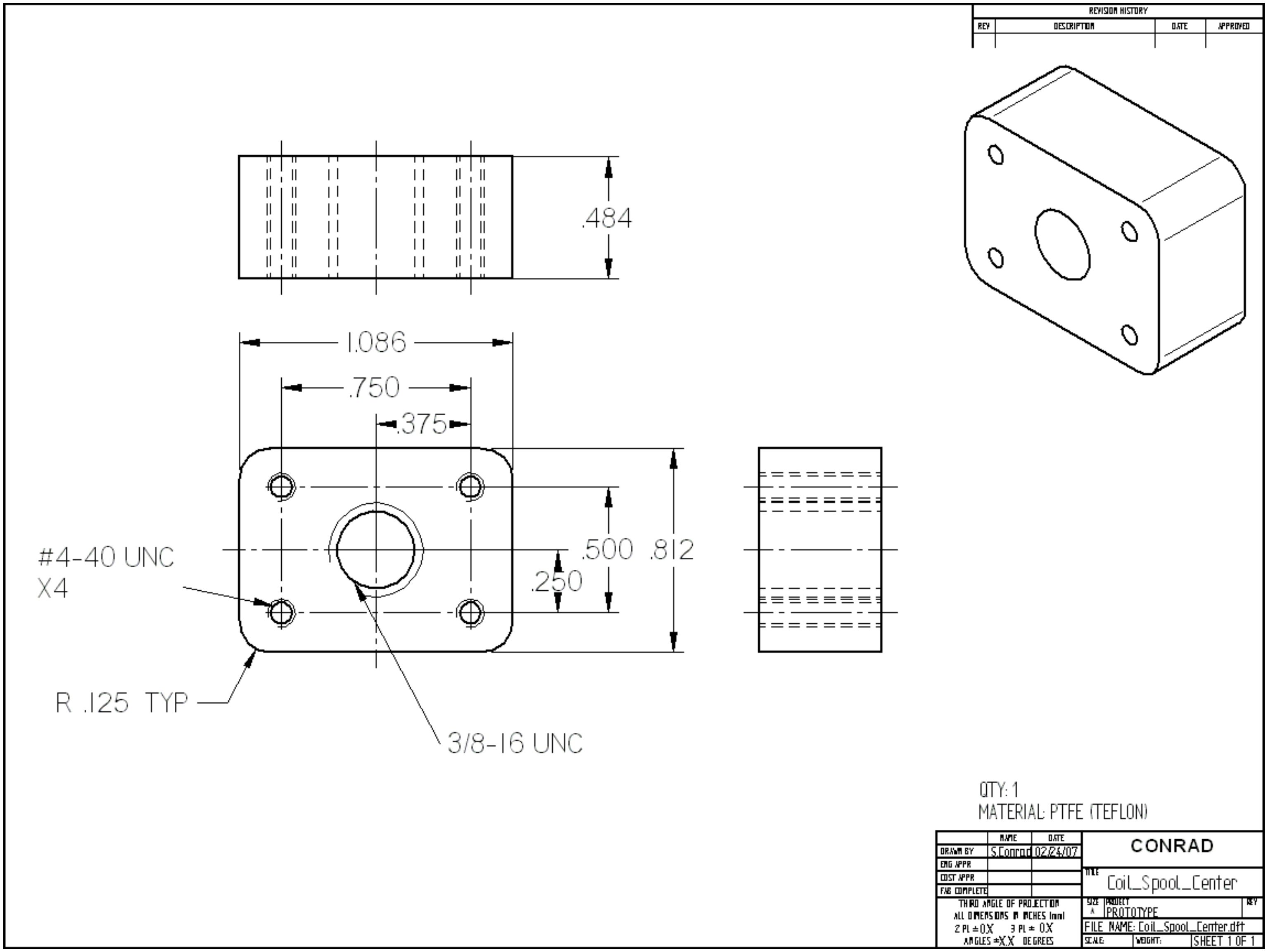

Figure B-46: Coil Winding Fixture - Center

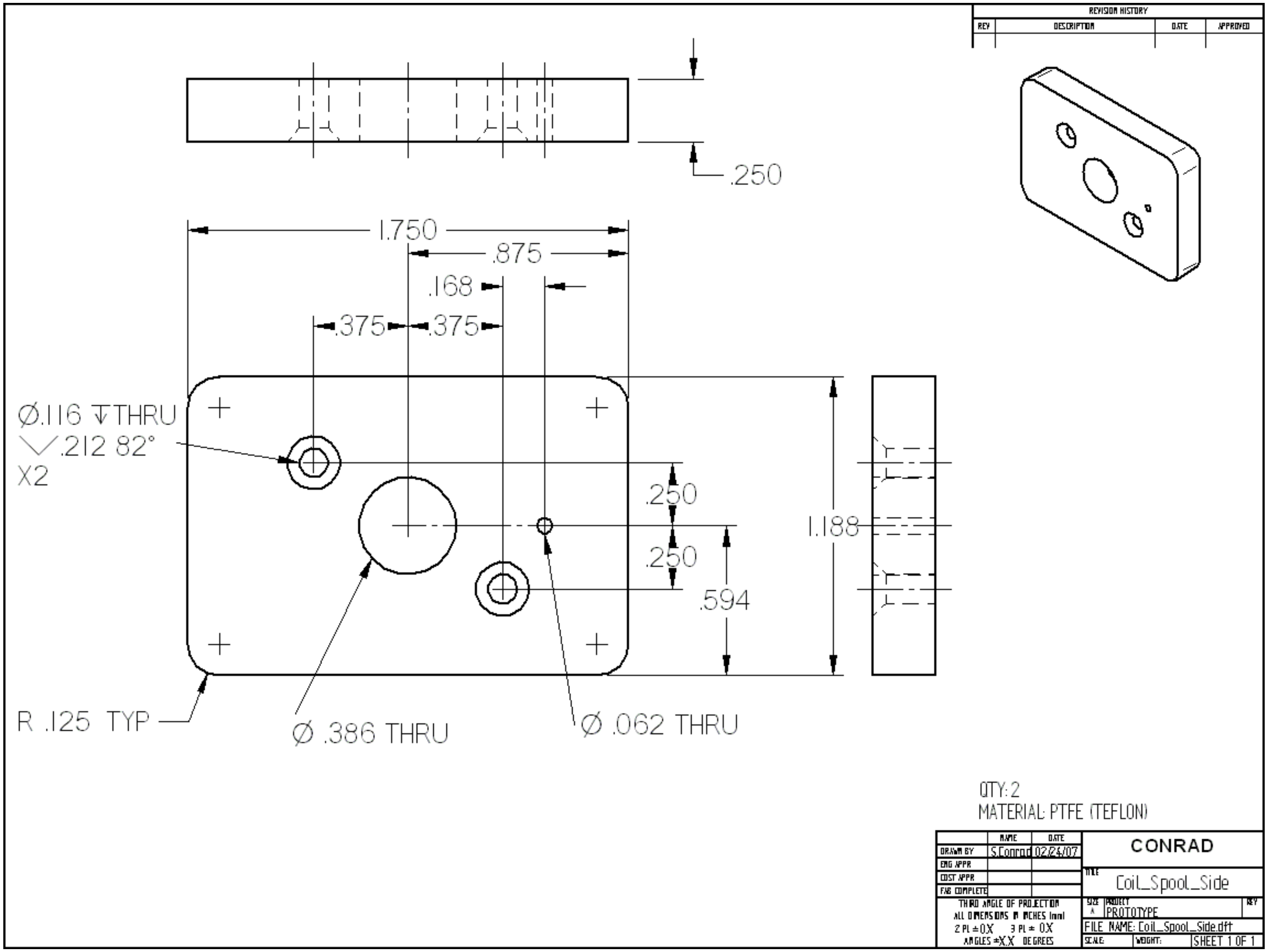

Figure B-47: Coil Winding Fixture - Side

Table B.1: Purchased parts used in prototype assembly.

Description	Qty	McMaster Part Number
Bearing, Needle Roller, 1/4" ID, 7/16" OD, 5/16 Wd	2	5905K21
Bearing, Ball, 3/16" ID, 1/2" OD, 5/32 Wd	5	60355K52
Bearing, Ball, 1/8" ID, 3/8" OD, 5/32 Wd	7	60355K51
PTFE Thrust Bearing, 1/4" ID, 5/8" OD, 1/16" THK	2	2796T11
Shoulder Screw, 3/16" Dia x 3/4", Alloy Steel	3	92012A207
Shoulder Screw, 1/8" Dia x 5/16", Alloy Steel	6	92012A517
Spacer, .192 ID, 5/16" OD, x 1/8", Aluminum	7	92510A560
Spacer, .140 ID, 1/4" OD, x 3/16", Aluminum	7	92510A441
Shaft, 1/4" x 6", 440C Stainless	1	6253K11
Shaft, 3/16" x 6", 17-4 PH Stainless	1	1162K52
Snap Rings, 3/16" Shaft	1	97633A120
Set Screw, #4-40 x .187"	4	92311A105
Screw, #1-64 x .187", Flat Head	4	91771A065
Screw, #1-64 x .25", Pan Head	3	91792A166
Screw, #4-40 x .250", Pan Head	10	91792A106
Screw, #4-40 x .500", Flat Head	44	91771A110
Screw, #4-40 x .750", Pan Head	2	92446A113
Screw, #6-32 x .875", Flat Head	4	91771A152
Screw, #6-32 x .750, Hex Head	8	93075A151
Screw, #10-24 x .625", Flat Head	4	91771A244
Bolt, 1/4"-20 x .875", Grade 5, Full Thread	4	92865A541
Bolt, 1/4"-20 x 1.5", Grade 5, Partial Thread	4	91247A546
Washer, 1/4"	8	90126A029
Nut #8-32	2	90480A009

Appendix C

Spin Stand Controls

The following figures show the details of the Control Desk Layout and the Simulink model that were used to automate the spin stand.

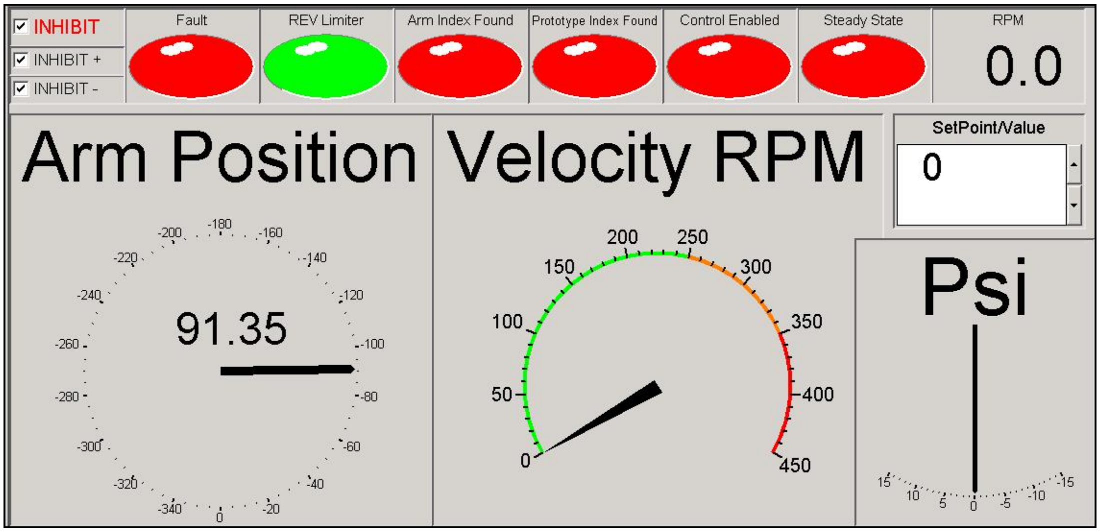

☑ INHIBIT
☑ INHIBIT +
☑ INHIBIT -

SetPoint/Value: 0

Figure C-1: Spin stand control desk layout

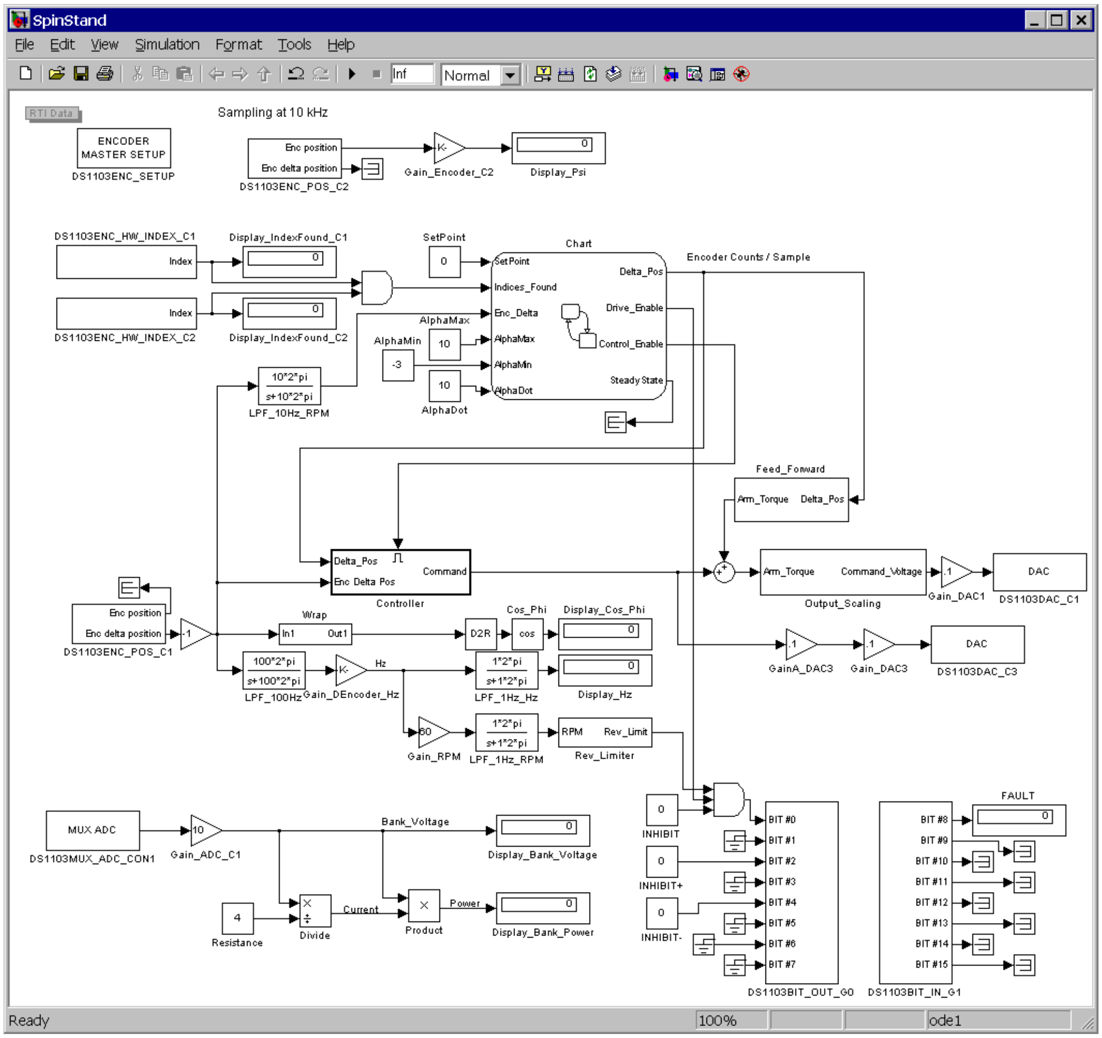

Figure C-2: Simulink model compiled to the DS1103 dSPACE board for spin stand control.

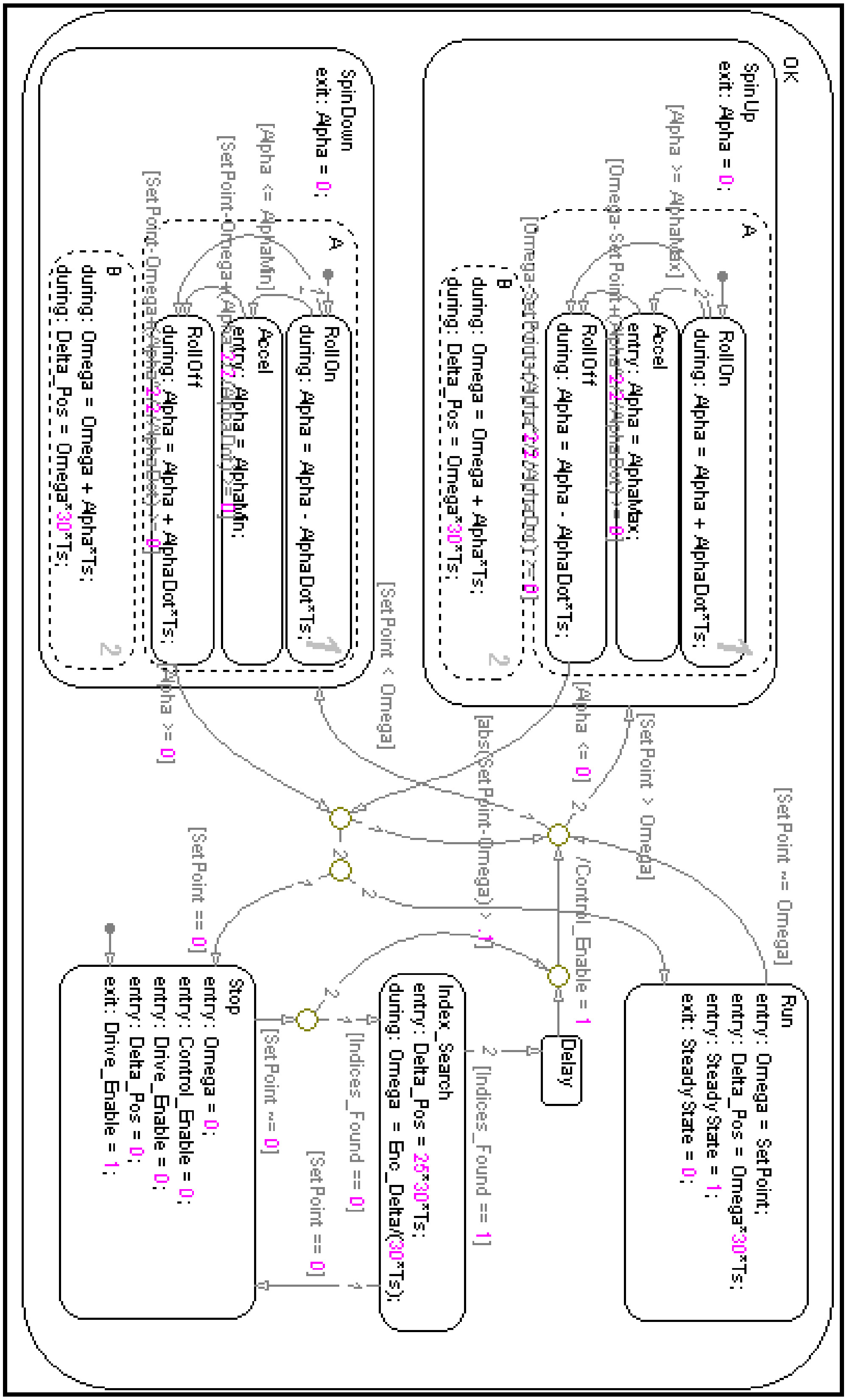

Figure C-3: Stateflow chart used for open loop indexing of the encoders and smooth trajectory generation.

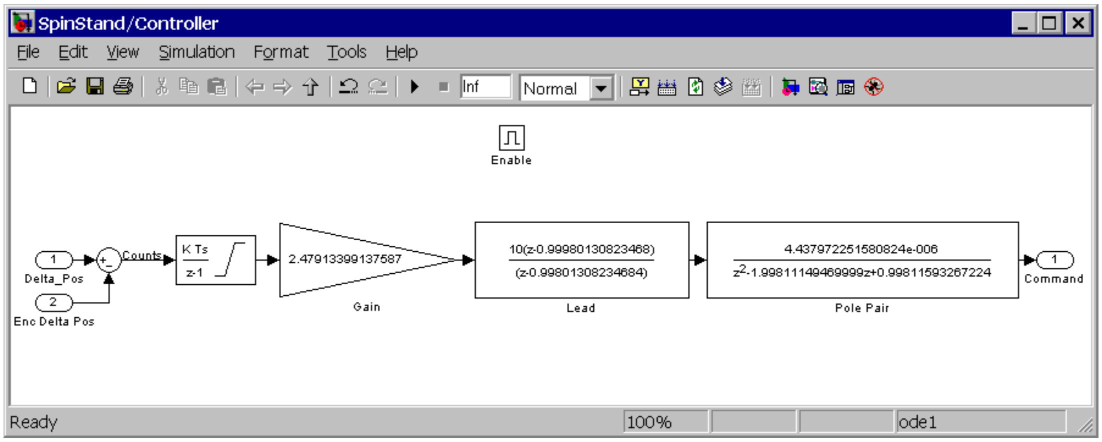

Figure C-4: Controller subsystem. Discrete time control blocks used for closed loop feedback control of arm position.

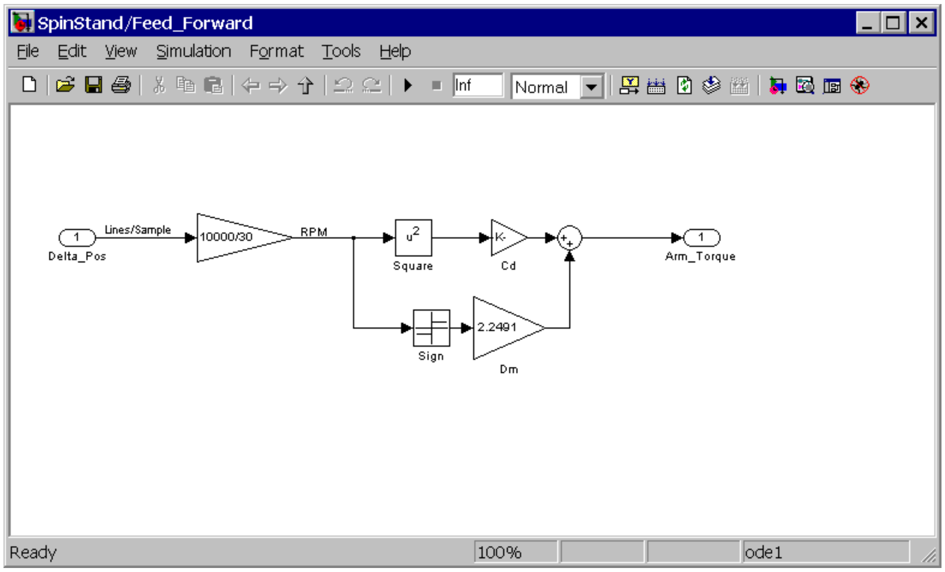

Figure C-5: Feed forward subsystem. Generates expected torque necessary to overcome wind drag and mechanical friction.

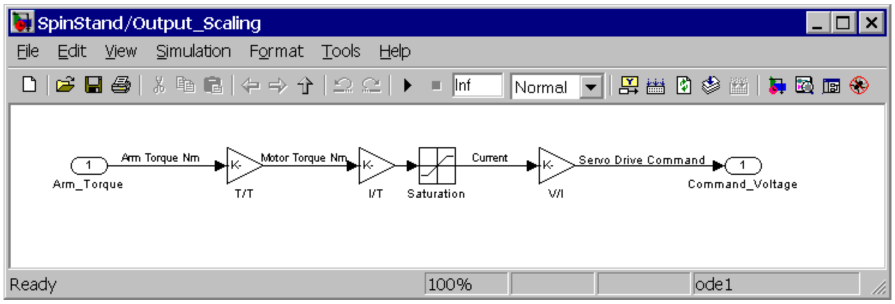

Figure C-6: Scaling subsystem. Converts from torque desired to voltage command from gear ratio, motor torque constant, and amplifier gain. Includes saturation to protect motor and amp in the event of any failure elsewhere in the diagram.

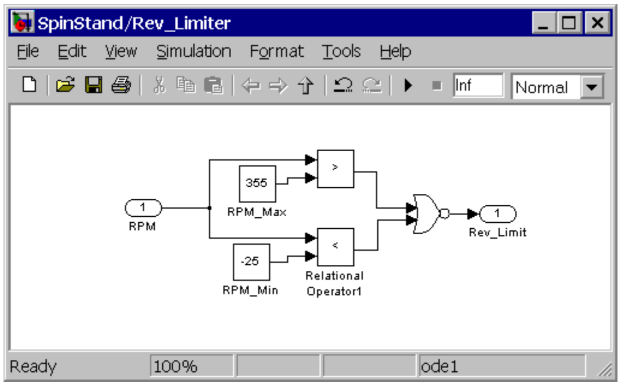

Figure C-7: Rev-limiter subsystem. Generates a signal to cut power to the amplifier if arm speed exceeds the forward or backward limits.

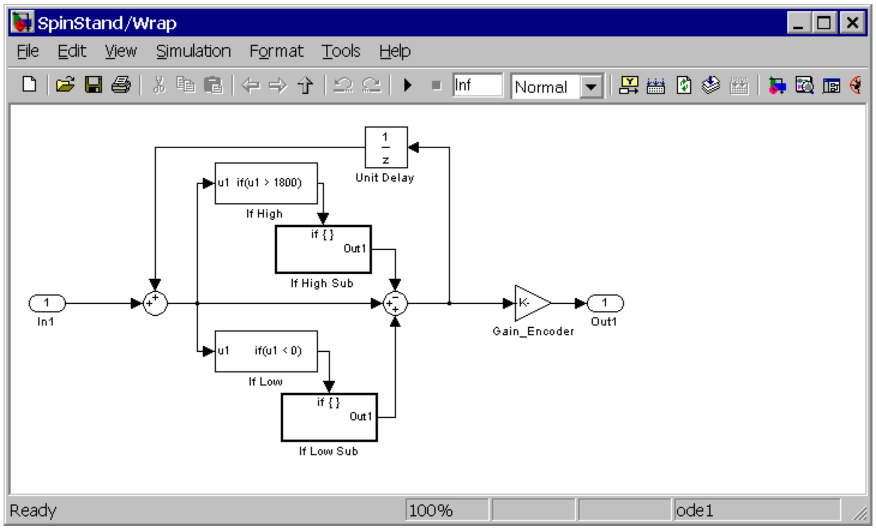

Figure C-8: Wrap subsystem. Keeps track of arm position as $0° \leq \phi \leq 360°$ without overflowing during extended continuous operation.

Bibliography

[1] J. Chambers. Personal communication. Documentation and electronic media, Nov 2004.

[2] A. Kasyap, J. Lim, D. Johnson, S. Horowitz, T. Nishida, K. Ngo, M. Sheplak, and L. Cattafesta. Energy reclamation from a vibrating piezoceramic composite beam. In *Proceedings of 9th International Congress on Sound and Vibration*, 2002. Orlando, FL, Paper No. 271.

[3] W. Kim and H. Maheshwari. High-precision control of a maglev linear actuator with nanopositioning capability. *Proceedings of the 2002 American Control Conference*, 5:4279–4284, May 2002.

[4] K. Lilienkamp and D. Trumper. Dynamic signal analyzer for dSPACE. In *Proceedings of the dSPACE User's Conference*, May 2000.

[5] P. Mitcheson, T. Green, E. Yeatman, and A. Holmes. Analysis of optimized micro-generator architectures for self-powered ubiquitous computers. In *Adjunct Proceedings UBICOMP 2002, Ubiquitous Computing 4th International Conference*, pages 5–6, Oct 2002.

[6] D. Opila, A. Annaswamy, W. Krol, and S. Raghu. Biomimetic reduction of wake deficit using tail articulation at low Reynolds number. *IEEE Transactions on Ocean Engineering*, 29(3):766–776, July 2004.

[7] G. Ottman, H. Hofmann, and G. Lesieutre. Optimized piezoelectric energy harvesting circuit using step-down converter in discontinuous conduction mode. *IEEE Transactions on Power Electronics*, 18(2):696–703, Mar 2003.

[8] S. Roundy. On the effectiveness of vibration-based energy harvesting. *Journal of Intelligent Material Systems and Structures*, 16(10):809–823, 2005.

[9] S. Roundy, E. Leland, J. Baker, E. Carleton, E. Reilly, E. Lai, B. Otis, J. Rabaey, V. Sundararajan, and P. Wright. Improving power output for vibration-based energy scavengers. *IEEE Pervasive Computing*, 04(1):28–36, 2005.

[10] S. Roundy, P. Wright, and J. Rabaey. A study of low level vibrations as a power source for wireless sensornodes. *Computer Communications*, 26(11):1131–1144, July 2003.

[11] S. Roundy and Y. Zhang. Toward self-tuning adaptive vibration-based microgenerators. In *Proceedings of the SPIE, Smart Structures, Devices, and Systems II*, volume 5649, pages 373–384, Feb 2005.

[12] R. Torah, S. Beeby, M. Tudor, T. O'Donnell, and S. Roy. Development of a cantilever beam generator employing vibration energy harvesting. In *Proceedings of The 6th International Workshop on Micro and Nanotechnology for Power Generation and Energy Conversion Applications*, pages 181–184, 2006.

[13] M. Umeda, K. Nakamura, and S. Ueha. Analysis of the transformation of mechanical impact energy to electric energy using piezoelectric vibrator. *Japanese Journal of Applied Physics*, 35:3267–3273, May 1996.

[14] S. Verma, Won jong Kim, and H. Shakir. Multi-axis maglev nanopositioner for precision manufacturing and manipulation applications. *IEEE Transactions on Industry Applications*, 41(5):1159–1167, Sept-Oct 2005.

[15] T. von Büren, P. Lukowicz, and G. Tröster. Kinetic energy powered computing - An experimental feasibility study. In *Proceedings of the Seventh IEEE International Symposium on Wearable Computers*, pages 22–24, 2003.

[16] C. Williams, C. Shearwood, M. Harradine, P. Mellor, T. Birch, and R. Yates. Development of an electromagnetic microgenerator. *Electronics Letters*, 33(22):1883–1884, Oct 1997.

[17] C. Williams and R. Yates. Analysis of a micro-electric generator for microsystems. *The 8th International Conference on Solid-State Sensors and Actuators*, 1:369–372, Jun 1995.